UNIVERSITAT POLITÈCNICA
DE CATALUNYA
BARCELONATECH

Computational uncertainty quantification in pressure-driven fracture processes

Hasini Garikapati

UNIVERSITAT POLITÈCNICA
DE CATALUNYA
BARCELONATECH

Computational uncertainty quantification in pressure-driven fracture processes

PROEFSCHRIFT

ter verkrijging van de graad van doctor aan de
Technische Universiteit Eindhoven, op gezag van de
rector magnificus prof.dr.ir. F.P.T. Baaijens, voor
een commissie aangewezen door het College voor
Promoties, in het openbaar te verdedigen op
dinsdag 10 maart 2020 om 13:30 uur

door

Hasini Garikapati
geboren te Guntur, India

Dit proefschrift is goedgekeurd door de promotoren en de samenstelling van de promotiecommissie is als volgt:

voorzitter:	prof.dr.ir.	L.P.H. de Goey
1e promotor:	prof.dr.ir.	E.H. van Brummelen
2e promotor:	prof.dr.	P. Díez (Polytechnic University of Catalonia)
copromotoren:	dr.ir.	C.V. Verhoosel
	dr.	S. Zlotnik (Polytechnic University of Catalonia)
leden:	prof.dr.	L. De Lorenzis (Technical University of Braunschweig)
	dr.	F. Nobile (Swiss Federal Institute of Technology in Lausanne)
	prof.dr.ir.	D.M.J. Smeulders

Het onderzoek of ontwerp dat in dit proefschrift wordt beschreven is uitgevoerd in overeenstemming met de TU/e Gedragscode Wetenschapsbeoefening.

Computational uncertainty quantification in pressure-driven fracture processes

Hasini Garikapati

The work in this dissertation has been funded by the European Commission EACEA Agency, Framework Partnership Agreement Erasmus Mundus Action 1b, as a part of the *EM Joint Doctorate Simulation in Engineering and Entrepreneurship Development (SEED).*

Printed by ADC Dereumaux
Cover design by Hasini Garikapati

A catalogue record is available from the Eindhoven University of Technology Library
ISBN: 978-90-386-5008-1

Preface

My fascination for computational mechanics started when I was working at the Indian Space Research Organization where I used Ansys and Solidworks to simulate solid stage casting and, design structures that support solid propulsion stage in a launch vehicle. It took a decade to convert my interest to reality in the form of masters and a PhD in this field.

This dissertation titled Computational uncertainty quantification in pressure-driven fracture processes has been a result of my work from May 2015 to January 2020. This is a part of the Erasmus Mundus Joint Doctorate program Simulation in Engineering and Entrepreneurship Development (EMJD-SEED). The research has been carried at Multiscale Engineering Fluid Dynamics group - Eindhoven University of Technology and Mathematical and Computational Modeling group - Polytechnic University of Catalonia (UPC).

With an increase in computational power and available data resources, computational uncertainty quantification has been gaining popularity. Computational uncertainty quantification is a broad field involving methods of sensitivity analysis, inverse analysis, and uncertainty propagation. In this thesis, state-of-the-art uncertainty quantification techniques are applied in simulation techniques for pressure-driven fracturing processes.

This dissertation is a collaboration of all the meetings, insights, constructie criticism that came from my supervisors. Firstly I would like to express my gratitude to Harald van Brummelen who has given me this opportunity to work in his group. My daily supervisor Clemens Verhoosel whose incessant guidance has helped me to improve my work all along. Next, I would like to thank my supervisors Pedro Díez and Sergio Zlotnik at UPC. I am glad to be associated with such experts from this community of computational mechanics.

I sincerely thank my committee members Laura De Lorenzis, Fabio Noble and David Smeulders for reading my thesis and providing such valuable feedback.

I had thoroughly enjoyed and gained a lot of knowledge in discussions with my colleagues at Eindhoven and Barcelona. A special mention to Gertjan van Zwieten for his unwavering support and assistance of Nutils software. While

supervising Jassin van de Poll's master thesis, my understanding of Bayesian methods improved as a result of many fruitful discussions. A special mention to Albert Sibileau who helped me to expedite my understanding of Proper Generalized Decomposition while I was in Barcelona.

Through my PhD, I learnt that the only certainty is uncertainty, yet there are ways to quantify and prepare for it. This journey has only increased my fascination with computational mechanics.

Hope you enjoy reading.

Hasini Garikapati,
Veldhoven, February 2020.

Contents

Chapter 1

Introduction

1.1 Motivation and background

A proper understanding of pressure-driven fracture processes can benefit a wide range of areas in science and engineering. Pressure-driven fracture processes are of particular interest in the field of hydraulic stimulation, which has been applied for decades in the oil and gas industry to increase the productivity of low permeability reservoirs. This method can broadly be defined as a well-stimulation technique that injects a hydraulic fracturing fluid into a well, to create or propagate fractures in the oil or gas reservoir rock, which facilitates the extraction of oil and gas (see Figure 1.1). For instance, in the United States, the number of fossil fuel reserves considerably increased due to the advent of hydraulic fracturing technology. Hydraulic stimulation has also been applied in other geomechanical fields, including the disposal of underground waste drill-cuttings [1], heat extraction from geothermal reservoirs [2], carbon dioxide sequestration [3], coal bed methane recovery [4], and gas control in coal mines [5].

Despite the commercial benefits of hydraulic fracturing, it has not passed the exploratory phase in either The Netherlands or the EU in general. In fact, there is currently no shale gas extracted in The Netherlands. One of the main risks associated with hydraulic fracturing is the contamination of groundwater resources, due to the usage of chemicals in the process. Such risks can be assessed by developing high fidelity models which can accurately predict the process, so that sufficient care can be taken in order not to interfere with groundwater resources. However, one of the challenges with the hydraulic fracturing process is the vast uncertainty associated with the surrounding process parameters, particularly involving reservoir properties. Since the process happens deep below the earth's surface, it is difficult and often expensive to accurately measure the

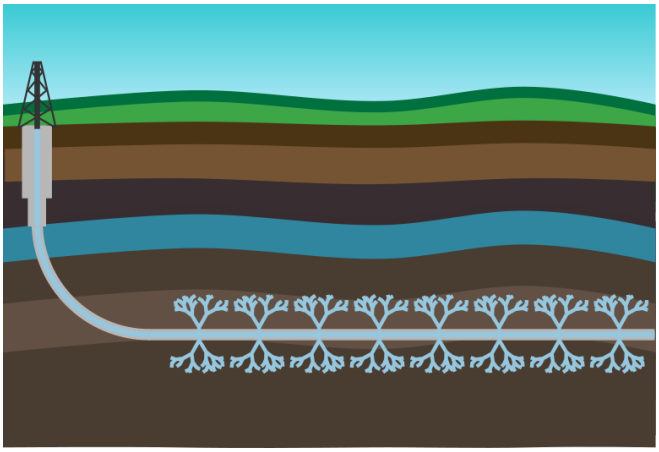

Figure 1.1: Hydraulic fracturing is a reservoir stimulation technique that enhances reservoir connectivity by fracturing of, typically, low permeable formations. Containment of the fractures in the layers that are targeted for stimulation is of essence, as failure to do so may lead to groundwater contamination.

process parameters. Using micro-seismic acoustic monitoring, tiltmeter mapping, and treatment pressure analysis, however, it is possible to measure certain indirect quantities.

Uncertainty quantification is important in assessing and predicting the performance of complex engineering systems and processes, especially in the absence of adequate experimental or real-world data. Due to the vast increase in computing power, computational uncertainty quantification has played an increasingly important role in decision making processes. Although a myriad of numerical approaches has been developed for the simulation of the hydraulic fracturing process [6–11], only limited research has been performed in the direction of uncertainty quantification [12–18]. Despite most analysts underscoring the significance of uncertainty, simulation methods in hydraulic fracturing models do not address them. In this dissertation, we therefore examine computational uncertainty quantification for hydraulic fracturing processes. Furthermore, we investigate the application of available indirect measurements, to provide a better understanding of the uncertainty and sensitivity of predictions of the hydraulic fracturing process.

This introduction first provides background information about hydraulic fracturing and uncertainty quantification, in Section 1.2 and 1.3, respectively. Subsequently, Section 1.4 states the objectives of this thesis and presents the outline and main contributions.

1.2 Hydraulic fracturing

The hydraulic fracturing (HF) process is challenging to model, as it involves a range of different aspects, such as poro-mechanical deformations, fluid flow in fractures, fluid and thermal diffusion processes, and fracture propagation. Furthermore, all of these processes are coupled. The foundation for hydraulic fracturing modeling has been laid in the last 50 years by several key publications [19–22]; see, *e.g.*, Ref. [23–27] for contemporary reviews.

In Section 1.2.1 we first review the most prominent models for hydraulic fracturing, encompassing two-dimensional and (pseudo-)three-dimensional models which have been developed for different conditions. In Section 1.2.2 we then present the most important numerical methods being used to solve these models.

1.2.1 Models for pressure-driven fracture propagation

Over the past decades, *two-dimensional models* for pressure-driven fractures have been used extensively in research and engineering. The most prominent two-dimensional models, all of which evidently make specific assumption on the fracture geometry, are the radial fracture model, the PKN (Perkins-Kern-Nordgren) model, and the KGD (Kristianovich-Geertsma-de Klerk) model. The *radial fracture model* describes the evolution of a *penny-shaped crack*, as introduced by Sneddon [28]. This model is representative of fractures that propagate evenly in all directions. The *PKN model* [29] is based on an adaptation of Sneddon's solution for a fracture of fixed height and elliptical cross section which propagates horizontally in one direction. The original model was proposed by Perkins and Kern [29] and later amended by Nordgren [30] to include the effects of fluid leak-off. The PKN model is widely used in the industry for hydraulic fracture design [31]. The *KGD model* [32, 33] is similar to the PKN model but with different assumptions regarding the fracture aperture profile. Like the PKN model, also the KGD model is used for the design of stimulation treatments.

To overcome the modeling limitations that follow directly from the assumption of two-dimensional fractures without the need to resort to full three-dimensional models, so-called *pseudo three-dimensional models* have been developed. The P3D and PL3D models are two of the most prominent models in this class. *P3D models* [34] generalize the two-dimensional PKN model by allowing for spatial variations in the fracture height along the length of the fracture. The added height variation of the fracture can either be linear or parabolic. P3D models are known to suffer from numerical instabilities when the system contains non-monotonically varying confining stresses in a layered system or when there is an unconfined growth of fractures in the height. In the *PL3D model* [35], a plane in which fracture propagation can occur is discretized. Within this predefined plane, the geometry of the induced fracture can be arbitrary, depending on the

mechanical parameters and loading conditions. The more regular description of the fracture front in comparison to the P3D model enhances the numerical stability of this method.

Various *three-dimensional models* have been proposed that take into account the full geometric complexity of the hydraulic fracturing process, see, *e.g.*, Ref. [8, 36–38]. Generally, the proposed models are developed based on the theory of linear elastic fracture mechanics, coupled with the effects of complex fluid flow patterns inside fractures [39]. In contrast to the pseudo three-dimensional models, fractures can propagate in arbitrary directions in three-dimensional models [31, 39]. A disadvantage of three-dimensional models is that they are highly computationally expensive, with simulation times of over a month using dedicated computational resources being reported in the literature [39, 40]. It is for this reason that full three-dimensional simulations are currently impractical for the design and optimization of stimulation treatments. The computational effort of three-dimensional models also impedes their suitability in the context of uncertainty quantification, which typically involves the consideration of a large number of simulations.

1.2.2 Numerical methods for pressure-driven fracture propagation

Hydraulic fracturing models as discussed above are inherently non-linear on account of the coupling between the various sub-problems and the moving boundary associated with the evolving fracture. Moreover, the models are generally time-dependent and subject to singular solution behavior related to the sharp fracture front. It is for these reasons that hydraulic fracture models, even in their simplified two-dimensional and pseudo three-dimensional forms, are challenging to solve. Therefore, over the past decades, several numerical methods have been developed for the simulation of the hydraulic fracturing process, the most significant of which are discussed below.

When considering geometrically-simplified models such as PKN or KGD, *finite difference methods* provide a straightforward solution strategy. In fact, finite difference techniques are especially popular in industry on account of their conceptual simplicity and their ease of use. Various finite difference simulators are listed in the test case study by Warpinski [41].

Since mass conservation is an essential ingredient in many of the models for pressure-driven fracture propagation, *finite volume methods*, which provide excellent conservation properties, have been widely considered in the context of hydraulic fracturing [42]. Specifically, for the fluid flow equations, Cartesian finite volume formulations are employed, which were introduced by Calhoun and Le Veque [43]. Volume conservation within a planar fracture is accurately approx-

imated in this context by using the partially-filled element concept introduced by Ryder and Napier [44]. The work by Pierce [42] highlights the use of finite volume methods in hydraulic fracturing simulations.

The versatility of *finite element methods* – both in terms of geometry representation and in terms of its ability to solve both solid and fluid problems – has made it an attractive solution technique for hydraulic fracturing. Several notable works based on finite element techniques can be found in, *e.g.*, Refs. [45–47], with the implicit moving mesh algorithm proposed in Ref. [48] being particularly noteworthy. Solution techniques based on finite elements generally couple separate solid and fluid models, and track the moving fracture edge either by explicit remeshing strategies or by the *extended finite element method (XFEM)*, see, *e.g.*, Refs. [49–51]. An additional advantage of XFEM techniques is that they facilitate enrichment of the finite element spaces using dedicated shape functions. The use of singular tip functions, for example, prevents the use of highly refined meshes in the vicinity of the fracture front. Similarly, steep pressure gradients in the vicinity of the fracture surface can be captured by discontinuous pressure shape functions [52, 53].

In recent years, various other advanced discretization techniques have been studied in the context of fluid-driven fracture propagation. *Boundary element methods* – in which finite element techniques are applied to discretize boundary integral equations – have been considered, for example, to alleviate the computational burden associated with solving the poro-elastic response of the reservoir [54]. *Phase-field formulations* [55–58] have also been considered for hydraulic fracturing processes, as the smeared representation of fractures in this modeling paradigm provides a natural framework for the consideration of complex fracture patters, including features such as crack branching and merging, which are inherent to crack propagation. A downside of phase-field models is that high-resolution meshes are required in the vicinity of the smeared fractures in order to accurately represent the phase field. In the context of evolving fractures, from a computational effort point of view, this requires the use of adaptive finite element methods.

All methods discussed above provide simulation frameworks for hydraulic fracturing problems. The methods that are applied in this dissertation, are selected to provide an optimal balance between model features, accuracy, and computational effort in the context of uncertainty quantification.

1.3 Uncertainty quantification

From a historical point of view, uncertainty quantification dates back more than 300 years, in particular to the famous work of Jacob Bernoulli, *Ars Conjectandi* (meaning art of conjecturing), which created a completely new approach to prob-

ability theory [59]. This work was extended by De Moivre with the development of probabilistic methods, and later by Francis Galton, who developed the concepts of correlation and regression. Ever since, uncertainty quantification has been applied in a wide range of areas such as climate, weather, finance, planetary science, and many more.

The main objective of computational uncertainty quantification is to predict and assess processes that are surrounded by uncertainty. In this dissertation we investigate the methods by which we can represent and propagate uncertainties in pressure-driven fracturing processes. This section presents an overview of computational uncertainty quantification techniques, with an emphasis on the ones applied in this thesis.

1.3.1 Computational uncertainty quantification approaches

Observation, theory and computational methods are generally recognized as the three cornerstones of science (Oden et al. [60]). The scientific procedure to study any system would combine all these three elements. In this regard, let us assess the different types of mathematical modeling of any physical reality. *Forward modeling* is the use of physical laws in order to simulate an outcome. We use theory and model parameters to make predictions of the results of observable parameters. *Inverse modeling*, on the other hand, is the use of available observables in combination with model parameters and theory to infer the actual values of the model parameters. Inverse modeling typically involves the frequent evaluation of the forward model, which motivates the development of *reduced-order models* to significantly reduce the computational effort.

Following the concepts of forward and inverse modeling discussed above, there exist two major types of problems in uncertainty quantification, *viz.*: *(i)* the forward propagation of uncertainties, where the various sources of uncertainty are propagated through the model to predict the overall uncertainty in the system's response, and *(ii)* the inverse assessment of uncertain model parameters by using the model to calibrate those parameters to observational data. There has been a proliferation of research on the former problem and a large number of uncertainty-analysis techniques were developed for it. On the other hand, the latter problem is drawing increasing attention in the computational engineering community, since uncertainty quantification of a model and the subsequent predictions of the true system's response are of great interest.

When building a mathematical model to describe the behavior of a physical system, one has to face a certain level of uncertainty in the characterization of the model parameters. Besides, there can be imperfections and incompleteness with respect to the model itself. Uncertainties arise, for example, from imprecise data and observations, errors in measurement devices, and errors in numerical methods

in the form of discretization errors. All these uncertainties can be broadly divided in two categories [61], *viz.*: *(i) aleatoric uncertainties*, which are associated to natural randomness and are therefore inherent to a system, and *(ii) epistemic uncertainties*, which are related to incompleteness in the information about a system. Both types of uncertainties can typically described using probability distributions.

In uncertainty quantification, the abstract notion of uncertainty is precisely expressed in the form of a probability measure. Using this measure, the uncertainty can be quantified, such that it can be expressed by a probability distribution. In this dissertation we follow the *Bayesian approach* to uncertainty quantification, which targets the logical combination of prior information on the model parameters with observational data, all represented as probability distributions. Mathematical-physical models fit in seamlessly in this approach, as they provide the relation between the model parameters and the data. The reader is referred to, *e.g.*, Ref. [62–66], for discussions regarding alternative approaches to uncertainty quantification such as the *Frequentist approach*.

1.3.2 Numerical methods for uncertainty quantification

The computational uncertainty framework considered in this work incorporates various stochastic analysis techniques, such as sensitivity analysis, Monte Carlo sampling, spectral methods, and Bayesian inference. Here we will briefly discuss these techniques in order to put them into the context of the framework to be developed. The reader is referred to, *e.g.*, Refs. [60, 67–70] for reviews of stochastic techniques and computational methods for uncertainty quantification.

An important first step in uncertainty quantification is to establish the influence of model input parameter on model observables through a *sensitivity analysis* [71]. Such an analysis – in which variations on the input are made to assess their influence on the model output – is instrumental in assessing which variables and models to consider in the uncertainty analysis. A parameter with significant variations can have little effect on the quantities of interest, or vice versa. Besides providing understanding regarding the influence of the model parameters, sensitivity analyses can, in many cases, also be used to directly assess the statistical moments of response quantities by considering the parameter sensitivities in the context of *perturbation methods* [72, 73]. Similarly, sensitivity analyses provide a basis for *reliability analyses* [74] and *regression analyses* [75].

To study the propagation of uncertainties through the considered models we employ *Monte Carlo sampling* methods. The pivotal idea of such sampling techniques is to represent the uncertain parameters (stochastic variables) by sequences of realizations, and to use the model to relate each realization of the input parameters to their corresponding output parameters [76]. Monte Carlo methods

provide a means of integrating probability distributions over high-dimensional model parameter domains. Although Monte Carlo methods are generally computationally demanding on account of the requirement to solve the underlying deterministic model many times they are appraised for their versatility in the sense that they do not impose fundamental restrictions on the class of problems that can be considered [77]. An additional advantage of sampling techniques is that they are generally non-intrusive from an implementation point of view, which allows to use them in combination with existing deterministic solvers.

As an alternative to representing uncertainties by samples or by sensitivities, they can also be approximated using shape functions defined over the parameter domain. The most prominent class of stochastic methods that are based on the shape function concept are *spectral methods* [78–80], in which, generally, globally (over the parameter domain) defined modes are employed to represent the randomness in the system. Spectral stochastic methods can be used to approximate the propagation of input uncertainties through a model [80], but will in this dissertation only be considered in the context of representing random input fields using *Karhunen-Loève (KL) expansions* [81]. Such KL expansions facilitate the low-dimensional representation of correlated random fields, which, in the context of this work is particularly useful for the representation of the spatially varying heterogeneities.

In addition to a representation of the stochastic variables, a methodology is required to determine the stochastic parameters from the stochastic outputs (data). In this work we employ the *Bayesian approach* to the stochastic inverse problem. Bayesian techniques systematically combine prior model parameter information with observational data based on Bayes' theorem

$$P(A|B) = \frac{P(B|A)P(A)}{P(B)}, \tag{1.1}$$

in which, in this context, A represents the information on the model parameters and B the observational data. Bayes' theorem can be conceived of as an update of the prior information on A, represented by the probability distribution $P(A)$, with the probability distribution on the data, $P(B)$, to acquire updated information on the model parameters in the form of the conditional posterior $P(A|B)$. In order to attain this posterior one must establish the likelihood of the model parameters in the form of the conditional probability distribution, $P(B|A)$, which is a measure for the evidence of the model parameters provided by the data.

A schematic representation of this Bayesian inference method is shown in Figure 1.2. The essential characteristic of Bayesian methods is that all information is provided through probability distributions. From a procedural perspective, Bayesian inference can be considered as a three-step procedure [82]:

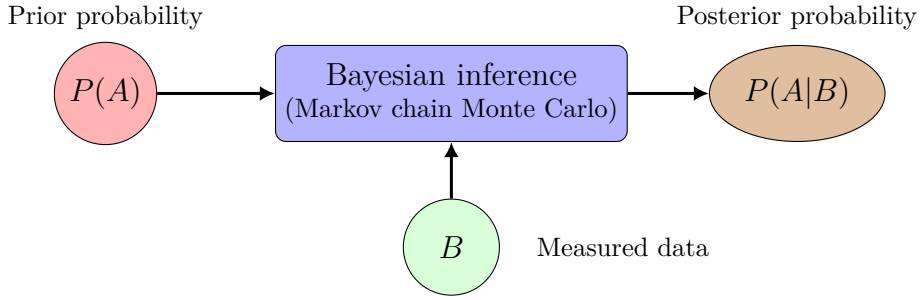

Figure 1.2: Schematic representation of the Bayesian inference method

1. The probability of all information has to be represented. That is, both the prior knowledge on the input parameters (typically based on experts' opinions) and the observational data must be represented in the form of probability distributions. These sources of information must then be combined in a *joint model-data probability distribution.*

2. The prior information is conditioned on the observed data through the application of Bayes' theorem (1.1), which results in an updated distribution *i.e., the posterior distribution of the model parameters.*

3. The *adequacy of the posterior distribution* is assessed based on its fit with the model and data. If the posterior is found to be inadequate, for example because the compatibility between the prior information and the data is insufficient, the inference procedure must be repeated with updated information.

An essential computational ingredient in this procedure is the inverse solver used to condition the model information in the second step. In general, Bayes' update rule cannot be evaluated analytically. Like for forward uncertainty analysis, Monte Carlo techniques provide a versatile framework to approximate the Bayesian inference rule in the form of sample representations. In this dissertation we resort to *Markov chain Monte Carlo methods* [83], and specifically the *Metropolis-Hastings algorithm* [84], as these methods provide a natural computational framework for the combination of prior information, model relations, and observational data. The reader is referred to, *e.g.*, Refs. [85, 86] for an overview of sampling techniques, such as, for example, *rejection sampling* [87], the *Metropolis algorithm* [84, 88–90], and *Gibbs sampling* [67, 91–94].

1.4 Objectives and outline

This introduction has discussed the motivation to consider uncertainty quantification in the context of hydraulic fracturing, the available models for hydraulic stimulation, and the techniques for computational uncertainty quantification. Effectively and efficiently combining the models and solution strategies for hydraulic fracturing with the methods for uncertainty quantification is far from trivial, as modeling aspects, model discretization techniques and stochastic solution procedures and intricately related. This gives rise to the primary objective of this dissertation, which is stated as:

> *To develop a computational uncertainty quantification framework for pressure-driven fracture propagation processes based on the method of Bayesian inference.*

The development of this uncertainty quantification framework encompasses the following research questions:

- What is a typical setting for the uncertainty quantification framework in the context of hydraulic stimulation procedures? That is, what physical system parameters are generally known with certainty, what quantities can be observed, and what uncertain quantities are to be derived through Bayesian inference?

- What models for hydraulic fracturing are practical in the context of the typical setting of uncertainty quantification? The considered Bayesian inference technique on the one hand puts requirements on the physical modeling capabilities, while, on the other hand, the involved computational effort should remain practical.

- Can reduced-order modeling (ROM) techniques be used to enhance the computational tractability of uncertainty quantification for hydraulic fracturing, and can the offline-online paradigm be used to consider Bayesian inference in real-time applications?

- How does one setup a stochastic inverse solver for computational uncertainty quantification for hydraulic fracturing, and how can the probabilistic information handled by this solver (prior, likelihood, posterior) be represented? Moreover, the question arises how one controls the accuracy and computational effort of the stochastic solver.

To address these research question, in Chapter 2 we commence with a study of uncertainty propagation in hydraulic fracturing based on the Perkins-Kern-Nordgren (PKN) model. This chapter discusses the governing equations and the assumptions involved in the PKN model, and puts a special focus on the incorporation of rock heterogeneities. Furthermore, an enhanced finite element technique is proposed that enables the study of sensitivities of the model to various input parameters. The influence of random input variables on the model is discussed, where rock properties are considered as random fields using the Karhunen-Loève expansion. Numerical results are presented to study the influence of input uncertainties on the hydraulic fracturing process.

In Chapter 3 we explore the possibilities of using a reduced-order model for the mechanical deformation and fracture propagation components of the hydraulic fracturing model, based on the theory of linear elastic fracture mechanics. The method of choice is the Proper Generalized Decomposition (PGD) technique, which is a reduced-order modeling technique specifically designed to reduce the high-dimensionality induced by the typically large number of system parameters. We study the various features of PGD and consider it in a stochastic setting, where we again use the Karhunen-Loève expansion to represent random heterogeneous material properties. Furthermore, we present results using a Monte Carlo technique to illustrate the efficiency of this PGD technique in a stochastic setting.

In Chapter 4 we present the PKN model in an inverse uncertainty quantification setting. This chapter outlines the Bayesian inference setting for the PKN model for hydraulic fracturing. Using a stochastic inverse solver in the form of a Markov chain Monte Carlo method, we combine the model with available observations to update prior information about uncertain parameters. Based on test cases with synthetic data, we illustrate how the Bayesian framework can be combined with hydraulic fracturing models to assist in the prediction of well-stimulation processes.

Finally, we present our conclusions and recommendations for further research in Chapter 5.

Chapter 2

Sampling-based stochastic analysis of the PKN model for hydraulic fracturing

Hydraulic fracturing processes are surrounded by uncertainty, as available data is typically scant. In this work we present a sampling-based stochastic analysis of the hydraulic fracturing process by considering various system parameters to be random. Our analysis is based on the Perkins-Kern-Nordgren (PKN) model for hydraulic fracturing. This baseline model enables computation of high fidelity solutions, which avoids pollution of our stochastic results by inaccuracies in the deterministic solution procedure. In order to obtain the desired degree of accuracy of the computed solution we supplement the employed time-dependent moving-mesh finite element method with two new enhancements: i) global conservation of volume is enforced through a Lagrange-multiplier; ii) the weakly-singular behavior of the solution at the fracture tip is resolved by supplementing the solution space with a tip enrichment function. This tip enrichment function enables the computation of the tip-speed directly from its associated solution coefficient. A novel incremental-iterative solution procedure based on a backward-Euler time-integrator with sub-iterations is employed to solve the PKN model. Direct Monte Carlo sampling is performed based on random variable and random field input parameters. The presented stochastic results quantify the dependence of the fracture evolution process – in particular the fracture length and fracture opening – on variations in the elastic properties and leak-off coefficient of the formation, and the height of the fracture.

This chapter is reproduced from [95]: H. Garikapati, C.V. Verhoosel, E.H. van Brummelen, S. Zlotnik and P. Díez. Sampling-based stochastic analysis of the PKN model for hydraulic fracturing. *Computational Geosciences*, 2019.

2.1 Introduction

Hydraulic fracturing processes – *i.e.* the fracturing of rock formations by a pressurized liquid to improve connectivity of reservoirs and geothermal formations – are surrounded by uncertainty, as rock formations are highly heterogeneous and available formation data is limited. Further improvement of models and simulation tools to understand this process is instrumental to increasing operational effectivity and to reliably quantify the risks and uncertainties that are involved.

Hydraulic fracturing models involve the coupling of three sub-models: *i)* a solid mechanics model which describes the deformation of the rock formation induced by the fluid load; *ii)* a fluid flow model to describe the fracturing-fluid in the crack, as well as its leak-off into the rock formation; *iii)* a fracture mechanics model including a fracture propagation criterion. Intrinsic characteristics of such models are the (strong) non-linearities related to the coupling between the solid and fluid, the singularities in the physical fields near the fracture front, the moving (fracture) domain boundaries, the degeneration of the governing equations near the tip region, and pronounced multiscale effects with the length scales varying from millimeters for the fracture opening near the tip to kilometers for the length of the fracture.

Various practical model simplifications – most commonly restricting the model to a single two-dimensional planar fracture – have been proposed, the most prominent of which are: *i)* The Perkins-Kern-Nordgren (PKN) model [96, 97] for a fracture of fixed height and elliptical cross section (leveraging the Sneddon solution for the elasticity problem [98]) which propagates horizontally in one direction; *ii)* The radial model for a horizontal Penny-shaped crack that evolves evenly in all directions in accordance with Sneddon's solution [99]; *iii)* The Khristianovic-Geertsma-De Klerk (KGD) model [100–102] for a vertical fracture of fixed height that propagates horizontally in one direction. Various pseudo-three-dimensional (P3D) models [103] and planar-three-dimensional (PL3D) models [104, 105] have been proposed over the years to enable consideration of more complex fracture patterns and fractures in multi-layer formations. These P3D models typically extend the above-mentioned two-dimensional models by considering a variation of fracture height in combination with fracture length and width. Although these classical models are generally based on restrictive and often ad-hoc assumptions, they are still widely used in the industry [106].

Despite the simplifications in the above-mentioned models, analytical solutions can only be obtained in limiting cases (*e.g.*, [97, 100, 101]). General solution strategies for these models rely on the use of computational techniques. Versatile and reliable simulators for hydraulic fracturing processes are indispensable in gaining further understanding of the process, in particular because direct observation possibilities (typically several kilometers below the earth surface) are limited.

The most prominent computational techniques used for hydraulic fracturing are Finite Volume Methods (*e.g.*, [107]), Finite Element Methods (*e.g.*, [108–110]), Boundary Integral Methods (*e.g.*, [111]) and Discrete Element Methods (*e.g.*, [112]). Recent advancements in numerical methods for hydraulic fracturing that are particularly noteworthy are the eXtended Finite Element Techniques (X-FEM) (*e.g.*, [52, 53, 113, 114]) and phase-field methods (*e.g.*, [115–118]).

Although the importance of considering realistic geological situations is acknowledged [119], hydraulic fracture evolution in formations with uncertain heterogeneous rock properties (*e.g.*, elastic moduli, compression/tensile strength, porosity, permeability) have not been studied in detail. In [120] a reliability analysis is conducted using analytical models for hydraulic fracturing. The possibility of considering stochastic heterogeneities in combination with computational models has been explored in [121], where the initiation and evolution of fracture has been studied using Monte Carlo sampling. The main challenge in such studies relates to the computational feasibility, in the sense that the computational effort of the deterministic simulations (whose error must be controlled in relation to the stochastic variations) is prohibitive in the context of sampling-based stochastic techniques.

In this work we present a detailed probabilistic analysis of the hydraulic fracturing process based on Monte Carlo simulations. The computational tractability of the stochastic framework considered herein motivates the use of the two-dimensional PKN model. We represent the (epistemic) uncertain parameters of the PKN model as random variables and/or random fields, and investigate the influence of these uncertain input parameters on the fracture geometry (in particular the fracture length and opening at the well bore). As part of the stochastic analysis we present a sensitivity analysis of the deterministic model. It is worth mentioning that similar analyses can be found in the literature for the deterministic setting [122, 123]. The primary focus of this work is the direct analysis of the propagation of heterogeneous uncertainties in the hydraulic fracturing process. As part of this study we present a detailed derivation of the PKN model in the context of random (spatially correlated) heterogeneous data. Control over accuracy of the numerical approximation of the PKN model is of paramount importance, because excessive numerical errors would pollute the stochastic uncertainty quantification. In this regard we propose to use two new features in the numerical method for the PKN model to control its accuracy: *i)* a Lagrange multiplier method to enforce the conservation of volume; *ii)* a special enrichment function for the finite element discretization of the PKN model to overcome tip singularity issues.

In Section 2.2 the governing equations are discussed, with a special focus on the incorporation of rock heterogeneities in the PKN model. In Section 2.3, the weak formulation and finite element discretization of the

model are presented including various algorithmic details. The stochastic setting and Monte Carlo method are introduced in Section 2.4, where the random field discretization of the heterogeneous properties using the Karhunen-Loève expansion is also discussed. Numerical simulations are presented in Section 2.5 to study the influence of input uncertainties in hydraulic fracturing. Finally, conclusions are presented in Section 2.6.

2.2 The PKN model for hydraulic fracturing

In this section we review the PKN model for hydraulic fracturing in the context of stochastic analyses with heterogeneous random fields. The PKN model – which was originally formulated by Perkins and Kern [96] and later amended with a leak-off model by Nordgren [97] and a propagation condition by Kemp [124] – is a practical candidate for preliminary studies of the probabilistic behavior of hydraulic fracturing by virtue of its computational tractability. Although highly simplified, the PKN model is based on fundamental physical principles and is capable of generating practically meaningful results [125].

2.2.1 Problem definition

The key assumption of the PKN model is that it considers a planar fracture with a constant height H; see Figure 2.1. Displacements and displacement gradients in the surrounding solid are assumed to remain small, and the material is assumed to be linear elastic and isotropic. The fracture surface resides in the xy-plane, while the fracture opens in the z-direction. The fracture aperture in the fracture plane is denoted by $w(x, y, t)$, and the aperture at the $y = 0$ center line by $\hat{w}(x, t)$. The fracture connects to the well at $x = 0$ and its evolving front is situated at $x = L(t)$.

A Newtonian fluid is injected into the fracture at the well with a controlled flow rate $i(t)$, and the flow inside the permeable crack is assumed to be laminar. The fracture process is assumed to be in the viscosity-based regime, where toughness effects can be neglected (propagation is governed by friction and leak-off effects). At the front of the fracture fluid lag is assumed to be zero, *i.e.*, the fracture front coincides with the fluid front. Moreover, spurt losses due to the creation of new fracture surface (see *e.g.* [125]) are ignored.

2.2.2 Governing equations

In this section the governing equations of the sub-models are reviewed. In the presented derivations we focus on those aspects of the sub-models that need careful consideration in the context of the stochastic analysis discussed in the remainder of this work.

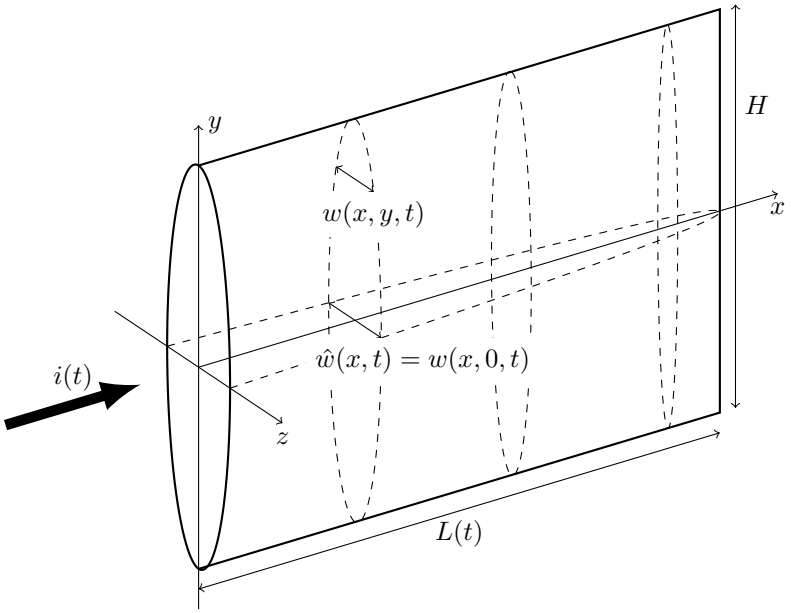

Figure 2.1: Schematic representation of the fracture geometry and boundary conditions for the PKN model. Note that both the fracture aperture, w, and the fracture length, L, are time dependent.

Fluid flow model

The PKN model is based on the conservation of mass of the fluid, which establishes a link between the injected volume, the created fracture volume and the leak-off volume. The differential material balance for the fracturing fluid is given by

$$\frac{\partial q}{\partial x} + \frac{\partial A}{\partial t} = -s_{c_l} \tag{2.1}$$

for all $x \in (0, L(t))$, where $q(x,t)$ is the volume rate of flow through the cross-sectional area $A(x,t) = \int_{-H/2}^{H/2} w(x,y,t)\,\mathrm{d}y$ and $s_{c_l}(x,t)$ is the rate of fluid volume loss per unit length of the fracture. At the well ($x = 0$) the flow rate is equal to the injection rate according to $q(0,t) = i(t)$.

The flow rate inside the fracture is related to the pressure gradient by assuming Poiseuille flow [126]. For such a flow the advective terms are assumed to remain small, so that the incompressible Navier-Stokes equations reduce to the Stokes equations. The PKN model moreover assumes a horizontal slot flow [127] with a parabolic fluid velocity profile

$$v = -\frac{1}{2\mu_f}\frac{\partial p}{\partial x}\left(\frac{w^2}{4} - z^2\right) \tag{2.2}$$

where $w(x,y,t)$ is the opening of the fracture and μ_f is the fluid viscosity. As will be discussed in more detail in the context of the solid model (Section 2.2.2), the assumptions of the PKN model lead to an ellipsoidal cross-section. The fracture aperture is then given by

$$w = \hat{w}\sqrt{1 - 4y^2/H^2}, \tag{2.3}$$

where $\hat{w}(x,t)$ is the maximum aperture at $y = 0$. The cross-sectional area is $A(x,t) = \frac{\pi}{4} H \hat{w}(x,t)$ and the fluid flow follows by integration of the fluid velocity in equation (2.2) as

$$\begin{aligned} q &= \int_{-H/2}^{H/2}\int_{-w/2}^{w/2} v\,\mathrm{d}y\mathrm{d}z = -\frac{1}{12\mu_f}\frac{\partial p}{\partial x}\int_{-H/2}^{H/2} w^3\,\mathrm{d}y \\ &= -\frac{\pi H \hat{w}^3}{64\mu_f}\frac{\partial p}{\partial x}. \end{aligned} \tag{2.4}$$

The leak-off volume rate per unit length of fracture in equation (2.1) follows the phenomenological law proposed by Carter [128]:

$$s_{c_l} = \frac{2Hc_l}{\sqrt{t-\tau}} \tag{2.5}$$

In this expression c_l is the leak-off coefficient and $\tau(x)$ is the arrival time of the fracture tip at location L, *i.e.*, $\tau(x) = L^{-1}(x)$. The main assumptions behind this model are that: *i)* the fracturing fluid deposits a thin layer of relatively low permeability material (known as the filter cake) on the inner faces of the fracture, with the deposition rate being proportional to the leak-off rate, and *ii)* the viscosity of the filtrate is high enough to fully displace the fluid already present in the rock pores.

Substitution of equations (2.4) and (2.5) in the material balance (2.1) then yields the fluid flow mass balance for all $x \in (0, L(t))$:

$$\frac{\pi H}{64\mu_f}\frac{\partial}{\partial x}\left(\hat{w}^3\frac{\partial p}{\partial x}\right) = \frac{2Hc_l}{\sqrt{t-\tau(x)}} + \frac{\pi H}{4}\frac{\partial \hat{w}}{\partial t} \tag{2.6}$$

Solid deformation model

To derive the relation between the fluid pressure and the solid deformation as used in the PKN model we consider the infinite domain $\Omega = \mathbb{R}_+ \times \mathbb{R} \times \mathbb{R}$ with material coordinates $\boldsymbol{x} = (x, y, z)$ and an evolving fracture surface (see Figure 2.1):

$$\Gamma_c(t) = \{\boldsymbol{x} \in \Omega \mid x \leq L(t), -\frac{H}{2} \leq y \leq \frac{H}{2}, z = 0\} \tag{2.7}$$

Assuming inertia and gravity effects to be negligible, the solid deformation, $\boldsymbol{u} = (\xi, \eta, \zeta)$, follows from the momentum balance

$$\nabla \cdot \boldsymbol{\sigma} = \mathbf{0} \qquad \text{in } \Omega, \tag{2.8}$$

where $\boldsymbol{\sigma}$ is the Cauchy stress tensor. The Cauchy stress follows Hooke's law for isotropic materials

$$\boldsymbol{\sigma} = 2\mu_s\boldsymbol{\varepsilon} + \lambda_s \mathrm{tr}(\boldsymbol{\varepsilon})\boldsymbol{I}, \tag{2.9}$$

where $\boldsymbol{\varepsilon} = \nabla^{\mathrm{s}}\boldsymbol{u}$ is the infinitesimal strain tensor. In the context of the stochastic analysis considered herein, the Lamé parameters $\mu_s(\boldsymbol{x})$ and $\lambda_s(\boldsymbol{x})$ are heterogeneous fields directly related to the Young's modulus, $E(\boldsymbol{x})$, and Poisson's ratio, $\nu(\boldsymbol{x})$. Under the horizontal slot-flow assumption, the viscous contribution to the normal stress along the fracture surface vanishes, and the solid is loaded by the fluid pressure, *i.e.*, $\boldsymbol{\sigma}\boldsymbol{n} = -p\boldsymbol{n}$ on Γ_c where $\boldsymbol{n}$ is the normal vector internal to the fluid domain.

An important aspect of the PKN model is that it relies on a planar deformation solid mechanics sub-model, which provides a local relation between the pressure and the fracture aperture. This reduction of the elasticity problem (2.8) – which in the literature is generally considered with homogeneous material properties – is key to the computational tractability of the PKN model, but evidently

hinges on the postulation of additional modeling assumptions, *viz.*: *i)* The deformations are planar, in the sense that the solid does not deform in the direction of the fracture propagation ($\xi = 0$), and that a plane strain condition in that direction applies ($\varepsilon_{xx} = \varepsilon_{xy} = \varepsilon_{xz} = 0$); *ii)* Heterogeneous variations perpendicular to the fracture propagation direction are assumed to be negligible, *i.e.*, the model parameters are independent of the y and z coordinates.

The assumptions that lead to the local solid mechanics model evidently restrict the applicability of the model. Even in the generally considered case of heterogeneous material properties, the planarity assumption is debatable in the vicinity of the fracture tip, where both the geometry and pressure loading vary significantly in the x-direction (see, *e.g.*, [129]). Although highly simplified, the local elasticity model is widely recognized to yield meaningful results in a variety of simulation scenarios [125]. An important point to make in the context of this contribution is that we consider the material properties to be random fields (see Section 2.4), which are parametrized by a mean value, a standard deviation, and an auto-correlation length, ℓ. This auto-correlation length is a measure of the correlation between any two material points in a random field, where a large correlation length implies that the spatial frequency of the heterogeneous field is low. In order for the planarity assumption to be meaningful, we consider sufficiently large auto-correlation lengths. More specifically, high wavenumber variations in the material properties along the x-axis are not considered herein. Moreover, the heterogeneities in the planes perpendicular to the x-direction are assumed to be negligible, at least in the sense that their influence is averaged out when considering the integrated opening of the fracture. In line with these assumptions, in this manuscript we only consider random heterogeneities in the direction of propagation with sufficiently large auto-correlation lengths.

Under the assumptions discussed above, the deformation in an arbitrary plane perpendicular to the x-direction can be deduced from the momentum balance (2.8) and constitutive relation (2.9), which, written out in components, yields:

$$\begin{aligned} 2\mu_s(x)\frac{\partial^2\eta}{\partial y^2} + \lambda_s(x)\left(\frac{\partial^2\eta}{\partial y^2} + \frac{\partial^2\zeta}{\partial y\partial z}\right) + \mu_s(x)\left(\frac{\partial^2\eta}{\partial z^2} + \frac{\partial^2\zeta}{\partial y\partial z}\right) &= 0 \\ \mu_s(x)\left(\frac{\partial^2\eta}{\partial y\partial z} + \frac{\partial^2\zeta}{\partial y^2}\right) + 2\mu_s(x)\frac{\partial^2\zeta}{\partial z^2} + \lambda_s(x)\left(\frac{\partial^2\eta}{\partial y\partial z} + \frac{\partial^2\zeta}{\partial z^2}\right) &= 0 \end{aligned} \tag{2.10}$$

Supplemented with the boundary conditions $\sigma_{zz}(x) = -p(x)n_z$ and $\sigma_{yz} = 0$ on the fracture boundary and vanishing far field conditions, this problem can be solved analytically. The fracture opening in the case of a constant pressure in the yz-plane is given by (see *e.g.* Lowengrub [130] and Sneddon [98] for details)

$$
\begin{aligned}
w(x,y) &= 4p(x)\int_y^{H/2} \frac{\bar{y}(1-\nu(x)^2)}{E(x)\sqrt{\bar{y}^2-y^2}}\,\mathrm{d}\bar{y} \\
&= \frac{2Hp(x)}{E'(x)}\sqrt{1-4y^2/H^2} \qquad |y| \le \frac{H}{2},
\end{aligned}
\tag{2.11}
$$

where $E'(x) = E(x)/(1-\nu(x)^2)$ is the plane strain modulus which is heterogeneous only in the x-direction. We note that the elliptical profile in equation (2.3) is a direct result of the setting of the elasticity problem considered here, with the maximum aperture equal to

$$
\hat{w}(x) = \frac{2Hp(x)}{E'(x)}. \tag{2.12}
$$

An essential property of this solution is that along the crack path the fracture aperture is linearly related to the pressure. The local nature of this relation is a direct consequence of the assumed planar deformation. Note that the stress field and displacement field can be derived in the form of integral representations [131].

Fracture propagation model

In the PKN model it is assumed that once the fracture has exceeded a certain distance, the energy dissipation associated with the fracture of the rock material is small compared to energy dissipation associated with the viscous flow of the fracturing fluid. This effectively neglects the fracture toughness, and fracture propagation is purely driven by the fluid velocity. Herein we adopt the standard assumption of zero fluid lag [97] – *i.e.*, the velocity of the fluid at the fluid front and the tip propagation speed are equal – so that tip propagation follows the Stefan condition

$$
v(L(t),t) = \lim_{x\to L(t)} \frac{q(x,t)}{A(x,t)} = \dot{L}(t). \tag{2.13}
$$

Substitution of the flow rate (2.4) and surface area then yields:

$$
\dot{L}(t) = -\frac{1}{16\mu_f} \lim_{x\to L(t)} \hat{w}^2 \frac{\partial p}{\partial x} \tag{2.14}
$$

The limits in (2.13) and (2.4) are one-sided, from below.

2.2.3 The coupled initial boundary value problem

The hydraulic fracture problem is characterized by a strong coupling of the sub-models discussed above. The solid deformation is coupled to the fluid through the

pressure loading along the fracture surface, while the fluid depends on the fracture opening though the Poiseuille flow profile. The fracture propagation condition is coupled directly to the fluid flow through the Stefan condition (2.13), and in turn influences the fluid flow by virtue of the fact that fracture propagation extends the fluid flow domain. The pointwise relation between pressure and the fracture opening in equation (2.12) allows the formulation of a single-field free-boundary problem. Herein we consider the initial boundary value problem for the fracture opening on the time interval $(0,T) \ni t$ with evolving domain $(0,L(t)) \ni x$:

$$
\begin{cases}
\dfrac{\pi}{128\mu_f}\dfrac{\partial}{\partial x}\left(\hat{w}^3\dfrac{\partial\left(E'\hat{w}\right)}{\partial x}\right) = \dfrac{2Hc_l}{\sqrt{t-\tau}} + \dfrac{\pi H}{4}\dfrac{\partial \hat{w}}{\partial t} & \forall x \in (0,L(t)) \\ & \forall t \in \times(0,T) \qquad (2.15a) \\
-\dfrac{\pi}{128\mu_f}\left(\hat{w}^3\dfrac{\partial\left(E'\hat{w}\right)}{\partial x}\right)\Bigg|_{x=0} = i(t) & \forall t \in (0,T) \qquad (2.15b) \\
\hat{w}(L(t),t) = 0 & \forall t \in (0,T) \qquad (2.15c) \\
\hat{w}(x,0) = 0 & \forall x \in (0,L_0) \qquad (2.15d) \\
\dot{L}(t) = -\dfrac{1}{96\mu_f H}\dfrac{\partial\left(E'\hat{w}^3\right)}{\partial x}\Bigg|_{x=L(t)} & \forall t \in (0,T) \qquad (2.15e) \\
L(0) = L_0 & \qquad (2.15f)
\end{cases}
$$

Note that the omission of fluid lag in the model results in the tip boundary condition $\hat{w}(L(t),t) = 0$, reflecting zero fracture opening at the tip. This boundary condition leads to singular behavior of the fracture opening (and pressure) at the tip, which is an important characteristic of the coupled problem (2.15). In Refs. [106, 132, 133] it is shown that in the viscosity-dominated regime, the toughness of the solid is small enough that the solution of a hydraulic fracture can be approximated by the zero toughness solution and the aperture solution in the proximity of the tip is proportional to:

$$
\hat{w}(x,t) \propto \sqrt[3]{L(t)-x} \qquad (2.16)
$$

We note that, due to the nature of this singularity, and assuming a finite plane strain modulus, the tip-propagation relation (2.15e) results in a finite propagation speed.

2.3 Deterministic computational methodology

In this section we present a methodology that enables the computation of solutions of the PKN model with an accuracy that makes it suitable for conducting a sampling-based stochastic analysis. In Section 2.3.1 we first discuss

the incremental-iterative solution procedure which is used to integrate the time-dependent moving-boundary problem. In Section 2.3.2 we then discuss the spatial finite element discretization of the nonlinear system of equations introduced above, including two essential enhancements, *viz.* incorporation of a Lagrange multiplier to enforce the volume-conservation constraint, and a solution space enrichment to resolve the singularity at the fracture tip.

2.3.1 Incremental-iterative solution procedure

To solve the time-dependent moving-boundary problem (2.15) we employ the incremental-iterative solution procedure outlined in Algorithm 1. We denote the time step size and index by Δt and $\imath = 0, \ldots, n_t$, respectively, such that $t^\imath = \imath \Delta t$ and $T = n_t \Delta t$. The solution at time step $\imath$ and sub-iteration $\jmath = 0, 1, 2, \ldots$ is written as $w^\imath_\jmath(x)$ and $L^\imath_\jmath$. The sub-iteration index $\jmath$ is omitted for converged solutions, *i.e.*, $w^\imath(x)$ and $L^\imath$.

We consider the implicit time-integration of both the fracture aperture and the fracture length, such that the coupled system (2.15) is discretized in time as

$$
\begin{cases}
\frac{\pi}{128\mu_f}\frac{\partial}{\partial x}\left(\left(\hat{w}^\imath\right)^3 \frac{\partial\left(E'\hat{w}^\imath\right)}{\partial x}\right) = \frac{2Hc_l}{\sqrt{t^\imath - \tau^{\imath-1}}} + \frac{\pi H}{4}\frac{\hat{w}^\imath - \hat{w}^{\imath-1}}{\Delta t} \\
\qquad\qquad\qquad\qquad\qquad\qquad\qquad\qquad \forall x \in (0, L(t)) & \text{(2.17a)} \\
-\frac{\pi}{128\mu_f}\left(\left(\hat{w}^\imath\right)^3 \frac{\partial\left(E'\hat{w}^\imath\right)}{\partial x}\right)\Big|_{x=0} = i(t^\imath) & \text{(2.17b)} \\
\hat{w}^\imath(L^\imath) = 0 & \text{(2.17c)} \\
\dfrac{L^\imath - L^{\imath-1}}{\Delta t} = -\dfrac{1}{96\mu_f H}\dfrac{\partial\left(E'\left(\hat{w}^\imath\right)^3\right)}{\partial x}\Big|_{x=L^\imath} & \text{(2.17d)}
\end{cases}
$$

for all $\imath = 1, \ldots, n_t$ with initial conditions $\hat{w}^0(x) = 0$ and $L^0 = L_0$.

To solve this moving-boundary problem at time step $\imath = 1, \ldots, n_t$, within each time step we sub-iterate between the aperture problem (2.17a)–(2.17c) and the propagation problem (2.17d) until convergence is achieved. The solution of the aperture problem (`solve_aperture` in Algorithm 1) is approximated using a finite element discretization in combination with a Newton-Raphson procedure to resolve the non-linearity. Details regarding the finite element discretization will be discussed in Section 2.3.2. The propagation problem is solved by using the *regula falsi* method to find the root of the residual function

$$
r^\imath_\jmath = r(L^\imath_\jmath) = L^\imath_\jmath - (L^{\imath-1} + \Delta t \dot{L}^\imath_\jmath). \tag{2.18}
$$

Input: $\mathbf{m} = \{L_0, T, \ldots\}$, $\mathbf{n} = \{\Delta t, \Delta L, \mathrm{tol}_L, \ldots\}$ # model parameters, numerical parameters
Output: $\{(L^\imath, w^\imath(x))\}_{\imath=1}^{n_t}$ # discrete solution

Initialization ($t^\imath = \imath\Delta t = 0$)
$L^0 = L_0$
$\tau^0(x) = 0$
$w^0(x) = 0$

Time-iteration loop
for $\imath$ **from** 1 **to** $T/\Delta t$**:**
  # Sub-iteration initialization ($\jmath = 0, 1$)
  $L_0^\imath = L^{\imath-1}$
  $w_0^\imath(x) =$ solve_aperture($L_0^\imath$, $w^{\imath-1}(x)$, $\tau^{\imath-1}(x)$, $\mathbf{m}$, $\mathbf{n}$)
  $\dot{L}_0^\imath =$ evaluate_tip_speed($w_0^\imath(x)$, $\mathbf{m}$)
  $r_0^\imath = -\Delta t \dot{L}_0^\imath$
  $L_1^\imath = L^{\imath-1} + \Delta L$
  $w_1^\imath(x) =$ solve_aperture($L_1^\imath$, $w^{\imath-1}(x)$, $\tau^{\imath-1}(x)$, $\mathbf{m}$, $\mathbf{n}$)
  $\dot{L}_1^\imath =$ evaluate_tip_speed($w_1^\imath(x)$, $\mathbf{m}$)
  $r_1^\imath = \Delta L - \Delta t \dot{L}_1^\imath$

  # Sub-iteration loop
  while $|L_\jmath^\imath - L_{\jmath-1}^\imath| \geq \mathrm{tol}_L$**:**
    # Increment sub-iteration index ($\jmath = 2, 3, \ldots$)
    $\jmath = \jmath + 1$
    # Secant computation
    $L_\jmath^\imath = L_{\jmath-1}^\imath - r_{\jmath-1}^\imath (L_{\jmath-2}^\imath - L_{\jmath-1}^\imath)/(r_{\jmath-2}^\imath - r_{\jmath-1}^\imath)$
    $w_\jmath^\imath(x) =$ solve_aperture($L_\jmath^\imath$, $w^{\imath-1}(x)$, $\tau^{\imath-1}(x)$, $\mathbf{m}$, $\mathbf{n}$)
    $\dot{L}_\jmath^\imath =$ evaluate_tip_speed($w_\jmath^\imath(x)$, $\mathbf{m}$)
    $r_\jmath^\imath = L_\jmath^\imath - L^{\imath-1} - \Delta t \dot{L}_\jmath^\imath$
    # False position update
    if $r_\jmath^\imath \cdot r_{\jmath-1}^\imath > 0$**:**
      $L_{\jmath-1}^\imath = L_{\jmath-2}^\imath$
      $r_{\jmath-1}^\imath = r_{\jmath-2}^\imath$
    end
  end
  # Set converged solution
  $L^\imath = L_\jmath^\imath$
  $w^\imath(x) = w_\jmath^\imath(x)$
  $\tau^\imath(x) =$ update_tau($\tau^{\imath-1}(x)$, $L^\imath$)
end

Algorithm 1: Incremental-iterative solution procedure

Given an iterate for the fracture length, $L_j^\imath$, the corresponding fracture aperture $w_j^\imath$ is computed using the `solve_aperture` procedure, after which the procedure `evaluate_tip_speed` is called to determine the associated tip speed in accordance with:

$$\dot{L}_j^\imath = -\frac{1}{96\mu_f H}\left.\frac{\partial\left(E'\left(\hat{w}_j^\imath\right)^3\right)}{\partial x}\right|_{x=L_j^\imath} \tag{2.19}$$

The *regula falsi* procedure is initialized with the fracture length at the previous time step, $L_0^\imath = L^{\imath-1}$, and with the forced propagation, $L_1^\imath = L^{\imath-1} + \Delta L$. We note that the residual $r_0^\imath = -\Delta t \dot{L}_j^\imath$ is non-negative as a consequence of the non-negativity of the propagation speed. The residual $r_1^\imath = \Delta L - \Delta t \dot{L}_j^\imath$ is forced to be positive by selecting the numerical parameter $\Delta L > 0$ to be sufficiently large. For all simulations in Section 2.5 we set ΔL equal to the element size at the fracture tip, and take a time-step that is sufficiently small to ensure positivity of the residual $r_1^\imath$.

The sub-iteration procedure is terminated when the fracture length converges to a specified tolerance, *i.e.*, $|L_j^\imath - L_{j-1}^\imath| < \mathrm{tol}_L$. The converged iterates $\hat{w}_j^\imath(x)$ and $L_j^\imath$ for the fracture aperture and length are then used as the initial conditions for the next time step. The fracture arrival function $\tau^\imath(x)$ for the next time step is updated in the `update_tau` routine. Since the arrival time function is evaluated by linear interpolation in the list $\{(L^{\hat{\imath}}, t^{\hat{\imath}})\}_{\hat{\imath}=0}^\imath$, this update routine merely appends the converged fracture length to this list. Note that we assume zero leak-off in the initial crack, so that we do not need to evaluate the arrival function for $x \leq L^0$. For $x > L^{\imath-1}$ the arrival time is taken as the time at which the crack reached $L^{\imath-1}$. As a result $t^\imath - \tau^{\imath-1}(x) \geq \Delta t$, everywhere in the interval $(L^0, L^\imath)$ which effectively bypasses the occurrence of a singularity in the leak-off term at the fracture tip.

2.3.2 Finite element discretization

The `solve_aperture` routine uses the finite element method to compute the fracture aperture $\hat{w}_j^\imath$ based on the fracture length $L_j^\imath$ and the aperture and arrival time at the previous time step, $w^{\imath-1}$ and $\tau^{\imath-1}$, respectively. To derive the finite element formulation the weak form of (2.17) is considered, where the sub-iteration index has been dropped for notational convenience:

$$\begin{cases} \text{Find } \hat{w}^\imath \in \mathcal{V}^\imath \text{ such that:} \\ \dfrac{\pi}{4} \displaystyle\int_0^{L^\imath} \left(\frac{(\hat{w}^\imath)^3}{32\mu_f} \frac{\partial \left(E' \hat{w}^\imath\right)}{\partial x} \frac{\partial v}{\partial x} + \frac{H}{\Delta t} \hat{w}^\imath v \right) \mathrm{d}x = \\ \qquad \dfrac{\pi H}{4\Delta t} \displaystyle\int_0^{L^{\imath-1}} \hat{w}^{\imath-1} v \, \mathrm{d}x - 2H c_l \int_{L_0}^{L^\imath} \frac{v}{\sqrt{t^\imath - \tau^{\imath-1}}} \, \mathrm{d}x + i(t^\imath) v(0) \quad \forall v \in \mathcal{V}^\imath \end{cases} \tag{2.20}$$

The time-dependent test and trial space $\mathcal{V}^\imath$ specified below are defined such that the Dirichlet boundary conditions at the tip are satisfied, and all integrals in the above formulation are bounded. Note that the right-hand-side integral involving the fracture aperture at the previous time step is computed over the fracture domain at the previous time step, which reflects the fact that ahead of the fracture tip the aperture is equal to zero. Moreover, the initial crack is excluded from the integration domain for the right-hand-side term involving the leak-off, which results from the assumption that there is no leak-off in the initial crack.

The weak formulation (2.20) is discretized using the finite element method by approximating the maximum aperture as

$$\hat{w}^{\imath,h}(x) = \sum_{i \in \mathcal{I}^\imath} N_i^\imath(x) a_i^\imath, \tag{2.21}$$

where the index set $\mathcal{I}^\imath$ contains the indices of the shape functions $\{N_i\}_{i \in \mathcal{I}^\imath}$ constructed over a mesh $\mathcal{T}^\imath$ that partitions the evolving domain $(0, L^\imath)$. The corresponding discrete trial and test space are given by $\mathcal{V}^{\imath,h} = \operatorname{span}\left(\{N_i\}_{i \in \mathcal{I}^\imath}\right) \subset \mathcal{V}^\imath$.

The finite element discretization considered in this work is based on linear Lagrange finite elements, where the linear basis function associated with the tip node is constrained in accordance with the zero-aperture Dirichlet condition at the tip. Because of the nature of the solution we grade the mesh toward the tip by specifying the element size at the tip, the increase ratio between two adjacent elements, and the maximal element size that is approached toward the inflow boundary. A schematic representation of such a graded mesh is shown in Figure 2.2. Note that the first right-hand-side integral term in equation (2.20) involves the product of functions defined on two different meshes, and hence requires evaluation on an overlay mesh.

A discretization of the problem (2.20) based on linear finite elements – even though graded toward the tip – leads to an unacceptable loss of accuracy at meshes that are computationally tractable within the scope of this work. This performance deterioration is a consequence of: *i)* the flux (2.4) being highly nonlinearly dependent on the fracture aperture; and *ii)* the singular behavior at the

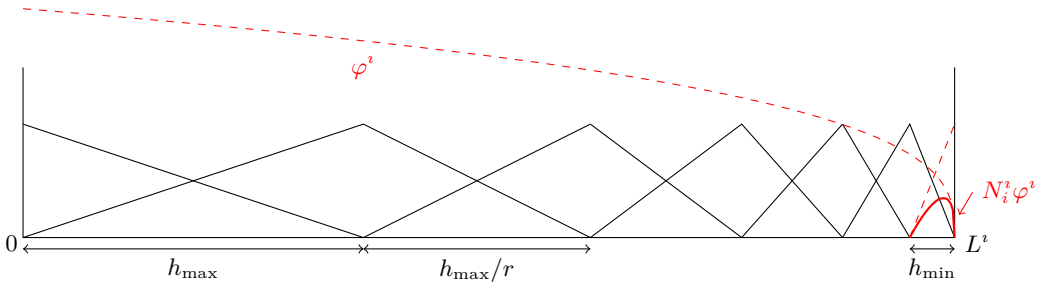

Figure 2.2: Schematic representation of the time-dependent graded finite element mesh with a linear finite element basis and a tip enrichment function.

tip not being represented by the linear finite element basis. In the remainder of this subsection we propose two enhancements to ameliorate this performance degradation. In Section 2.5.1 the numerical performance of these enhancements will be assessed in the scope of a benchmark simulation.

Mass conservation constraint

Although the weak formulation (2.20) is consistently derived from the mass balance equation (2.6), the finite element approximation of (2.20) does not strictly comply with the local mass balance and its integrated global version. Since adequate representation of the conservation of mass is of critical importance for obtaining accurate solutions, we herein propose to explicitly enforce global conservation in our approximation. We obtain the global balance of mass by integration of the time-discrete version of (2.6) over the entire domain:

$$i(t^\imath) = 2Hc_l \int_{L_0}^{L^\imath} \frac{1}{\sqrt{t^\imath - \tau^{\imath-1}}}\,\mathrm{d}x + \frac{\pi H}{4\Delta t} \int_0^{L^{\imath-1}} \hat{w}^\imath - \hat{w}^{\imath-1}\,\mathrm{d}x + \frac{\pi H}{4\Delta t} \int_{L^{\imath-1}}^{L^\imath} \hat{w}^\imath\,\mathrm{d}x \quad (2.22)$$

This global balance clearly shows that the injected volume is conserved by leak-off through the fracture (first term), fracture opening (second term), and fracture propagation (third term). We explicitly enforce the global conservation law (2.22) in the weak formulation (2.20) by means of a Lagrange multiplier, $\Lambda^\imath$:

$$
\begin{cases}
\text{Find } \hat{w}^\imath \in \mathcal{V}^\imath \text{ and } \Lambda^\imath \in \mathbb{R} \text{ such that:} \\
\dfrac{\pi}{4}\displaystyle\int_0^{L^\imath}\left(\frac{(\hat{w}^\imath)^3}{32\mu_f}\frac{\partial\left(E'\hat{w}^\imath\right)}{\partial x}\frac{\partial v}{\partial x}+\frac{H}{\Delta t}\hat{w}^\imath v\right)\mathrm{d}x-\Lambda^\imath\left(\frac{\pi H}{4\Delta t}\displaystyle\int_0^{L^\imath} v\,\mathrm{d}x\right)= \\
\quad \dfrac{\pi H}{4\Delta t}\displaystyle\int_0^{L^{\imath-1}}\hat{w}^{\imath-1}v\,\mathrm{d}x-2Hc_l\int_{L_0}^{L^\imath}\frac{v}{\sqrt{t^\imath-\tau^{\imath-1}}}\,\mathrm{d}x+i(t^\imath)v(0) \quad \forall v\in\mathcal{V}^\imath \\
\Psi\left(\begin{array}{c} i(t^\imath)-2Hc_l\displaystyle\int_{L_0}^{L^\imath}\frac{1}{\sqrt{t^\imath-\tau^{\imath-1}}}\,\mathrm{d}x \\ -\frac{\pi H}{4\Delta t}\displaystyle\int_0^{L^{\imath-1}}\hat{w}^\imath-\hat{w}^{\imath-1}\,\mathrm{d}x-\frac{\pi H}{4\Delta t}\int_{L^{\imath-1}}^{L^\imath}\hat{w}^\imath\,\mathrm{d}x\end{array}\right)=0 \qquad \forall\Psi\in\mathbb{R}
\end{cases}
\tag{2.23}
$$

Singular tip enrichment

As discussed in Section 2.2.3, the aperture solution to the problem (2.15) is singular at the tip in accordance with equation (2.16). Evidently, this singular solution behavior is approximated poorly by the linear finite element basis. As a matter of fact, when solely using the linear finite element basis, the tip propagation speed will always vanish when evaluated through equation (2.15e). To improve the finite element approximation, we enrich the test and trial space $\mathcal{V}^\imath$ with the tip asymptote (2.16):

$$\varphi^\imath(x)=\sqrt[3]{L^\imath-x} \tag{2.24}$$

We localize this enrichment function to the tip region using the partition-of-unity method (see, *e.g.*, [134]). The enriched finite element interpolation of the aperture is then given by

$$\hat{w}^{\imath,h}(x)=\sum_{i\in\mathcal{I}^\imath}N_i^\imath(x)a_i^\imath+\sum_{j\in\mathcal{J}^\imath}N_j^\imath(x)\varphi^\imath(x)b_j^\imath \tag{2.25}$$

where the index set $\mathcal{J}^\imath\subset\mathcal{I}^\imath$ contains the indices of the nodes that are enriched. In the numerical simulations considered in Section 2.5 we only enrich the linear finite element function associated with the tip, which we have found to be effective. A schematic representation of this enrichment is shown in Figure 2.2.

2.4 Stochastic setting

In this section we introduce the stochastic setting of the PKN problem. Section 2.4.1 introduces the Monte Carlo method that we use in this work. In

Section 2.4.2 we discuss the random variables and random fields for the model parameters. We do this in an abstract setting, where we denote the set of model parameters by $\mathbf{m} = \{m^1, m^2, \ldots\}$. For a given set of model parameters we can compute the response of the system, which is characterized by the fracture length $L(t)$ and space-time-dependent fracture aperture function $\hat{w}(x,t) : [0, L(t)] \to \mathbb{R}$ defined over the moving domain. From this response we can deduce the observable parameters as $\mathbf{d} = \{d^1, d^2, \ldots\}$. In the remainder of this work we will consider some of the model parameters to be uncertain, *viz.* the plane strain modulus $\tilde{E}'$, the leak-off coefficient, $\tilde{c}_l$, and the fracture height $\tilde{H}$. We use the tilde diacritic to indicate that these parameters are stochastic. As observable parameters we will focus on the final fracture length, $\tilde{L}(T)$, and the maximum fracture mouth opening, $\tilde{\hat{w}}(T)$.

2.4.1 Direct Monte Carlo sampling

In this work we use direct Monte Carlo sampling to compute the stochastic response of the PKN model. The primary reason for using direct Monte Carlo sampling is that it does not pose any restrictions on the distributions of the model parameters and the observables. Moreover, the non-intrusive character of the method enables its direct application to the PKN model. More advanced stochastic techniques such as perturbation methods or spectral methods (see [135] for an overview) can aid in reducing the computational effort of the stochastic problem, but application of such techniques to the highly non-linear moving boundary problem considered here is non-standard and beyond the scope of the current work.

We denote a realization, or sample, of the random set of model parameters $\tilde{\mathbf{m}}$ by $\mathbf{m}_k$, where the subscript k is the index of the sample. The direct Monte Carlo method generates a sequence of model parameter realizations, $\{\mathbf{m}_1, \mathbf{m}_2, \ldots, \mathbf{m}_N\}$, and applies the model to construct the corresponding sequence of observables, $\{\mathbf{d}_1, \mathbf{d}_2, \ldots, \mathbf{d}_N\}$, where N denotes the number of samples. An estimate of the stochastic set of observables, $\tilde{\mathbf{d}}$, can then be obtained through statistical analysis of the sequence of samples. In particular, the mean and standard deviation of an observable, $\tilde{d}^i$, are computed by the estimators

$$\mu_{d^i} \approx \frac{1}{N} \sum_{k=1}^{N} d_k^i, \qquad \sigma_{d^i} \approx \sqrt{\frac{1}{N-1} \sum_{k=1}^{N} \left(d_k^i - \mu_{d^i}\right)^2}, \tag{2.26}$$

where the symbols μ_{d^i} and σ_{d^i} denote the mean and standard deviation, respectively. Evidently, the accuracy of the estimators depends on the number of samples N. Given a confidence level C_μ for the estimated mean μ (omitting the subscript d^i for notational convenience) – meaning that the estimated mean has

a relative accuracy of $\pm(1-C_\mu)/2$ with probability C_μ – the minimal number of samples can be estimated by [136, 137]

$$N \gtrsim \left(\frac{\Phi^{-1}(\frac{1+C_\mu}{2})}{1-C_\mu} \right)^2 V_{d^i}^2, \tag{2.27}$$

where Φ is the cumulative density function of a standard normal random variable, and $V_{d^i} = \sigma_{d^i}/\mu_{d^i}$ is the coefficient of variation of the random observable $\tilde{d}^i$. A rough estimate of this coefficient of variation can be obtained using a Monte Carlo simulation with a small number of samples.

From (4.48) it becomes apparent that a draw-back of the direct Monte Carlo method is the slow convergence of the sampling error (an increase in confidence level) with increase in the number of samples. In the context of computational models such as that considered in this work this practically means that the stochastic simulations are computationally very intensive in the case of practically meaningful confidence levels. The fact that Monte Carlo sampling is non-intrusive – in the sense that it is a method that does not interfere with the deterministic model – makes parallelization possible. We have implemented a parallel master/slave algorithm for our simulations, which shows excellent scalability.

2.4.2 Random variable and random field parametrization

In this work we represent the considered scalar model parameters, $\tilde{m}^i$, by means of log-normal distributions, which are parametrized by the mean value and the standard deviation. Log-normal distributions are considered to avoid physically impossible negative realizations. We employ standard random number generators [138] to obtain the sequence of samples required for Monte Carlo sampling.

In the case of heterogeneous random fields, $\tilde{m}^i(x)$, we employ stationary log-normal random fields whose spatial correlation is represented by the auto-correlation function

$$\rho_{m^i}(x_1, x_2) = \exp\left(-\frac{|x_1 - x_2|}{l_{m^i}} \right), \tag{2.28}$$

where x_1 and x_2 are two points in a background domain which is larger than all fracture length realizations, and l_{m^i} is the correlation length. To generate samples of the random field, $\tilde{m}^i(x)$, it must be discretized. To obtain a discretization the log-normal random field is considered as the exponential of an underlying stationary normal random field $\tilde{g}^i$:

$$\tilde{m}^i(x) = \exp(\tilde{g}^i(x)) \tag{2.29}$$

The statistical moments of the underlying Gaussian distribution can be expressed in terms of those of the random field $\tilde{m}^i(x)$ by (see, *e.g.*, [139])

$$\mu_{g^i} = \ln(\mu_{m^i}) - \frac{1}{2}\ln(1+V_{m^i}^2), \qquad V_{g^i} = \sqrt{\ln(1+V_{m^i}^2)}, \tag{2.30}$$

where $V_{m^i} = \sigma_{m^i}/\mu_{m^i}$ is the coefficient of variation of the model parameter m^i. Similarly the auto-correlation function can be written as

$$\rho_{g^i}(x_1,x_2) = \frac{\ln\left(1+\rho_{m^i}(x_1,x_2)V_{m^i}^2\right)}{\ln(1+V_{m^i}^2)}. \tag{2.31}$$

Discretization of the underlying Gaussian random field $\tilde{g}^i(x)$ is then achieved by means of the Karhunen-Loève expansion (see, *e.g.*, [140])

$$\tilde{g}^i(x) \approx g(x,\tilde{\mathbf{z}}) = \mu_{g^i} + \sum_{j=1}^{n} \sqrt{\xi_j} r_j(x)\tilde{z}_j, \tag{2.32}$$

where $\tilde{\mathbf{z}}$ is a vector of n independent standard normal random variables, and where ξ_j and $r_j(x)$ are the eigenvalues and eigenfunctions corresponding to the spatial covariance function $\sigma_{g^i}^2\rho_{g^i}(x_1,x_2)$, respectively. We discretize the eigenfunctions in space by means of a uniform linear finite element discretization over the background domain, which results in a generalized eigenvalue problem that we solve using a direct eigenvalue solver (see, *e.g.*, Ref. [135] for details). In Figure 2.3a the first 12 numerically determined eigenfunctions are shown for the auto-correlation function (2.28) with $l_{m^i} = 10\,\mathrm{m}$. To illustrate the effectiveness of the Karhunen-Loève expansion, Figure 2.3b shows the auto-correlation function reconstructed from the Karhunen-Loève expansion (blue dots), which conveys that for this selection of the correlation length, an excellent approximation of the auto-correlation function is attained using 12 modes.

The log-normal random field $\tilde{m}^i(x)$ is then obtained by back-substitution of (2.32) into the transformation (2.29):

$$\tilde{m}^i(x) \approx \frac{\mu_{m^i}}{\sqrt{1+V_{m^i}^2}} \prod_{j=1}^{n} \exp(\sqrt{\xi_j} r_j(x)\tilde{z}_j). \tag{2.33}$$

Realizations of the random field $\tilde{m}^i(x)$ can now be generated by sampling a sequence of n independent standard normal random variables.

2.5 Numerical simulations

In this section we present numerical results based on the methodology presented above. In Section 2.5.1 we first validate our methodology in a deterministic

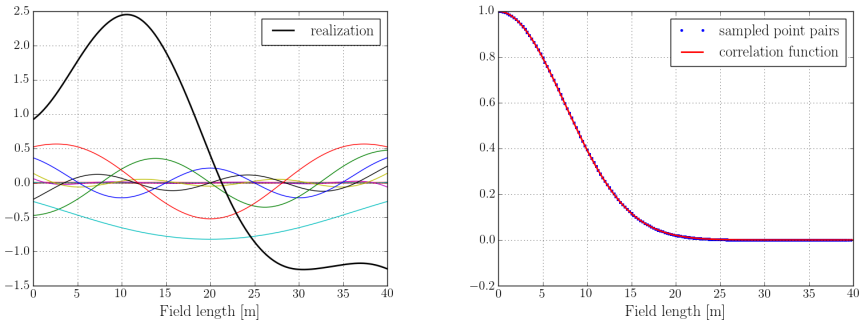

(a) Karhunen-Loève modes **(b)** Auto-correlation function

Figure 2.3: *(a)* Karhunen-Loève modes, $r_j(x)$, and a single realization (solid black line) in accordance with the expansion (2.32). *(b)* Prescribed and approximated auto-correlation function $\rho_{m^i}(x_1, x_2)$ for a correlation length of $l_{m^i} = 10\,\mathrm{m}$.

setting by consideration of the benchmark results presented in the comparative study by Warpinski *et al.* [141]. In this section we demonstrate the necessity to use a tip enrichment function and enforcement of volume conservation, and we study the influence of the mesh size and time-step size on the numerical results. In Section 2.5.2 the sensitivity of the observables – in particular the fracture length and aperture – to the uncertain model parameters is studied, which serves as a starting point for the stochastic simulations discussed in Section 2.5.3. In the stochastic setting the uncertain model parameters are represented by discrete random fields.

2.5.1 Deterministic benchmark

To demonstrate the validity of the presented methodology we consider the benchmark case studied by Warpinski *et al.* [141], which is based on a staged-field experiment of the Gas Research Institute [141, p. 26]. The considered model parameters are assembled in Table 2.1. The injection rate is gradually increased until the indicated value, and then held constant for 200 minutes. The material parameters resemble that of a tight gas sand reservoir, for which spurt losses are omitted.

In Figure 2.4 we show the evolution of the fracture in time, where it should be noted that the height of the fracture, H, is constant. Since the width is symmetric with respect to the x axis, Figure 2.4 displays half of the aperture. The shown results are based on a mesh size of $\Delta x = 1\ m$ and a time step size of $\Delta t = 1\ s$. As we will study in detail below, these results are objective

Leak-off coefficient	c_l	9.84×10^{-6}	$m/s^{1/2}$
Spurt losses	S_p	0	m
Fracture height	H	51.8	m
Plane strain modulus	E'	6.13×10^{10}	Pa
Viscosity	μ_f	0.2	Pa.s
Injection rate	i	0.0662	m^3/s
Pumping time	T	12000	s

Table 2.1: Reservoir data used for the validation of the deterministic problem

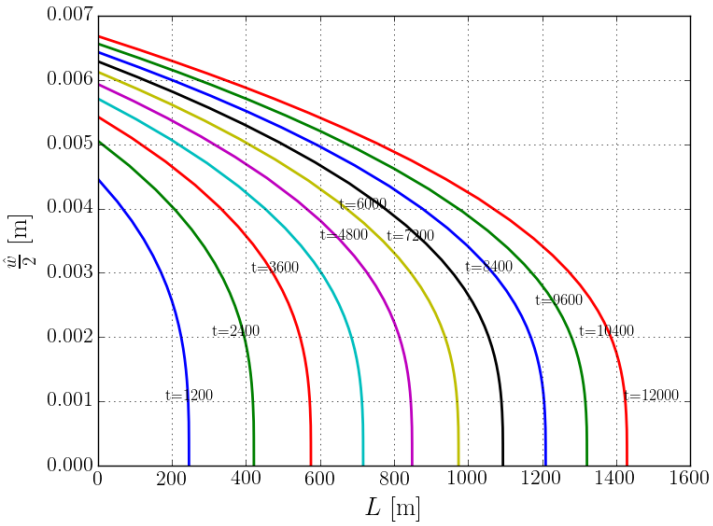

Figure 2.4: Aperture profiles evolving in time for the PKN benchmark simulation.

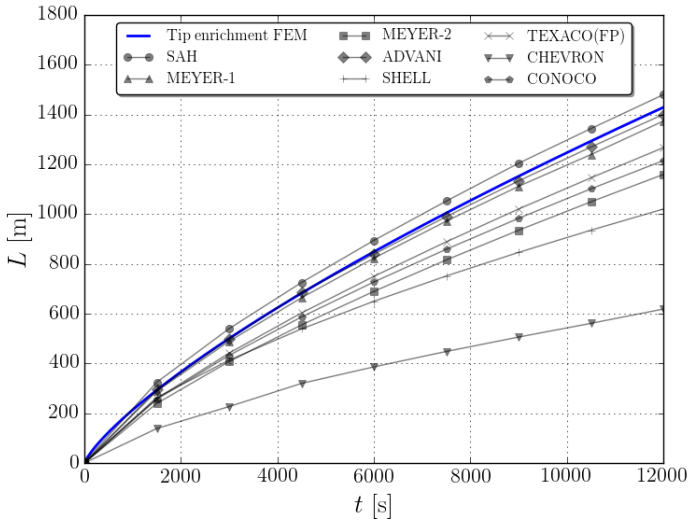

(a)

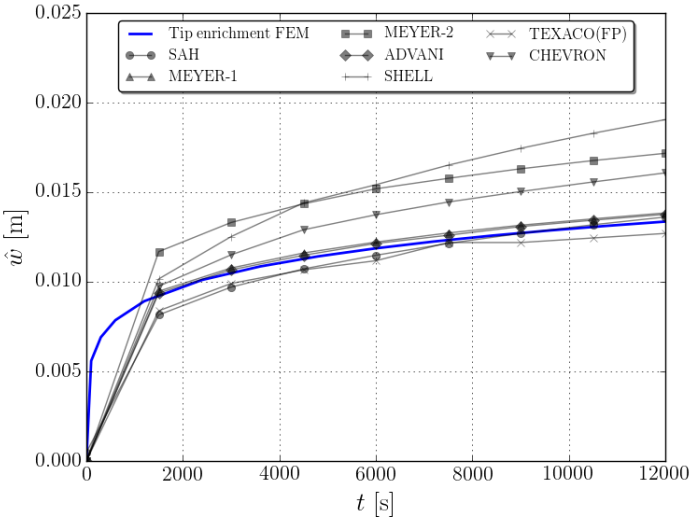

(b)

Figure 2.5: Evolution of *(a)* the fracture length and *(b)* the maximum aperture over time as computed by the finite element methodology proposed in this contribution (solid blue line). The benchmark results reported in Ref. [141] are displayed for references. See Appendix 2.A for further details.

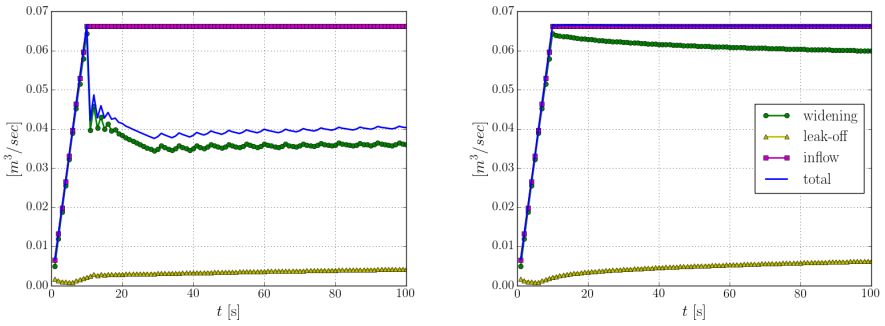

(a) Without Lagrange multiplier **(b)** With Lagrange multiplier

Figure 2.6: Influence of the Lagrange multiplier on the conservation of volume.

with respect to these numerical parameters. Figure 2.5 shows the corresponding increase in fracture length and fracture mouth opening over time. The observed time evolution corresponds well with the results reported for various simulators in [141] (displayed in Figure 2.5 for reference). It is noted that the reported results in [141] vary significantly as a result of variations in model assumptions and simulation frameworks. The fracture length of 1429 m as computed here also corresponds reasonably well with the analytical model in [125], which – using additional simplifying assumptions – predicts a fracture length of 1340 m. Note that in the absence of leak-off our model predicts a fracture length of 1730 m. This stipulates that leak-off is appropriately represented in our numerical simulations. The fracture length and fracture opening computed by our methodology are in the higher part of the spectrum of simulators considered in [141] and analytical models, which we attribute to the explicit enforcement of the volume constraint, which will be discussed in detail below.

Our benchmark results are based on the formulation including the enrichment of the tip functions and the enforcement of the global volume conservation constraint; see Section 2.3. The results in Figure 2.6 and Figure 2.7 serve to illustrate that both these aspects are essential to obtain numerical results with an acceptable level of accuracy for meshes and time step sizes that are computationally tractable in the scope of stochastic simulations.

Figure 2.6 displays the behavior of the global volume conservation without and with Lagrange multiplier constraint. The total volume rate – which is the sum of the leak-off rate and fracture-widening rate – should equate to the input flow rate. Note that in the absence of the Lagrange multiplier constraint, a significant mismatch between the total rate and the inflow rate is observed. The presented figure is based on on a mesh size of $\Delta x = 1\ m$ and a time step size of $\Delta t = 1\ s$. The mismatch between the rates depends on these discretization parameters, as it

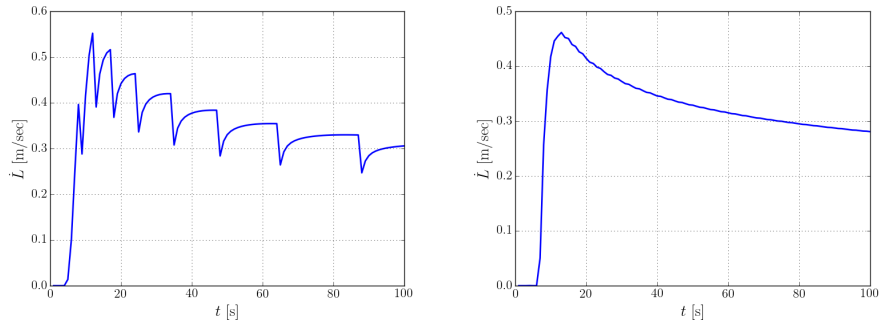

(a) Without enrichment **(b)** With enrichment

Figure 2.7: Influence of the enrichment function on the tip propagation velocity.

originates from significant errors in the local volume balance in the finite element discretization (2.17). These local inaccuracies in the finite element solution are closely related to the highly nonlinear character of the constitutive relation. By enforcing global conservation of volume using a Lagrange multiplier – as shown in Figure 2.6b – the global loss of volume is rigorously resolved. As observed the total volume rate in this case matches that of the inflow rate.

In Figure 2.7 we display the tip velocity over time, without and with tip enrichment function. For both simulations a mesh size of $\Delta x = 1\ m$ and a time step size of $\Delta t = 1\ s$ is used. In the case of tip enrichment, equation (2.14) is used to compute the tip speed. In the absence of enrichment the tip speed cannot be obtained by this equation, as the adequate singular tip behavior is then not represented in the discrete solution space. The speed results presented in Figure 2.7a are based on the finite difference approximation

$$\dot{L}(t) = -\frac{E'}{96\mu_f H}\left(\frac{\hat{w}^3|_{L(t)} - \hat{w}^3|_{(L(t)-\Delta x)}}{\Delta x}\right) \tag{2.34}$$

From Figure 2.7 it is observed that without the use of the enrichment function, for the computational setting considered here significant oscillations in the fracture propagation speed occur. Enriching the solution space with the tip singularity dramatically reduces these oscillations, and hence significantly improves the quality of the obtained result.

The enforcement of the volume constraint by means of a Lagrange multiplier, and the representation of the tip behavior by means of an enrichment function, provide numerical approximations with a level of accuracy that enables studying stochastic variations. In Figure 2.8 and Figure 2.9 we show the dependence of the results on independent variations in the time step size and mesh size, respectively.

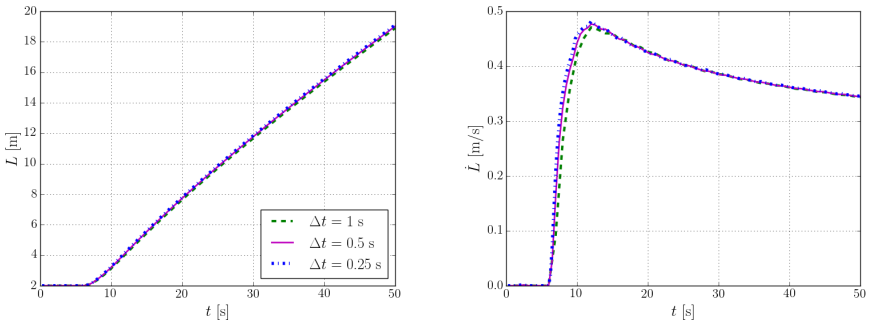

(a) **(b)**

Figure 2.8: (a) Fracture length with time for constant mesh size $\Delta x = 1\,\mathrm{m}$, and (b) Tip velocity profile with time for constant mesh size $\Delta x = 1\,\mathrm{m}$

Note that in all simulations we consider a duration of 50 s only, in order to make the converge studies feasible in terms of computational effort.

Figure 2.8 displays the results for a mesh size of $\Delta x = 1\,\mathrm{m}$ using three time step sizes, *viz.* $\Delta t = 1.0, 0.5, 0.25\,\mathrm{s}$. From both the length evolution plot and the tip speed evolution plot it is observed that the variations with the time step size are very limited. The most notable difference is observed at the onset of fracture, where the maximum tip speed for $\Delta t = 0.25\,\mathrm{s}$ is observed to be 2% higher than that for $\Delta t = 1.0\,\mathrm{s}$. This difference is significantly smaller once steady propagation occurs, *e.g.* at $t = 50\,\mathrm{s}$, where the difference is only 0.8%. Since the length of the fracture is generally not dominated by the onset phase, the observed variation in fracture length is generally also very small. At $t = 50\,\mathrm{s}$, the fracture length for $\Delta t = 1.0$ underestimates that of $\Delta t = 0.25$ by 0.5%. Although not presented here for the sake of brevity, similar results can be established for other indicators such as the fracture mouth opening.

The evolution of the fracture length and tip speed for $\Delta t = 0.5\,s$ and $\Delta x =$ 0.5, 1, $2\,m$ are depicted in Figure 2.9. The figures show that although a mesh size of $\Delta x = 2.0\,\mathrm{m}$ correctly mimics the tip speed behavior, fluctuations in the speed can be observed as a consequence of the mesh coarseness. These fluctuations can be attributed to the fact that due to the limited number of elements in this simulation (*i.e.*, only 10 elements at $t = 50\,\mathrm{s}$) the spatial discretization errors resulting from the employed moving mesh approach are significant. Upon mesh refinement these fluctuations vanish. The maximum tip speed at the onset of fracture for a mesh with $\Delta x = 0.5\,\mathrm{m}$ is only 0.5% lower than that using a twice coarser mesh. When the fracture is steady at $t = 50\,\mathrm{s}$, this relative difference is even smaller. In terms of the fracture length at $t = 50\,\mathrm{s}$, the result for $\Delta x = 1.0\,\mathrm{m}$ underestimates that for $\Delta x = 0.5\,\mathrm{m}$ by a mere 0.5%.

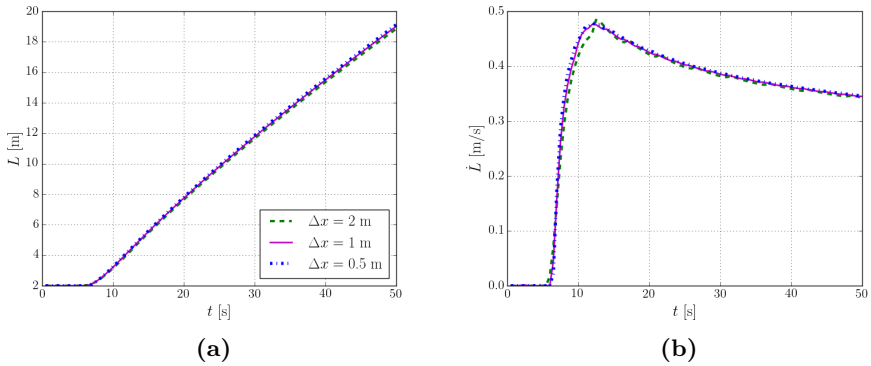

(a) **(b)**

Figure 2.9: (a) Fracture length with time for constant time step $\Delta t = 0.5\,\mathrm{s}$, and (b) Tip velocity profile for constant time step $\Delta t = 0.5\,\mathrm{s}$

In the context of the sensitivity studies and stochastic simulations considered in the remainder of this section, it is essential that the numerical errors do not pollute the results. This means that the variations discussed above should be negligible in comparison to the stochastic variations in the input parameters. On the other hand, making the mesh sizes and time step sizes too small will dramatically increase the computational effort due to the large number of samples that is required in accordance with (4.48). Herein we select a mesh size of $\Delta x = 1.0\,\mathrm{m}$ and a time step size $\Delta t = 1.0\,\mathrm{s}$, which provides a good balance between numerical accuracy (see above) and computational effort.

2.5.2 Sensitivity analysis

In this section we apply the deterministic model outlined above to identify the input factors that drive the variation in the output. As output observables we consider the fracture length and fracture aperture. As input parameters we consider the model parameters that cannot be established with a high degree of certainty in reality, *viz.* the plane strain modulus E', the fracture height, H, and the leak-off coefficient, c_l. In our sensitivity analysis we independently vary the input factors and study their impact on the output observables. This screening procedure is often considered as the first step in a forward uncertainty analysis, since it identifies the dominant sources of randomness.

In Figure 2.10 we consider the effect of the plane strain modulus on the fracture geometry, while keeping all other model parameters unchanged. A range of plane strain moduli from $1 \times 10^3\,\mathrm{MPa}$ to $1 \times 10^4\,\mathrm{MPa}$ is considered. Figure 2.10 conveys that a stiffer formation results in a longer and narrower fracture, com-

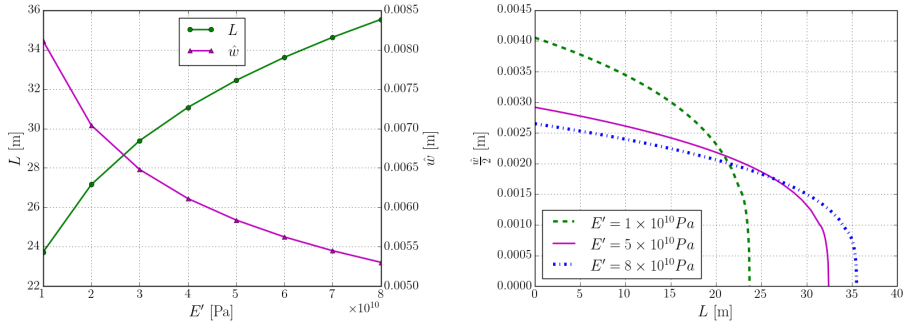

(a) **(b)**

Figure 2.10: (a) Fracture length and aperture with varying plane strain modulus, and (b) Fracture geometry profile with varying plane strain modulus

pared to a more compliant formation. Considering the nature of the model – which revolves around the conservation of volume – this is plausible, since in the case of a stiff formation fracture propagation is favored over fracture widening. From Figure 2.10a we observe that the dependence of the output observables on the plane strain modulus is highly nonlinear, in the sense that the rate of change of the output observables is significantly lower than that of the plane strain modulus. For example, an increase of 45% in the fracture length is observed when increasing the plane strain modulus by a factor of 8. This same increase in plane strain modulus moreover leads to a reduction of the fracture mouth opening by only 35%. As a result, the well pressure – which is proportional to the product of the fracture mouth opening and plane strain modulus – increases with an increase in formation stiffness, which is in line with the experimental results in [141]. In addition, this sensitivity analysis conveys that the response of the observables is non-symmetric, in the sense that the rate of change of the length and fracture mouth opening for stiff formations is smaller than for compliant formations.

Figure 2.11 shows the dependence of the output observables on a range of leak-off coefficients, ranging from the impermeable case ($c_l = 0$ m/s$^{1/2}$) to $c_l = 5e^{-5}$ m/s$^{1/2}$, which is 50% more than the value taken in the GRI experiment [141] based on tight gas sands. As anticipated from the conservation of volume, an increasing leak-off coefficient yields a shorter and narrower crack. Increasing the deterministic value considered in the previous section by a factor of 5 yields a decrease in fracture length of 14% and a decrease in fracture mouth opening of 7%. From Figure 2.11b it is observed that the fracture profile shape is insensitive to the leak-off coefficient. In contrast to the dependence on the plane strain modulus considered above, the rate of change of the observables is practically constant for the considered range of leak-off coefficients.

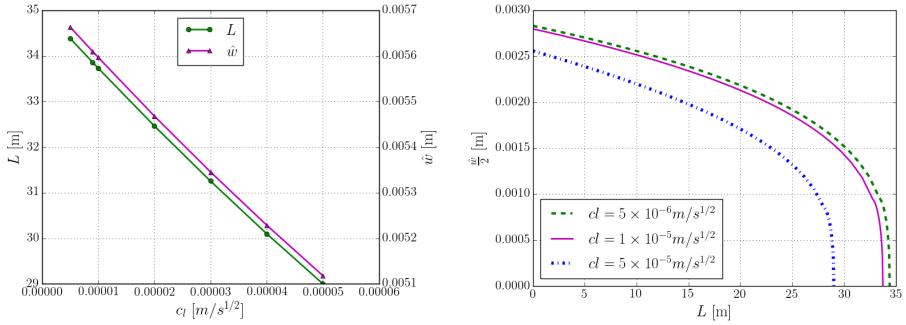

(a) **(b)**

Figure 2.11: (a) Fracture length and aperture with varying leak-off coefficient, and (b) Fracture geometry profile with varying leak-off coefficient

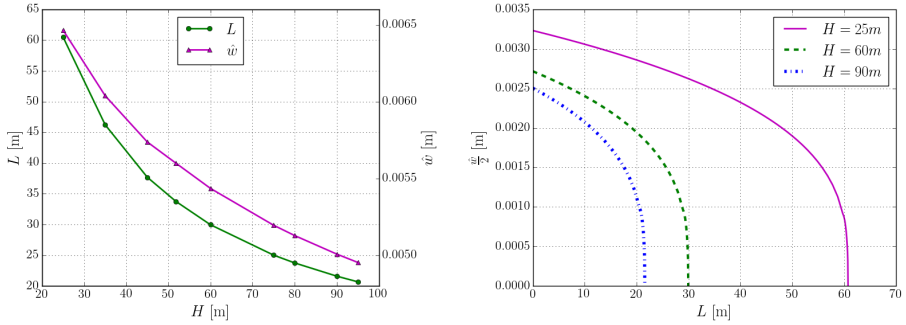

(a) **(b)**

Figure 2.12: (a) Fracture length and aperture with varying fracture height, and (b) Fracture geometry profile with varying fracture height

Figure 2.12 displays the variation of the output observables for fracture heights ranging from 25 m to 95 m. Doubling the fracture height from 25 m reduces the fracture mouth opening by 15% and the fracture length by 44%. As expected from volume conservation (where in this particular case leak-off effects are not pronounced) the product of these two observables is approximately reduced by a factor of two. The direct impact of the fracture height on the volume conservation model results in a strong sensitivity of the output observables. The non-symmetry of the response observables is consistent with the expected behavior in the extreme cases, for which a large height should yield a very short and narrow crack, and a small height should yield an extremely long and wide fracture.

2.5.3 Stochastic setting

In this section we present the results of Monte Carlo simulations. In Section 2.5.3 we first study the stochastic results for the case where each of the uncertain input parameters is varied independently, which closely connects this section to the sensitivity analysis presented above. The stochastic analysis presented here provides insight into the evolution of the randomness in time, and on the dependence of the uncertain observables on the magnitude of the random input variables. In Section 2.5.3 we then consider the case of a random field for the plane strain modulus, which elucidates the dependence of the observables on the spatial correlation of the uncertain input parameter. The reported sample sizes are all based on the estimate (4.48) with a confidence level for the estimator of the mean fracture length.

Independent variation of uncertain parameters

We first consider the plane strain modulus, E', to be the only uncertain parameter. Since the plane strain modulus is positive by definition, we represent this uncertain parameter by a log-normal distribution with mean value $\mu_{E'} = 6.13 \times 10^4\,\text{MPa}$ and coefficient of variation $V_{E'} = 50\%$. To achieve a confidence level of 98% for the mean fracture length, a sample size of $N = 304$ is required. To avoid pollution of the stochastic results by excessive discretization errors for this 98% confidence interval, a mesh size $\Delta x = 1\,\text{m}$ and a time step size $\Delta t = 1\,\text{s}$ is used in combination with the volume conservation constraint and tip enrichment function. In this computational setting, a single realization with $T = 800\,\text{s}$ requires 96 minutes on a Intel Core i5 vPro processor. Without the use of the volume constraint and enrichment function, significantly smaller mesh and time step sizes would be required to achieve the numerical accuracy required for a 98% confidence interval, which would dramatically increase the total simulation time of the Monte Carlo simulation.

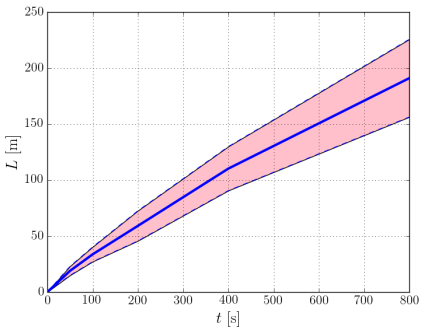

Figure 2.13: Evolution of the mean (solid blue line) and 98% confidence interval (shaded area) of the fracture length in time corresponding to a variation in the plane strain modulus of $V_{E'} = 50\%$.

t	μ_L	σ_L	V_L	$\mu_{\hat{w}}$	$\sigma_{\hat{w}}$	$V_{\hat{w}}$
100	33.619	3.348	9.9	0.0056	0.0005	8.9
200	59.040	5.790	9.8	0.0066	0.0006	9.1
400	110.166	10.030	9.1	0.0076	0.0007	9.2

Table 2.2: Statistical moments of the fracture length and fracture aperture corresponding to a coefficient of variation $V'_E = 50\%$ for the plane strain modulus.

In Figure 2.13 we show the evolution of the fracture length in time, where the mean value is represented by the solid line, and the shaded area indicates the 98% confidence interval of the fracture length. Typical distributions for the fracture length and fracture mouth opening at $t = 100\,\mathrm{s}$ are displayed in Figure 2.14, from which we infer that the distributions are unimodal. The error bars in Figure 2.13 show that the standard deviation of the fracture length (and with that its confidence interval) increases proportionally with the mean. This observation is confirmed in Table 2.2, from which it is observed that the coefficients of variation of the length and fracture mouth opening only vary moderately.

In Figure 2.15 we study the dependence of the results on the coefficient of variation of the plane strain modulus at two time instances. Note that the used sample size is different for each coefficient of variation in order to achieve the same confidence level for the mean estimator of the fracture length. At both time instances we observe that the coefficient of variation of the fracture length is proportional to that of the input parameter. This behavior can be explained by considering the dependence of the mean and the standard deviation on the

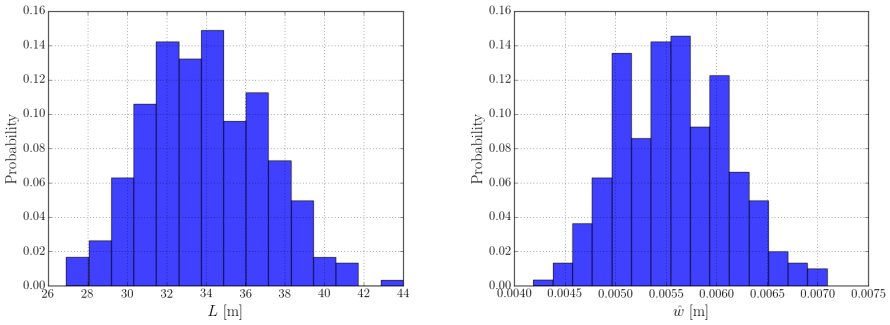

(a) Fracture length, L **(b)** Maximum aperture, $\hat{w}$

Figure 2.14: Histograms of the fracture length and maximum fracture aperture for 50% variation of the plane strain modulus, E', at $t = 100\,\mathrm{s}$

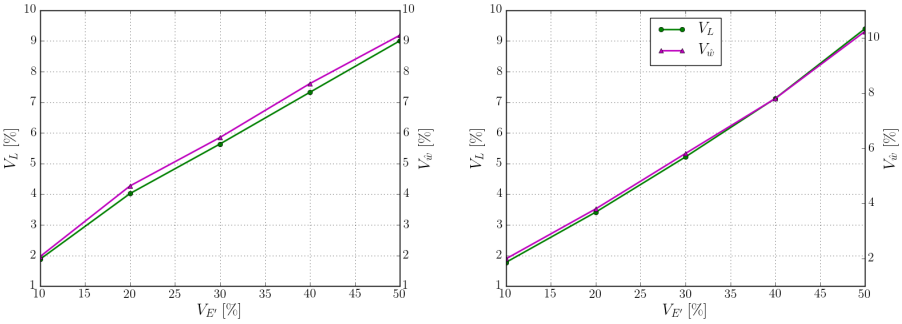

(a) $t = 100\,\mathrm{s}$ **(b)** $t = 500\,\mathrm{s}$

Figure 2.15: Coefficients of variation of the fracture length, L, and maximum aperture, $\hat{w}$, as a function of the variation of the plane strain modulus, E', at different time instances.

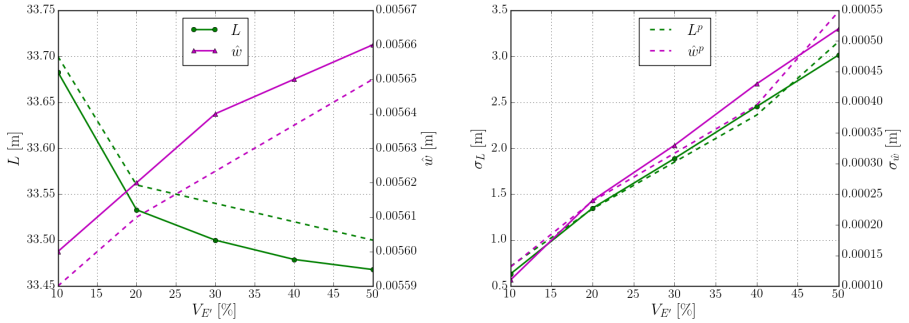

(a) Mean **(b)** Standard deviation

Figure 2.16: Statistical moments of the fracture length, L, and maximum aperture, $\hat{w}$, as a function of the variation of the plane strain modulus, E', at $t = 100\,\mathrm{s}$. The perturbation results, L^p and $\hat{w}^p$, are indicated by the dashed lines.

coefficient of variation of the input, as displayed in Figure 2.16. This figure conveys that the standard deviation of the fracture length increases with an increasing variation of the plane strain modulus. Using the results from the sensitivity analysis presented above, we verify the correspondence of the observed behavior with that predicted by a first-order perturbation analysis [135],

$$\sigma_L \approx \left|\frac{\partial L}{\partial E'}\right|_{E'=\mu_{E'}} \frac{\partial E}{\partial z} \approx \left|\frac{\partial L}{\partial E'}\right|_{E'=\mu_{E'}} \sigma_{E'}, \tag{2.35}$$

which is displayed in Figure 2.16b by the dashed lines. The observed decrease in the mean value is also in good agreement with the results of the sensitivity analysis, as shown by the dashed lines in the Figure 2.16a, where the mean values are approximated using second-order perturbation theory [135]:

$$\mu_L \approx L|_{E'=\mu_{E'}} + \frac{1}{2}\frac{\partial^2 L}{\partial E'^2}\sigma^2_{E'} \tag{2.36}$$

For the case considered here the variation in the mean of the fracture length is moderate (Figure 2.16a), as a result of which the observed behavior of the coefficient of variation in Figure 2.15 is governed by the behavior of the standard deviation of the fracture length. Similarly, the results for the fracture mouth opening are also observed to correspond well with the sensitivity analysis.

In Figure 2.17 we show the evolution of the fracture length for the case in which the leak-off coefficient is described by a log-normal distribution with mean value $\mu_{c_l} = 9.84 \times 10^{-6}\ \mathrm{m/s^{1/2}}$ and coefficient of variation $V_{c_l} = 50\%$. The

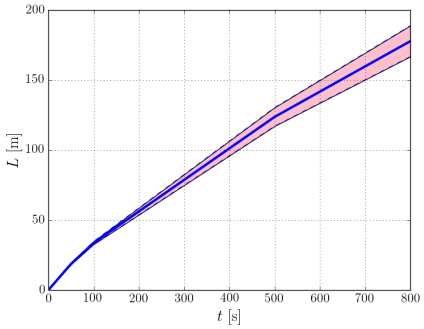

Figure 2.17: Evolution of the mean (solid blue line) and 98% confidence interval (shaded area) of the fracture length in time corresponding to a variation in the leak-off coefficient of $V_{c_l} = 50\%$.

probability distributions at $t = 100\,\mathrm{s}$ are shown in Figure 2.18. Figure 2.19 presents the corresponding relation between the coefficients of variation of the observables, *viz.* the fracture length and maximum aperture, and that of the leak-off coefficient at two time instances, where the sample sizes have been selected in accordance with the confidence level of the mean estimator of the fracture length. From Figure 2.19 one can observe that the coefficients of variation of the output observables increase only modestly (by approximately a factor of 2 from $t = 100\,s$ to $t = 500\,s$) in time. The observed relation between the coefficients of variation of the input and output is explained by the fact that the mean value is affected minimally by the coefficient of variation of the leak-off coefficient, while the standard deviation increases proportionally with it. From Figure 2.20 it is observed that the behavior of the mean and standard deviation of the observables is in good agreement with the perturbation results following from the sensitivity analysis.

We finally consider the independent random variation of the fracture height, which is represented by a log-normal distribution with mean $\mu_H = 51.8$ m and coefficient of variation $V_H = 50\%$. A sample size of $N = 553$ (providing a confidence level of 95%) is selected to compute the time evolution of the fracture length as shown in Figure 2.21, for which the probability distributions of fracture length L and maximum aperture $\hat{w}$ at time $t = 100\,s$ are shown in Figure 2.22. The coefficient of variation is essentially invariant in time, which is confirmed by comparison of the relation between the input and output coefficients of variation at two time instances as shown in Figure 2.23. From Figure 2.24 we observe that both the mean and the standard deviation of the observables match well with the results from the sensitivity analysis.

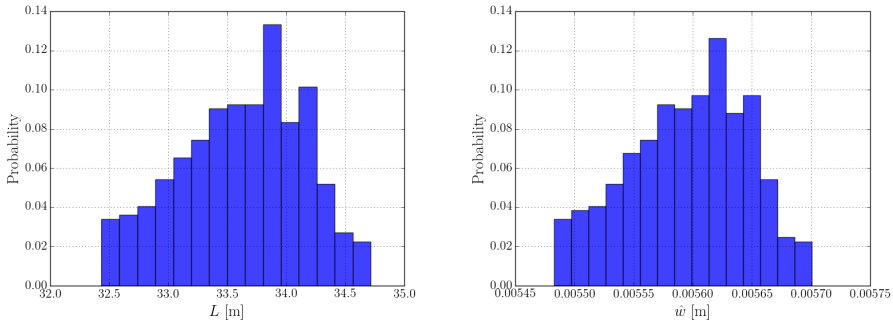

(a) Fracture length, L **(b)** Maximum aperture, $\hat{w}$

Figure 2.18: Histograms of the fracture length and maximum fracture aperture for 50% variation of the leak-off coefficient, c_l, at $t = 100\,\mathrm{s}$.

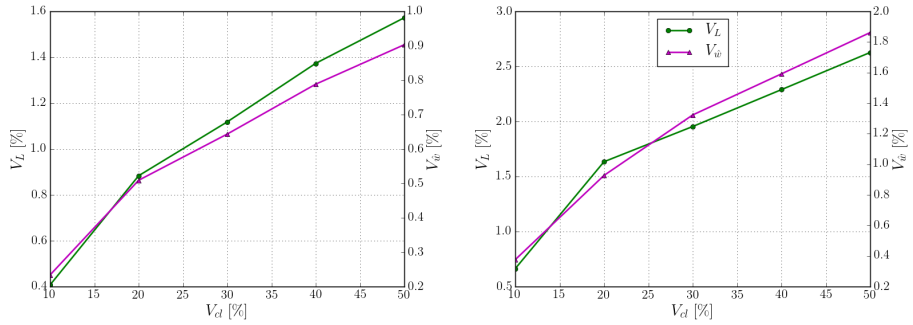

(a) $t = 100\,\mathrm{s}$ **(b)** $t = 500\,\mathrm{s}$

Figure 2.19: Coefficients of variation of the fracture length, L, and maximum aperture, $\hat{w}$, as a function of the variation of the leak-off coefficient, c_l, at different time instances.

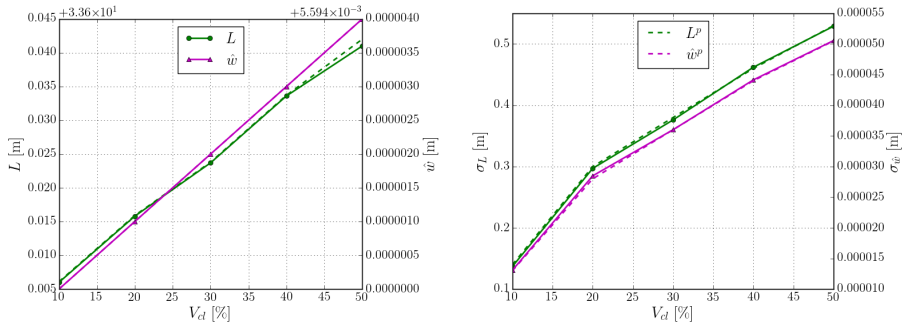

(a) Mean **(b)** Standard deviation

Figure 2.20: Statistical moments of the fracture length, L, and maximum aperture, $\hat{w}$, as a function of the variation of the leak-off coefficient, c_l, at $t = 100\,\text{s}$. The perturbation results, L^p and $\hat{w}^p$, are indicated by the dashed lines.

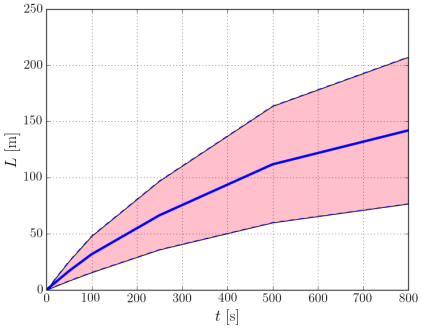

Figure 2.21: Evolution of the mean (solid blue line) and 95% confidence interval (shaded area) of the fracture length in time corresponding to a variation in the fracture height of $V_H = 50\%$.

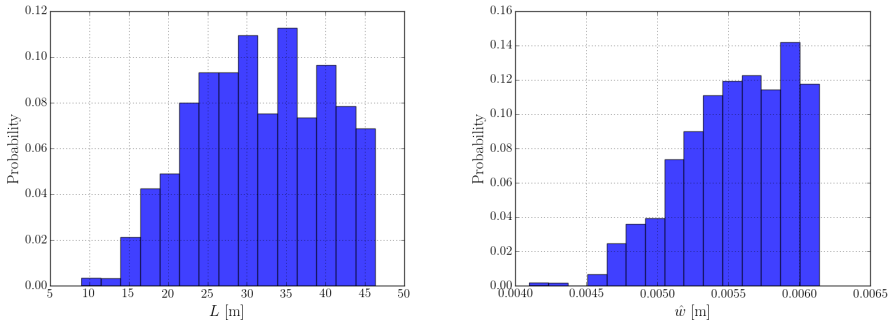

(a) Fracture length, L **(b)** Maximum aperture, $\hat{w}$

Figure 2.22: Histograms of the fracture length and maximum fracture aperture for 50% variation of the fracture height, H, at $t = 100\,\mathrm{s}$.

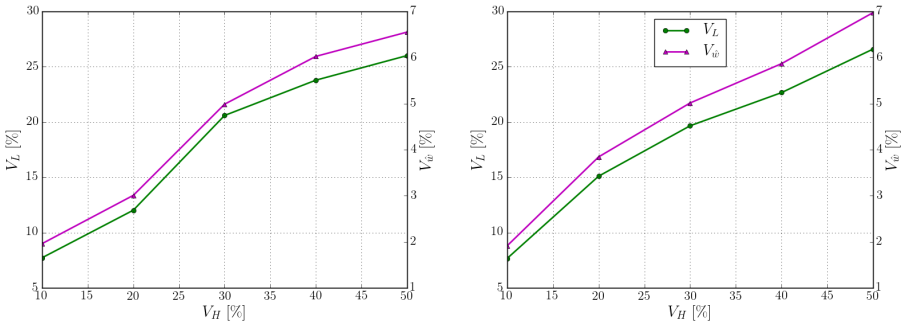

(a) $t = 100\,\mathrm{s}$ **(b)** $t = 500\,\mathrm{s}$

Figure 2.23: Coefficients of variation of the fracture length, L, and maximum aperture, $\hat{w}$, as a function of the variation of the fracture height, H, at different time instances.

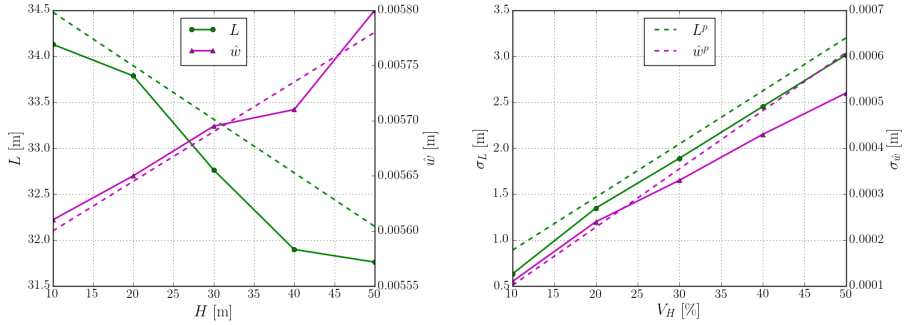

(a) Mean **(b)** Standard deviation

Figure 2.24: Statistical moments of the fracture length, L, and maximum aperture, $\hat{w}$, as a function of the variation of the fracture height, H, at $t = 100\,\mathrm{s}$. The perturbation results, L^p and $\hat{w}^p$, are indicated by the dashed lines.

Comparing the effects of the random input variable on the fracture length reveals that it is more sensitive to randomness in the plane strain modulus (Figure 2.15 on page 49) than to randomness in the leak-off coefficient (Figure 2.19 on page 52), in the sense that a coefficient of variation in the fracture length of $V_L \approx 2.5\%$ corresponds to a coefficient of variation of the plane strain modulus of $V_{E'} \approx 15\%$ and a coefficient of variation of the leak-off coefficient of $V_{c_l} = 50\%$ (results at $t = 500\,\mathrm{s}$). The sensitivity to the fracture height is observed to be even stronger (Figure 2.23 on the facing page), in the sense that $V_L \approx 10\%$ corresponds to coefficients of variation of $V_{E'} \approx 50\%$ and $V_H \approx 15\%$ for the plane strain modulus and fracture height, respectively.

Heterogeneous random plane strain modulus field

We now consider the case in which the plane strain modulus, E', is described by a heterogeneous random field instead of a scalar variable. We consider a random field with mean $\mu_{E'} = 6.13 \times 10^3\,\mathrm{MPa}$ and coefficient of variation $V_{E'} = 50\%$. We vary the length scale of the auto-correlation function in equation (4.50) from $l_{E'} = 5\,\mathrm{m}$ to $l_{E'} = 25\,\mathrm{m}$. The random field for the plane strain modulus is discretized using 12 Karhunen-Loève modes, which is sufficient for the representation of the random field corresponding to the smallest correlation length considered. Table 2.3 lists the statistical moments of the observables at $t = 100\,\mathrm{s}$ based on a Monte-Carlo simulation with $N = 384$, which is in accordance with a 95% confidence level for the mean estimator in the fracture length.

$l_{E'}$ [m]	μ_L [m]	σ_L [m]	V_L[%]	$\mu_{\hat{w}}$ [m]	$\sigma_{\hat{w}}$ [m]	$V_{\hat{w}}$[%]
5	27.545	6.682	24.3	0.0071	0.0030	42.3
10	28.496	7.177	25.2	0.0078	0.0041	52.6
15	29.319	6.204	21.2	0.0075	0.0037	49.3
20	29.735	6.601	22.2	0.0074	0.0029	39.2
25	31.091	6.158	19.8	0.0067	0.0021	31.3
∞	33.619	3.348	9.9	0.0056	0.0005	8.9

Table 2.3: Statistical moments of the fracture length, L, and the maximum aperture, $\hat{w}$, at $t = 100\,\mathrm{s}$ corresponding to a variation of the plane strain modulus of $V_{E'} = 50\%$ for random fields with varying correlation lengths, $l_{E'}$. Note that the case of $l_{E'} = \infty$ corresponds to the homogeneous case discussed in Section 2.5.3.

The most notable observation from the results in Table 2.3 is that the coefficient of variation of the output observables is significantly higher than in the case of a homogeneous plane strain modulus with equal coefficient of variation (see Table 2.2). To better understand this observation, in Figure 2.25 we perform a closer inspection of the realizations that lead to Table 2.3. In the rows of this figure we collect the Monte-Carlo results for the correlation lengths reported in Table 2.3, starting with the smallest correlation length. In the second and third column we show the probability distributions for the fracture length and the fracture mouth opening, respectively. The first column displays the plane strain modulus field that leads to three distinct realizations in the sample, *viz.* the smallest fracture length, the largest fracture length, and the fracture length closest to the mean value. We observe that the realizations of the plane strain modulus field that lead to the smallest fracture lengths in all cases correspond to the situation in which the elastic modulus is very small near the well. When this happens the injected fluid causes fracture widening near the well, rather than fracture propagation into the formation. More generally, in the case of heterogeneous fields, local zones in which the formation is very compliant can lead to blockage of propagation, as the injected fluid volume can be locally accumulated in this zone. Long fractures are obtained in the case that the plane strain modulus is large near the well, and high (in a spatially averaged sense) compared to the mean value. In such situations the blockage of propagation due to a compliant zone does not occur, and the injected fluid volume is effectively transferred to the crack tip.

In terms of the dependence of the results on the correlation length it is observed that the mean fracture length decreases as the correlation length decreases. This is explained by the fact that in the case of a smaller correlation length, the chance of a locally compliant zone in the formation increases. The blockage of propagation in such zones is then more frequent, which leads to a reduction in

fracture length expectation. From Table 2.3 we moreover observe a moderate increase in coefficient of variation of the fracture length as the correlation length increases.

From the distributions of the fracture mouth opening in Figure 2.25 (c1–c5) we observe a notable difference in comparison to that for the homogeneous random plane strain modulus case (Figure 2.14b). In the homogeneous case there exists a strong correlation between the fracture length and the fracture mouth opening, in the sense that long cracks are narrow by virtue of the fact that their volume is similar (assuming leak-off effects to be limited). Figure 2.10 in the sensitivity study clearly confirms this observation; see also the discussion in Section 2.5.2. Although the fracture length and fracture width in the case of a heterogeneous field are not uncorrelated, the fracture mouth opening is most strongly influenced by the local plane strain modulus near the well. Since the fracture opening in the PKN model depends locally on the plane strain modulus, the log-normal distribution of the plane strain modulus reflects directly on that of the fracture mouth opening, as can be seen in the third column of Figure 2.25. The sensitivity of the fracture mouth opening to local variations in the plane strain modulus field also results in coefficients of variation that are significantly higher than those in the homogeneous case (see Table 2.3).

2.6 Conclusions

We have presented a sampling-based stochastic analysis of the hydraulic fracturing process based on the Perkins-Kern-Nordgren (PKN) model. The consideration of this model is motivated by the fact that in the deterministic case high-accuracy solutions can be computed with feasible computational effort, which makes its application in the context of direct Monte Carlo sampling practical. Although this model significantly simplifies the hydraulic fracturing process, it bears practical relevance, especially for fractures in the viscosity-dominated regime. A limitation of the model pertains to the local elasticity relation in the PKN model, which restricts its application to low-frequency spatial variations of the model parameters.

In order to compute high-fidelity solutions that do not pollute stochastic analyses with numerical errors, a moving-mesh finite element method is developed. The employed backward-Euler time integration scheme is supplemented with a sub-iteration technique, such that the mesh propagation relation becomes implicit. The non-linearity of the model is solved using Newton iterations. We have performed detailed mesh size and time integration step convergence studies. We have found that in order to attain solutions with acceptable accuracy in the context of the stochastic analysis, the finite element methodology had to be enhanced in two manners. First, the global conservation of volume was found to be

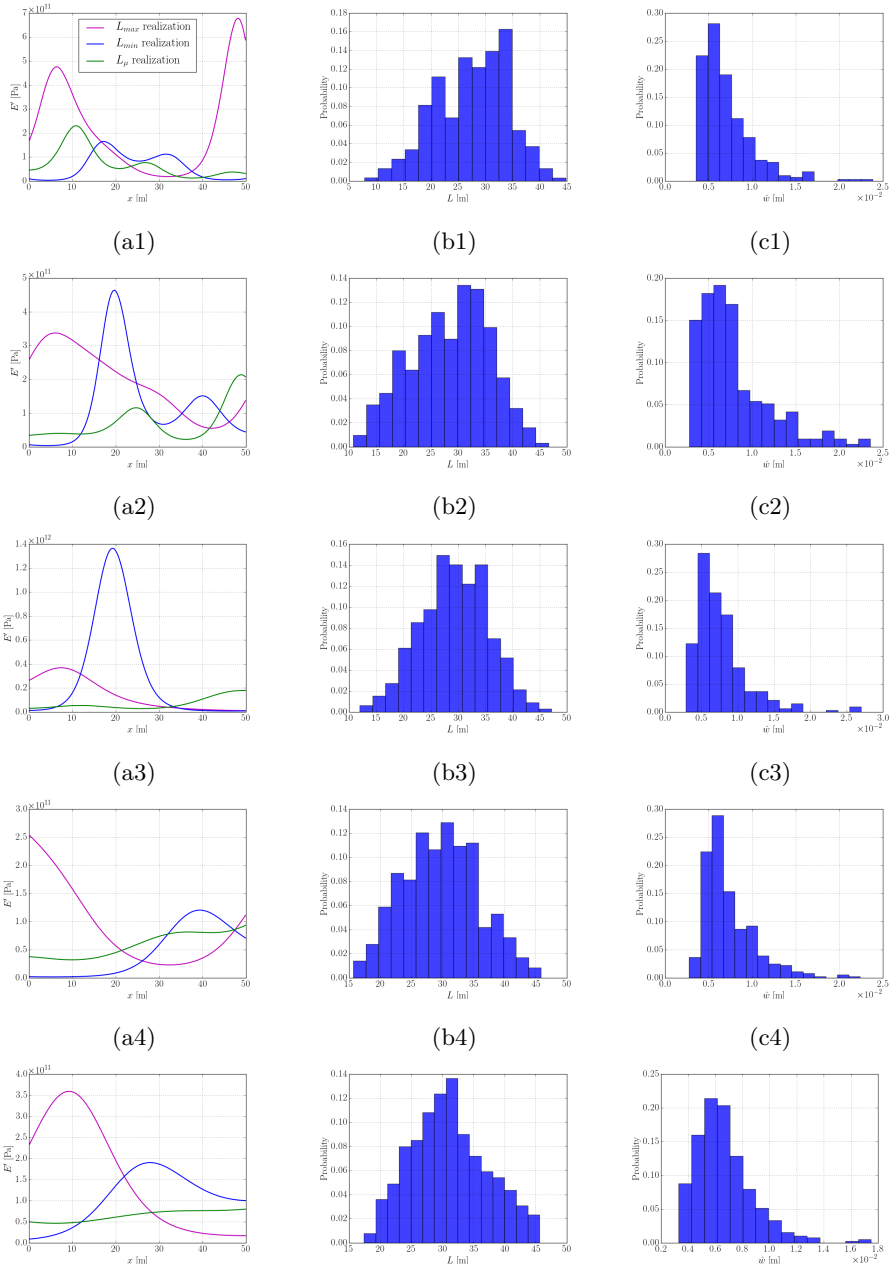

Figure 2.25: (a1-a5) Examples of realization for $l_{E'} = (5, 10, 15, 20, 25)$ m, respectively. (b1-b5) Histograms of the fracture length for $l_{E'} = (5, 10, 15, 20, 25)$ m, respectively. (c1-c5) Histograms of the maximum aperture for $l_{E'} = (5, 10, 15, 20, 25)$ m, respectively.

significantly violated due to the highly non-linear character of the model. The observed loss of volume led to significant underestimation of the fracture length. To circumvent this problem, volume conservation was enforced explicitly by means of a Lagrange multiplier approach. Second, the weakly singular behavior of the fracture opening and pressure at the tip was found to be troublesome in the case of a standard finite element basis. On one hand the improper representation of the singularity by the basis required the use of an *ad hoc* tip velocity relation. On the other hand, the mesh resolution of the uniform finite element mesh was found to be insufficient. These issues were resolved by enrichment of the standard finite element space with a singular tip function. We established that in the deterministic setting, our finite element simulations show very good agreement with results reported in literature for a realistic test case even on relatively coarse meshes.

The sensitivity of the fracture evolution process with respect to various random input parameters was studied. From the direct Monte Carlo simulations it was found that the mean and standard deviation of the fracture length and fracture mouth opening correspond well to those values obtained using perturbation theory. This observation conveys that – at least for the test case considered – linearization of the model provides meaningful information on the behavior of the stochastic moments, despite the complexity of the model and its solution procedure.

To demonstrate the suitability of the developed methodology for studying random heterogeneities in formation properties we have considered a test case in which the formation stiffness was described by a random field. The random dimension was discretized using a Karhunen-Loéve expansion. The sampling results demonstrate that the response uncertainty is amplified by the heterogeneous character of the random material property field. For the fracture length this is explained by the fact that fracture propagation is sensitive to local variations in the elastic properties of the formation because locally compliant regions can inhibit transfer of the fracturing fluid and, hence, propagation of the crack. For the fracture mouth opening an even stronger amplification is observed as a consequence of the fact that the fracture opening is directly related to the material property. Although this observation can be explained well based on the structure of the PKN model, it requires further study to understand to what extend a similar conclusion can be drawn for more sophisticated hydraulic fracturing models.

Although the results presented herein provide fundamental insight into the primary characteristics of the stochastic behavior of the hydraulic fracturing process, it is evident that more detailed information can be obtained by more versatile models and simulation strategies. In particular the PKN model does not rely on a fracture mechanics model based on the material's fracture toughness, which

restricts the scope of this work to fractures in the viscosity-dominated regime. When considering uncertainty quantification using physically richer models it will remain key to not pollute the results with numerical errors, which will inevitably lead to computationally complex Monte Carlo methods. The use of alternative stochastic techniques, such as the perturbation method can be expected to yield meaningful results at a much lower cost than direct Monte Carlo sampling.

2.A Benchmark results

In Section 2.5.1 we have considered the deterministic benchmark result based on the case study by Warpinski *et al.* [141]. The parameters for the considered simulation can be found in Table 2.1. Figure 2.5 in Section 2.5.1 shows the results for this benchmark case as obtained using the finite element technique developed in this manuscript, as well as the results for the simulators included in Ref. [141]. Note that the results of these simulators have been reported with intervals of 1200 s. For completeness, in Table 2.4 we report the results obtained by the method proposed herein with a mesh size of $\Delta x = 1\,\mathrm{m}$ and a time step size of $\Delta t = 1\,\mathrm{s}$. Note that the presented results have been rounded off to 4 decimals.

Time t [s]	Fracture height H [m]	Fracture length L [m]	Maximum aperture $\hat{w}$ [m]
0	51.8	2.0000	0.0037
1200	51.8	246.1651	0.0089
2400	51.8	421.3913	0.0101
3600	51.8	575.4035	0.0109
4800	51.8	716.5376	0.0114
6000	51.8	848.7358	0.0119
7200	51.8	974.0853	0.0122
8400	51.8	1093.9648	0.0126
9600	51.8	1209.3184	0.0129
10400	51.8	1320.8104	0.0131
12000	51.8	1428.9438	0.0134

Table 2.4: Numerical output of the model considered in this manuscript formatted consistently with the results in Ref. [141].

Chapter 3

A PGD approach to crack propagation in brittle materials

Understanding the failure of brittle heterogeneous materials is essential in many applications. Heterogeneities in material properties are frequently modeled through random fields, which typically induces the need to solve finite element problems for a large number of realizations. In this context, we make use of reduced order modeling to solve these problems at an affordable computational cost. This paper proposes a reduced order modeling framework to predict crack propagation in brittle materials with random heterogeneities. The framework is based on a combination of the Proper Generalized Decomposition (PGD) method with Griffith's global energy criterion. The PGD framework provides an explicit parametric solution for the physical response of the system. We illustrate that a non-intrusive sampling-based technique can be applied as a post-processing operation on the explicit solution provided by PGD. We first validate the framework using a global energy approach on a deterministic two-dimensional linear elastic fracture mechanics benchmark. Subsequently, we apply the reduced order modeling approach to a stochastic fracture propagation problem.

This chapter is reproduced from [142]: H. Garikapati, C.V. Verhoosel, E.H. van Brummelen, S. Zlotnik and P. Díez. A Proper Generalized Decomposition (PGD) approach to crack propagation in brittle materials: With application to random field material properties. *Computational Mechanics 2019*.

3.1 Introduction

One of the important goals in engineering design is to avoid catastrophic failure. Besides, in many applications, it is often crucial to understand the failure processes. To realistically model failure processes in engineering systems it is often essential to study the impact of uncertainties in the system parameters, such as loading conditions, specimen geometry, material properties, etc. Taking into account such uncertainties in an analysis typically implies that the number of times that a solution must be computed increases rapidly with an increase in the number of uncertain parameters. The use of reduced order models is then indispensable as these make it practical to solve the problem for many parameter realizations at an affordable computational effort.

While Reduced Order Modeling (ROM) is a well-established concept in the field of linear elastic solid mechanics [143–145], its application to fracture mechanics problems has remained essentially unexplored, with Ref. [146] providing a notable exception. In the present work, a new ROM technique for fracture propagation is presented which allows failure to be studied as a post-processing operation of a parameterized solution that incorporates varying loads, crack lengths and material uncertainties. We propose a parameterization of the crack on the one hand, and a method to take into account the fracture propagation criterion in the reduced order model setting on the other hand. Furthermore, we extend the framework to include random heterogeneities in the material properties.

The reduction method of choice in this work is the Proper Generalized Decomposition (PGD) method, which is a reduced order modeling technique specifically designed to counter the curse of dimensionality induced by the increase in system parameters to be considered in an analysis [147]. The PGD method is comprised of two stages: *i)* An *offline stage*, where the solution is obtained in the whole computational vademecum [148, 149] in an efficient way which breaks down the computational complexity of the high-dimensional parametric problem. This is achieved by a separated representation of the solution. *ii)* An *online stage*, where, in real time, the solution can be readily obtained as a post-processed result [150, 151].

Our work is based on the concept of linear elastic fracture mechanics (LEFM), which is a frequently used model for brittle fracture [152]. We consider Griffith's fracture propagation criterion, which evaluates the stability of a fracture based on an energy balance between the work done by external loads, the elastic energy stored within the system, and the energy dissipated through the fracture surface. Griffith's theory in its basic form is restricted to elastic brittle materials in which there is no plastic deformation near the crack tip. The simulation of fracture evolution in the LEFM framework typically involves a stepwise incrementation of the crack path based on the evaluation of the fracture criterion, which implies

that a linear elasticity problem (with a tip singularity) must be solved at each step in the propagation process. This finite element procedure is typically computationally expensive because, on account of accuracy and stability requirements, the crack length increments must generally be small, and because some form of mesh adaptation is required to accommodate changes in fracture geometry. The PGD approach in this work conveniently bypasses these problems, as the fracture length is considered as one of the coordinates of the obtained parametric solution, and differentiation with respect to the fracture length provides a suitable propagation measure in the form of the energy release rate at all configurations in the parametric domain.

This paper is organized as follows. The model problem considered in this work is introduced in Section 3.2. Section 3.3 demonstrates how a separable form of the problem can be obtained in regard to the fracture length, which is a prerequisite for the application of the PGD method discussed in Section 3.4. We herein adapt the PGD formulation to solve a linear system of equations, which we refer to as the PGD solver [153]. Section 3.5 studies the accuracy of the fracture length parametrization in the setting of a stationary fracture. Section 3.6 then describes the application of the PGD framework to Griffith's fracture model, along with the consideration of an LEFM benchmark test case [154]. Section 3.7 then presents an application in the stochastic setting, where we use the Karhunen-Loève expansion [140, 155] to discretize random field material properties. A Monte Carlo based stochastic analysis is then performed that demonstrates the efficiency of the PGD framework. Conclusions are presented in Section 3.8.

3.2 Model fracture problem

As a model problem we consider a straight fracture in a homogeneous linear elastic two-dimensional ($d = 2$) continuum, see Figure 3.1. The crack propagates in response to an external traction imposed on the system. Inertia, gravity and body forces are neglected. Assuming small deformations and deformation gradients, along with plane strain assumptions, the solid deformation is governed by the momentum balance

$$\nabla \cdot \boldsymbol{\sigma} = \mathbf{0} \qquad \text{in } \Omega,$$

where the Cauchy stress, $\boldsymbol{\sigma}$, follows Hooke's law for isotropic materials

$$\begin{aligned} \boldsymbol{\sigma} &= 2\mu\,\boldsymbol{\varepsilon} + \lambda\,\mathrm{tr}(\boldsymbol{\varepsilon})\,\mathbf{I}, \\ \boldsymbol{\varepsilon} &= \nabla^s \boldsymbol{u} = \frac{1}{2}(\nabla \boldsymbol{u} + (\nabla \boldsymbol{u})^{\mathsf{T}}), \end{aligned} \tag{3.1}$$

where $\boldsymbol{u} = (u_x, u_y)$ denotes the displacement field, and $\boldsymbol{\varepsilon}$ the infinitesimal strain field. The Lamé parameters μ and λ are directly related to the Young's modulus,

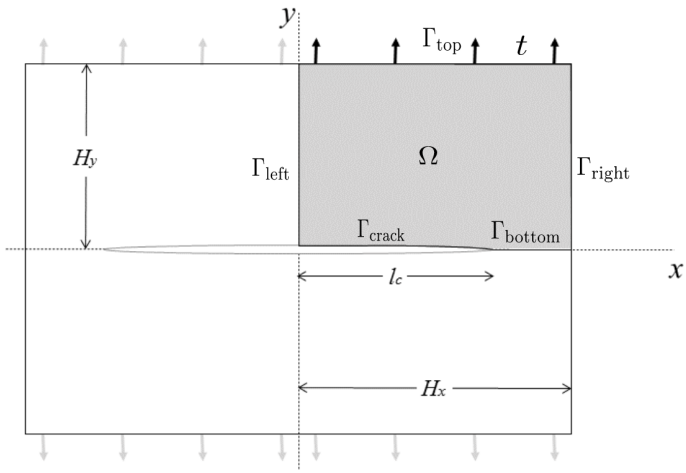

Figure 3.1: Setup of the model fracture problem. Note that the computational domain, Ω, is taken as a quarter of the specimen because of symmetry conditions.

E, and Poisson's ratio, ν. Exploiting the symmetry of the two-dimensional model, the boundary conditions are given by

$$\begin{aligned}
\boldsymbol{\sigma}\boldsymbol{n} &= \boldsymbol{t} && \text{on} \quad \Gamma_{\text{top}},\\
\boldsymbol{\sigma}\boldsymbol{n} &= \boldsymbol{0} && \text{on} \quad \Gamma_{\text{right}} \cup \Gamma_{\text{crack}},\\
\boldsymbol{u}\cdot\boldsymbol{n} &= 0 && \text{on} \quad \Gamma_{\text{bottom}} \cup \Gamma_{\text{left}},\\
\boldsymbol{\sigma}\boldsymbol{n}\times\boldsymbol{n} &= \boldsymbol{0} && \text{on} \quad \Gamma_{\text{bottom}} \cup \Gamma_{\text{left}},
\end{aligned}$$

where $\boldsymbol{n}$ is the outward pointing normal vector and $\boldsymbol{t}$ is the imposed boundary traction.

Defining the function space for the vector-valued displacement field as

$$\mathcal{V} := \{\boldsymbol{u} \in [\mathcal{H}^1(\Omega)]^{\text{d}} : \boldsymbol{u}\cdot\boldsymbol{n} = 0 \text{ on } \Gamma_{\text{bottom}} \cup \Gamma_{\text{left}}\},$$

the weak form of the problem reads as follows:

$$\begin{cases} \text{find } \boldsymbol{u} \in \mathcal{V} \text{ such that,} \\ a(\boldsymbol{u},\boldsymbol{v}) = \ell(\boldsymbol{v}) \quad \forall \boldsymbol{v} \in \mathcal{V}. \end{cases} \tag{3.2}$$

The bilinear and linear operators in (3.2) are defined as,

$$a(\boldsymbol{u},\boldsymbol{v}) := \int_\Omega \nabla\boldsymbol{v} : \mathbf{C} : \nabla^s\boldsymbol{u}\,\mathrm{d}\Omega \quad \text{and} \quad \ell(\boldsymbol{v}) := \int_{\Gamma_{\text{top}}} \boldsymbol{v}\cdot\boldsymbol{t}\,\mathrm{d}\Gamma \tag{3.3}$$

where $\mathbf{C}$ is the fourth-order elasticity tensor in accordance with Hooke's law (3.1), *i.e.*, $\boldsymbol{\sigma} = \mathbf{C} : \boldsymbol{\varepsilon}$.

The finite element discretization of the displacement field is given by

$$\boldsymbol{u}(\boldsymbol{x}) = \sum_{i=1}^{n} \mathbf{N}_i(\boldsymbol{x})\hat{u}_i, \tag{3.4}$$

where $\{\mathbf{N}_i(\boldsymbol{x})\}_{i=1}^n$ denotes the set of n vector-valued finite element basis functions that conform to the space $\mathcal{V}$, and $\{\hat{u}_i\}_{i=1}^n$ are the corresponding coefficients. Discretization of the weak problem (3.2) then yields the linear system of equations

$$\mathbf{K}\hat{\mathbf{u}} = \mathbf{f}, \tag{3.5}$$

where the vector $\hat{\mathbf{u}} = (\hat{u}_1, \cdots, \hat{u}_n)$ contains the solution coefficients, and the coefficients of the stiffness matrix $\mathbf{K}$ and load vector $\mathbf{f}$ are given by:

$$K_{ij} = a(\mathbf{N}_i, \mathbf{N}_j), \qquad f_i = \ell(\mathbf{N}_i). \tag{3.6}$$

Evidently, the finite element problem (3.5) depends on the parameters of the model. In the case that one is interested in a single parameter configuration, this would simply require the assembly of the finite element system for that particular setting, and then to solve that system to find the approximate solution. In the context of this work, however, the central idea is that the system (3.5) must be assembled and solved for many different parameters. To this end, we introduce the parametric solution to the problem, $\boldsymbol{u}(\boldsymbol{x}; \boldsymbol{\mu})$, where the (scalar) problem parameters $\boldsymbol{\mu} = (\mu_1, \cdots, \mu_{n_\mu})$ are defined over the parameter domains $\mathcal{I}_{\boldsymbol{\mu}} = \mathcal{I}_{\mu_1} \times \cdots \times \mathcal{I}_{\mu_{n_\mu}}$.

The pivotal idea of the PGD method is to attain $\boldsymbol{u}(\boldsymbol{x}; \boldsymbol{\mu})$ as the solution to a problem posed on the higher-dimensional domain $\Omega \times \mathcal{I}_{\boldsymbol{\mu}}$, the spatial semi-discretization of which can be written as:

$$\mathbf{K}(\boldsymbol{\mu})\hat{\mathbf{u}}(\boldsymbol{\mu}) = \mathbf{f}(\boldsymbol{\mu}) \qquad \forall \boldsymbol{\mu} \in \mathcal{I}_{\boldsymbol{\mu}}. \tag{3.7}$$

The general PGD strategy to obtaining this solution is to formulate a higher-dimensional weak form problem corresponding to (3.2), and then to discretize this higher-dimensional problem in space and in the parametric dimensions; see, *e.g.*, [147, 156] for the fundamentals of PGD. An essential aspect of the PGD framework is that in order to efficiently compute the parametric solution, a separable form of the weak form problem (or its discrete version) must be available. With respect to the spatially discretized system (3.5) this means that the stiffness matrix and force vector should be of the form:

$$\mathbf{K}(\boldsymbol{\mu}) = \sum_{i=1}^{n_k} \mathbf{K}^i \prod_{j=1}^{n_\mu} \phi_j^i(\mu_j), \tag{3.8a}$$

$$\mathbf{f}(\boldsymbol{\mu}) = \sum_{i=1}^{n_f} \mathbf{f}^i \prod_{j=1}^{n_\mu} \psi_j^i(\mu_j), \tag{3.8b}$$

where n_k and n_f denote the total number of terms needed to represent the parametric stiffness matrix and parametric force vector, respectively. Note that when these affine representations are not available, it is possible to construct affine separable forms that approximate the stiffness matrix and force vector.

A non-standard aspect in relation to the fracture problem considered in this work, is that the crack length parameter, l_c, enters the problem through the definition of the domain. As a consequence, the separable forms (3.8), with l_c as one of the parameters, will not follow naturally from (3.5). Obtaining separable forms instead requires recasting of the formulation in a canonical form through a pull back of the problem to a reference configuration. This reformulation of the problem is considered in the next section.

3.3 Fracture length parametrization

In this section we consider the parametrization of the system of equations with respect to the fracture length, $l_c \in \mathcal{I}_{l_c} = [l_c^{\min}, l_c^{\max}]$. For the sake of simplicity, we here consider this fracture length to be the only parameter, such that (3.8) reduces to:

$$\mathbf{K}(l_c) = \sum_{i=1}^{n_k} \mathbf{K}^i \, \phi^i(l_c) \quad \text{and} \quad \mathbf{f}(l_c) = \sum_{i=1}^{n_f} \mathbf{f}^i \, \psi^i(l_c). \tag{3.9}$$

The matrices $\mathbf{K}^i$ and the vectors $\mathbf{f}^i$ do not depend on the parameter l_c, and the functions $\phi^i(l_c)$ and $\psi^i(l_c)$ depend on the parameter only.

In order to determine the parametric forms in (3.9), a reference domain and a mapping function are introduced as illustrated in Figure 3.2. The mapping function, $\mathcal{M} : \Omega^{\text{ref}} \to \Omega$, which depends on the parameter l_c, transforms the parameter-independent reference domain, $\Omega^{\text{ref}} \ni \boldsymbol{X} = (\mathrm{X}, \mathrm{Y})$, into a physical domain, $\Omega \ni \boldsymbol{x} = (x, y)$, where the length of the crack is equal to l_c. Through this mapping, the crack length can be described by applying the corresponding mapping to the reference domain. We here consider the following choice for the mapping $\boldsymbol{x} = \mathcal{M}(\boldsymbol{X}, l_c)$:

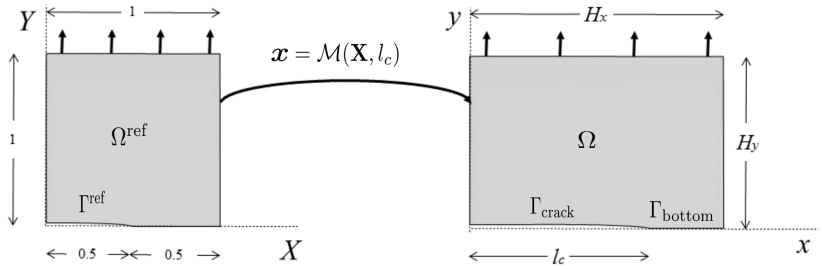

Figure 3.2: Mapping from a unit reference domain Ω^{ref} with a fracture of length 0.5 to the physical domain Ω with variable fracture length l_c.

$$\begin{aligned} x &= \begin{cases} 2\,l_c\,X & \text{for } X \leq 0.5 \\ H_x + 2(H_x - l_c)(X-1) & \text{for } X > 0.5, \end{cases} \\ y &= H_y\,Y. \end{aligned} \tag{3.10}$$

The Jacobian of this mapping follows as:

$$\mathbf{J}(\boldsymbol{X}; l_c) = \frac{\partial \boldsymbol{x}}{\partial \boldsymbol{X}} = \begin{cases} \begin{bmatrix} 2l_c & 0 \\ 0 & H_y \end{bmatrix} & X \leq 0.5 \\ \begin{bmatrix} 2(H_x - l_c) & 0 \\ 0 & H_y \end{bmatrix} & X > 0.5. \end{cases} \tag{3.11}$$

The inverse of this Jacobian can be obtained analytically and allows for an exact separable representation as the sum of products of matrices that do not depend on the parameter l_c and functions that depend only on that parameter:

$$\mathbf{J}^{-1}(\boldsymbol{X}; l_c) = \begin{cases} \begin{bmatrix} 0 & 0 \\ 0 & \frac{1}{H_y} \end{bmatrix} + \frac{1}{l_c} \begin{bmatrix} \frac{1}{2} & 0 \\ 0 & 0 \end{bmatrix} & \text{for } X \leq 0.5 \\ \begin{bmatrix} 0 & 0 \\ 0 & \frac{1}{H_y} \end{bmatrix} + \frac{1}{(H_x - l_c)} \begin{bmatrix} \frac{1}{2} & 0 \\ 0 & 0 \end{bmatrix} & \text{for } X > 0.5. \end{cases} \tag{3.12}$$

A separable form of the determinant of the Jacobian can similarly be obtained:

$$\det \mathbf{J}(\boldsymbol{X}; l_c) = \begin{cases} 2H_y l_c & \text{for } X \leq 0.5 \\ 2H_y(H_x - l_c) & \text{for } X > 0.5. \end{cases} \tag{3.13}$$

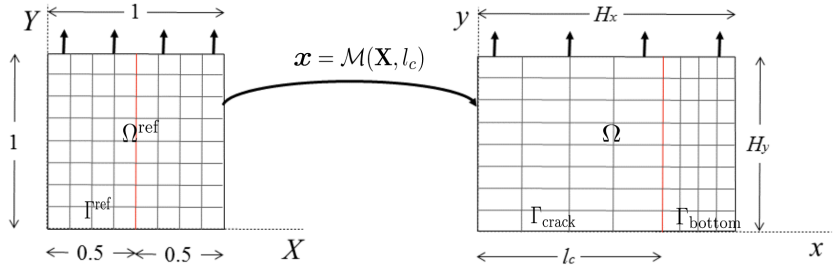

Figure 3.3: Schematic representation of the finite element mesh constructed over the reference domain. The crack tip coincides with a mesh line in the X direction by virtue of the fact that an even number of elements is used in that direction. The mapping onto the physical domain results in non-uniformly spaced elements in the physical mesh.

The matrix and vector components in equation (3.6) can now be transformed via the mapping $\mathcal{M}(\boldsymbol{X}, l_c)$ into equivalent integrals over the reference domain as

$$K_{ij} = \int_{\Omega^{\text{ref}}} \mathbf{J}^{-1}\nabla\mathbf{N}_i : \mathbf{C} : \mathbf{J}^{-1}\nabla^s\mathbf{N}_j \det(\mathbf{J})\, \mathrm{d}\Omega^{\text{ref}}, \tag{3.14a}$$

$$f_i = \int_{\Gamma^{\text{ref}}_{\text{top}}} \mathbf{N}_i \cdot (\boldsymbol{t} \circ \mathcal{M})\, \frac{\partial x}{\partial X}(X; l_c)\, \mathrm{d}\Gamma^{\text{ref}}, \tag{3.14b}$$

where use has been made of the operators defined in (3.3), and where $\Gamma^{\text{ref}}_{\text{top}} = [0, 1]$ is the top boundary of the reference domain. The basis functions $\mathbf{N}$ here are defined over the reference domain. Note that the mapping function affects the entire domain and that therefore the traction at the top boundary needs to be mapped onto the reference domain to be integrated via the surface measure $d\Gamma = \frac{\partial x(X;l_c)}{\partial X}\, d\Gamma^{\text{ref}}$.

The linear system of equations corresponding to (3.14) is discretized using a finite element mesh constructed over the reference domain Ω^{ref}. A regular, uniformly spaced, mesh is used, with an even number of elements in each direction (see Figure 3.3). As a result, the boundary at $X = 0.5$, across which the mapping function (3.10) is non-smooth, coincides with an element boundary. This has been found to be advantageous from an implementation point of view, as an element is either completely in the left side of the reference domain, $\Omega^{\text{ref}}_{\text{left}} = \{\boldsymbol{X} \in \Omega^{\text{ref}} \mid \mathrm{X} \leq 0.5\}$, or completely in the right side of the reference domain, $\Omega^{\text{ref}}_{\text{right}} = \{\boldsymbol{X} \in \Omega^{\text{ref}} \mid \mathrm{X} > 0.5\}$. Although this particular choice of the reference-domain mesh is favorable from the vantage point of implementation and accuracy, the methodology presented herein is not restricted to this choice of the mesh, and could equally well be applied to unstructured meshes.

A fundamental difference between the finite element discretization over the reference grid, equation (3.14), and the system obtained using a direct discretization over the physical domain, equation (3.6), is that the crack length parameter in (3.14) appears inside the integrands of the matrix components, and not in the domain boundary (and constraints) definitions. This makes it possible to obtain the separable forms of the stiffness matrix and force vector required for the PGD framework.

Substitution of the definitions of the inverse Jacobian (3.12), and the determinant of the Jacobian (3.13) into equation (3.14) yields a system of the form (3.9). From this substitution it directly follows that the separable form of the stiffness matrix is composed of $n_k = 4$ parametric basis functions:

$$\phi^1(l_c) = 1, \qquad \phi^2(l_c) = l_c, \qquad \phi^3(l_c) = \frac{1}{H_x - l_c}, \qquad \phi^4(l_c) = \frac{1}{l_c}. \tag{3.15}$$

The corresponding stiffness matrices are obtained as:

$$K^1_{ij} = \int_{\Omega^{\text{ref}}} \begin{bmatrix} H_y & 0 \\ 0 & 0 \end{bmatrix} \nabla \mathbf{N}_i : \mathbf{C} : \begin{bmatrix} 0 & 0 \\ 0 & 2 \end{bmatrix} \nabla^s \mathbf{N}_j \, \mathrm{d}\Omega^{\text{ref}}, \tag{3.16a}$$

$$K^2_{ij} = \int_{\Omega^{\text{ref}}} \begin{bmatrix} 0 & 0 \\ 0 & 2 \end{bmatrix} \nabla \mathbf{N}_i : \mathbf{C} : \begin{bmatrix} 0 & 0 \\ 0 & 2 \end{bmatrix} \nabla^s \mathbf{N}_j \, \mathrm{d}\Omega^{\text{ref}}, \tag{3.16b}$$

$$K^3_{ij} = \int_{\Omega^{\text{ref}}_{\text{left}}} \begin{bmatrix} H_y & 0 \\ 0 & 0 \end{bmatrix} \nabla \mathbf{N}_i : \mathbf{C} : \begin{bmatrix} H_y & 0 \\ 0 & 0 \end{bmatrix} \nabla^s \mathbf{N}_j \, \mathrm{d}\Omega^{\text{ref}}_{\text{left}}, \tag{3.16c}$$

$$K^4_{ij} = \int_{\Omega^{\text{ref}}_{\text{right}}} \begin{bmatrix} H_y & 0 \\ 0 & 0 \end{bmatrix} \nabla \mathbf{N}_i : \mathbf{C} : \begin{bmatrix} H_y & 0 \\ 0 & 0 \end{bmatrix} \nabla^s \mathbf{N}_j \, \mathrm{d}\Omega^{\text{ref}}_{\text{right}}. \tag{3.16d}$$

Similarly, $n_f = 2$ parametric shape functions are found for the force vector:

$$\psi^1(l_c) = 1, \qquad \psi^2(l_c) = l_c.$$

The corresponding vector components are found as:

$$f^1_i = \int\limits_{\Gamma^{\text{ref}}_{\text{topright}}} 2H_x \, \mathbf{N}_i \cdot (\boldsymbol{t} \circ \mathcal{M}) \, \mathrm{d}\Gamma^{\text{ref}}_{\text{topright}}, \tag{3.17a}$$

$$f^2_i = \int\limits_{\Gamma^{\text{ref}}_{\text{topleft}}} 2 \, \mathbf{N}_i \cdot (\boldsymbol{t} \circ \mathcal{M}) \, \mathrm{d}\Gamma^{\text{ref}}_{\text{topleft}} - \int\limits_{\Gamma^{\text{ref}}_{\text{topright}}} 2 \, \mathbf{N}_{\mathrm{i}} \cdot (\boldsymbol{t} \circ \mathcal{M}) \, \mathrm{d}\Gamma^{\text{ref}}_{\text{topright}}. \tag{3.17b}$$

The system composed of these separable forms for the stiffness matrix and force vector assumes the canonical form (3.7).

3.4 The Proper Generalized Decomposition (PGD) method

The parametric problem (3.7) is solved here using the Proper Generalized Decomposition (PGD) method [157–159]. The particular use of the PGD method considered here follows the idea presented in [153, 160], where the method is applied to a discretized (in both space and parametric dimensions) system of linear equations. This differs from the standard use of PGD, where the method is applied to the weak form of the problem (*e.g.*, [148, 149, 161, 162]).

The separated form of the PGD approximation, $\hat{\mathbf{u}}_{\text{pgd}}(\boldsymbol{\mu})$, takes a form similar to the separated versions of the stiffness matrix, $\mathbf{K}$, and external force vector, $\mathbf{f}$, in equation (3.8), *viz.*:

$$\hat{\mathbf{u}}_{\text{pgd}}(\boldsymbol{\mu}) = \sum_{i=1}^{n_{pgd}} \hat{\mathbf{u}}^i \prod_{j=1}^{n_\mu} G_j^i(\mu_j) = \sum_{i=1}^{n_{pgd}} \beta^i \bar{\mathbf{u}}^i \prod_{j=1}^{n_\mu} \bar{G}_j^i(\mu_j), \tag{3.18}$$

where the vectors $\hat{\mathbf{u}}^i$, for $i = 1, \ldots, n_{pgd}$, are constant vectors of the same size as a standard spatial finite element solution, and the scalar functions $G_j^i(\mu_j)$ are independent of space with $\mu_1, \mu_2, \ldots, \mu_{n_\mu}$ as parameters and n_μ being the total number of parameters. Note that the parametric functions $G_j^i(\mu_j)$ are represented discretely by a nodal vector associated with a mesh over the parameter domains $\mathcal{I}_{\mu_j}$ in accordance with

$$G_j^i(\mu_j) = \sum_{k=1}^{m_j} M_{j,k}(\mu_j) \hat{G}_{j,k}^i, \tag{3.19}$$

where $\{M_{j,k}\}_{k=1}^{m_j}$ is the set of linear finite element basis functions over the parameter domain $\mathcal{I}_{\mu_j}$, and where $\hat{\mathbf{g}}_j^i = (\hat{G}_{j,1}^i, \cdots, \hat{G}_{j,m_j}^i)$ is the corresponding vector of coefficients. In equation (3.18) the vectors $\bar{\mathbf{u}}^i$ and functions $\bar{G}_j^i(\mu_j)$ are the spatial and parametric modes normalized with respect to the Euclidean norms $\|\hat{\mathbf{u}}^i\|$ and $\|\hat{\boldsymbol{g}}_j^i\|$, respectively, such that the modal amplitudes, β^i, are given by:

$$\beta^i = \|\hat{\mathbf{u}}^i\| \prod_{j=1}^{n_\mu} \|\hat{\boldsymbol{g}}_j^i\|. \tag{3.20}$$

We employ the PGD solver algorithm as presented in Ref. [153], the main ingredients of which are:

- The PGD algorithm requires the *determination of separable forms* of the stiffness matrix and force vector as input. As discussed in detail in Section 3.3, the discrete operator $\mathbf{K}(l_c)$ for the parametric problem with the crack length l_c as a parameter admits an exact separable representation. This is not generally the case, as we will discuss, for example, in the stochastic test case considered in Section 3.7. In situations where the linear system cannot be separated analytically, it is often replaced by a separable approximation (*e.g.*, [148, 163]). There exist several methods to compute such separated approximations. For higher-dimensional parameter domains various methods have been proposed in the literature, such as: an approximation based on the PGD concept [164], Singular Value Decomposition (SVD) type approximations [165], approximations based on the CANDECOMP/PARAFAC methods [166, 167], and Tucker decomposition type approximations [168]. An overview of these techniques can be found in, *e.g.*, Ref. [169]. It is noted that in the case of high-dimensional parameter domains, the computation of separable forms can be computationally demanding.

- A *greedy algorithm* [150, 170] is used to sequentially compute the terms to the PGD approximation $\hat{\mathbf{u}}_{\text{pgd}}$ in equation (3.18). Given the PGD approximation with $n_{pgd}-1$ terms, here denoted by

$$\hat{\mathbf{u}}_{\text{pgd}}^{n_{pgd}-1}(\boldsymbol{\mu}) = \sum_{i=1}^{n_{pgd}-1} \hat{\mathbf{u}}^i \prod_{j=1}^{n_\mu} G_j^i(\mu_j). \tag{3.21}$$

  an enrichment term $\hat{\mathbf{u}}^{n_{pgd}} \prod_{j=1}^{n_\mu} G_j^{n_{pgd}}$ is computed as to obtain the PGD approximation with n_{pgd} terms:

$$\hat{\mathbf{u}}_{\text{pgd}}^{n_{pgd}}(\boldsymbol{\mu}) = \hat{\mathbf{u}}_{\text{pgd}}^{n_{pgd}-1}(\boldsymbol{\mu}) + \hat{\mathbf{u}}^{n_{pgd}} \prod_{j=1}^{n_\mu} G_j^{n_{pgd}}(\mu_j). \tag{3.22}$$

  Each enrichment term is computed one at a time, constructing the summation progressively until the convergence criterion

$$\frac{\beta^{n_{pgd}}}{\beta^1} = \frac{\|\hat{\mathbf{u}}^{n_{pgd}}\| \prod_{j=1}^{n_\mu} \|\hat{\boldsymbol{g}}_j^{n_{pgd}}\|}{\|\hat{\mathbf{u}}^1\| \prod_{j=1}^{n_\mu} \|\hat{\boldsymbol{g}}_j^1\|} \leq \epsilon_{glob}, \tag{3.23}$$

  is met with a user-defined tolerance of ϵ_{glob}. Each step in the greedy algorithm, *i.e.*, computing each of the enrichment terms, involves the computation of the enrichment modes in space, $\hat{\boldsymbol{u}}^i$ in discrete form, and in the parameter spaces, $G_j^i(\mu_j)$. We herein compute these enrichments iteratively using an alternate direction solver, which is discussed in detail below.

- An *alternating direction solution strategy* [171] is used to compute the enrichment terms $\hat{\mathbf{u}}^{n_{pgd}} \prod_{j=1}^{n_\mu} G_j^{n_{pgd}}$. Leveraging the separable forms, in this alternating direction strategy the spatial and parametric directions are treated sequentially as to reduce the higher-dimensional parametric problem to a series of low dimensional problems. This iterative process is repeated until a fixed point is reached within a defined tolerance. For the explanation of this alternating direction strategy we will consider $n_\mu = 1$ with the fracture length $\mu_1 = l_c$ as the only parameter.

  For the alternate direction solution strategy, the parametric problem (3.7) is considered in its weighted residual form:

$$\int_{\mathcal{I}_{l_c}} \delta\hat{\boldsymbol{v}}(l_c)^{\mathsf{T}} \left[\mathbf{K}(l_c)\left(\hat{\mathbf{u}}_{\text{pgd}}^{n_{pgd}-1}(l_c) + \hat{\tilde{u}}^{n_{pgd}} G_{l_c}^{n_{pgd}}(l_c)\right) - \mathbf{f}(l_c)\right] \mathrm{d}l_c = 0 \quad \forall \delta\hat{\boldsymbol{v}}(l_c). \tag{3.24}$$

  The unknowns in this system are the spatial and parametric enrichment modes, $\hat{\tilde{u}}^{n_{pgd}}$ and $G_{l_c}^{n_{pgd}}(l_c)$, respectively. The corresponding test functions are defined as:

$$\delta\hat{\boldsymbol{v}}(l_c) = \delta\left(\hat{\tilde{u}}^{n_{pgd}} G_{l_c}^{n_{pgd}}(l_c)\right) = \delta\hat{\tilde{u}}^{n_{pgd}} G_{l_c}^{n_{pgd}}(l_c) + \hat{\tilde{u}}^{n_{pgd}} \delta G_{l_c}^{n_{pgd}}(l_c). \tag{3.25}$$

  In the alternate direction strategy, the system (3.24) is solved per spatial or parametric dimension:

  – Given an approximation (or initial guess) for the parametric enrichment mode $G_{l_c}^{n_{pgd}}$, the system (3.24) reduces to the linear system:

$$\int_{\mathcal{I}_{l_c}} G_{l_c}^{n_{pgd}}(l_c) \left[\mathbf{K}(l_c)\left(\hat{\mathbf{u}}_{\text{pgd}}^{n_{pgd}-1}(l_c) + \hat{\tilde{u}}^{n_{pgd}} G_{l_c}^{n_{pgd}}(l_c)\right) - \mathbf{f}(l_c)\right] \mathrm{d}l_c = \mathbf{0}. \tag{3.26}$$

    Using the separable forms for the stiffness matrix and force vector in equation (3.9), this system can be rewritten as

$$\begin{aligned}
&\left[\sum_{i=1}^{n_k} \mathbf{K}^i \int_{\mathcal{I}_{l_c}} G_{l_c}^{n_{pgd}}(l_c)\phi^i(l_c) G_{l_c}^{n_{pgd}}(l_c)\mathrm{d}l_c\right] \hat{\tilde{u}}^{n_{pgd}} = \\
&\quad \sum_{i=1}^{n_f} \mathbf{f}^i \int_{\mathcal{I}_{l_c}} G_{l_c}^{n_{pgd}}(l_c)\psi^i(l_c)\mathrm{d}l_c \\
&- \sum_{i=1}^{n_k} \mathbf{K}^i \int_{\mathcal{I}_{l_c}} G_{l_c}^{n_{pgd}}(l_c)\phi^i(l_c)\hat{\mathbf{u}}_{\text{pgd}}^{n_{pgd}-1}(l_c)\mathrm{d}l_c.
\end{aligned} \tag{3.27}$$

with $n_k = 4$ and $n_f = 2$. An essential idea of the PGD method is that the parametric integrals in this equation can be evaluated efficiently on account of the fact that these are low-dimensional integrals (in this particular case one-dimensional). We herein use a standard trapezoidal integration rule for the evaluation of these integrals.

– Given the spatial enrichment mode $\hat{\bar{u}}^{n_{pgd}}$ computed through the system (3.27), the parametric enrichment mode $G_{l_c}^{n_{pgd}}$ can be obtained from the system (3.24). From (3.24) it follows that for all $\delta G_{l_c}^{n_{pgd}}(l_c)$:

$$\int_{\mathcal{I}_{l_c}} \delta G_{l_c}^{n_{pgd}}(l_c) \left[(\hat{\boldsymbol{u}}^{n_{pgd}})^{\mathsf{T}} \mathbf{K}(l_c) \left(\hat{\mathbf{u}}_{\text{pgd}}^{n_{pgd}-1}(l_c) + \hat{\bar{u}}^{n_{pgd}} G_{l_c}^{n_{pgd}}(l_c) \right) - \mathbf{f}(l_c) \right] \mathrm{d}l_c = 0. \tag{3.28}$$

Equivalently, it holds that for each fracture length l_c

$$\left[(\hat{\boldsymbol{u}}^{n_{pgd}})^{\mathsf{T}} \mathbf{K}(l_c) \left(\hat{\mathbf{u}}_{\text{pgd}}^{n_{pgd}-1}(l_c) + \hat{\bar{u}}^{n_{pgd}} G_{l_c}^{n_{pgd}}(l_c) \right) - \mathbf{f}(l_c) \right] = 0, \tag{3.29}$$

from which the parametric enrichment mode follows directly as:

$$G_{l_c}^{n_{pgd}}(l_c) = \frac{(\hat{\boldsymbol{u}}^{n_{pgd}})^{\mathsf{T}} \left(\mathbf{f}(l_c) - \mathbf{K}(l_c) \hat{\mathbf{u}}_{\text{pgd}}^{n_{pgd}-1} \right)}{\| \hat{\boldsymbol{u}}^{n_{pgd}} \|^2}. \tag{3.30}$$

Substitution of the separable forms for the stiffness matrix and force vector then finally yields:

$$G_{l_c}^{n_{pgd}}(l_c) = \frac{(\hat{\boldsymbol{u}}^{n_{pgd}})^{\mathsf{T}} \left(\sum_{i=1}^{n_f} \mathbf{f}^i \psi^j(l_c) - \sum_{i=1}^{n_k} \phi^i(l_c) \mathbf{K}^i \hat{\mathbf{u}}_{\text{pgd}}^{n_{pgd}-1} \right)}{\| \hat{\boldsymbol{u}}^{n_{pgd}} \|^2}. \tag{3.31}$$

This expression for the parametric enrichment mode can be evaluated quickly by virtue of the fact that the dimensions are separated in the sense that it is not required to reassemble the finite element system for each fracture length. The parametric enrichment mode is represented discretely by projection onto the parametric basis in equation (3.19). Since this discretization pertains to a linear finite element basis, the coefficients $\hat{\boldsymbol{g}}_{l_c}^{n_{pgd}}$ can be computed by evaluation of equation (3.31) in the parametric nodes.

The above alternate direction steps are repeated until the relative difference between two successive steps is smaller than a prescribed tolerance, ϵ_{local},

$$\frac{\left\| \hat{\boldsymbol{u}}^{n_{pgd}} G_{l_c}^{n_{pgd}}(l_c) \big|_{iter+1} - \hat{\boldsymbol{u}}^{n_{pgd}} G_{l_c}^{n_{pgd}}(l_c) \big|_{iter} \right\|}{\left\| \hat{\boldsymbol{u}}^{n_{pgd}} G_{l_c}^{n_{pgd}}(l_c) \big|_{iter+1} \right\|} < \epsilon_{local}, \tag{3.32}$$

Domain width	H_x	4	m
Domain height	H_y	4	m
Young's modulus	E	1	GPa
Poisson ratio	ν	0.1	
Traction on top boundary	$\boldsymbol{t}$	$(0, 100)$	MPa
Parameter domain	$\mathcal{I}_{l_c}$	[1,3]	m
Enrichment tolerance	ϵ_{glob}	10^{-3}	
Fixed-point tolerance	ϵ_{local}	10^{-6}	

Table 3.1: Convergence study parameter settings

with the subscript *iter* denoting the alternate direction step, and with the norms defined as:

$$\left\|\hat{\boldsymbol{u}}^{n_{pgd}} G_{l_c}^{n_{pgd}}(l_c)\right\| = \|\hat{\boldsymbol{u}}^{n_{pgd}}\| \int_{\mathcal{I}_{l_c}} |G_{l_c}^{n_{pgd}}(l_c)| \mathrm{d}l_c. \tag{3.33}$$

3.5 Numerical analysis of the PGD approximation behavior

Before considering the application of the PGD framework to fracture problems, in this section we first present a numerical study on the approximation properties of the PGD expansion introduced above. We specifically study the convergence behavior of the approximation under finite element mesh refinement, and the approximation behavior with respect to the number of PGD terms, n_{pgd}. All results presented in this section are based on the consideration of the fracture length, l_c, as the single quantity to be parametrized. Table 3.1 lists all parameters that are fixed throughout this section.

In the setting considered here, the separable form derived in Section 3.3 is exact up to integration accuracy. Since the integrals are herein evaluated with Gauss schemes of sufficiently high degree, the separable forms are accurate up to floating point precision. In general, however, the separable form (3.9) is not exact, as we will consider, for example, in the context of the stochastic analysis presented in Section 3.7. An important first step in studying the approximation behavior of the PGD approximation is then to study the accuracy of the separable form (3.9). This accuracy can be assessed by comparison of the matrix and right hand side obtained through the separable form (3.9) with their corresponding original finite element counterparts. Evidently, one has to perform this accuracy assessment in such a way that the parameter variations admitted by the PGD expansion are properly taken into account.

3.5.1 Spatial mesh size dependence

We first study the dependence of the PGD approximation (3.18) on the spatial finite element mesh size parameter, h, defined as the average element size in horizontal direction ($h = H_x/n_{\text{elems},x}$). For the discretization of the parameter domain, $\mathcal{I}_{l_c}$, we consider 136 elements, and we use the PGD solver presented above to obtain an expansion comprising $n_{pgd} = 10$ terms. In Figure 3.4 the various components of this expansion are illustrated, *viz. (a)* the spatial modes $\hat{\boldsymbol{u}}^i$, *(b)* the parameter modes $G^i_{l_c}(l_c)$, and *(c)* the amplitudes β^i. The amplitudes convey that the influence of the modes decreases significantly for increasing mode numbers, indicating that the displacement of the system is well characterized in the considered setting with 10 modes. A detailed study of the dependence of the PGD approximation on the modes is considered below.

To study the approximation behavior of the PGD expansion, we consider the relative energy error with respect to the original finite element solution:

$$\begin{aligned} e_{\text{pgd}}(l_c) &= \frac{\|\hat{\mathbf{u}}_{\text{pgd}}(l_c) - \hat{\mathbf{u}}(l_c)\|_{\mathbf{K}}}{\|\hat{\mathbf{u}}(l_c)\|_{\mathbf{K}}}, \\ &= \frac{\sqrt{[\hat{\mathbf{u}}_{\text{pgd}}(l_c) - \hat{\mathbf{u}}(l_c)]^{\mathsf{T}}\, \mathbf{K}(l_c)\, [\hat{\mathbf{u}}_{\text{pgd}}(l_c) - \hat{\mathbf{u}}(l_c)]}}{\sqrt{\hat{\mathbf{u}}(l_c)^{\mathsf{T}} \mathbf{K}(l_c) \hat{\mathbf{u}}(l_c)}}, \end{aligned} \tag{3.34}$$

where $\hat{\mathbf{u}}_{\text{pgd}}(l_c)$ is the parametric solution provided by PGD and $\hat{\mathbf{u}}(l_c)$ is the solution provided by the direct FE analysis (3.5) when the parameter is fixed to the value l_c. Note that while the evaluation of $\hat{\mathbf{u}}_{\text{pgd}}(l_c)$ for a certain crack length l_c involves merely the evaluation of the PGD expansion (3.18), the computation of $\hat{\mathbf{u}}(l_c)$ involves the assembly and solution of a finite element system. In addition to the parameter-dependent error (3.34) we consider the mean energy error over the parameter domain:

$$E_{\text{pgd}} = \frac{1}{l_c^{\max} - l_c^{\min}} \int_{\mathcal{I}_{l_c}} e_{\text{pgd}}(l_c)\, \mathrm{d}l_c. \tag{3.35}$$

In contrast to (3.34), this error measure provides one scalar error value for the complete parametric solution and has no dependency on l_c. Figure 3.5 displays both error measures for various spatial mesh sizes, h, and a fixed parametric mesh size $h_{l_c} \approx 0.015\,\text{m}$. The parameter dependent error (3.34) displayed in Figure 3.5a conveys that for a certain mesh size, the error in the PGD solution is dependent on the crack length. The reason for this is that the uniformity of the mesh in the physical domain is affected by the parameter-dependent mapping function (3.10), which in general causes the error to increase when the crack tip position deviates from $l_c/H_x = 0.5$ (*i.c.*, $l_c = 2$) provided that the mesh resolution is of sufficient accuracy. The error $e_{\text{pgd}}(l_c)$ is especially significant at the boundaries

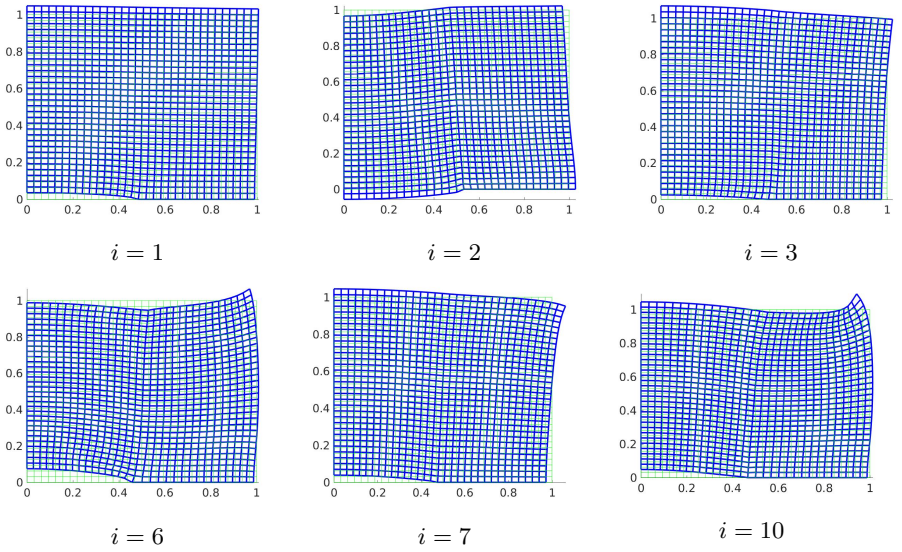

(a) Normalized displacement modes $\bar{\boldsymbol{u}}^i(\boldsymbol{x})$ of the PGD expansion. Note that only a selection of modes is shown.

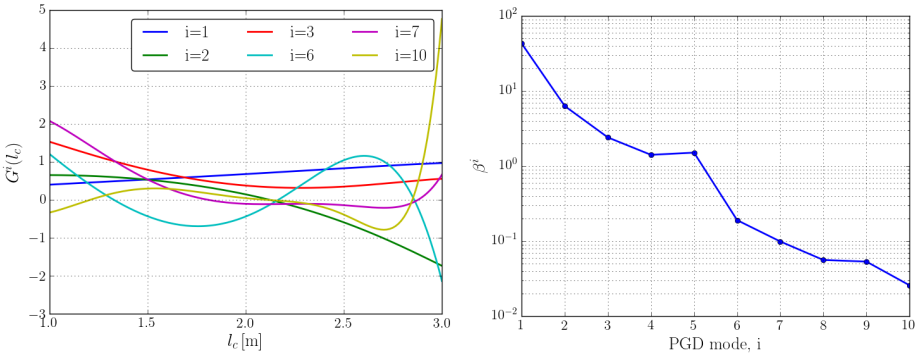

(b) Normalized parametric modes $\bar{G}^i(l_c)$.

(c) Modal amplitudes β^i.

Figure 3.4: The three components of the $\mathbf{u}_{\text{pgd}}(l_c)$ solution for $n_{pgd} = 10$. Only a selection of modes is shown for conciseness. Note that all plotted functions are normalized.

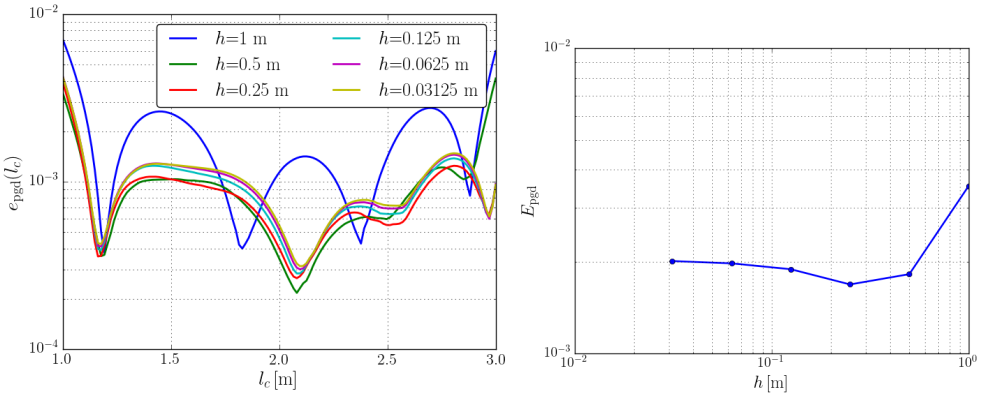

(a) $e_{\mathrm{pgd}}(l_c)$ *vs* crack length l_c **(b)** E_{pgd} *vs* mesh size h

Figure 3.5: Energy errors of the PGD approximation with respect to the original finite element solution as defined in equations (3.34) and (3.35).

of the parameter domain, $\mathcal{I}_{l_c}$, because at those points the non-uniformity caused by the mapping onto the physical domain (see Figure 3.3) is largest.

When we compute the mean of the error $e_{\mathrm{pgd}}(l_c)$ over the complete parameter domain, *i.e.*, error measure (3.35), we observe from Figure 3.5b that this mean energy error is essentially independent of the mesh size for the finer meshes ($h \lesssim 0.25$). This conveys that for these meshes the studied error is dominated by the PGD approximation, which is expected, as we compare the PGD solution with the FE solution on the same mesh.

To study the mesh size contribution to the PGD approximation error, in Figure 3.6 we display the mean L^2 error between a PGD approximation $\mathbf{u}_{\mathrm{pgd}}(\boldsymbol{x}; l_c)$ computed with mesh size h and a PGD approximation, $\mathbf{u}^{\star}_{\mathrm{pgd}}(\boldsymbol{x}; l_c)$, with a high resolution mesh with $h^{\star} = 0.03125$:

$$E_h = \frac{1}{l_c^{\max} - l_c^{\min}} \int_{\mathcal{I}_{l_c}} \left\| \mathbf{u}_{\mathrm{pgd}}(l_c) - \mathbf{u}^{\star}_{\mathrm{pgd}}(l_c) \right\| \mathrm{d}l_c. \tag{3.36}$$

Both the number of PGD terms and the discretization of the parametric mesh are identical for both of the compared solutions, so that this error measure pertains to the mesh size contribution only. For comparison the finite element convergence plots for various settings of the fracture length are displayed in Figure 3.6. This comparison conveys that the PGD solution converges with the mesh size with the same rate as the finite element approximation. The observed error offsets for various settings of the fracture length in the finite element simulations are a result of the non-uniformity of the mesh resulting from the geometric mapping considered in this work.

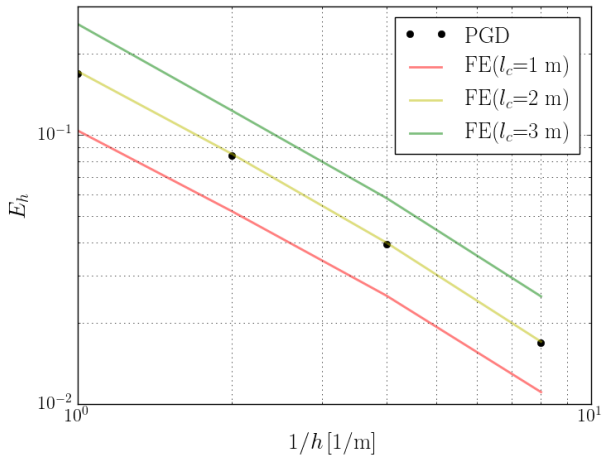

Figure 3.6: Convergence of the mean L^2 error, E_h of the PGD approximation (markers) under mesh refinement with respect to the PGD solution computed with a high resolution spatial mesh ($h^\star = 0.03125$). The convergence results for direct FE analyses with various fracture lengths (lines) are shown for comparison.

In Figure 3.7 the mean energy error E_{pgd} is plotted versus the number of PGD terms, n_{pgd}, for various mesh sizes. The observed systematic decrease in this error with the increase in number of terms is as expected, as the PGD approximation (3.18) converges toward the finite element solution. The fluctuations with respect to the mesh size are in agreement with the errors plotted in Figure 3.5.

3.5.2 Parametric mesh size dependence

All results presented above were based on a fixed parametric mesh size of $h_{l_c} \approx 0.015$ and variations in the spatial mesh size. We now consider the influence of variations in the parametric mesh size under a fixed spatial mesh size of $h = 0.0625\,\mathrm{m}$.

Figure 3.8 shows that both the parameter-dependent energy error (3.34) and mean energy error (3.35) are virtually independent of the parametric mesh size even on parametric meshes as coarse as $h_{l_c} = 0.125\,\mathrm{m}$ (8 elements). This conveys that, in the setting considered here, the accuracy is governed by the number of PGD modes rather than by the resolution of the parametric mesh.

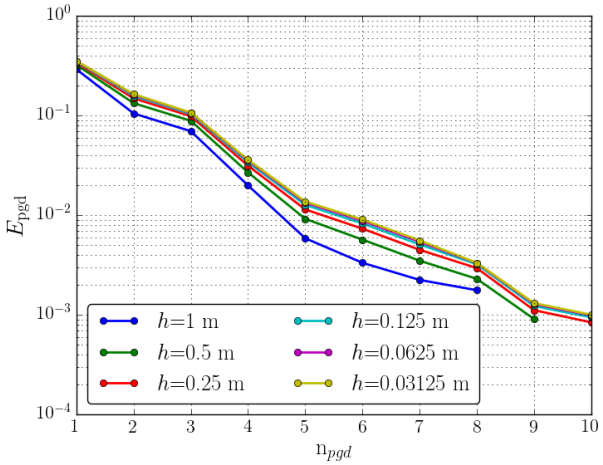

Figure 3.7: Mean energy error for various numbers of PGD modes and different mesh sizes.

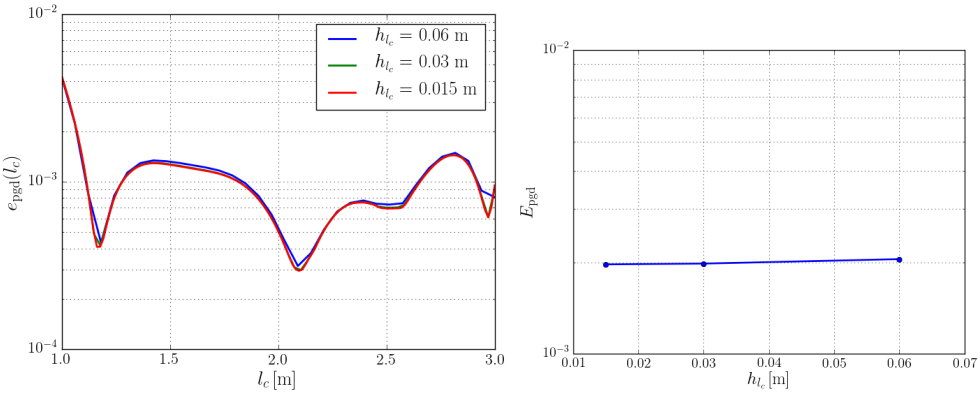

(a) $e_{\text{pgd}}(l_c)$ **(b)** E_{pgd}

Figure 3.8: Energy errors of the PGD approximation with respect to the original finite element solution as defined in equations (3.34) and (3.35), considering various parametric mesh sizes.

3.6 Application of the PGD framework to propagating fractures

In this section we apply the PGD framework outlined above to the simulation of fracture propagation using Griffith's energy criterion [172]. In Section 3.6.1 we commence with the formulation of the propagation criterion based on the PGD solution. Since the evolution of the fracture is driven by the external load, we herein use the PGD framework to compute the parametric solution with respect to both the fracture length (as already considered above) and with respect to the external load,

$$\hat{\mathbf{u}}_{\text{pgd}}^{n_{pgd}}(l_c\,,\lambda) = \sum_{i=1}^{n_{pgd}} \beta^i \hat{\boldsymbol{u}}^i G_1^i(l_c) G_2^i(\lambda), \tag{3.37}$$

where λ denotes a load scale parameter such that $\boldsymbol{t} = \lambda\hat{\boldsymbol{t}}$ with $\hat{\boldsymbol{t}}$ being a load vector defined as $\hat{\boldsymbol{t}} = (0,1)\,\text{MPa}$. For simplicity in notation, from hereon we denote $\hat{\mathbf{u}}_{\text{pgd}}$ for $\hat{\mathbf{u}}_{\text{pgd}}^{n_{pgd}}$. The separable forms of the stiffness matrix and force vector are a straightforward extension of those in Section 3.3 as a consequence of the fact that the external force vector scales linearly with the load scale λ. As a result, we only have to consider a single linear parametric shape function for the load scale parameter for the force vector in equation (3.8b), such that:

$$\psi^1(l_c) = \lambda, \qquad\qquad \psi^2(l_c) = \lambda l_c.$$

In Section 3.6.2 we will demonstrate the application of the PGD framework to a fracture propagation benchmark problem, where the advantages of the PGD framework become apparent as it allows for the fast evaluation of the fracture propagation criterion throughout the evolution process of the fracture, without the need for solving additional finite element problems. For all the simulations we assume plane strain conditions with Young's modulus $E = 2$ GPa and the other input values taken from Table 3.1. For the parametric domain of the load scale we use $\mathcal{I}_\lambda = [6.25\,,62.5]$. Furthermore, we define the resultant force $F = \int_{\Gamma_{\text{top}}} \boldsymbol{t}\cdot\boldsymbol{n}\,\mathrm{d}\Gamma$ as a quantity of interest, where we assume the specimen to be of unit thickness.

3.6.1 The fracture propagation criterion

We consider Griffith's model [172] for crack propagation in brittle materials. The conceptual idea of this model is that a fracture will propagate if the energy stored in the material is sufficiently large to overcome the fracture energy associated with the creation of new fracture surface. For linear elastic materials an equivalent interpretation of this energy-based model is provided through the concept of stress intensity factors [173]. In the context of the PGD framework we find the

energy perspective most suitable, as it provides the possibility to evaluate the propagation criterion directly based on the parametric solution (3.37).

For a fracture in a given configuration, *i.e.*, with a certain length l_c and a given load scale λ, it can be determined whether or not the fracture will propagate by evaluation of the energy release rate. To derive the PGD form of the energy release rate, we consider the energy of the system:

$$P(l_c,\lambda) = \frac{1}{2}\hat{\mathbf{u}}_{\text{pgd}}(l_c,\lambda)^{\mathsf{T}}\mathbf{K}(l_c)\hat{\mathbf{u}}_{\text{pgd}}(l_c,\lambda) - \hat{\mathbf{u}}_{\text{pgd}}(l_c,\lambda)^{\mathsf{T}}\mathbf{f}(l_c,\lambda). \tag{3.38}$$

The energy release rate is then defined as :

$$\begin{aligned}\mathcal{G}(l_c,\lambda) &= -\frac{\partial P}{\partial l_c}(l_c,\lambda)\\ &= -\frac{\partial \hat{\mathbf{u}}_{\text{pgd}}(l_c,\lambda)}{\partial l_c}^{\mathsf{T}}\left[\mathbf{K}(l_c)\hat{\mathbf{u}}_{\text{pgd}}(l_c,\lambda) - \mathbf{f}(l_c,\lambda)\right]\\ &\quad - \frac{1}{2}\hat{\mathbf{u}}_{\text{pgd}}(l_c,\lambda)^{\mathsf{T}}\frac{\partial \mathbf{K}(l_c)}{\partial l_c}\hat{\mathbf{u}}_{\text{pgd}}(l_c,\lambda) + \hat{\mathbf{u}}_{\text{pgd}}(l_c,\lambda)^{\mathsf{T}}\frac{\partial \mathbf{f}(l_c,\lambda)}{\partial l_c}.\end{aligned} \tag{3.39}$$

When the parametric problem $\mathbf{K}(l_c)(l_c,\lambda)\hat{\mathbf{u}}_{\text{pgd}} \approx \mathbf{f}(l_c,\lambda)$ is solved using the PGD solver with sufficient accuracy, *i.e.*, with small enough tolerances, the energy release rate is given by,

$$\mathcal{G}(l_c,\lambda) = -\frac{1}{2}\hat{\mathbf{u}}_{\text{pgd}}(l_c,\lambda)^{\mathsf{T}}\frac{\partial \mathbf{K}(l_c)}{\partial l_c}\hat{\mathbf{u}}_{\text{pgd}}(l_c,\lambda) + \hat{\mathbf{u}}_{\text{pgd}}(l_c,\lambda)^{\mathsf{T}}\frac{\partial \mathbf{f}(l_c,\lambda)}{\partial l_c}. \tag{3.40}$$

According to Griffith's energy balance, a crack will propagate when the energy release rate surpasses the critical energy release rate or fracture toughness, $\mathcal{G}_c$, *i.e.*:

$$\mathcal{G}(l_c,\lambda) \geq \mathcal{G}_c. \tag{3.41}$$

This implies that for any crack configuration in the parametric space, *i.e.*, $(l_c,\lambda) \in \mathcal{I}_{l_c} \times \mathcal{I}_\lambda$, it can be readily evaluated whether or not the crack propagates. The PGD expansion (3.37) is crucial in this regard as: *i)* The expansion allows for the analytical evaluation of the *shape derivatives* $\left(\frac{\partial}{\partial l_c}\right)$ in equation (3.40), this in contrast to the traditional FE setting, in which this derivative is typically evaluated using alternative techniques (*e.g.*, J-integrals [173]). *ii)* Evaluation of the fracture criterion at an arbitrary parametric coordinate is merely an evaluation of the expansion, and hence, does not require the solution of an FE model.

3.6.2 Numerical example: a center-crack under tensile loading

The numerical example discussed here demonstrates the PGD-based evaluation of the energy release rate $\mathcal{G}$ in two ways: (*i*) the energy release rate, $\mathcal{G}$, is used to compute the stress intensity factor; (*ii*) PGD is used to mimic the fracture propagation process while loading the specimen.

Stress intensity factors

As a means to assess the PGD approximation of the energy release rate, we study the stress intensity factor for a given fracture length l_c, and various ratio's of horizontal and vertical specimen dimensions, H_x and H_y, respectively. The results presented in this section consider the parameters H_x and H_y as additional parameters in the PGD expansion. The separable forms based on these parameters can be obtained without special treatment, and are omitted here for the sake of brevity. The stress intensity factor is defined as

$$\mathcal{K}_1(l_c, H_x, H_y) = \sqrt{\mathcal{G}(l_c, H_x, H_y)E'}, \tag{3.42}$$

and hence is directly related to the energy release rate (3.40). The material parameter E' in equation (3.42) is defined as $E' = E/(1-\nu^2)$ for the plane strain problems considered herein.

Figure 3.9 shows the dimensionless stress intensity factors $\mathcal{K}_1/\mathcal{K}_0$ for various parameter configurations, *i.e.*, different l_c/H_x and H_x/H_y (see Ref. [154] for a benchmark result). Note that the plotted factors are non-dimensionalized using $\mathcal{K}_0 = (\lambda\hat{\boldsymbol{t}}\cdot\boldsymbol{n})\sqrt{\pi l_c}$, where $\lambda\hat{\boldsymbol{t}}\cdot\boldsymbol{n}$ gives the magnitude of the applied tensile traction. Figure 3.9 compares the PGD results based on the settings mentioned in Table 3.1 for a mesh size $h = 0.0625\,\mathrm{m}$. However, note that this plot of non-dimensional stress intensity factors is independent of the input values, *i.e.*, even for different values of geometry and load, similar curves for $\mathcal{K}_1/\mathcal{K}_0$ are obtained. This figure conveys that for the given PGD settings, the stress intensity factor can be computed accurately using the PGD expansion (3.37). While each point in Figure 3.9 would typically represent a finite element simulation in the traditional FEM setting, in the PGD case these are all mere evaluations of the expansion.

Fracture propagation

Now that we have established that the PGD expansion accurately approximates the stress intensity factor, we will here use it to predict the evaluation of the loading force under fracture propagation. To this end, we define the energy functional

$$\mathcal{E}(l_c, \lambda) = P(l_c, \lambda) - l_c\mathcal{G}_c, \tag{3.43}$$

such that we can distinguish between three cases in the energy landscape over the $\mathcal{I}_{l_c} \times \mathcal{I}_\lambda$ parameter domain:

1. The region where the crack is stable:

$$\frac{\partial \mathcal{E}}{\partial l_c} < 0 \qquad \text{or} \qquad \mathcal{G}(l_c, \lambda) < \mathcal{G}_c.$$

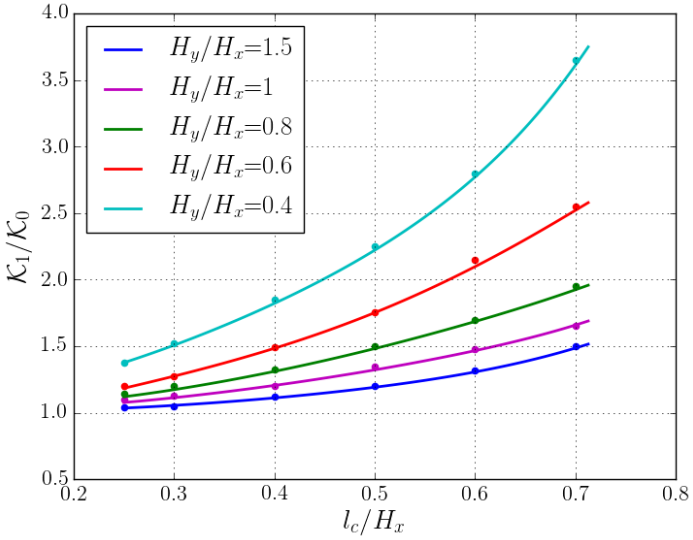

Figure 3.9: Dimensionless stress intensity factors $\mathcal{K}_1/\mathcal{K}_0$ for various crack lengths in specimens of various dimensions loaded in tension. The solid lines represent the results computed through the PGD framework, while the markers indicate the reference values reported in Ref. [154].

2. The region where the energy balance is critical:

$$\frac{\partial \mathcal{E}}{\partial l_c} = 0 \qquad \text{or} \qquad \mathcal{G}(l_c, \lambda) = \mathcal{G}_c.$$

3. The unstable propagation region:

$$\frac{\partial \mathcal{E}}{\partial l_c} > 0 \qquad \text{or} \qquad \mathcal{G}(l_c, \lambda) > \mathcal{G}_c.$$

The energy landscape is plotted in Figure 3.10a along with the values indicating the energy in kJ of the system. Note that plotting this landscape is computationally feasible using the PGD expansion, but would require a large number of FE solves in the case of a non-reduced model. The presented results are based on the assumption of plane strain conditions with material parameter $E' = 2.01$ GPa and the other settings listed in Table 3.1 with a fracture toughness of $\mathcal{G}_c = 700\,\mathrm{kJ/m^2}$, and with the parameter ranges for l_c and λ defined as $\mathcal{I}_{l_c} = [1, 3]\,\mathrm{m}$ and $\mathcal{I}_\lambda = [6.25, 62.5]$ respectively (so the range of the force $F = [25, 250]\,\mathrm{MN}$).

For a particular load scale, until the critical point is reached the crack is stable (green region in Figure 3.10a), and beyond the maximum point the crack is unstable (red region in Figure 3.10a). The critical energy states are connected in the form of a curve which gives the critical load value for each fracture length. This curve can be identified in Figure 3.10a as the line separating the green area from the red area. The key insight is to recognize that, for a shorter crack length, which is left of the critical value point, the total energy (3.43) of the system increases with increasing crack length. Therefore, additional energy must be stored into the material before the crack can propagate, and hence the crack is stable. However, at longer crack lengths, which is right of the maximum value, an increase in crack length leads to a decrease in total energy, which therefore leads to unstable crack propagation. Evidently, the load-bearing capacity of the specimen decreases as the fracture propagates.

A common way of representing the fracture evolution process is by plotting the load versus the average displacement of the loading boundary, which is depicted in Figure 3.10b for a initial crack length of $l_c^0 = 2.495\,\mathrm{m}$. Note that the elastic loading branch (label I. in Figure 3.10) corresponds to the region where the crack is stable, *i.e*, the force varies with $\frac{\partial \mathcal{E}}{\partial l_c} < 0$. The resultant force at which the crack becomes unstable, *i.e.*, when $\frac{\partial \mathcal{E}}{\partial l_c} = 0$, is defined as the critical loading force, F_c. This corresponds to the maximum force in Figure 3.10b. This critical loading force is related to the dimensionless stress intensity factors of Figure 3.9 by:

$$F_c = \frac{\mathcal{K}_0}{\mathcal{K}_1} \frac{H_x \sqrt{\mathcal{G}_c E'}}{(\hat{\boldsymbol{t}} \cdot \boldsymbol{n}) \sqrt{\pi l_c}}. \tag{3.44}$$

The softening branch (label II. in Figure 3.10) reflects the critical values in Figure 3.10a for $l_c \geq l_c^0$. This part of the curve resembles the unstable propagation part of the process. The total area under the force displacement curve represents the energy carried by the system, which, upon complete failure is equal to the total energy dissipated by the fracturing, *i.e.*, $\mathcal{G}_c(H_x - l_c^0)$. Such force-displacement curves can be plotted for all $l_c^0 \in \mathcal{I}_{l_c}$ by virtue of the explicit availability of the energy functional in (3.43) in the PGD framework.

3.7 Application to fracture propagation in random heterogeneous materials

In this section we extend the PGD framework for crack propagation to a stochastic setting. We introduce randomness in the material properties by representation of the Young's modulus by a random field $\tilde{E}(\boldsymbol{x})$, where the tilde indicates the randomness. A truncated Karhunen-Loève expansion [140] is used for the parameterization of the Gaussian field $\tilde{E}(\boldsymbol{x})$, which is defined as

$$\tilde{E}(\boldsymbol{x}) = \mu_E + \sum_{\alpha=1}^{n_{kl}} \sqrt{\xi_\alpha} r_\alpha(\boldsymbol{x}) \tilde{z}_\alpha, \tag{3.45}$$

where μ_E is the stationary mean of the Young's modulus and where ξ_α and $r_\alpha(\boldsymbol{x})$ are the eigenvalues and eigenfunctions corresponding to the spatial covariance function $\sigma_E^2 \rho_E(\boldsymbol{x}_1, \boldsymbol{x}_2)$, with σ_E the stationary standard deviation. The autocorrelation function is taken as

$$\rho_E(\boldsymbol{x}_1, \boldsymbol{x}_2) = \exp\left(-\frac{|\boldsymbol{x}_1 - \boldsymbol{x}_2|}{l_E}\right), \tag{3.46}$$

where $\boldsymbol{x}_1$ and $\boldsymbol{x}_2$ are two points in the domain and l_E is the correlation length. The n_{kl} Karhunen-Loève modes, $R_\alpha(\boldsymbol{x}) = \sqrt{\xi_\alpha} r_\alpha(\boldsymbol{x})$, in equation (3.45) are scaled by independent standard normal random variables $\tilde{z}_\alpha$.

On account of (3.45) the Young's modulus at any fixed location, $\tilde{E}(\boldsymbol{x})$, is normally distributed. The variation σ_E^2 is selected such that physically impossible negative realizations are avoided. Although not considered herein, the PGD framework can be applied without modification to, *e.g.*, log-normal random fields. It is noted that we herein construct the random field over the computational domain, thereby implicitly assuming that the random material properties adhere to the symmetries of the homogeneous problem. Preservation of the symmetries is in line with the considered parametrization of the fracture problem, as non-symmetries would result in deviations of the fracture path from the x-axis. Although such variations are evidently physical, consideration of these within the PGD framework is beyond the scope of this manuscript.

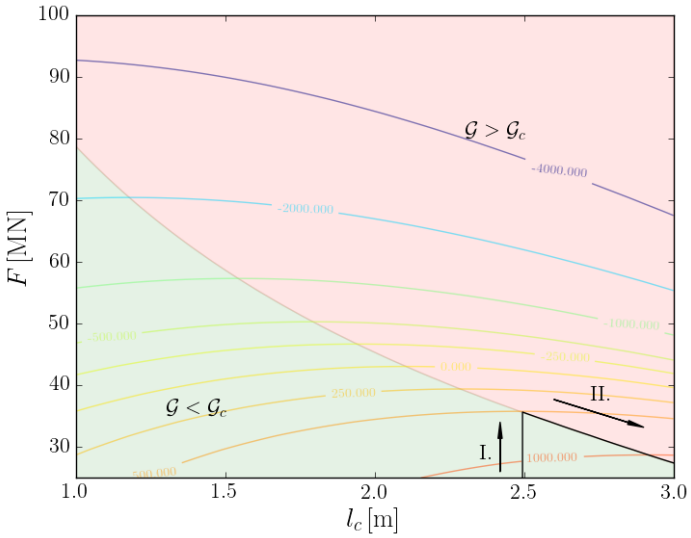

(a) Energy functional (3.43) over the (F, l_c)-parameter domain.

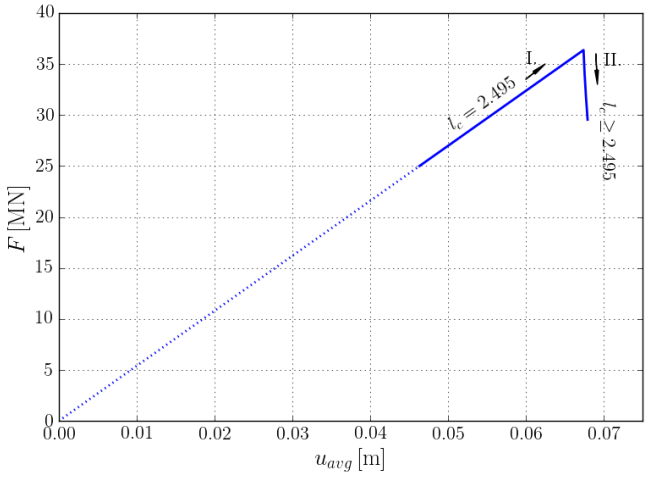

(b) Loading force *vs.* average displacement over the loading boundary for an initial crack length of $l_c^0 = 2.495\,\text{m}$.

Figure 3.10: Representation of the loading and fracture evolution process in terms of (a) the energy landscape and (b) the force-displacement curve. The elastic loading branch is labeled as I., whereas the softening/propagation branch is labeled as II. The observed critical loading force of $F_c \approx 36.3$ MN is in agreement with equation (3.44) and the corresponding stress intensity factor reported in Figure 3.9.

In the context of the stochastic analysis considered here, we use the PGD framework to compute the parametric solution with respect to the fracture length, external load, and with the random variables $\tilde{z}_\alpha$ that parametrize the random Young's modulus field:

$$\hat{\mathbf{u}}_{\text{pgd}}(l_c, \lambda, \tilde{\boldsymbol{z}}) = \sum_{i=1}^{n_{pgd}} \beta^i \hat{\boldsymbol{u}}^i G_1^i(l_c) G_2^i(\lambda) \prod_{\alpha=1}^{n_{kl}} G_{\alpha+2}^i(\tilde{z}_\alpha) \tag{3.47}$$

A prerequisite to apply our framework is to express the stiffness matrix and force vector also in this separated format. The separable forms of the stiffness matrix and force vector required here cannot be obtained in an analytical way like in Sections 3.3 and 3.6. Therefore, in Section 3.7.1 we first discuss how the random heterogeneities, which are parametrized by the random variables $\tilde{\boldsymbol{z}}$, can be expressed in a separable form for the stiffness matrix numerically. Furthermore, in Section 3.7.2 we outline the computational procedure for a sampling-based stochastic analysis based on the Monte-Carlo method. This stochastic analysis is highly efficient as it leverages the PGD approximation to quickly compute critical force values for realizations of the heterogeneous field of elastic properties. Numerical results for the stochastic test case are presented in Section 3.7.3.

3.7.1 Separable representation of the random system of equations

The random field (3.45) enters the formulation through the elasticity tensor in the bilinear operator (3.14a), which, in the context of the stochastic setting considered here, is expressed as

$$\tilde{\mathbf{C}}(\boldsymbol{X}; l_c, \tilde{\boldsymbol{z}}) = \tilde{E}(\boldsymbol{X}; l_c, \tilde{\boldsymbol{z}})\mathbf{D} = \left(\mu_E + \sum_{\alpha=1}^{n_{kl}} \{R \circ \mathcal{M}\}_\alpha \tilde{z}_\alpha\right) \mathbf{D}, \tag{3.48}$$

where the constant tensor $\mathbf{D}$ depends on the Poisson ratio and on the assumed plane strain state. Since the elasticity tensor is evaluated over the reference domain, the KL modes $\{R \circ \mathcal{M}\}_{\alpha=1}^{n_{kl}}$ are pulled back to the reference configuration using the geometric mapping function (3.10). Since this mapping function is dependent on the fracture length parameter l_c, the random elasticity tensor (3.48) also becomes dependent on the fracture length.

Substitution of the random tensor (3.48) into equation (3.14a) yields a random stiffness matrix of the form

$$\tilde{\mathbf{K}}(l_c, \tilde{\boldsymbol{z}}) = \mathbf{K}_0(l_c) + \sum_{\alpha=1}^{n_{kl}} \mathbf{K}_\alpha(l_c) \tilde{z}_\alpha, \tag{3.49}$$

with the stiffness matrix contributions defined as

$$K_{0,ij} = \int_{\Omega^{\text{ref}}} \mathbf{J}^{-1}\nabla\mathbf{N}_i : [\mu_E\mathbf{D}] : \mathbf{J}^{-1}\nabla^s\mathbf{N}_j \det(\mathbf{J})\,\mathrm{d}\Omega^{\text{ref}}, \tag{3.50a}$$

$$K_{\alpha,ij} = \int_{\Omega^{\text{ref}}} \mathbf{J}^{-1}\nabla\mathbf{N}_i : [\{R\circ\mathcal{M}\}_\alpha] : \mathbf{J}^{-1}\nabla^s\mathbf{N}_j \det(\mathbf{J})\,\mathrm{d}\Omega^{\text{ref}}, \tag{3.50b}$$

where the index 0 corresponds to the mean contribution, and the index $\alpha = 1, \cdots, n_{kl}$ to the stiffness contributions of the KL modes.

The separable form (3.8a) of the mean stiffness matrix (3.50a) is identical to that presented in equations (3.15) and (3.16) with the elasticity tensor set to $\mathbf{C} = \mu_E\mathbf{D}$, which we denote by

$$\mathbf{K}_0(l_c) = \sum_{i=1}^{n_k} \mathbf{K}_0^i \phi^i(l_c). \tag{3.51}$$

The derivation of an analytical separable form for the KL contributions to the stiffness matrix, equation (3.50b), is obstructed by the appearance of the geometric mapping, $\mathcal{M}$, in the Karhunen-Loève modes, R_i. A semi-analytical separable form can, however, be obtained through the singular-value decomposition of the discretized KL modes. For the construction of this decomposition, we first interpolate the KL modes on the spatial mesh and crack length parameter domain mesh used for the PGD approximation as:

$$R_\alpha(\boldsymbol{X}, l_c) \approx \sum_{i=1}^{n}\sum_{j=1}^{m} N_i(\boldsymbol{X}) M_j(l_c) R_{\alpha,ij}. \tag{3.52}$$

The coefficients of this interpolation, represented by the matrix $\hat{\mathbf{R}}_\alpha$, are computed using the KL modes constructed on a significantly refined mesh compared to that used for the PGD approximation. Since (bi)linear Lagrangian basis functions are used for both the spatial domain and the parameter domain, the coefficients are determined by evaluation in all nodal coordinates, $(\boldsymbol{X}, l_c)$, in the higher-dimensional parameter domain, where the mapping (3.10) is used to transfer data between the physical domain and the reference domain. The interpolation (3.52) on the mesh used for the PGD approximation is convenient from an implementation perspective, but the usage of this specific mesh is not necessary to attain the separable form of the stiffness matrix.

A separable form of the discrete KL modes (3.52) is then obtained through the singular-value decomposition

$$\hat{\mathbf{R}}_{\alpha,ij} = \sum_{\beta=1}^{\min(n,m)} \sigma_{(\alpha,\beta)} \hat{h}_{(\alpha,\beta),i}\, \hat{m}_{(\alpha,\beta),j}, \tag{3.53}$$

where $\sigma_{(\alpha,\beta)}$ is the β-th singular value for KL mode α, and where $\hat{\vec{h}}_{(\alpha,\beta)}$ and $\hat{\vec{m}}_{(\alpha,\beta)}$ are the corresponding spatial and parametric modal vectors, respectively. For reasons of efficiency this singular-value decomposition is truncated to a number of terms, n_{svd}, that is significantly smaller than the total system size. Substitution of this decomposition into equation (3.52) then yields the singular-value decomposition for the KL modal functions,

$$R_\alpha(\boldsymbol{X}, l_c) \approx \sum_{\beta=1}^{n_{svd}} \sigma_{(\alpha,\beta)} h_{(\alpha,\beta)}(\boldsymbol{X})\, m_{(\alpha,\beta)}(l_c), \tag{3.54}$$

where the modal functions are defined as

$$h_{(\alpha,\beta)}(\boldsymbol{X}) = \sum_{i=1}^{n} N_i(\boldsymbol{X}) \hat{h}_{(\alpha,\beta),i}, \tag{3.55a}$$

$$m_{(\alpha,\beta)}(l_c) = \sum_{j=1}^{m} M_j(l_c) \hat{m}_{(\alpha,\beta),j}. \tag{3.55b}$$

The singular value decomposition of the Karhunen-Loève modes (3.54) involves two approximations, *viz.*: *i)* an approximation related to the interpolation step (3.52); and *ii)* an approximation associated with the truncation of the decomposition (3.53).

Now that we have obtained an approximate separable form for the KL modes in the form of equation (3.54), separation of the stiffness matrix follows from substitution of this decomposition into the KL stiffness matrix contributions (3.50b):

$$\mathbf{K}_\alpha(l_c) = \sum_{\beta=1}^{n_{svd}} \sigma_{(\alpha,\beta)} m_{(\alpha,\beta)}(l_c) \mathbf{K}_{(\alpha,\beta)}(l_c). \tag{3.56}$$

The components of the matrices $\mathbf{K}_{(\alpha,\beta)}(l_c)$ are given by:

$$K_{(\alpha,\beta),ij}(l_c) = \int_{\Omega^{\text{ref}}} \mathbf{J}^{-1} \nabla \mathbf{N}_i : \left[h_{(\alpha,\beta)}(\boldsymbol{X}) \mathbf{D} \right] : \mathbf{J}^{-1} \nabla^s \mathbf{N}_j \det(\mathbf{J})\, \mathrm{d}\Omega^{\text{ref}}. \tag{3.57}$$

Since the spatial modes, $h_{(\alpha,\beta)}(\boldsymbol{X})$, are independent of the parameter l_c, the matrices $\mathbf{K}_{(\alpha,\beta)}$ can be separated analogously to the equations (3.15) and (3.16) with the elasticity tensor set to $\mathbf{C} = \mathbf{D} h_{(i,\beta)}(\boldsymbol{X})$. Similarly to the separable form of the mean stiffness contribution in equation (3.51), we express this separable form as:

$$\mathbf{K}_{(\alpha,\beta)}(l_c) = \sum_{j=1}^{n_k} \mathbf{K}^j_{(\alpha,\beta)} \phi^j(l_c). \tag{3.58}$$

Substitution of this separable form for the SVD mode β into equation (3.56) then yields

$$\mathbf{K}_\alpha(l_c) = \sum_{\beta=1}^{n_{svd}} \sigma_{(\alpha,\beta)} m_{(\alpha,\beta)}(l_c) \sum_{j=1}^{n_k} \mathbf{K}^j_{(\alpha,\beta)} \phi^j(l_c), \tag{3.59}$$

with $n_k = 4$ in accordance with equation (3.15). Further substitution into the expansion of the random stiffness matrix (3.49) gives:

$$\tilde{\mathbf{K}}(l_c, \tilde{\boldsymbol{z}}) = \sum_{i=1}^{n_k} \left[\mathbf{K}^i_0 + \sum_{\alpha=1}^{n_{kl}} \sum_{\beta=1}^{n_{svd}} \sigma_{(\alpha,\beta)} m_{(\alpha,\beta)}(l_c) \mathbf{K}^i_{(\alpha,\beta)} \tilde{z}_\alpha \right] \phi^j(l_c). \tag{3.60}$$

Note that this equation is of the same form as the separable form (3.8a), with the parameter functions given by combinations of the functions in (3.15), the random variables, $\tilde{z}_\alpha$, and the singular-value modes for the length parameter, $m_{(\alpha,\beta)}$. From (3.60) it is observed that the total number of terms in the separable form is equal to $n_k(1 + n_{kl} n_{svd})$. Since the stiffness contributions $\mathbf{K}^i_0$ and $\mathbf{K}^i_{(\alpha,\beta)}$ are independent of the considered parameters, these can be precomputed. Hence, construction of the stiffness matrix in the PGD solver requires evaluation of (3.60) only, and not the assembly of a finite element system.

3.7.2 Monte Carlo analysis of the critical load

Using the separable form for the stiffness matrix as discussed in Section 3.7.1, the PGD solver discussed in Section 3.4 is used to attain the PGD solution (3.47). We here use this parametrized solution to perform a Monte Carlo simulation to attain the probability distribution and statistical moments of the critical loading force for specimens with various initial fracture lengths.

To construct the PGD solution (3.47) it is necessary to consider a finite dimensional domain for the random parameters, $\tilde{\boldsymbol{z}}$, which parametrize the Karhunen-Loève expansion for the Young's modulus (3.45). We herein truncate the random domain to $\mathcal{I}_{\tilde{z}_i} = [-5, 5]$ for $i = 1, \cdots, n_{kl}$, based on the idea that realizations beyond this range are unlikely and will have a minor effect on the mean and standard deviation of the critical force. We generate realizations of the uncorrelated random variables $\tilde{\boldsymbol{z}}$ using a random number generator, and we discard realizations outside of the truncated random domain.

Using the realizations of the random variables $\tilde{\boldsymbol{z}}$ we then employ Griffith's fracture model as discussed in Section 3.6 to compute the corresponding critical forces, F_c. The mean and standard deviation for the critical force are then obtained as

$$\mu_{F_c} = \frac{1}{n_{sample}} \sum_{i=1}^{n_{sample}} F_{c,i} \quad , \sigma_{F_c} = \sqrt{\frac{1}{n_{sample}-1} \sum_{i=1}^{n_{sample}} (F_{c,i} - \mu_{F_c})^2}, \quad (3.61)$$

where n_{sample} is the Monte-Carlo sample size.

In a typical FE-based Monte Carlo simulation, evaluation of the critical loads is computationally demanding, which practically restricts the sample sizes that can be considered. Therefore, in such cases, a sample size is selected that strikes an adequate balance between the confidence level of the attained statistical moments and the required computational effort. In the PGD setting considered here, the computational effort involved in determining the critical force for a given realization of the random field is negligible compared to the corresponding full finite element simulation. This allows for the consideration of sample sizes that are orders of magnitude larger than those that could be considered using direct FE analysis, which in turn enables the computation of the statistical moments with confidence levels that are practically beyond the reach of direct FE analyses. Evidently, the selection of the sample size should be based on a trade-off between the error in the PGD approximation and the confidence level of the Monte Carlo method.

3.7.3 Numerical example: a center-crack under tensile loading

We consider the same numerical experiment as introduced in Section 3.6.2 (see Table 3.1), but now with a random field of elastic properties. For the random field (3.45) we set the mean to $\mu_E = 2\,\text{GPa}$ and the standard deviation as $\sigma_E = 0.2\,\text{GPa}$ (a coefficient of variation of 10%). We consider moderate spatial fluctuations in the random field by selecting the correlation length in equation (3.46) as $l_E = 1.5\,H_x = 6\,\text{m}$. The parameter domain for the load scale is taken as $\mathcal{I}_\lambda = [6.25, 62.5]$.

We consider a Karhunen-Loève discretization consisting of $n_{kl} = 3$ modes, which are shown in Figure 3.11. In Figure 3.12 we show two realizations of the KL expansion, as well as a sampling-based reconstruction of the auto-correlation function (3.46). On account of the low spatial frequency of the variations, the KL expansion with only 3 terms is observed to already appropriately reproduce the auto-correlation function.

Using the tolerances specified in Table 3.1, the PGD solution (3.47) is truncated at $n_{pgd} = 27$ terms. The various components of the PGD solution are displayed in Figure 3.13. From the modal amplitudes it can be observed that the PGD approximation based on 27 terms approximates the finite element problem well, in the sense that the amplitudes of even higher-order modes will be negligible compared to the considered modes.

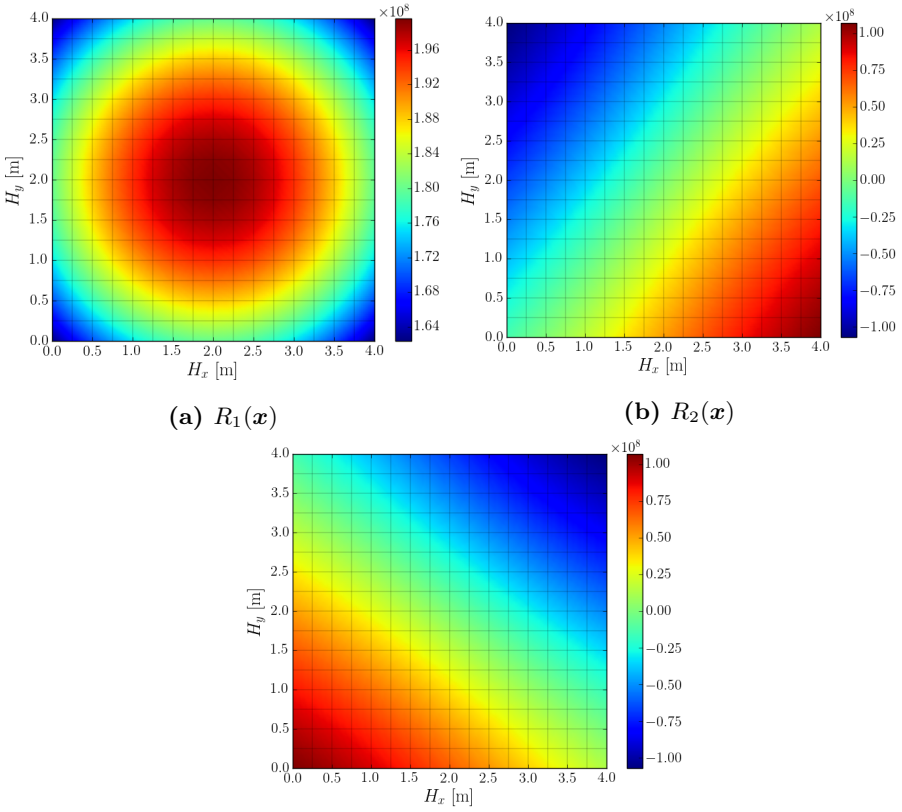

(a) $R_1(\boldsymbol{x})$

(b) $R_2(\boldsymbol{x})$

(c) $R_3(\boldsymbol{x})$

Figure 3.11: Karhunen-Loève modes for the Young's modulus field (3.45) with $n_{kl} = 3$.

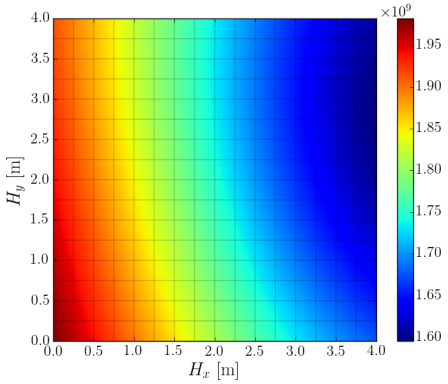

(a) Realization $E_1(\boldsymbol{x})$ Pa

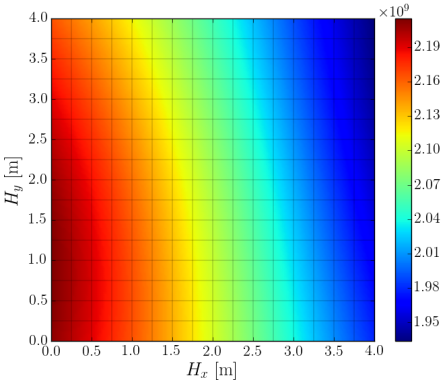

(b) Realization $E_2(\boldsymbol{x})$ Pa

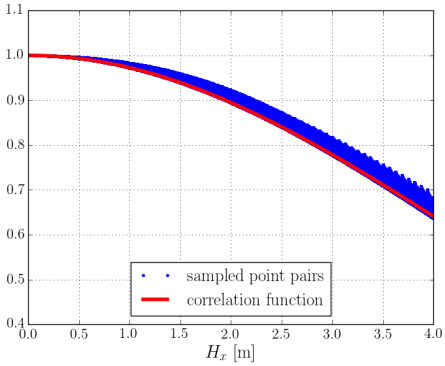

(c) Auto-correlation function

Figure 3.12: (a+b) Examples of realizations of the random elasticity field in accordance with (3.45). (c) Reconstruction of the auto-correlation kernel (3.46).

Figure 3.14 displays the probability distribution of the critical load for various settings of the initial crack length. The displayed results are based on a sample size of 5000. Note that for each of the displayed subplots in Figure 3.14 a separate Monte Carlo simulation is required, which would be computationally impractical using a direct FE approach. The efficiency with which realizations can be computed from the PGD approximation (3.47) allows us to perform Monte Carlo analyses for different settings in the parameter space. This results, for example, in the evaluation of the critical force versus the initial crack length as displayed in Figure 3.15a. The confidence level of the mean values displayed in this plot is approximately 98% based on a sample size of 5000 realizations. Such confidence levels are impractical to obtain using direct FE Monte Carlo.

Figures 3.14 and 3.15 show that the average critical load bearing capacity decreases with an increase in crack length, while a decrease in the standard deviation is observed. The deterministic result is plotted for reference, from which it is observed that the computed mean is slightly smaller than the deterministic value. The observed results from the Monte Carlo simulation are in good agreement with perturbation analysis results (see [135] for an overview) based on the analytical fracture loads for homogeneous specimens, which is to be expected on account of the considered low spatial frequency of the random input.

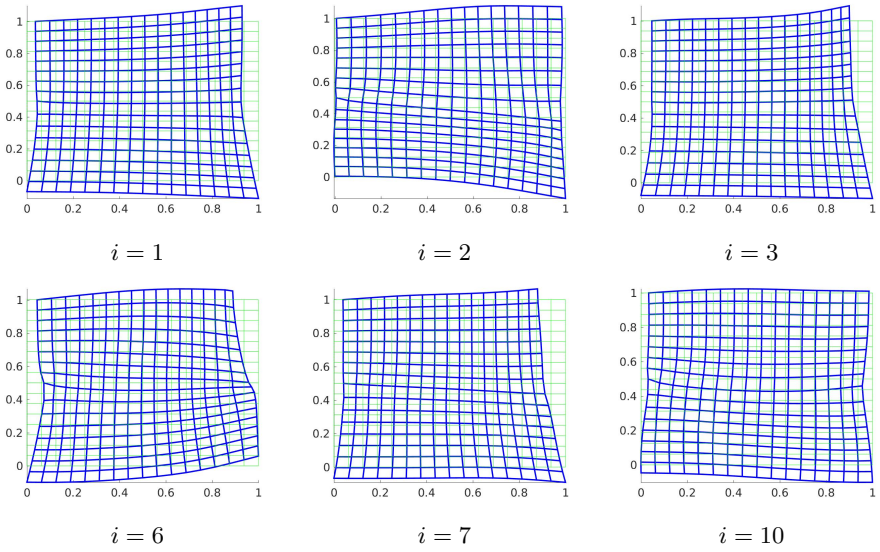

(a) Normalized displacement modes $\bar{\boldsymbol{u}}^i(\boldsymbol{x})$ of the PGD expansion. Note that only a selection of modes is shown.

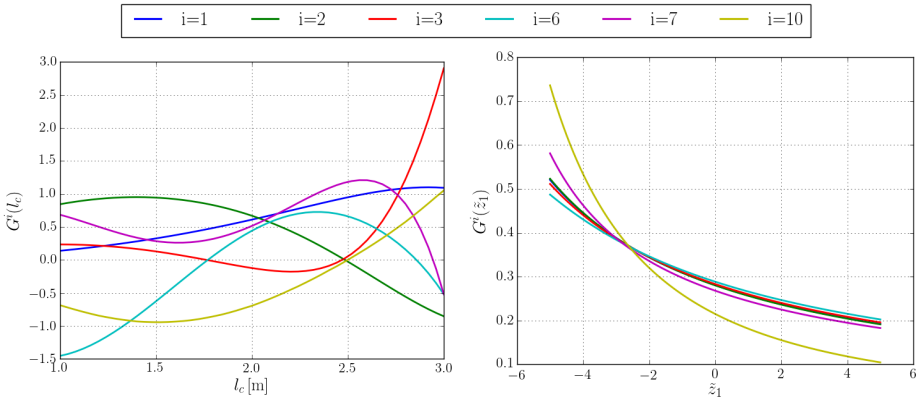

(b) Parametric modes for l_c.

(c) Parametric modes for $\tilde{z}_1$.

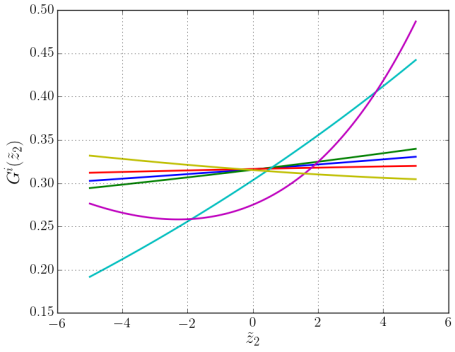

(d) Parametric modes for $\tilde{z}_2$.

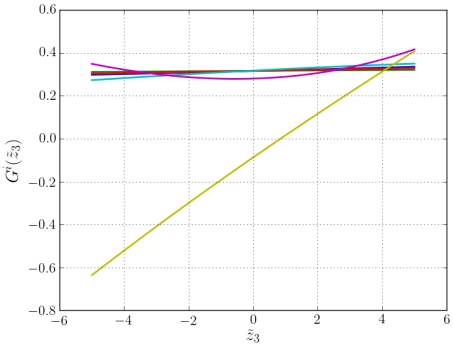

(e) Parametric modes for $\tilde{z}_3$.

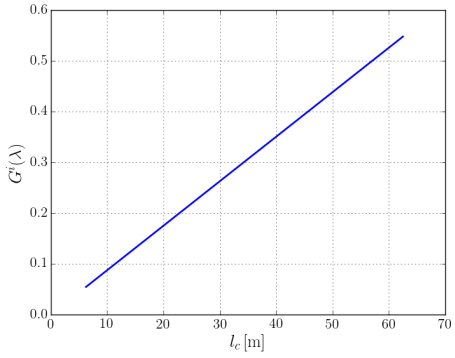

(f) Parametric modes for λ.

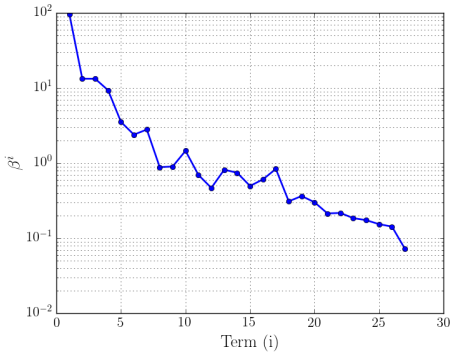

(g) Modal amplitudes β^i.

Figure 3.13: The seven components of the $\mathbf{u}_{\text{pgd}}(l_c, \tilde{z}_1, \tilde{z}_2, \tilde{z}_3, \lambda)$ solution for $n_{pgd} = 27$. Only a selection of modes is shown for conciseness. Note that all plotted functions are normalized.

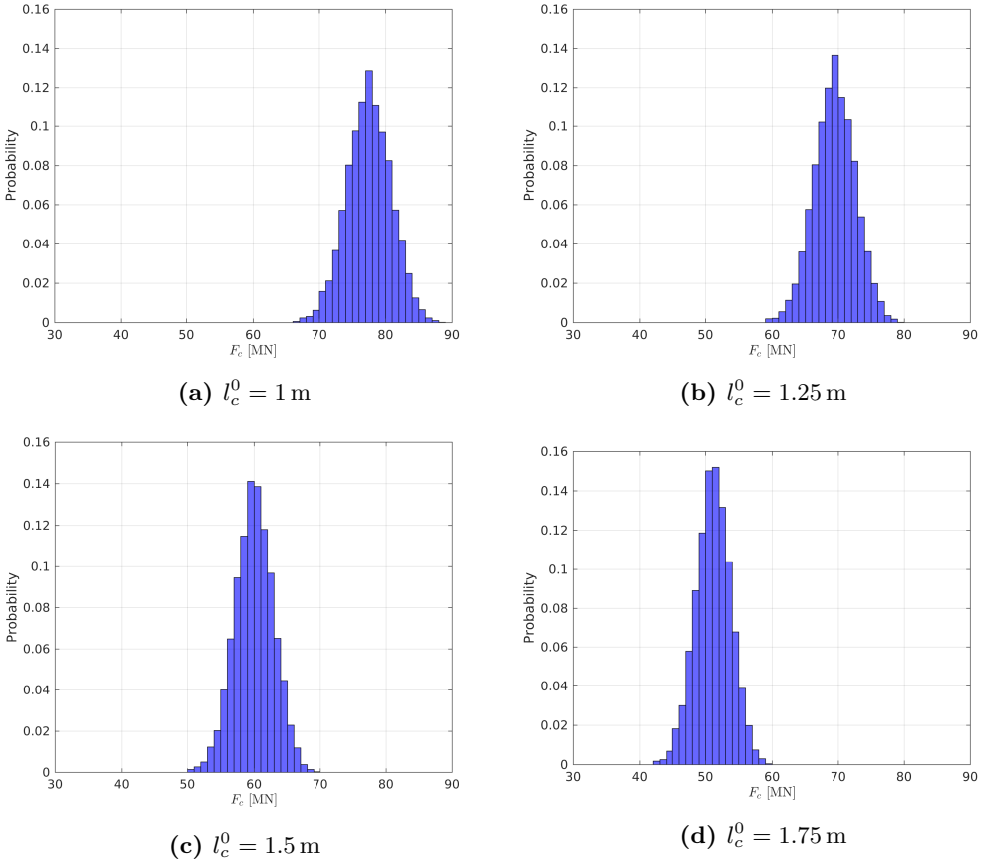

(a) $l_c^0 = 1\,\mathrm{m}$ **(b)** $l_c^0 = 1.25\,\mathrm{m}$

(c) $l_c^0 = 1.5\,\mathrm{m}$ **(d)** $l_c^0 = 1.75\,\mathrm{m}$

Figure 3.14: Histograms of the critical force for different initial crack lengths l_c^0 corresponding to a 10% variation in the Young's modulus.

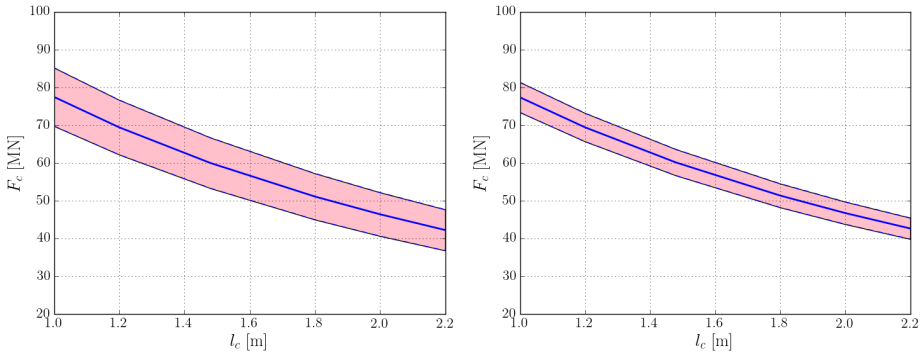

(a) Coefficient of variation: 10% **(b)** Coefficient of variation: 5%

Figure 3.15: Dependence of the mean critical force (solid blue line) on the initial crack length with a 98% confidence interval (shaded area) for 10% variation and 5% variation in the Young's modulus.

The Monte Carlo analysis allows us to inspect which realizations of the input lead to a certain response in terms of the fracture load. Figure 3.16 shows three interesting realizations for the case of an initial crack length of $l_c^0 = 1\,\mathrm{m}$ and a coefficient of variation of the Young's modulus of 10%, *viz.*:

a. The realization *closest to the mean fracture load* of 77.5 MN corresponds to a Young's modulus field which is very close to its mean value everywhere in the specimen.

b. The realization with the *largest fracture load* of 88.5 MN corresponds to a Young's modulus field which is very high throughout the specimen (on average approximately 25% higher than its mean value), and is particularly large near the tip of the initial crack.

c. The realization with the *smallest fracture load* of 66.6 MN corresponds to a Young's modulus field which is very low throughout the specimen (on average approximately 25% lower than its mean value), and particularly near the tip.

In the context of the PGD approach employed in this work it is noted that, in order to inspect these realizations, only the parameters corresponding to the realization (random variable realizations) have to be stored. The input and output corresponding to these parameters is generated through post-processing of the PGD approximation. This contrasts the direct FE setting, in which either the FE solution would have to be stored, or the FE problem would have to be solved again to acquire all results corresponding to a realization.

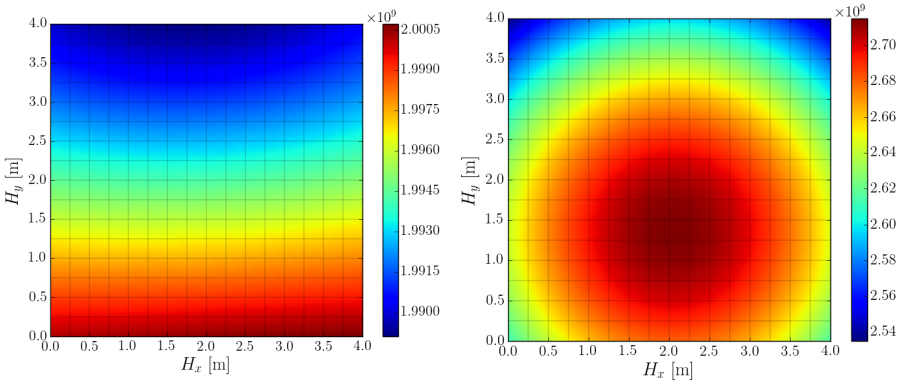

(a) $E_i(\boldsymbol{x})$ Pa closest to mean F_c

(b) $E_i(\boldsymbol{x})$ Pa for maximum F_c

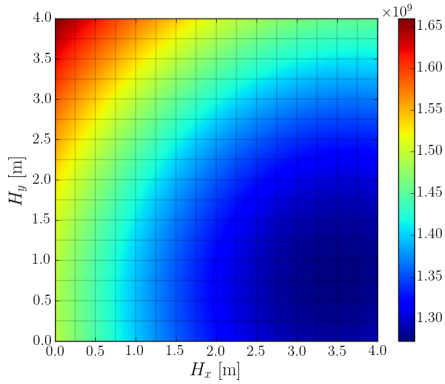

(c) $E_i(\boldsymbol{x})$ Pa for minimum F_c

Figure 3.16: Realizations of the Young's modulus field corresponding to the mean fracture load, maximum fracture load and minimum fracture load. All results pertain to an initial fracture length of $l_c^0 = 1\,\text{m}$.

3.8 Conclusions

In this work we have proposed a reduced-order modeling technique for a prototypical linear elastic fracture mechanics problem. An essential ingredient in the proposed approach is to introduce the parametrization of the crack through a geometric mapping. For the considered model problem it then follows that a separable form of the stiffness matrix and external force vector can be obtained analytically, which makes it possible to apply the Proper Generalized Decomposition method to obtain a solution to the parametric problem.

The suitability and performance of the proposed framework is demonstrated using a series of numerical test cases, starting with a convergence study for the parametric decomposition. This study conveys that the introduced geometric mapping function for the fracture parameter behaves in accordance with the well-understood behavior of the PGD framework. The PGD fracture framework is further demonstrated using two propagating fracture test cases.

In the first test case it is demonstrated how Griffith's propagation criterion can be evaluated efficiently using the PGD approximation. The representation of the fracture length in the PGD solution enables the straightforward computation of the energy release rate, which is in contrast with standard finite element methods, which generally require dedicated numerical techniques for the evaluation of the corresponding shape derivative.

In the second test case the PGD approximation is used to efficiently perform a fracture analysis in the presence of random material heterogeneities. Using a singular value decomposition for the interpolation of the random field of elastic properties pulled back to the reference configuration, an approximate separable form of the stiffness matrix is obtained. The random variable coefficients of the Karhunun-Loève field for the modulus of elasticity appear as parameters in this separable form. Since the fracture load can be computed as a post-processing operation on the PGD approximation, Monte-Carlo simulations can be performed with sample sizes (and confidence levels) that are beyond the typical reach of direct sampling-based stochastic finite element analyses.

Although the presented study clearly demonstrates that the PGD framework can be applied efficiently for the simulation of fractures in the considered model problem, the question naturally arises to what extend the proposed technique can be generalized to more complicated fracture problems. In this regard there are two aspects that must be considered in particular:

- While the considered fracture is parametrized by a single variable, namely the fracture length, this is evidently not possible in the case of more complex fractures. Of course, the range of applicability of the proposed technique can be extended to a reasonably sized class of fracture problems using a relatively low dimensional parameter space for the fracture geometry. Think

for example of slanted fractures in plane strain or plane stress settings, which, besides the length, would require the fracture angle as an additional parameter. In general, however, representing more complex fracture geometries will rapidly increase the number of parameters, which is detrimental to the performance of the PGD framework. This is particularly the case when one opts to consider a piecewise representation of fractures, which is natural to finite element methods.

- For more complex fracture patterns, constructing a suitable geometric mapping function will be considerably more challenging than in the prototypical benchmark considered in this work. Constructing a mapping analytically is very restrictive, but it is very well imaginable that one can construct discrete mapping operators (mapping nodal reference coordinates to nodal physical coordinates). Such more advanced mappings – the construction of which evidently warrants further investigation – will, however, pose several difficulties. For example, the analytical separation of the system of equations as obtained in this work will not be generally obtainable, which hence requires the consideration of potentially computationally demanding approximations for the separable forms. Moreover, an open research question remains how to deal with fractures with changing topology (*e.g.*, branching, merging), as topological changes can in general not be captured by the proposed mapping technique.

These complications when extending to more complex fractures are evidently very serious. Although future research developments can ameliorate some of these difficulties, obtaining PGD approximations that are able to accurately parametrize the complete high-dimensional solution space for complex fracture patterns will likely remain impractical. It should, however, be noted that reduced-order models typically do not serve the role of a direct replacement of high-fidelity finite element models. Instead, reduced-order models typically play the role of a relatively cheap surrogate to evaluate approximations of the corresponding high-fidelity model. In this regard it is imaginable that the high-dimensional parameter space associated with the fracture geometry in the finite element model can be reduced significantly, without compromising the properties of the reduced-order model to serve as a cheap approximation of the full model or to provide an improved prior.

Chapter 4

Uncertainty quantification for pressure-driven fracture processes

Fluid-driven fracture propagation processes are challenging to model on account of their multi-physics and moving boundary character. Moreover, in particular in the context of subsurface engineering, the hydraulic fracturing process is surrounded by uncertainties, as information on reservoir properties is typically incomplete. We develop a computational uncertainty quantification (UQ) framework capable of providing quantitative predictions of hydraulic fracturing processes based on the Perkins-Kern-Nordgren model. The Bayesian approach to uncertainty quantification is used to infer reservoir properties by combining prior information with well-pressure observations. The prior information on the model uncertainties is represented by Karhunen-Loève expansions of the random fields, and the observational data by a reduced-basis method. A Metropolis-Hastings sampler is used to infer the posterior distributions of the model uncertainties, and to attain distributions of quantities of interest such as the fracture length and aperture. The uncertainty quantification framework is tested in two scenarios with synthetically manufactured data, namely a data-abundant scenario and a data-scant scenario. These test cases illustrate the effectivity of the framework in combining prior model information with observational data.

This chapter is reproduced from [174]: H. Garikapati, J. van de Poll, E.H. van Brummelen, S. Zlotnik, P. Díez and C.V. Verhoosel .Uncertainty quantification for pressure-driven fracture processes: Sampling-based Bayesian inference using the PKN model. *in preparation*, .

4.1 Introduction

Pressure-driven fracture processes are often surrounded by uncertainties, especially in the context of subsurface engineering, where the information available on reservoir properties is frequently scant. The ability to quantitatively predict the behavior of such processes using models is highly needed, as this modeling is instrumental for risk assessment and operational decision-making.

Uncertainty quantification for pressure-driven fractures is particularly challenging on account of the fact that it combines the complications associated with stochastic analyses with mathematical-physical models that are non-trivial to solve. The models that are capable of incorporating the sources of uncertainty in a meaningful manner are time-dependent, involve a moving boundary in the form of a propagating fracture, are non-linear on account of the slit flow, and give rise to singular solution behavior in the vicinity of the fracture tip (see, *e.g.*, Ref. [125]). In Ref. [95] we have performed a stochastic analysis for such a model, *viz.* the Perkins-Kern-Nordgren (PKN) model [29, 30], by using a Monte Carlo method to compute the probabilistic response of the fracture process (*e.g.*, the probability distribution of the fracture length) related to uncertain model parameters (*e.g.*, random field reservoir properties). Similar types of *forward uncertainty analyses* for pressure-driven fracture processes are presented in Refs. [120, 121].

The capability of forward stochastic techniques to provide quantitative predictions is impeded when limited information on the system parameters is available. This is particularly the case in subsurface-engineering applications, where reservoir properties are highly uncertain, and measurements to assess such properties with meaningful accuracy are frequently unavailable or impractical. In such settings, one must resort to *inverse uncertainty quantification* procedures, which allow for the incorporation of measurement data to enhance the quantitative predictive capabilities of the modeling framework. In the context of pressure-driven fractures, such observations would typically pertain to injection rates and pressures, possibly supplemented with seismic data. Combining these measurements with the available model through the inversion process leads to data-calibrated reservoir properties, which in turn provide a model capable of quantitatively predicting the fracture evolution.

While computational uncertainty quantification (UQ) is a well-studied topic, see, *e.g.*, the reviews by Oden [60] and Tarantola [175], application of UQ in the context of pressure-driven fracturing is limited. While there have been no results presented in the literature for the PKN model or models of similar complexity, UQ for hydraulic fracturing processes has been considered in the context of related mathematical-physical models. Lecampion et al. [14, 15] have studied a real-time Bayesian inference framework to optimize stimulation procedures based on injected volume measurements. Ballester et al. [16] studied genetic algo-

rithms for non-linear inverse problems in the context of reservoir characterization. Other noteworthy contributions to inverse modeling for reservoir stimulation are Ref. [17] and Ref. [18], which discuss the inference of permeabilities using the Buckley-Leverett model for two-phase flows in porous media and the inference of fracture geometry using titlmeter measurements, respectively.

In this manuscript we propose a Bayesian inference framework for the uncertainty quantification of fluid-driven fracture propagation processes represented by the PKN model. The key ingredients of the proposed framework are: *(i)* the probabilistic characterizations of the system parameters (*e.g.*, reservoir properties) and the observable parameters (*e.g.*, well pressures); and *(ii)* the application of an inverse solver in the form of the Metropolis-Hastings sampling method. With respect to the characterization aspect, we propose to consider spatially varying random fields for the reservoir properties, and a reduced-basis method for the pressure data. To adequately incorporate these probabilistic sources of information in the inference framework, a Galerkin discretization of the PKN model is proposed. On the one hand this discretization endows the model with the capability to incorporate the specified information, while, on the other hand, it can be evaluated sufficiently fast in order to be applicable in the sampling algorithm.

This manuscript is outlined as follows. In Section 4.2 we commence with the introduction of the PKN model and its Ritz-Galerkin discretization. In Section 4.3 we then introduce the Bayesian inference framework, including detailed discussions on the representation of the uncertain parameters. Section 4.4 presents the inverse solver, with a particular focus on the computational aspects that are relevant in relation to the hydraulic stimulation context. In Section 4.5 we present a series of numerical test cases to assess the performance of the proposed framework. We consider two scenarios with manufactured data, which allow us to assess the accuracy of the results and to study the influence of a range of parameters. Conclusions are finally presented in Section 4.6.

4.2 The PKN model for hydraulic fracturing simulation

In this section we introduce the Perkins-Kern-Nordgren (PKN) model for hydraulic fracturing [29, 30], a prototypical model that is generally appraised for its balance between model simplicity and practical applicability. In Section 4.2.1 we present the mathematical-physical model formulation, where we briefly discuss the assumptions underlying this model. We refer the reader to Ref. [95] for a detailed discussion regarding the PKN model in a typical uncertainty quantification setting. In Section 4.2.2 we then introduce the solution method that is

employed to solve the PKN model.

4.2.1 Formulation of the PKN model

The PKN model mimics the horizontal (x-direction) propagation of a vertical (y-direction) fracture of fixed height, H [m], under the influence of a prescribed injection rate $i(t)$ [m^3/s], as illustrated schematically in Figure 4.1. The length of the fracture is denoted by $L(t)$ [m] and the fracture aperture along the center-line of the fracture by $\hat{w}(x,t)$ [m]. The opening profile of the fracture is assumed to be elliptic (in the yz-plane), and the opening is assumed to vanish at the tip of the fracture. In the initial situation, a completely closed fracture of length L_0 [m] is assumed, and propagation is considered until the final time T [s].

In terms of the fluid flow model, the PKN equations assume a Newtonian fluid, with viscosity μ_f [Pa $\cdot$ s], and Stokes flow through the elliptic cross-sectional profile of the fracture. These assumptions result in the well-known cubical scaling of the flow rate with the opening of the fracture [126]. Fluid leak-off to the reservoir is modeled through Carter's leak-off relation [128] with parameter c_l [m/s$^{\frac{1}{2}}$] and with the fracture arrival time $\tau(x)$ [s] defined as the time at which the fracture tip reaches to position x.

The PKN model relies on the usage of a planar deformation model, in the sense that for every point x along the fracture, the fracture aperture, $\hat{w}(x,t)$ [m], is related to the pressure inside the fracture, $p(x,t)$ [Pa], by the point-wise relation

$$\hat{w}(x,t) = \frac{2Hp(x,t)}{E'(x)}, \tag{4.1}$$

where $E'(x)$ [Pa] is the plane strain modulus of the formation. See Ref. [95] for a detailed discussion regarding the assumptions underlying this highly simplified mechanical model, in particular in relation to the consideration of a spatially varying field of elastic properties.

Fracture propagation is assumed to be viscosity driven in the PKN model, meaning that fracture toughness effects are ignored. Combination of the propagation model with the fluid model and the solid deformation model yields the initial boundary value problem for the fracture aperture $\hat{w}(x,t)$ and length $L(t)$:

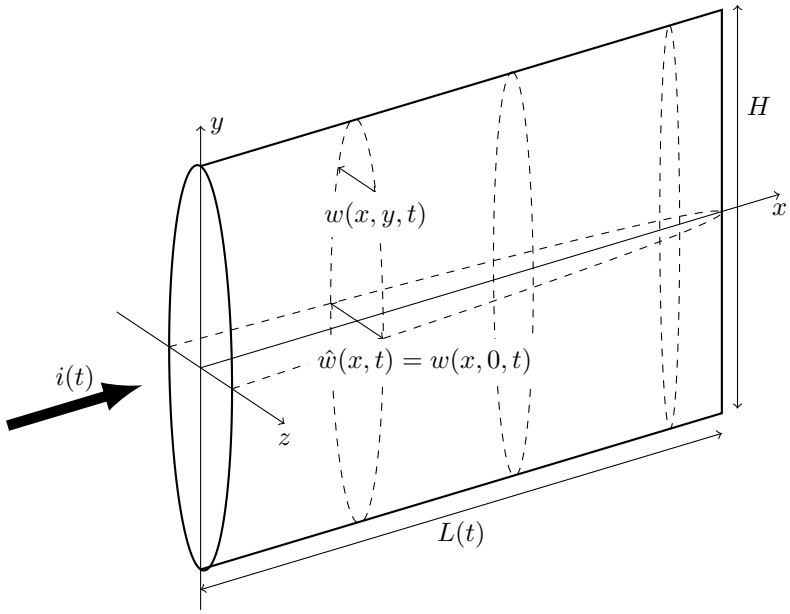

Figure 4.1: Schematic representation of the Perkins-Kern-Nordgren model for hydraulic fracturing

$$
\begin{cases}
\dfrac{\pi}{128\mu_f}\dfrac{\partial}{\partial x}\left(\hat{w}^3\dfrac{\partial\left(E'\hat{w}\right)}{\partial x}\right)=\dfrac{2Hc_l}{\sqrt{t-\tau}}+\dfrac{\pi H}{4}\dfrac{\partial\hat{w}}{\partial t} & \forall t\in(0,T),\ x\in(0,L(t)), \quad (4.2a)\\
-\dfrac{\pi}{128\mu_f}\left(\hat{w}^3\dfrac{\partial\left(E'\hat{w}\right)}{\partial x}\right)\Big|_{x=0}=i(t) & \forall t\in(0,T) \quad (4.2b)\\
\hat{w}(L(t),t)=0 & \forall t\in(0,T) \quad (4.2c)\\
\hat{w}(x,0)=0 & \forall x\in(0,L_0) \quad (4.2d)\\
\dfrac{dL(t)}{dt}=-\dfrac{1}{96\mu_f H}\dfrac{\partial\left(E'\hat{w}^3\right)}{\partial x}\Big|_{x=L(t)} & \forall t\in(0,T) \quad (4.2e)\\
L(0)=L_0 & (4.2f)
\end{cases}
$$

Note that, although the above initial boundary value problem is posed over a one-dimensional domain, determination of its solution is challenging on account of the fact that: *(i)* the domain has a moving boundary in the form of the fracture tip $L(t)$; *(ii)* the differential equation is non-linear due to the cubic dependence of the flow rate on the fracture opening; *(iii)* the solution is weakly singular at the fracture tip. These complications hinder the use of analytical methods and instead require the consideration of numerical solution techniques. In the next section we will discuss the computational methods used to solve the PKN model (4.2) in the context of the uncertainty quantification framework considered in this work.

4.2.2 Time discretization of the PKN model

To solve the moving boundary problem (4.2) we discretize the time interval $[0,T]$ using time steps of size Δt, such that $t_\imath=\imath\Delta t$, with $\imath=0,1,\ldots,n_t$. Let $\hat{w}^\imath(x)$ and $L^\imath$ denote the approximations of $\hat{w}(x,t_\imath)$ and $L(t_\imath)$, respectively. We consider a backward Euler discretization in time for the fracture aperture and a forward Euler scheme for the fracture length. That is, equations (4.2a) and (4.2e) are semi-discretized in time as:

$$
\frac{\pi}{128\mu_f}\frac{d}{dx}\left((\hat{w}^\imath)^3\frac{d\left(E'\hat{w}^\imath\right)}{dx}\right)=\frac{2Hc_l}{\sqrt{t_i-\tau}}+\frac{\pi H}{4}\frac{\hat{w}^\imath-\hat{w}^{\imath-1}}{\Delta t}\qquad\forall x\in(0,L_{\imath-1}) \tag{4.3}
$$

and

$$
\frac{L^\imath-L^{\imath-1}}{\Delta t}=-\frac{\Delta t}{96\mu_f H}\frac{d\left(E'(\hat{w}^{\imath-1})^3\right)}{dx}\Big|_{x=L^{\imath-1}}. \tag{4.4}
$$

respectively. Starting from the initial conditions $L^0 = L_0$ and $\hat{w}^0 = 0$, the solution of the moving boundary problem is solved by sequentially updating the fracture length and the fracture aperture. Both these updates are discussed in the remainder of this section.

Updating the fracture length

Given the fracture aperture and fracture length at the time step $\imath - 1$, *i.e.*, $\hat{w}^{\imath-1}$ and $L^{\imath-1}$, the discretization of the Stefan condition (4.4) can be used directly to obtain the fracture length at time step $\imath$ according to:

$$L^{\imath} = L^{\imath-1} - \frac{\Delta t}{96\mu_f H} \left. \frac{d\left(E'(\hat{w}^{\imath-1})^3\right)}{dx} \right|_{x=L^{\imath-1}} . \tag{4.5}$$

Based on the updated fracture length, subsequently the fracture aperture is updated.

Updating the fracture aperture

Given the fracture aperture at the time step $\imath - 1$, *i.e.*, $\hat{w}^{\imath-1}$, and the updated fracture length, $L^{\imath}$, the mass conservation balance in (4.2a) is solved to determine the updated fracture aperture $\hat{w}^{\imath}$.

In Ref. [95] we have proposed to solve the aperture problem using an enriched finite element discretization. This study confirms that, for moderate spatial variations in the input parameters, the fracture aperture can be accurately approximated by

$$\hat{w}^{\imath}(x) = \hat{w}_0^{\imath} \sqrt[3]{1 - \frac{x}{L^{\imath}}} \tag{4.6}$$

with $\hat{w}_0^{\imath} = \hat{w}^{\imath}(0)$ the aperture at the inflow boundary ($x = 0$). For the sake of computational efficiency, in this work we resort to a Galerkin discretization based on this single mode shape. That is, we define the solution space for the fracture aperture as

$$\mathcal{V}^{\imath} = \text{span}\left(\left\{ \sqrt[3]{1 - \frac{x}{L^{\imath}}} \right\} \right) \tag{4.7}$$

and use this space to solve the weak formulation corresponding to (4.2):

$$\begin{cases} \text{Find } \hat{w}^\imath \in \mathcal{V}^\imath \text{ such that } \forall v \in \mathcal{V}^\imath\text{:} \\ \dfrac{\pi}{4} \displaystyle\int_0^{L^\imath} \left(\frac{(\hat{w}^\imath)^3}{32\mu_f} \frac{\partial \left(E' \hat{w}^\imath\right)}{\partial x} \frac{\partial v}{\partial x} + \frac{H}{\Delta t} \hat{w}^\imath v \right) \mathrm{d}x = \\ \qquad \dfrac{\pi H}{4\Delta t} \displaystyle\int_0^{L^{\imath-1}} \hat{w}^{\imath-1} v \, \mathrm{d}x - 2H c_l \int_{L_0}^{L^\imath} \frac{v}{\sqrt{t^\imath - \tau^{\imath-1}}} \, \mathrm{d}x + i(t^\imath) v(0) \end{cases} \tag{4.8}$$

Note that, since the dimension of the considered space (4.7) is equal to 1, this weak form problem in fact translates into a scalar problem for the maximum aperture $\hat{w}_0$ as defined in equation (4.6). In order to determine the solution to this scalar problem, at every time step the integrals in the weak form (4.8) must be evaluated. On account of the material heterogeneities, $E'(x)$, and arrival time function $\tau(x)$, these integrals require numerical evaluation.

4.3 The stochastic inverse problem

In this section we outline the uncertainty quantification framework considered for the hydraulic fracturing model introduced above. We first put the framework in the setting of the PKN model in Section 4.3.1 by defining the uncertain input and output quantities, along with defining the role of the model introduced in Section 4.2. We then introduce the inverse problem in the form of the Bayesian inference method in Section 4.3.2. Subsequently, in Section 4.3.3 we discuss in detail the data representations being considered in this work.

4.3.1 Model parameters, data parameters & the forward operator

As uncertain model parameters we, in general, consider the plane strain modulus, $\tilde{E}'(x)$, the fracture height, $\tilde{H}(x)$, and the leak-off coefficient, $\tilde{c}_l(x)$, all being considered as random (indicated by the tilde) fields over the spatial domain Ω. We denote these uncertain model parameters by

$$\mathbf{m} = \{\tilde{E}'(x), \tilde{H}(x), \tilde{c}_l(x)\}, \tag{4.9}$$

which can be considered as an n_p-dimensional, not necessarily Cartesian, coordinate in the *model space*, *i.e.*, $\mathbf{m} \in \mathfrak{M}$. Note that the random fields in the model parameters are generally discretized, which implies that they are represented by

a finite number of random variables. The remaining model parameters, *viz.* the fluid viscosity, μ_f, the initial fracture length, L_0, and the injection rate, $i(t)$, are assumed to be deterministic, in the sense that their variability is negligible in comparison to the uncertain parameters in $\mathbf{m}$, and are therefore omitted from the parameter set.

The time-dependent pressure, $\tilde{p}(t)$, is considered as an observable system parameter, in the sense that measurement data for this parameter can be acquired. As additional *quantities of interest*, for which observations are not available, we consider the time response of the fracture opening, $\tilde{w}(t)$, and the evolution of the fracture length, $\tilde{L}(t)$. These derived quantities of interest are part of the output of the model and are therefore considered as part of the data space, despite the fact that there might be no observations available on these output parameters. The observations and quantities of interest are all considered as temporal random fields, and are represented by the data parameters

$$\mathbf{d} = \{\tilde{p}(t), \tilde{w}(t), \tilde{L}(t)\}, \tag{4.10}$$

which are to be interpreted as a coordinate in the *data space*, *i.e.*, $\mathbf{d} \in \mathfrak{D}$.

The model space and data space are related through physical laws, which, assuming model inadequacies to be negligible, we represent by the *forward model operator*, $\mathbf{g}$, such that:

$$\mathbf{d} = \mathbf{g}(\mathbf{m}) \tag{4.11}$$

For a particular model, as encoded by the parameter values $\mathbf{m}$, the forward operator, $\mathbf{g}$, determines the corresponding observable parameters, $\mathbf{d}$. In the case of the model discussed in Section 4.2 it is assumed that given a realization of the uncertain parameters in (4.9) and the deterministic parameters not included in $\boldsymbol{m}$, the response in the form of the quantities of interest in the data parameters in (4.10) can be be obtained with certainty. This implies that uncertainties with respect to the model, for example related to the employed solution procedure, are assumed to be negligible in comparison to the variations in the model parameters and related quantities of interest.

In the context of the stochastic inverse problem, the deterministic mapping (4.11) can be considered as a special case of the joint probability density function that relates the data space to the model space, *i.e.*,

$$\Theta(\mathbf{d}, \mathbf{m}) = \delta(\mathbf{d} - \mathbf{g}(\mathbf{m}))\, \mu_M(\mathbf{m}), \tag{4.12}$$

with δ denoting the delta distribution, and with μ_M the homogeneous probability density for the model space. The corresponding conditional probability density is given by

$$\theta(\mathbf{d} \mid \mathbf{m}) = \delta(\mathbf{d} - \mathbf{g}(\mathbf{m})). \tag{4.13}$$

4.3.2 Bayesian inference: combining prior information with observational data

We consider the inverse problem in a Bayesian inference setting, in an analogous manner as in Ref. [175]. In the stochastic inverse problem, prior information on the model parameters $\boldsymbol{m}$ is provided through the probability density function $\rho_M(\mathbf{m})$. This prior information on the model is generally based on experts' opinion, which is, for example, motivated by earlier experiences with the model.

The prior information considered in this work is represented by random fields for the relevant reservoir parameters, *i.e.*, the plane strain modulus, the fracture height, and the leak-off coefficient. Each of these fields is characterized by a Karhunen-Loève (KL) expansion [176], which is, in general, parametrized by a mean value, a standard deviation, and a spatial correlation length. Details regarding these expansions are discussed in Section 4.3.3.

Through the use of Karhunen-Loève expansions we provide information content to the model parameters in the form of the underlying point-wise probability distribution and by the specified auto-correlation function. A measure of the information content in the prior is provided through Shannon's measure of information content [175], which is zero in the case of a non-informative prior (the homogeneous probability distribution), and positive when the prior is informative. In the case of KL expansions of the uncertain model parameters, the information content increases with a decrease in the variation of the underlying normal distribution, and with an increase in the correlation length.

In the stochastic inverse problem, also the observable data, $\mathfrak{D}$, is provided through a probability density, $\rho_D(\mathbf{d})$. The data parameters considered herein on the one hand pertain to the pressure observations, $\tilde{p}(t)$, which are assumed to be available as noisy experimental data. A singular value decomposition is used to represent this source of information through the probability density function, $\rho_p(p)$, details of which will be discussed in Section 4.3.3. On the other hand, the other quantities of interest, *viz.*, the pressure aperture and fracture length, are deterministically related to the pressure observations, in the sense that their values are acquired through the deterministic forward model operator (4.11). In terms of the probabilistic representation, this implies that the conditional probability density function for these derived quantities of interest is represented by a delta distribution, which can be combined with the pressure probability density to acquire the joint probability density function $\rho_D(\mathbf{d})$ on the entire data space.

Given that the observations are generally independent of the prior information, the correspondence between the data and the model space is captured by the joint probability density function

$$\rho(\mathbf{d}, \mathbf{m}) = \rho_D(\mathbf{d})\rho_M(\mathbf{m}). \tag{4.14}$$

The pivotal idea of Bayesian inversion [177] is to combine this information on the data-model space with the forward operator (4.13) to establish the posterior model distribution density

$$\sigma_M(\mathbf{m}) = k\rho_M(\mathbf{m})L(\mathbf{m}) \tag{4.15}$$

with likelihood function

$$L(\mathbf{m}) = \int_{\mathfrak{D}} \frac{\rho_D(\mathbf{d})\theta(\mathbf{d} \mid \mathbf{m})}{\mu_D(\mathbf{d})}\,\mathrm{d}\mathbf{d} \tag{4.16}$$

and with normalization constant k and homogeneous data space probability density $\mu_D(\boldsymbol{d})$. Under the assumption of negligible forward model inadequacies, *i.e.*, equation (4.13), the likelihood reduces to

$$L(\mathbf{m}) = \int_{\mathfrak{D}} \frac{\rho_D(\mathbf{d})\delta(\mathbf{d} - \mathbf{g}(\mathbf{m}))}{\mu_D(\mathbf{d})}\,\mathrm{d}\mathbf{d} = \frac{\rho_D(\mathbf{g}(\mathbf{m}))}{\mu_D(\mathbf{g}(\mathbf{m}))}, \tag{4.17}$$

and the normalization constant in (4.15) to

$$k^{-1} = \int_{\mathfrak{M}} \rho_M(\mathbf{m})L(\mathbf{m})\mathrm{d}\mathbf{m} = \int_{\mathfrak{M}} \frac{\rho_M(\mathbf{m})\rho_D(\mathbf{g}(\mathbf{m}))}{\mu_D(\mathbf{g}(\mathbf{m}))}\mathrm{d}\mathbf{m}. \tag{4.18}$$

The likelihood function (4.17) establishes a measure for how well a model, $\mathbf{m}$, fits the data, $\mathfrak{D}$. From this expression it is apparent that the maximum likelihood of a model is, in general, different from the maximum of the probability density function of the corresponding observable, as it is scaled by the homogeneous data space distribution. In the case of a linear data space, as will also be considered in this work, the homogeneous data space distribution μ_D is constant. Upon substitution of (4.17) and (4.18) into the expression for the posterior (4.15), it follows that the posterior distribution is independent of μ_D.

The posterior model distribution (4.15) is regarded as the solution to the stochastic inverse problem, in the sense that this is the probability distribution that logically combines the observational data, prior information, and forward model operator. In contrast to deterministic inverse problems, the stochastic inverse problem is generally well-posed, in the sense that the posterior σ_M provides *unique* information on the model, and that this posterior exists (*i.e.*, is not empty) provided that the input sources of information are compatible [175]. In this regard, it is generally required that the prior information is sufficiently uninformative, meaning that the variations in the prior random fields should be sufficiently large.

4.3.3 Representation of probabilistic quantities

An essential aspect of the stochastic inverse problem is that all quantities are represented by probability distributions. For the sake of self-containedness and

to establish notation, in the remainder of this section we review the most important aspects of the representation of the random quantities. In Section 4.3.3 we first discuss the Karhunen-Loève (KL) expansions used to represent the prior information on the spatially varying model parameters. Using the KL expansion, these fields are discretized using a finite number of standard normal random variables. We then discuss the singular value decomposition (SVD) used to represent time-dependent well-pressure data in Section 4.3.3. For all considered random variables (including discretized random fields) we rely on the usage of analytical probability distributions (*e.g.*, uniform, normal, log-normal) and data binning to represent their probability density. Details regarding the employed binning procedure are discussed in Section 4.3.3.

Karhunen-Loève expansion of a spatial random field

To elaborate the details of the used KL expansions, we consider the random plane strain modulus field, $\tilde{E}'(\boldsymbol{x})$, with $\boldsymbol{x} \in \Omega$. This field is characterized by a stationary (*i.e.*, constant in space) probability density function, $f_{E'}(E')$, with mean $\mu_{E'}$, standard deviation $\sigma_{E'}$, and auto-correlation function

$$\rho_{E'E'}(\boldsymbol{x}_1, \boldsymbol{x}_2) = \exp\left(-\frac{\|\boldsymbol{x}_1 - \boldsymbol{x}_2\|^2}{l_{E'}^2}\right), \tag{4.19}$$

with correlation length $l_{E'}$ and the exponential function being used as an example of a typical decaying function. The corresponding spatial covariance is then given by $\Sigma_{E'E'}(\boldsymbol{x}_1, \boldsymbol{x}_2) = \sigma_{E'}^2 \rho_{E'E'}(\boldsymbol{x}_1, \boldsymbol{x}_2)$.

In order to discretize the random field, $\tilde{E}'(\boldsymbol{x})$, we assume that we can express this field as a function of an underlying Gaussian random field, $\tilde{G}(\boldsymbol{x})$, through the mapping

$$\tilde{E}(\boldsymbol{x}) = \ell(\tilde{G}(\boldsymbol{x})) \qquad \forall \boldsymbol{x} \in \Omega, \tag{4.20}$$

such that the mean, μ_G, and covariance function, $\Sigma_{GG}(\boldsymbol{x}_1, \boldsymbol{x}_2)$, are expressible in terms of the mean and covariance of the field $\tilde{E}'(\boldsymbol{x})$. For the plane strain modulus we generally consider a log-normal random field, for which the function ℓ is taken equal to the exponential function, *i.e.*,

$$\tilde{E}'(\boldsymbol{x}) = \exp\left(\tilde{G}(\boldsymbol{x})\right), \tag{4.21}$$

and the Gaussian field mean and covariance follow as [178]

$$\mu_G = \ln(\mu_{E'}) - \frac{1}{2}\ln(1 + V_{E'}^2) \qquad \sigma_G^2 = \ln(1 + V_{E'}^2), \tag{4.22}$$

with coefficient of variation $V_{E'} = \sigma_{E'}/\mu_{E'}$. Let us note that in the identity (4.21) the units of the left member have tacitly been suppressed. Similarly, the auto-correlation function of the Gaussian field follows as:

$$\rho_{GG}(\boldsymbol{x}_1, \boldsymbol{x}_2) = \frac{\ln\left(1 + \rho_{E'E'}(\boldsymbol{x}_1, \boldsymbol{x}_2) V_{E'}^2\right)}{\ln(1 + V_{E'}^2)}. \tag{4.23}$$

We discretize the Gaussian random field, $\tilde{G}(\boldsymbol{x})$, using the Karhunen-Loève expansion [179],

$$\tilde{G}(\boldsymbol{x}) = \mu_G + \sum_{\alpha=1}^{n_{kl}} \zeta_\alpha(\boldsymbol{x}) \tilde{z}_\alpha \tag{4.24}$$

with $\{\tilde{z}_\alpha\}_{\alpha=1}^{n_{kl}}$ a set of n_{kl} independent standard normal random variables, and $\{\zeta_\alpha(\boldsymbol{x})\}_{\alpha=1}^{n_{kl}}$ a corresponding set of spatial modes. The KL modes follow from the integral eigenvalue problem

$$\int_\Omega \Sigma_{GG}(\boldsymbol{x}_1, \boldsymbol{x}_2) \zeta_\alpha(\boldsymbol{x}_2) \, \mathrm{d}\boldsymbol{x}_2 = \lambda_\alpha \zeta_\alpha(\boldsymbol{x}_1) \qquad \alpha = 1, \ldots, n_{kl}, \tag{4.25}$$

where Σ_{GG} is the covariance function according to $\Sigma_{GG} = \sigma_G^2 \rho_{GG}$. The modes in (4.25) are normalized according to

$$\int_\Omega \zeta_\alpha(\boldsymbol{x})^2 \, \mathrm{d}\boldsymbol{x} = \lambda_\alpha \qquad \alpha = 1, \ldots, n_{kl}. \tag{4.26}$$

In specific cases, mainly in one dimension, the integral equation (4.25) can be solved analytically (see, *e.g.*, [180]). However, in this contribution we follow the more general approach of constructing the KL expansion using a spatial discretization of the modes of the form

$$\zeta_\alpha(\boldsymbol{x}) = \sum_{i=1}^{n} \phi_i(\boldsymbol{x}) \hat{\zeta}_{\alpha i} = \boldsymbol{\phi}(\boldsymbol{x})^T \hat{\boldsymbol{\zeta}}_\alpha \qquad \alpha = 1, \ldots, n_{kl}, \tag{4.27}$$

with spatial basis functions $\boldsymbol{\phi}(\boldsymbol{x}) = \{\phi_i(\boldsymbol{x})\}_{i=1}^n$ and corresponding coefficients vector $\hat{\boldsymbol{\zeta}}_\alpha = \{\hat{\zeta}_{\alpha i}\}_{i=1}^n$ for every $\alpha = 1, \cdots, n_{kl}$. Using this spatial discretization, Galerkin's method can then be employed to approximate the integral problem (4.25) through the solution of the generalized eigenvalue problem

$$\begin{aligned} &\left[\int_\Omega \int_\Omega \Sigma_{GG}(\boldsymbol{x}_1, \boldsymbol{x}_2) \boldsymbol{\phi}(\boldsymbol{x}_1) \boldsymbol{\phi}(\boldsymbol{x}_2)^T \, \mathrm{d}\boldsymbol{x}_1 \mathrm{d}\boldsymbol{x}_2\right] \hat{\boldsymbol{\zeta}}_\alpha = \\ &\qquad \lambda_\alpha \left[\int_\Omega \boldsymbol{\phi}(\boldsymbol{x}_1) \boldsymbol{\phi}(\boldsymbol{x}_1)^T \, \mathrm{d}\boldsymbol{x}_1\right] \hat{\boldsymbol{\zeta}}_\alpha \qquad \alpha = 1, \ldots, n_{kl}, \end{aligned} \tag{4.28}$$

where the eigenvectors $\hat{\boldsymbol{\zeta}}_\alpha$ are normalized in accordance with

$$\int_\Omega \left(\boldsymbol{\phi}(\boldsymbol{x})^T \hat{\boldsymbol{\zeta}}_\alpha\right)^2 \, \mathrm{d}\boldsymbol{x} = \lambda_\alpha \qquad \alpha = 1, \ldots, n_{kl}. \tag{4.29}$$

Reduced-basis representation of discrete-time signals

We consider the random pressure observation, $\tilde{p}(t)$, to elaborate the details of the employed singular value decompositions for time-dependent random processes. The pressure process, $\tilde{p}(t)$, is discretized in time using a uniform partitioning of the time domain, $t = (i-1)\Delta t$, with $i = 1, \ldots, n_t$, such that the signal is represented by the random vector $\tilde{\boldsymbol{p}} = (\tilde{p}_1, \tilde{p}_2, \ldots, \tilde{p}_{n_t}) \in \mathbb{R}^{n_t}$. The randomness of the signal can then be described by a joint probability density function $f_{\boldsymbol{p}}(\boldsymbol{p})$ defined over the parameter domain $\boldsymbol{\Xi}_{\boldsymbol{p}} \in \mathbb{R}^{n_t}$.

In the case that the random time-discrete process is characterized by a sample of realizations, $\{\boldsymbol{p}_\imath\}_{\imath=1}^{n_p}$, the probability density function $f_{\boldsymbol{p}}(\boldsymbol{p})$ can be approximated using data binning, as will be discussed in Section 4.3.3. Binning will be impractical, however, in cases where the number of time steps is large, as the sample size required to appropriately approximate the probability density function is affected by the dimensionality of the parameter domain $\boldsymbol{\Xi}_{\boldsymbol{p}} \subset \mathbb{R}^{n_t}$.

When the process is spatially correlated, a lower dimensional representation of the process can be obtained using a truncated singular value decomposition. This approach is similar to reduced-basis methods in reduced order modeling, principal component analysis in statistics, and proper orthogonal decomposition in dynamics. In contrast to the original data set, this lower dimensional representation of the process poses less severe restrictions on the required sample size on account of the reduction in dimensionality of the random process.

To construct the singular value decomposition of the process $\tilde{\boldsymbol{p}}$, we collect the data of all realizations, $\{\boldsymbol{p}_\imath\}_{\imath=1}^{n_p}$, in a matrix, $\mathbf{D} \in \mathbb{R}^{n_p \times n_t}$, of size $n_p \times n_t$, so that each row in this matrix corresponds to a realization of the process. The singular value decomposition of this matrix then reads

$$\boldsymbol{D} = \sum_{\alpha=1}^{\min(n_t, n_p)} \sigma_\alpha \boldsymbol{u}_\alpha \boldsymbol{v}_\alpha^T, \tag{4.30}$$

where σ_α are the singular values sorted in descending order, and $\boldsymbol{u}_\alpha \in \mathbb{R}^{n_p}$ and $\boldsymbol{v}_\alpha \in \mathbb{R}^{n_t}$ are the corresponding left and right singular vectors. The right singular vectors, $\boldsymbol{v}_\alpha$, or, equivalently, the vectors $\boldsymbol{D}^T \boldsymbol{u}_\alpha$, form an orthonormal basis for the process realizations, where the singular values σ_α assign importance to the modes. For temporally correlated processes, this means that typically the process can be captured well by considering a truncated basis that only contains the modes corresponding to the $n_{\text{svd}} \ll \min(n_t, n_p)$ largest singular values. This truncated singular value representation can be expressed as

$$\boldsymbol{p}_\imath \approx \sum_{\alpha=1}^{n_{\text{svd}}} \boldsymbol{v}_\alpha \xi_{\imath\alpha} \qquad \imath = 1, \ldots, n_p, \tag{4.31}$$

where the coefficient vectors $\boldsymbol{\xi}_\imath \in \mathbb{R}^{n_{\mathrm{svd}}}$ are determined by the minimization problem

$$\boldsymbol{\xi}_\imath = \underset{\boldsymbol{y}\in\mathbb{R}^{n_{\mathrm{svd}}}}{\operatorname{argmin}} \|\boldsymbol{p}_\imath - \sum_{\alpha=1}^{n_{\mathrm{svd}}} \boldsymbol{v}_\alpha y_\alpha\|, \tag{4.32}$$

with $\|\cdot\|$ denoting the L^2 vector norm. Making use of the orthonormality of the left singular vectors, the minimization problem (4.32) solves as

$$\xi_{\imath\alpha} = \boldsymbol{v}_\alpha^T \boldsymbol{p}_\imath. \tag{4.33}$$

Since it follows from (4.30) that $\xi_{\imath\alpha} = \sigma_\alpha u_{\alpha\imath}$, the relative truncation error corresponding to (4.31) can be expressed in relation to the singular values of the system as

$$\begin{aligned}
\frac{\sqrt{\sum_{\imath=1}^{n_p} \|\boldsymbol{p}_\imath - \sum_{\alpha=1}^{n_{\mathrm{svd}}} \boldsymbol{v}_\alpha \xi_{\imath\alpha}\|^2}}{\sqrt{\sum_{\imath=1}^{n_p} \|\boldsymbol{p}_\imath\|^2}} &= \frac{\sqrt{\sum_{\imath=1}^{n_p} \left\|\sum_{\alpha=n_{\mathrm{svd}}+1}^{\min(n_t,n_p)} \boldsymbol{v}_\alpha \sigma_\alpha u_{\alpha\imath}\right\|^2}}{\sqrt{\sum_{\imath=1}^{n_p} \left\|\sum_{\alpha=1}^{\min(n_t,n_p)} \boldsymbol{v}_\alpha \sigma_\alpha u_{\alpha\imath}\right\|^2}} \\
&= \frac{\sqrt{\sum_{\alpha=n_{\mathrm{svd}}+1}^{\min(n_t,n_p)} \sigma_\alpha^2 \|\boldsymbol{v}_\alpha\|^2 \|\boldsymbol{u}_\alpha\|^2}}{\sqrt{\sum_{\alpha=1}^{\min(n_t,n_p)} \sigma_\alpha^2 \|\boldsymbol{v}_\alpha\|^2 \|\boldsymbol{u}_\alpha\|^2}} \\
&= \frac{\sqrt{\sum_{\alpha=n_{\mathrm{svd}}+1}^{\min(n_t,n_p)} \sigma_\alpha^2}}{\sqrt{\sum_{\alpha=1}^{\min(n_t,n_p)} \sigma_\alpha^2}} \leq \epsilon
\end{aligned} \tag{4.34}$$

where the error $0 < \epsilon < 1$ governs the selection of the relevant singular modes in accordance with

$$\sum_{\alpha=1}^{n_{\mathrm{svd}}} \sigma_\alpha^2 \geq (1-\epsilon^2) \sum_{\alpha=1}^{\min(n_t,n_p)} \sigma_\alpha^2. \tag{4.35}$$

If the realizations $\{\boldsymbol{p}_\imath\}_\imath^{n_p}$ are representative for the process $\tilde{\boldsymbol{p}}$ in the sense that the sample provides an adequate estimator for the average squared L^2-norm of the discrete pressure signal approximation error, inequality (4.34) implies the error estimate (see Ref. [181]):

$$\frac{\sqrt{\int_{\Xi_{\boldsymbol{p}}} \|\boldsymbol{p} - \sum_{\alpha=1}^{n_{\mathrm{svd}}} \boldsymbol{v}_\alpha \xi_\alpha(\boldsymbol{p})\|^2 \, \mathrm{d}\boldsymbol{p}}}{\sqrt{\int_{\Xi_{\boldsymbol{p}}} \|\boldsymbol{p}\|^2 \, \mathrm{d}\boldsymbol{p}}} \leq \epsilon \tag{4.36}$$

This error estimate conveys that the accuracy of the SVD approximation can be controlled directly and uniformly through the selection of the number of SVD modes in accordance with (4.35).

When the process, $\tilde{\boldsymbol{p}} \in \mathbb{R}^{n_t}$, is temporally correlated, its realizations, $\boldsymbol{p}_i \in \mathbb{R}^{n_t}$, can accurately be represented in the modal coordinates $\boldsymbol{\xi}_i \in \mathbb{R}^{n_{\text{svd}}}$ with $n_{\text{svd}} \ll n_t$. Hence, in such situations the process $\tilde{\boldsymbol{p}}$ can accurately be described by the modal coordinate process $\tilde{\boldsymbol{\xi}}$, the dimensionality of which is significantly reduced in comparison to $\tilde{\boldsymbol{p}}$. Consequently, this modal coordinate process is more suitable for data binning.

Remark 4.1 (Computation of the right singular vectors)**.** *The right singular vectors required in equation* (4.33) *can alternatively be computed by first evaluating the left singular vectors in equation* (4.30) *as the singular vectors of the system* $\mathbf{D}\mathbf{D}^T$*, which can be decomposed as*

$$\boldsymbol{D}\boldsymbol{D}^T = \sum_{\alpha=1}^{n_\xi} \sigma_\alpha^2 \boldsymbol{u}_\alpha \boldsymbol{u}_\alpha^T.$$

Subsequently, the right singular vectors can be computed as $\boldsymbol{v}_\alpha = \boldsymbol{D}\boldsymbol{u}_\alpha$*. Since the matrix* $\boldsymbol{D}\boldsymbol{D}^T$ *is of the size* $n_p \times n_p$*, the computation of the singular vectors of* (4.30) *through this alternative evaluation procedure is computationally favorable when* $n_p \ll n_t$*.*

Remark 4.2 (Noise filtering)**.** *Besides its capabilities of reducing the dimension of the data space, the singular value decomposition filters high frequency noise. For up to moderate noise levels, the noise-free signal dominates the largest singular values and corresponding singular vectors. By truncation of the SVD* (4.31)*, high frequency noise is therefore filtered. See,* e.g.*, [182] for details regarding the noise filtering properties of the singular value decomposition in the context of additive white noise. For high noise levels, additional noise filtering steps are generally required in a pre-processing step, see,* e.g.*, Ref. [183, 184] for an overview of noise filtering techniques.*

Data binning of random variable samples

Let us consider the vector-valued random variable $\tilde{\boldsymbol{\xi}} \in \boldsymbol{\Xi} \subseteq \mathbb{R}^{d_\xi}$ $(d_\xi \geq 1)$, for example the SVD-reduced pressure process discussed in Section 4.3.3, with probability density function $f_\xi(\boldsymbol{\xi})$. This probability density can be discretized by partitioning the random domain into elements $\boldsymbol{\Xi}_e$ ($\cup_e \boldsymbol{\Xi}_e = \boldsymbol{\Xi}$ and $\boldsymbol{\Xi}_{e_1} \cap \boldsymbol{\Xi}_{e_2} = \emptyset$ if $e_1 \neq e_2$). A probability can then be assigned to each element as

$$P(\boldsymbol{\Xi}_e) = \int_{\boldsymbol{\Xi}_e} f_\xi(\boldsymbol{\xi}) \, \mathrm{d}\boldsymbol{\xi}, \tag{4.37}$$

such that the probability density for each point $\boldsymbol{\xi} \in \Xi_e$ is found as $f_\xi(\boldsymbol{\xi}) \approx P(\Xi_e)/V_e$ with $V_e = \int_{\Xi_e} \mathrm{d}\boldsymbol{\xi}$. Similarly, when the probabilistic information on $\boldsymbol{\xi}$ is provided by a point cloud $\{\boldsymbol{\xi}_i\}_{i=1}^{n_\xi}$ of realizations, the discretized probability density function for $\boldsymbol{\xi} \in \Xi_e$ is given by $\#\{\boldsymbol{\xi}_i \in \Xi_e\}/n_\xi$.

In this work we will restrict ourselves to regular partitions of the rectangular random variable domain $\Xi = \otimes_{\delta=1}^{d_\xi}(\xi_\delta^{\min}, \xi_\delta^{\max})$, for which the elements are given by

$$\Xi_e = \otimes_{\delta=1}^{d_\xi} \left(\xi_\delta^{\min} + e_\delta h_\delta^\xi, \xi_\delta^{\min} + (e_\delta + 1) h_\delta^\xi \right), \tag{4.38}$$

where the element index e is interpreted as a multi-index $(e_1, e_2, \cdots, e_{d_\xi})$. The mesh size h_δ^ξ is related to the number of bins per direction, n_δ^{bins}, by $h_\delta^\xi = (\xi_\delta^{\max} - \xi_\delta^{\min})/n_\delta^{\text{bins}}$. The corresponding binned probability density is commonly visualized by a histogram with uniform bin sizes.

The choice of the bin size is particularly important in the case that a probability density function is created from a point cloud. In general, for a given number of points, a too large bin width results in a loss of accuracy, while a too small bin width yields a non-smooth representation of the probability distribution.

Various techniques to determine optimal bin sizes exist, see, *e.g.*, Refs. [185–188]. We employ the optimal bin size selection technique proposed in Ref. [186], which is based on the minimization of the mean integrated square error of the likelihood

$$e_{\text{MISE}} = \int_\Xi (\hat{f}_\xi(\boldsymbol{\xi}) - f_\xi(\boldsymbol{\xi}))^2 \, \mathrm{d}\boldsymbol{\xi}, \tag{4.39}$$

where $\hat{f}_\xi(\boldsymbol{\xi})$ represents the binned density function. See Ref. [186] for a discussion on minimization procedures to determine the optimal bin size from (4.39). The minimization of this error measure results in a decrease in bin width with an increase in sample size in accordance with [189]:

$$h^\xi \propto n_{\text{sample}}^{-1/(d_\xi+2)}. \tag{4.40}$$

This scaling relation conveys that, in the context of the reduced-basis approximation discussed in Section 4.3.3, with an increase in the number of singular value modes, and hence an increase in the dimensions of the parameter domain, $d_\xi = n_{\text{svd}}$, the resolution of the binned representation decreases, in the sense that the optimum bin size increases. This, of course, implies that, for a fixed sample size, the accuracy with which the probability distribution is represented decreases with an increase in number of considered singular value modes.

4.4 The inverse solver: Markov chain Monte Carlo sampling

The solution to the inverse problem (4.15) can generally not be computed analytically. On the one hand, for problems such as considered in this work, analytical solutions cannot be obtained due to the complexity of the forward model operator (4.11). On the other hand, the input data for the inverse problem, in particular the data space, is frequently available as sampled data rather than as an analytical probability density function.

In this work we will resort to sampling techniques to compute approximate solutions to the inverse problem. Specifically, we consider a Markov chain Monte Carlo method [190, 191] in the form of the Metropolis-Hastings algorithm [192, 193], which is a random walk sampler designed for problems where the dimensionality of the sampled space – in essence the number of uncertain model parameters – is high. In Section 4.4.1 we commence with the introduction of the Metropolis-Hastings algorithm as considered in this work. Next, in Section 4.4.2 we discuss the most prominent computational aspects related to the application of this algorithm for the computation of the posterior model parameters through the inverse problem (4.15).

4.4.1 The Metropolis-Hastings algorithm

The Metropolis-Hastings sampler that is used to solve the stochastic inverse problem is presented in Algorithm 2. From the definition of the inverse problem (4.15) and the associated Likelihood function (4.17) it can be seen that the input to the Metropolis-Hastings algorithm consists of probability densities for the prior information on the model parameters and for the observations in the data space, $\rho_M(\boldsymbol{m})$ and $\rho_D(\boldsymbol{d})$, respectively. In this work, the prior information is provided through Karhunen-Loève expansions for the considered spatial random fields; see Section 4.3.3. In the case that a large number of discrete-time pressure observations is available, this observational data is considered as a binned representation of the SVD-compressed data; see Section 4.3.3.

The Metropolis-Hastings algorithm is in essence a Monte Carlo method in which the model space is explored using a random walk procedure. The design of the random walk – which, amongst other aspects, involves the selection of an appropriate proposal distribution $\pi(\boldsymbol{m}_1, \boldsymbol{m}_2)$ and the specification of how many samples to reject in order to ensure independence between the realizations – is of essential importance for the effectivity and efficiency of the sampler. The design of the random walk will be discussed in Section 4.4.2.

Besides the random walk procedure, the other key ingredient of the Metropolis-Hastings algorithm is the acceptance condition for a proposed realization, $\boldsymbol{m}_{\text{proposal}}$.

Input: $\rho_M(\boldsymbol{m})$, $\rho_D(\boldsymbol{d})$ `#prior distribution, data`
$\pi(\boldsymbol{m}_1 \mid \boldsymbol{m}_2)$, n_{mc}, $n_{\text{burn-in}}$, n_{lag} `#numerical parameters`

Output: $\sigma_M(\boldsymbol{m}) \sim \{\boldsymbol{m}_i\}_{i=1}^{n_{\text{sample}}}$, $\{\boldsymbol{d}_i\}_{i=1}^{n_{\text{sample}}}$ `#posterior distribution`

`#initialization`
$\boldsymbol{m}_0 =$ `sample_distribution(`$\rho_M(\boldsymbol{m})$`)` `#random walk starting point`

`#MCMC loop`
for i **in** $\{1, \ldots, n_{\text{mc}}\}$**:**

`#sample from the proposal distribution`
$\boldsymbol{m}_{\text{proposal}} =$ `sample_distribution(`$\pi(\boldsymbol{m}|\boldsymbol{m}_{i-1})$`)`

`#evaluate the forward operator, Eq.` (4.11)
$\boldsymbol{d}_{\text{proposal}} = \boldsymbol{g}(\boldsymbol{m}_{\text{proposal}})$

`#evaluate the proposal likelihood, Eq.` (4.17)
$L_{\text{proposal}} = \rho_D(\boldsymbol{d}_{\text{proposal}})$

`#evaluate the proposal acceptance probability`
$r = \frac{\rho_M(\boldsymbol{m}_{\text{proposal}})}{\rho_M(\boldsymbol{m}_{i-1})} \frac{L_{\text{proposal}}}{L_{i-1}} \frac{\pi(\boldsymbol{m}_{i-1}|\boldsymbol{m}_{\text{proposal}})}{\pi(\boldsymbol{m}_{\text{proposal}}|\boldsymbol{m}_{i-1})}$ **if** $i > 1$ **else** 1

if $r \geq$ `sample_distribution(`$\mathcal{U}(0,1)$`)`**:**
`#accept the proposal`
$\boldsymbol{m}_i = \boldsymbol{m}_{\text{proposal}}$

`#store the data`
$\boldsymbol{d}_i = \boldsymbol{d}_{\text{proposal}}$

`#store the likelihood`
$L_i = L_{\text{proposal}}$
else
`#repeat the previous step`
$\boldsymbol{m}_i = \boldsymbol{m}_{i-1}$
$\boldsymbol{d}_i = \boldsymbol{d}_{i-1}$
$L_i = L_{i-1}$
end
end

`#removing burn-in and thinning`
$\{\boldsymbol{m}_i\}_{i=1}^{n_{\text{sample}}}$, $\{\boldsymbol{d}_i\}_{i=1}^{n_{\text{sample}}} =$ `thin_sample(`$\{\boldsymbol{m}_i\}_{i=n_{\text{burn-in}}}^{n_{\text{mc}}}$, $\{\boldsymbol{d}_i\}_{i=n_{\text{burn-in}}}^{n_{\text{mc}}}$, n_{lag}`)`

Algorithm 2: Metropolis-Hastings sampling algorithm

This proposal is randomly accepted when

$$\frac{\rho_M(\boldsymbol{m}_{\text{proposal}})}{\rho_M(\boldsymbol{m}_{\imath-1})}\frac{L_{\text{proposal}}}{L_{\imath-1}}\frac{\pi(\boldsymbol{m}_{\imath-1}|\boldsymbol{m}_{\text{proposal}})}{\pi(\boldsymbol{m}_{\text{proposal}}|\boldsymbol{m}_{\imath-1})} > P, \tag{4.41}$$

with P a realization of the uniform distribution $\mathcal{U}(0,1)$ on the unit interval, and with $L_{\text{proposal}} = g(\boldsymbol{m}_{\text{proposal}})$ and $L_{\imath-1} = g(\boldsymbol{m}_{\imath-1})$. This acceptance condition conveys that the chance of a proposal being accepted is related to the likelihood of the proposal. Details regarding the evaluation of the likelihood in the algorithm will be discussed in Section 4.4.2.

The output of Algorithm 2 consists of a sample of realizations of the posterior probability distribution for the model space, $\sigma_M(\boldsymbol{m})$, *i.e.*, $\{\boldsymbol{m}_\imath\}_{\imath=1}^{n_{\text{sample}}}$, where the number of realizations n_{sample} is, in general, significantly smaller than the length of the Markov chain, n_{mc}, on account of the post-processing operations performed to remove initialization effects and auto-correlation effects (see Section 4.4.2 for details). A further discussion on the sample size will be presented in Section 4.4.2.

In addition to the sampling of the model space, the algorithm also provides a sampling of the data space, $\{\boldsymbol{d}_\imath\}_{\imath=1}^{n_{\text{sample}}}$. Recall that this data space encompasses both the observational data *and* the derived quantities of interest on which no observations are available (see Section 4.3).

Remark 4.3 (The posterior normalization factor (4.18))**.** *An important aspect of the Metropolis-Hastings algorithm is that the normalization constant k for the posterior distribution* (4.15) *does not need to be computed, as it cancels out in the acceptance condition* (4.41)*. This is important, as evaluation of k is generally computationally demanding.*

Remark 4.4 (Symmetry of the proposal distribution)**.** *In the case of a symmetric proposal distribution,* i.e.*, $\pi(\boldsymbol{m}_1|\boldsymbol{m}_2) = \pi(\boldsymbol{m}_2|\boldsymbol{m}_1)$, for example in the form of a normal distribution centered around the latest accepted realization, the ratio of proposal distribution densities in* (4.41) *equates to one.*

4.4.2 Algorithmic aspects

Design of the random walk

The efficiency with which the model space is explored depends strongly on the design of the random walk. The random walk considered herein is based on the construction of a multi-variate, uncorrelated, normal proposal distribution centered around the previous realization, $\boldsymbol{\mu}_{\text{proposal}} = \boldsymbol{m}_{\imath-1}$, and with covariance $\boldsymbol{\Sigma}_{\text{proposal}} = \text{diag}(\boldsymbol{\sigma}^2_{\text{proposal}})$ with user-specified standard deviation $\boldsymbol{\sigma}_{\text{proposal}}$ per model parameter, so that the proposal probability density conforms to:

$$\pi(\boldsymbol{m}|\boldsymbol{m}_{\imath-1}) \sim \mathcal{N}\left(\boldsymbol{m}_{\imath-1}, \boldsymbol{\Sigma}_{\text{proposal}}\right) \tag{4.42}$$

The covariance of the proposal distribution governs the size of the steps in the random walk. Selection of an appropriate step size in the random walk process is a difficult, and problem-specific, task. Taking the covariance too large will result in large steps in the walk, which results in detours through the empty regions in the model space, resulting in large rejection rates with respect to the condition (4.41). Taking the proposal covariance too small will lead to correlation between subsequent realizations in the model space, thereby leading to faulty results. In order to attain uncorrelated samples, accepted proposals are only incorporated in the sample every once in $n_{\text{lag}} \geq 1$ times. In Algorithm 2, this so-called thinning of the sample is considered by the post-processing operation `thin_sample` with parameter n_{lag}.

Small steps in the random walk procedure are also potentially problematic with respect to the starting position of the random walk, $\boldsymbol{m}_0$, which is sampled directly from the prior distribution. The initial steps in the procedure will generally not follow the posterior distribution, which implies that a significant number of proposals that satisfy (4.41) should be rejected at the start of the procedure. In our algorithm this so-called burn-in period is controlled by the parameter $n_{\text{burn-in}}$.

Evaluation of the Likelihood function

The likelihood of a proposal, $\boldsymbol{m}_{\text{proposal}}$, is evaluated as the probability density associated with the corresponding data proposal, $\boldsymbol{d}_{\text{proposal}}$, which is determined using the forward model operator (4.11). When the observable data consists of multiple observations on the pressure process, $\tilde{p}(t)$, it is represented in the data space by the SVD-compressed coordinate $\tilde{\boldsymbol{\xi}} \in \mathbb{R}^{n_{\text{svd}}}$, *i.e.*, $\boldsymbol{d} = \{\tilde{\boldsymbol{\xi}}\}$ (see Section 4.3.3). To evaluate the likelihood of the proposal, $\rho_D(\boldsymbol{d}_{\text{proposal}})$, the time-discrete proposal pressure, $\boldsymbol{p} \in \mathbb{R}^{n_t}$, is first projected onto the reduced coordinate $\boldsymbol{\xi} \in \mathbb{R}^{n_{\text{svd}}}$ using equation (4.33), after which the corresponding probability density is obtained as a lookup in the binned representation of $\rho_D(\boldsymbol{d})$.

Convergence of the Markov chain: the effective sample size

Algorithm 2 generates Markov chains of length n_{mc}. As already discussed in Section 4.4.2, the random walk has an effect on the accuracy of the posterior and on the efficiency of the algorithm (*i.e.*, on the rejection rate). The parameters $n_{\text{burn-in}}$ and n_{lag} provide control over the accuracy and efficiency of the algorithm. To assess the accuracy of the posterior distribution provided by the Markov chain Monte Carlo method, we conduct two post-processing procedures, *viz.*: a convergence check based on the Gelman and Rubin diagnostic tool [194, 195], and an auto-correlation check and related estimate of the effective sample size [196, 197].

Both above-mentioned post-processing procedures are discussed below based on a random quantity of interest, $\tilde{Q} = Q(\tilde{\boldsymbol{m}})$, that can be deduced from the model parameters. It is noted, however, that these procedures can be generalized for the case of multiple quantities of interest.

The Gelman-Rubin convergence diagnostic Let us denote the Markov chain of length n_{mc} resulting from Algorithm 2 by $\mathcal{C}$. The Gelman-Rubin convergence diagnostic provides a convergence measure based on the comparison of within-chain and between-chain variances for $n_{\mathcal{C}}$ independently (*i.e.*, with different starting positions) generated chains, $\{\mathcal{C}_\alpha\}_{\alpha=1}^{n_{\mathcal{C}}}$ of length n_{mc}.

Denoting the quantity of interest at step $\imath$ of chain α by $Q_{\alpha\imath}$, the within-chain variance of the parameter $\tilde{Q}$ is estimated by

$$W = \frac{1}{n_{\mathcal{C}}} \sum_{\alpha=1}^{n_{\mathcal{C}}} \sigma_\alpha^2, \tag{4.43}$$

with chain variance $\sigma_\alpha^2 = \frac{1}{n_{\mathrm{mc}}-1} \sum_{\imath=1}^{n_{\mathrm{mc}}} \left(Q_{\alpha\imath} - \mu_\alpha\right)^2$ and chain mean $\mu_\alpha = \frac{1}{n_{\mathrm{mc}}} \sum_{\imath=1}^{n_{\mathrm{mc}}} Q_{\alpha\imath}$. The between-chain variance can be estimated by

$$B = \frac{n_{\mathrm{mc}}}{n_{\mathcal{C}} - 1} \sum_{\alpha=1}^{n_{\mathcal{C}}} \left(\mu_\alpha - \mu\right)^2, \tag{4.44}$$

with aggregated mean estimator $\mu = \frac{1}{n_{\mathcal{C}}} \sum_{\alpha=1}^{n_{\mathcal{C}}} \mu_\alpha$.

The variance of $\tilde{Q}$ can then be estimated as $\sigma^2 = \frac{n_{\mathrm{mc}}-1}{n_{\mathrm{mc}}} W + \frac{n_{\mathcal{C}}+1}{n_{\mathcal{C}} n_{\mathrm{mc}}} B$ [194], from which an adequate measure for convergence of the Markov chain can be derived in the form of the potential scale reduction factor (PSRF):

$$R = \frac{\sigma^2}{W} = \frac{n_{\mathrm{mc}} - 1}{n_{\mathrm{mc}}} + \frac{n_{\mathcal{C}} + 1}{n_{\mathcal{C}} n_{\mathrm{mc}}} \frac{B}{W} \tag{4.45}$$

This reduction factor converges to one when the chains, $\{\mathcal{C}_\alpha\}_{\alpha=1}^{n_{\mathcal{C}}}$, converge to the posterior distribution on account of the between-chain variance, B, going to zero.

In our simulations we use the Gelman-Rubin diagnostic in the form of a plot of the PSRF versus the number of Markov chain steps primarily to assess the appropriateness of the burn-in size, $n_{\mathrm{burn-in}}$. Specifically, we verify that after $n_{\mathrm{burn-in}}$ steps, the PSRF is close to one (typically within 5%). If this is indeed the case, it is concluded that the burn-in size was selected appropriately. Otherwise, the diagnostic will provide a means to reassess the selection of the burn-in size. When, based on the PSRF, the chains are concluded to be converged, the $n_{\mathcal{C}}$ chains can be aggregated. From a computational effort point of view, a disadvantage of this diagnostic is, however, that $n_{\mathrm{burn-in}}$ realizations are omitted from each chain.

Auto-correlation check and effective sample size The accuracy of the Markov chain can be assessed based on the mean value estimator for the quantity of interest

$$\mu = \frac{1}{n_{\text{sample}}} \sum_{\imath=1}^{n_{\text{sample}}} Q_\imath, \tag{4.46}$$

the mean and variation of which can be estimated by

$$\mu_\mu = \mu \qquad\qquad \sigma_\mu^2 = \frac{\sigma^2}{n_{\text{eff}}}, \tag{4.47}$$

with the variation of the estimator of the quantity of interest given by $\sigma^2 = \frac{1}{n_{\text{sample}}-1} \sum_{\imath=1}^{n_{\text{sample}}} (Q_\imath - \mu)^2$, and n_{eff} denoting the effective sample size. Using (4.47) the confidence level, C_μ, for the mean estimator (4.46) can be related to the effective sample size by [198]

$$\Phi\left(\frac{\sqrt{n_{\text{eff}}}}{V}(1 - C_\mu)\right) = \frac{1 + C_\mu}{2}, \tag{4.48}$$

where Φ is the cumulative density function of a standard normal random variable, and $V = \sigma/\mu$ is the coefficient of variation of the quantity of interest.

In Markov chain Monte Carlo methods, the effective sample size n_{eff} is typically smaller than the actual sample size n_{sample}, on account of the fact that the realizations in the chain are not completely uncorrelated and hence realizations must be discarded to restore independence. An estimate of the effective sample size is given by (see Ref. [196, 197] for details)

$$n_{\text{eff}} = \frac{n_{\text{sample}}}{1 + 2\sum_{\ell=1}^{\ell_{\max}} \rho_\ell} \tag{4.49}$$

with ρ_ℓ the lag-ℓ auto-correlation of the quantity of interest (with $1 \ll \ell_{\max} \ll n_{\text{sample}}$), defined as

$$\rho_\ell = \frac{1}{\sigma^2} \frac{1}{(n_{\text{sample}} - \ell)} \sum_{\imath=1}^{n_{\text{sample}}-\ell} (Q_\imath - \mu)(Q_{\imath+\ell} - \mu). \tag{4.50}$$

The definition (4.49) conveys that if the lag-ℓ correlation vanishes sufficiently fast, the effective size remains close to the actual sample size. In the limiting case of an uncorrelated sample, $n_{\text{eff}} = n_{\text{sample}}$. In the case that there is correlation within the sample, $n_{\text{eff}} < n_{\text{sample}}$.

As discussed above, auto-correlation within the sample can be controlled by thinning the sample, *i.e.*, by selecting every n_{lag}-th value. This thinning operation

Plane strain modulus	E'	61.3×10^9	Pa
Leak-off coefficient	c_l	9.84×10^{-6}	$\mathrm{m/s^{1/2}}$
Fracture height	H	51.8	m
Viscosity	μ_f	2.00×10^{-1}	Pa.s
Injection rate	i	6.62×10^{-2}	$\mathrm{m^3/s}$
Injection time	T	12.0×10^3	s

Table 4.1: Simulation data used for the deterministic model validation

would reduce the auto-correlation on the one hand, but would simultaneously reduce the sample size by a factor of n_{lag}. These two effects compete with each other in terms of the effective sample size, which implies that one has to properly assess the effect of thinning on the effective sample size.

4.5 Numerical simulations

In this section we demonstrate the capabilities of the developed uncertainty quantification framework for the simulation of fluid-driven fracture propagation. In Section 4.5.1 we first assess the adequacy of the PKN model and the associated solution procedure in a deterministic setting. Subsequently, we consider the uncertainty quantification framework based on synthetically created pressure observations for two scenarios, *viz.*: a data-abundant scenario and a data-scant scenario. The data-abundant scenario – for which parameters are inferred from multiple pressure observations – is motivated and studied in Section 4.5.2. The data-scant setting – which is based on a single pressure observation – is then considered in Section 4.5.3.

4.5.1 Deterministic PKN model simulation

Before we proceed with the numerical demonstration of the Bayesian inference framework, we first study the numerical solution of the deterministic forward model. In order to assess the accuracy of the numerical model presented in Section 4.2, we consider the benchmark case presented by Warpinski et al. [199], the model parameters of which are collected in Table 4.1.

In Figure 4.2 we show the pressure in the fracture and fracture aperture for various time instances. The illustrated results are based on a time step size of $\Delta t = 1\,[\mathrm{s}]$, such that the complete fracture evolution process is solved in $n_t = 12 \times 10^3$ steps. On a single core desktop computer a typical simulation takes a few seconds, where the majority of the computational effort is attributed

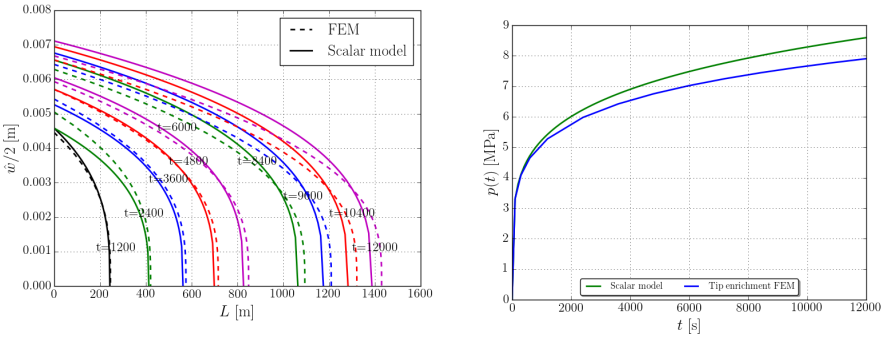

(a) **(b)**

Figure 4.2: Comparison of the scalar model proposed in Section 4.2.2 with the high-fidelity finite element model in Ref. [95] based on the evolution of (a) the fracture aperture and (b) the pressure in the fracture.

to the evaluation of the weak-form integrals using element-wise Gauss quadrature rules. The results obtained using the enriched finite element method of Ref. [95] using resolved spatial grid sizes and time step sizes is shown for comparison. This comparison conveys that the simplified model of Section 4.2.2 approximates the initial boundary value problem (4.2) well, in the sense that the obtained results are within 10% of those obtained using the high-fidelity finite element solver over the complete time interval. Qualitatively the simplified model captures the fracture behavior well. For reference we note that the high-fidelity FEM results require approximately 11 minutes per simulation on an Intel Core i5 vPro processor.

In Figure 4.3 we compare the time evolution of the fracture length and fracture opening at the inlet with the results presented in the benchmark study of Ref. [199] and the finite-element results of [95]. The results obtained using the scalar model of Section 4.2.2 closely resemble the finite element results, as well as the benchmark results. It is noted though that significant differences exist between the solvers considered in the benchmark study [199], which is due to both differences in modeling assumptions and method accuracy. In the context of uncertainty quantification it is important to note that the model uncertainties do influence the inferred results. Although we have herein assumed model inadequacies to be negligible, the Bayesian framework does, in principle, facilitate the consideration of model uncertainties. Although not considered in the current work, the results of the benchmark study by Warpinski et al. [199] do motivate to take such model inadequacies into account.

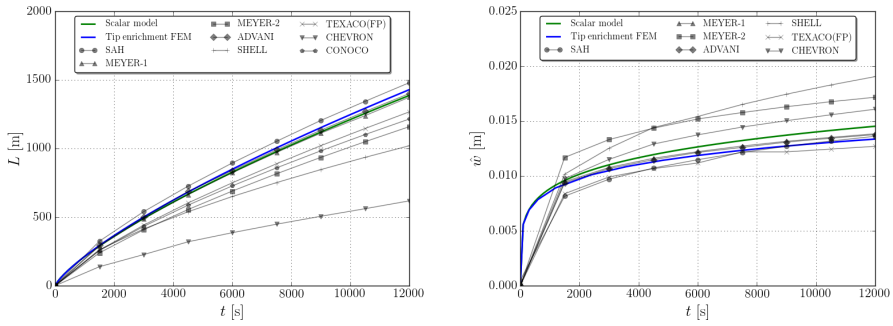

Figure 4.3: Comparison of the scalar model results with the benchmark studies reported by Warpinski et al. [199] and FEM results of [95] for (a) the evolution of the fracture length, and (b) the time response of the opening of the fracture at the fluid inlet.

4.5.2 Bayesian inference: the data-abundant scenario

In hydraulic fracturing it is typical that a large number of wells is drilled in an oil or gas field. For example, an extreme case with 162,000 wells in a reservoir of approximately 168,000 square kilometers, and with well-densities going as high as 56 wells per square kilometer, has been reported [200]. Typically, for each well in a reservoir, the pressure is recorded while injecting volume. Based on these observations, the Bayesian inference framework can be used to quantify the elastic properties of the entire reservoir, and to predict quantities of interest such as fracture propagation distances. We refer to this setting of the Bayesian inference framework as the *data-abundant scenario*.

Because in this scenario all wells correspond to the same field and their separation is assumed to be large relative to the heterogeneity of the field, the well properties can be conceived of as independent and identically distributed (i.i.d.) random parameters. It is assumed that the length scale associated with a single well, *i.e.*, the typical length of a hydraulic fracture, is of the same order as the length scale associated with the dominant spatial variations in the elastic properties of the field. Correspondingly, for each well the elastic field is conceived of as an i.i.d. spatially-correlated random field characterized by a mean, a standard deviation, and an auto-correlation length.

Since we do not have real data, we content ourselves with synthetic data. This synthetic data is manufactured by assuming the parameters of the random heterogeneous field for the elastic properties to be known, as to generate a plane

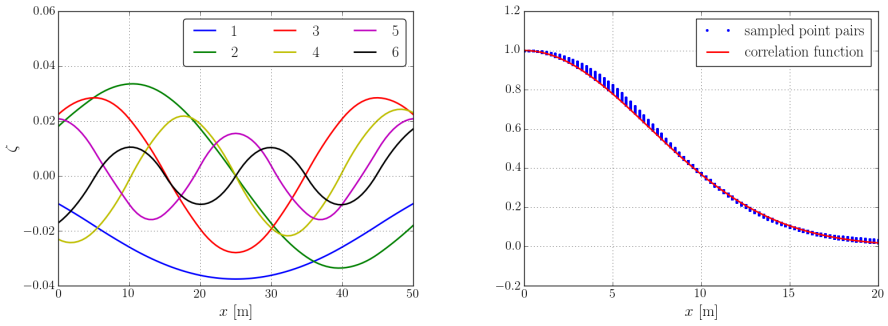

(a) **(b)**

Figure 4.4: A Karhunen-Loéve expansion is used to represent the random field for the plane strain modulus. (a) The Karhunen-Loève modes of the underlying Gaussian random field (4.20) and (b) the original and reconstructed auto-correlation function (4.50) for the random field for the plane strain modulus.

strain modulus field for each well. The forward model is then evaluated to attain pressure observations for all wells. Let us note that this manufactured-data setting can also be used for the verification of the implementation of the Bayesian inference framework, as the attained posterior distribution can be compared to the random fields for the model parameters from which the manufactured data is constructed.

For the data-abundant scenario we consider fracture evolution over a time interval of $T = 100\,[\mathrm{s}]$ in order to limit computation time. Corresponding to this time interval, the random field of elastic properties, $\tilde{E}'(x)$, is defined over the domain $[0, 50]\,[\mathrm{m}]$. The field is characterized by a log-normal random field with mean $\mu_{E'} = 90\,[\mathrm{GPa}]$, standard deviation $\sigma_{E'} = 4.5\,[\mathrm{GPa}]$ (such that the coefficient of variation is $V_{E'} = 5 \times 10^{-2}$), and with a correlation length of $l_{E'} = 10\,[\mathrm{m}]$ in correspondence with the auto-correlation function (4.50). For the construction of the synthetic data, we employ $n_{kl} = 6$ Karhunen-Loève terms for the discretization of this random field. The Karhunen-Loève modes and reconstructed auto-correlation function are displayed in Figure 4.4, from which it is observed that using $n_{kl} = 6$ modes, the auto-correlation structure of the random field is approximated well. In the remainder of this section, all other parameters are assumed to be deterministic, with their values as listed in Table 4.1.

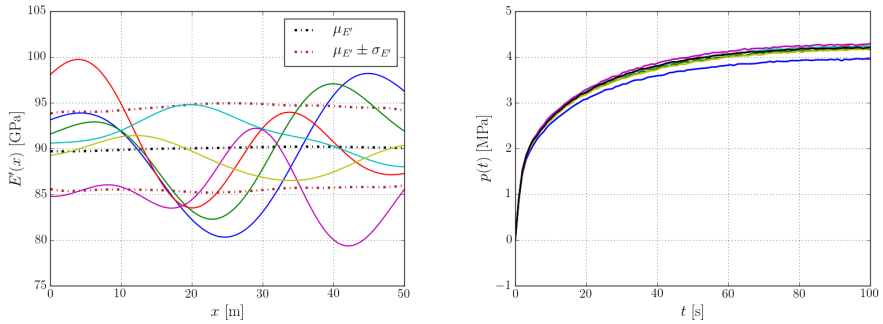

(a) **(b)**

Figure 4.5: Synthetic data is generated by sampling (a) realizations of the plane strain modulus and subsequently using the forward model to compute (b) the corresponding pressure observations. White noise is added to the pressure data to mimic measurement errors. Only a selection of the observations is displayed.

Synthetic data generation: forward uncertainty propagation

To construct synthetic data for the Bayesian inference framework we sample $n_p = 500$ realizations from the random field of elastic properties, and solve the forward model discussed in Section 4.2.2 with a time step size of $\Delta t = 1\,[\mathrm{s}]$ to obtain n_p discrete pressure signals of length $n_t = 100$. White noise with a standard deviation of $9\,[\mathrm{kPa}]$ is added to the computed pressure signals yielding a sequence of n_p noisy pressure signals, $\{\boldsymbol{p}_i\}_{i=1}^{n_p} \subset \mathbb{R}^{n_t}$.

Figure 4.5 displays instances of the sampled random fields and corresponding random pressure observations, along with their mean values and standard deviations. Note that, in accordance with its properties, the white noise in the pressure signals does not influence the mean of the pressure observations.

With the computation of the synthetically created pressure observations, we also obtain corresponding samples of the fracture length and fracture aperture. Although we will not use these derived quantities as observations in the Bayesian inference framework, they will be used to assess the quality of the attained posterior distributions.

Uncertainty quantification using Bayesian inference

Based on the manufactured pressure signal data we can now employ the Metropolis-Hastings algorithm to infer the uncertainties in the model parameters, *i.e.*, the random field for the plane strain modulus. We will discuss this inference procedure in three steps, *viz.*: *(i)* the construction of the likelihood function (4.17)

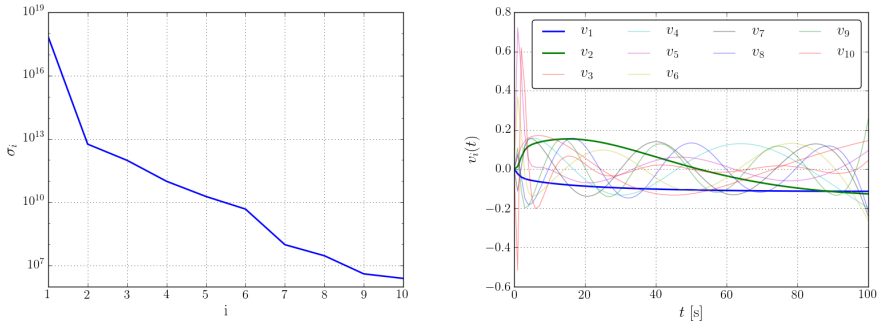

(a) **(b)**

Figure 4.6: (a) Singular values and (b) singular modes used for the reduced-basis approximation of the synthetically generated pressure data. Only the first 10 modes are displayed. For the inversion, only modes $v_1(t)$ and $v_2(t)$ are used.

based on the pressure observations; *(ii)* the postulation of the prior information on the uncertain model parameters and the inference of the posterior; and *(iii)* the uncertainty quantification of the derived quantities of interest.

(i) Construction of the likelihood function As discussed in Section 4.3.3 it is beneficial to represent random processes in low dimensional parameter spaces. We therefore employ the reduced-basis method discussed in Section 4.3.3 to represent the pressure observations shown in Figure 4.5b. Figure 4.6 displays the singular values and singular modes computed based on the set of $n_p = 500$ pressure observations. In correspondence with (4.36), by selecting the modes corresponding to the $n_{\text{svd}} = 2$ largest singular values, the relative ensemble error is bounded from above by $\epsilon = 2.5 \times 10^{-3}$. Let us note that the modes $v_i(t)$ are displayed in Figure 4.6 as time-dependent functions, but represented as vectors $\boldsymbol{v}_i$ in accordance with the discretization of the pressure output; see Section 4.3.3.

Figure 4.7 shows a selection of the noisy pressure observations and their corresponding reconstructed values based on the reduced-basis method with two modes. The comparison between the original and reconstructed signals clearly demonstrates the noise-filtering property of the singular value decomposition. The low dimensional representations of the pressure observations provide excellent approximations to the noise-filtered original data.

Figure 4.8a shows the pressure observations in the reduced-basis domain, *i.e.* Figure 4.8a displays the coefficients $\{\xi_{i1},\ \xi_{i2}\}$ of the reduced-basis approximations $\boldsymbol{p}_i \approx \xi_{i1}\boldsymbol{v}_1 + \xi_{i2}\boldsymbol{v}_2$ of the pressure data relative to the reduce basis vectors $\boldsymbol{v}_1$ and $\boldsymbol{v}_2$ in Figure 4.6b. Hence, each point in Figure 4.8a (accurately) rep-

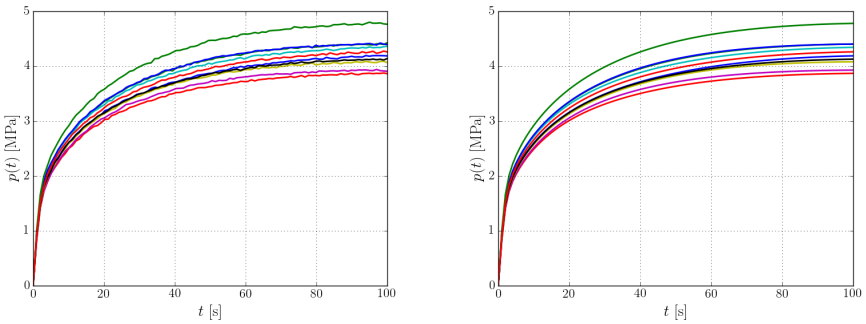

Figure 4.7: A selection of (a) the original noisy synthetic pressure observations, and (b) the corresponding signals reconstructed using $n_{\text{svd}} = 2$ singular modes.

resents a noise-filtered pressure observation. In accordance with the bin size selection discussed in Section 4.3.3, we define the reduced parameter domain as $[-41.14, -32.51] \times [-0.33, 0.27]\,[\text{MPa}]^2$ and subdivide it into 23×23 bins of equal size. Figure 4.8b displays the binned likelihood function for the pressure observations, which will serve as the basis to infer the model uncertainties.

(ii) Prior postulation and inference of posterior distributions To demonstrate the Bayesian inference framework we postulate a prior that is significantly different from the model parameters used to generate the synthetic data. More specifically, we consider as prior information a log-normal random field for the plane strain modulus with a mean of $\mu_{E',\text{prior}} = 50\,[\text{GPa}]$, a standard deviation of $\sigma_{E',\text{prior}} = 25\,[\text{GPa}]$ (such that the coefficient of variation is equal to $V_{E',\text{prior}} = 0.5$), and a spatial correlation length of $l_{E',\text{prior}} = 10\,[\text{m}]$. Note that the mean of this prior information field has a significant offset with respect to that of the expected outcome, and that the coefficient of variation is significantly larger than that of the outcome. The increased variation of this prior reduces its information content. Let us also note that we have treated the correlation length as specified deterministic data and have set its prior value $l_{E',\text{prior}}$ in accordance with that of the synthetic data. Alternatively, however, the correlation length can also be treated as an uncertain parameter.

We consider $n_{kl} = 3$ Karhunen-Loève modes to represent the prior for the plane-strain modulus field. This implies that the uncertainty in the system is parametrized by n_{kl} random variables, $\{\tilde{z}_\alpha\}_{\alpha=1}^{n_{kl}}$, in accordance with the expansion (4.24). In the prior state, these random variables are taken as independent standard normal random variables, which will lead to a close resemblance of the

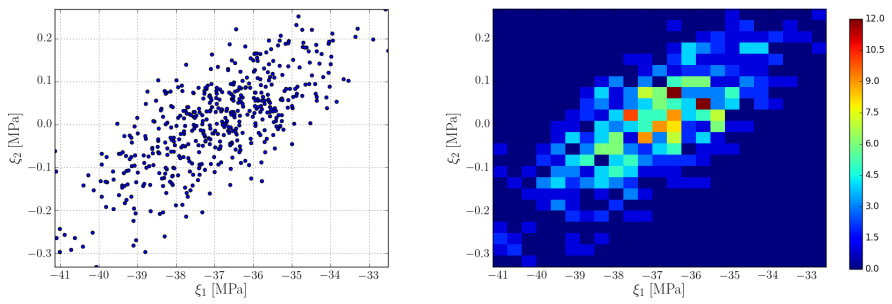

(a) **(b)**

Figure 4.8: (a) Pressure observations visualized on the reduced-basis coordinates and (b) the binned likelihood function corresponding to the pressure observations.

Mean plane-strain modulus $\tilde{E}'$	$\mu_{E',\text{prior}}$	50×10^9	Pa
Coefficient of variation	$V_{E',\text{prior}}$	0.5	–
Markov chain size	n_{mc}	5×10^3	–
Standard deviation of proposal distribution	$\sigma_{\tilde{z}_\alpha,\text{proposal}}$	0.35	–
Correlation length of plane-strain modulus	$l_{E'}$	10	m
Number of KL modes	n_{kl}	3	–

Table 4.2: Numerical parameters of the Metropolis-Hastings algorithm as used for the data-abundant synthetic data study

intended prior random field. The distribution of these random variables is updated in the inference process in accordance with the likelihood. Let us note that the mean of the Karhunen-Loève expansion is not included in the inference process. We have opted to disregard the mean, to investigate to what extent the KL modes are capable of approximating the distribution of the plane-strain-modulus field of the synthetic data.

Using the likelihood for the pressure observations and the prior for the uncertain plane strain modulus field as input, the Metropolis-Hastings algorithm is used to compute the posterior plane strain modulus field. The numerical parameters used for this algorithm are listed in Table 4.2. An n_{kl}-variate Gaussian proposal distribution with covariance $0.35^2 \times \boldsymbol{I}$ is selected. Since the standard deviation associated with this proposal is small in comparison to that of the prior information (which is unity by construction), this implies that relatively small steps are made in the random walk.

Panel (a) of Figure 4.9 shows the projection of the random walk $\{\tilde{\boldsymbol{z}}_1, \tilde{\boldsymbol{z}}_2, \ldots\}$ in the model parameter coordinates on the (z_1, z_2)-plane. Panel 4.9b shows the

corresponding random walk in the reduced-basis coordinates associated with the likelihood function. These figures convey that the random walk, which starts at a realization sampled from the prior distribution, gradually moves toward the region of high likelihood. Due to the discrepancy between the prior distribution and the likelihood, the random walk initially traverses an area of the (ξ_1, ξ_2)-plane that is non-realizable according to the likelihood, i.e. a region outside of the support of the likelihood. In the model parameter coordinates, this region is associated with a significant offset from the prior mean at $\boldsymbol{z} = \boldsymbol{0}$. From the random walk it is immediately observed that it takes a significant number of steps to move from the starting point toward the region of high likelihood, which is an indicator for the burn-in period.

Figures 4.10 and 4.11 present diagnostics of the Markov chains. In Figure 4.10a we study the potential scale reduction factor (PSRF) according to (4.45) based on 3 Markov chains. Panel 4.10b presents the z_1 components of the sequence of samples corresponding to the three chains. The PSRF becomes stationary in the sense that it stays within 5% of unity after approximately 3×10^2 realizations, indicating that a burn-in period of approximately $n_{\text{burn-in}} = 3 \times 10^2$ steps is required. From Figure 4.10b it can be observed that up to $n_{\text{burn-in}}$, the Markov chains display a significant dependence on the starting point. Figure 4.11a displays the sample auto-correlation function according to (4.50). The figure shows that the correlation between two realizations $\tilde{\boldsymbol{z}}_\imath$ and $\tilde{\boldsymbol{z}}_\jmath$ in the Markov chain is significant if the lag $|\imath - \jmath|$ is small. Based on the auto-correlation in Figure 4.11a, the sample sequence is thinned by using a lag interval $n_{\text{lag}} = 134$, thus reducing the auto-correlation between the retained samples to ≤ 0.2. Figure 4.11b plots the auto-correlation of the thinned sequence versus the lag. The figure conveys that for the thinned sequence, the auto-correlation is essentially independent of the lag and that its absolute value is indeed bounded by 0.2. Based on the effective sample size for auto-correlated sequences (4.49), we estimate that, in conjunction with the thinning procedure and the burn-in removal, the effective sample size corresponding to the three considered chains is equal to 212. This implies that approximately 70 forward-model solves are required for each member of the final sequence of realizations.

After thinning the Markov chain to account for the burn-in period and auto-correlation lag, a random walk is obtained that samples the posterior distribution, *i.e.* the random walk generates a sequence of identically distributed random variables conforming to the posterior probability distribution. Figure 4.12 displays the posterior marginals obtained by binning the components z_1, z_2, z_3 of the 212 realizations in the thinned sequence. The prior distribution of the coefficients, *viz.* the standard normal distribution $\mathcal{N}(0, 1)$, is displayed for comparison. This figure conveys that, based on the data, a significant shift in the random model parameters is induced from their respective prior distributions in order to provide

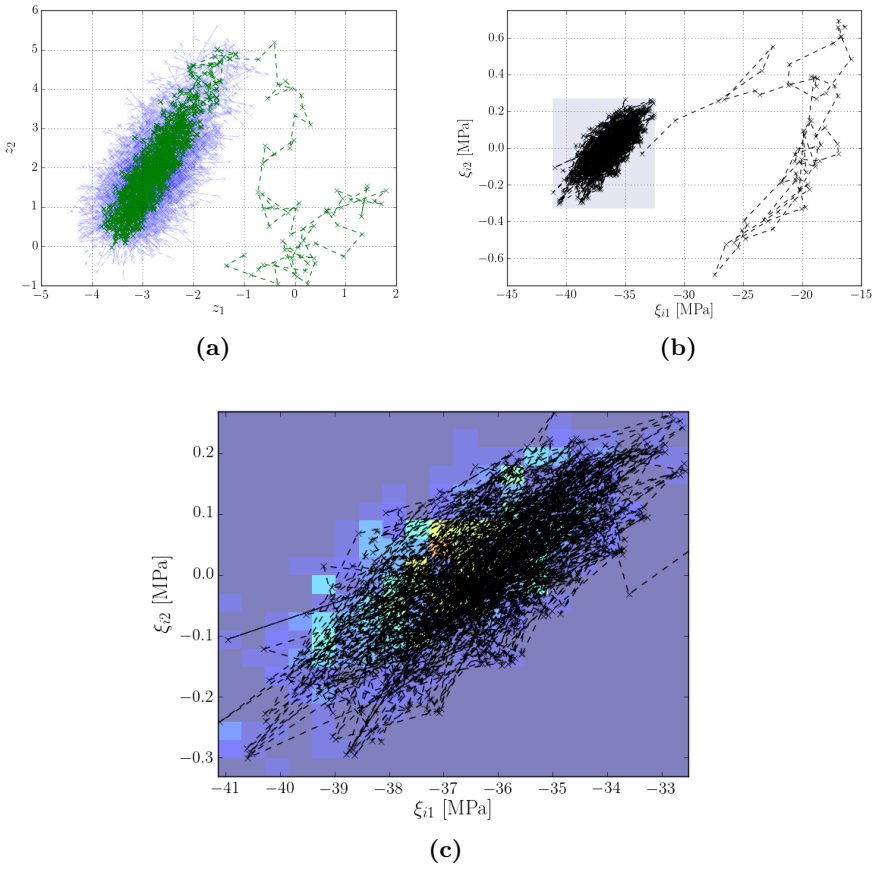

Figure 4.9: Random walk for the Bayesian inversion process before burn-in removal and thinning: (a) The model parameter coordinates representing the plane strain modulus field. The accepted proposals are plotted in green, whereas the rejected proposals are plotted in blue; (b) The reduced-basis coordinates for the pressure observations showing only the accepted proposals; Panel (c) provides a zoom of (b) in the support of the likelihood function. The likelihood function is displayed for reference in the background of the pressure-observation plot in Panel (c).

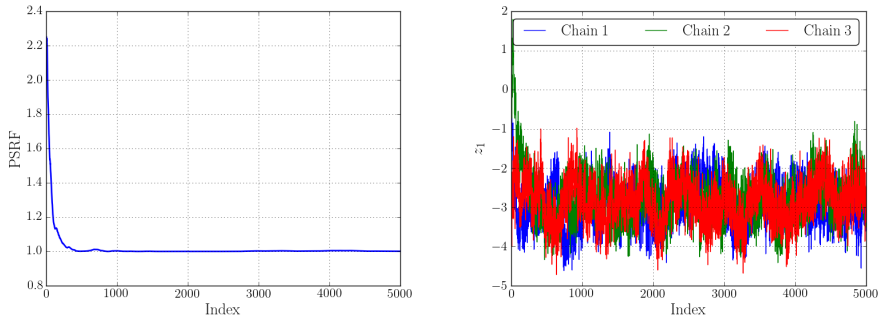

(a) **(b)**

Figure 4.10: Random walk diagnostic in the form of (a) the potential scale reduction factor (PSRF) and (b) trace plot of the z_1 parameter for multiple chains.

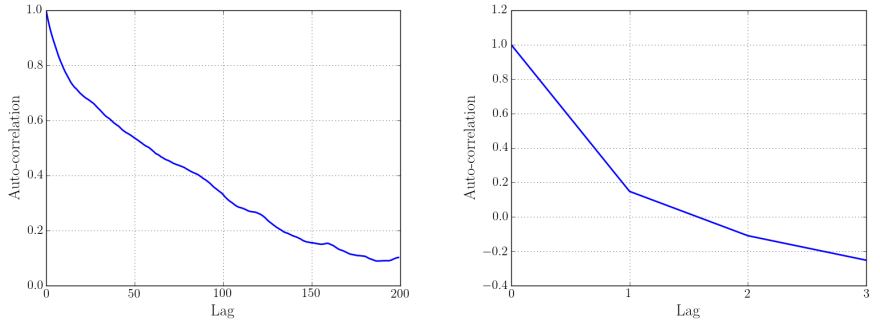

(a) **(b)**

Figure 4.11: Random walk diagnostics in the form of (a) auto-correlation and (b) auto-correlation after thinning for a lag of 134.

a closer match with the distribution of the pressure observations.

Figure 4.13 displays the mean and standard deviation of the posterior random field corresponding to Figure 4.12. This figure conveys that the plane strain modulus field exhibits significant spatial variations, while the field used to generate the synthetic data is spatially uniform. The spatial average of the posterior mean plane strain modulus is equal to 112 GPa with a standard deviation of 21 GPa (such that the coefficient of variation is equal to 0.19), which indicates that the pressure data improves upon the prior information ($\mu_{E',\text{prior}} = 50\,[\text{GPa}]$ and $V_{E',\text{prior}} = 0.5$) in a spatially-averaged sense. The spatial variations in the plane-strain modulus can be attributed to the fact that the three considered KL modes (*cf.* Figure 4.4a) do not enable a spatially-uniform shift of the mean plane strain modulus. As a result, substantial spatial variations in the posterior field are attained in the inference process. To improve the inferred posterior, the number of modes should be increased or an alternative representation of the random field should be employed.

(iii) Uncertainty quantification of fracture length and aperture In the process of the Bayesian inference procedure, also the probability distributions for the derived quantities of interest are generated by post-processing operations on the forward model evaluations. In the context of fluid-driven fracture propagation, two natural quantities of interest to consider are the fracture length and the fracture aperture.

In Figure 4.14 we consider the time evolution of the fracture length and fracture aperture, where we show the mean value and the standard deviation over time. Figure 4.15 presents an alternate view of the quantities of interest based on the histograms for the fracture aperture at the inflow and the fracture length at the final time $T = 100\,[\text{s}]$. The reference results computed in the construction of the synthetic data are shown for comparison in Figure 4.15. As can be seen, the uncertainty quantification framework is capable of finding a reasonable match to the reference results by using the pressure observations, despite the (deliberate) poor prior information and the restriction to three Karhunen-Loève modes, excluding the mean (note that 6 KL modes were used to generate the synthetic data). A closer match can be achieved by providing the model with a better informed prior or by extending the model by including additional random parameters, *e.g.* the mean of the posterior distribution or additional Karhunen-Loève modes.

4.5.3 Bayesian inference: the data-scant scenario

We now consider the scenario of a fracture-stimulation operation in a single well. In this so-called *data-scant scenario*, only a single pressure observation is avail-

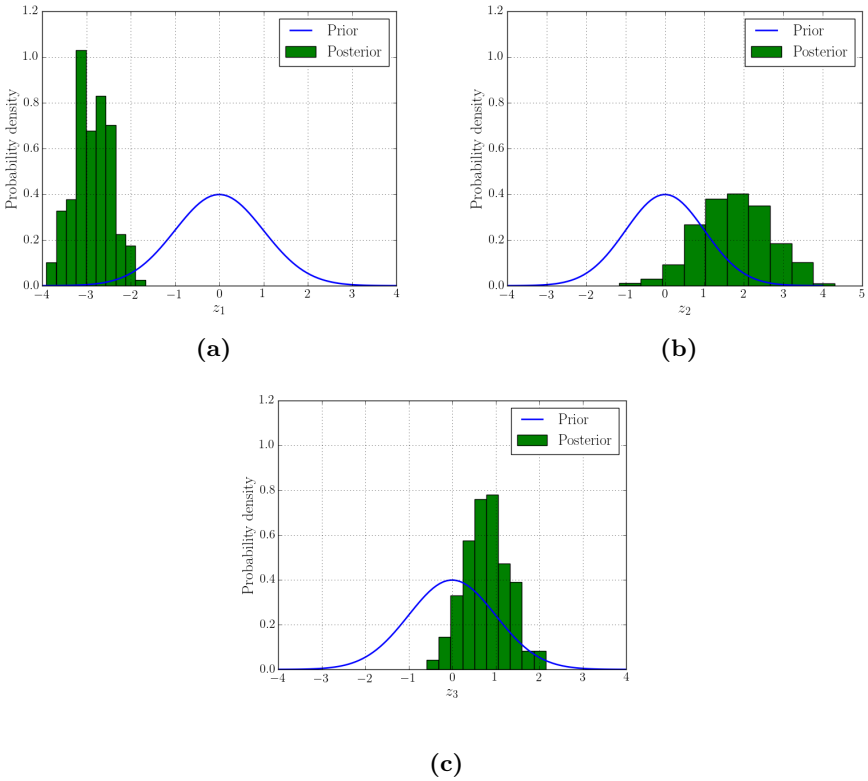

Figure 4.12: Binned representation of the marginal posterior distributions for the coefficients of the Karhunen-Loève expansion. The blue curves represent the prior distribution of the coefficients, $\mathcal{N}(0,1)$. Note that because of the different KL discretizations used for the synthetic data and for the prior/posterior, the observational data is not shown in this plot.

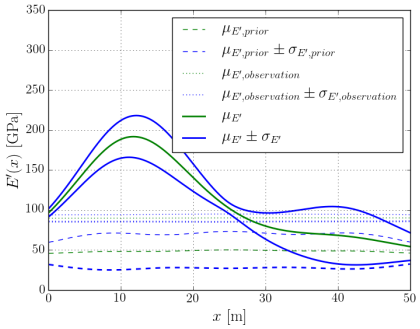

Figure 4.13: Mean $\mu_{E'}$ and confidence interval $\mu_{E'} \pm \sigma_{E'}$ of the posterior and prior distributions of the plane-strain-modulus field. The observation of the elastic field pertains to the synthetically created data.

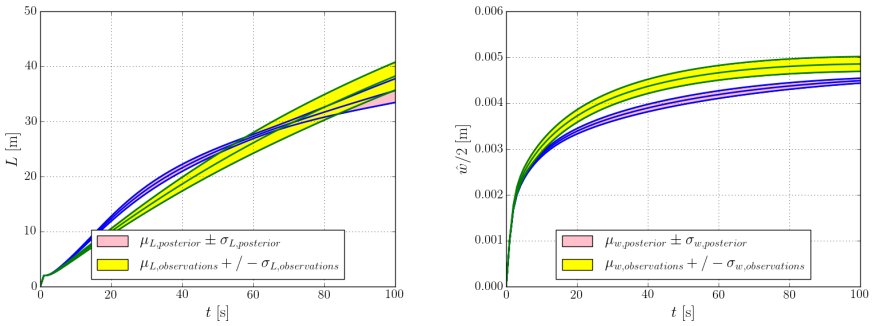

(a) **(b)**

Figure 4.14: Evolution of the mean and standard deviation of (a) the fracture length and (b) the fracture aperture at the inflow boundary obtained from the uncertainty quantification framework.

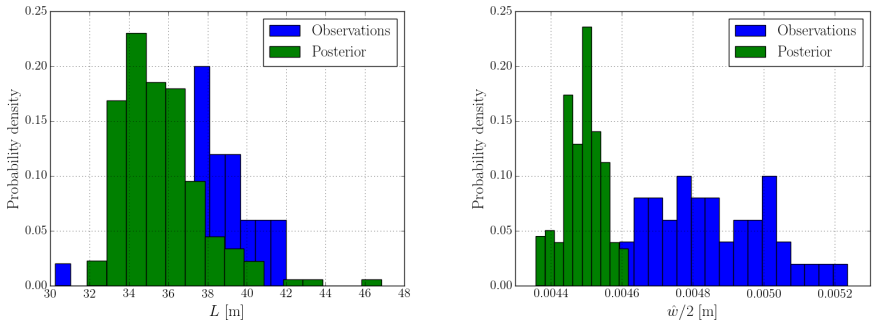

(a) **(b)**

Figure 4.15: Probability density functions at time $T = 100\,[\mathrm{s}]$ for (a) the fracture length, (b) the fracture aperture. The manufactured reference data is shown for comparison.

able. The objective of the Bayesian inference problem is to quantify the unknown subsurface properties and to infer the attained fracture propagation length for this single-well operation.

In contrast to the data-abundant (multiple-well) scenario of Section 4.5.2, in the case of a single well, we assume there to be one true, but unknown, heterogeneous field of elastic properties. Since we do not have real data, we synthesize this true field by selection of a realization of a log-normal random field with $\mu_{E'} = 90\,[\mathrm{GPa}]$, standard deviation $\sigma_{E'} = 4.5\,[\mathrm{GPa}]$, and auto-correlation length $l_{E'} = 10\,[\mathrm{m}]$. As for the data-abundant scenario, an injection interval of $T = 100\,[\mathrm{s}]$ is considered, such that it suffices to construct a random field of elastic properties over the interval $[0{,}50]\,[\mathrm{m}]$ using a Karhunen-Loève expansion with 6 modes. The constructed true elastic field is shown in Figure 4.16a. Note that high wave-number modes are removed from this heterogeneous field by virtue of the smoothness of the KL-representation.

Synthetic data generation: measurement noise

The pressure observation is generated by solving the forward problem with time steps of $\Delta t = 1\,[\mathrm{s}]$ based on the true elastic field $E'(x)$. Note that this forward simulation also provides us with the true fracture opening and length. White noise with a standard deviation of σ_{noise} is added to the discrete pressure function computed by the forward model as to obtain a single synthetic discrete pressure signal $\boldsymbol{p}_{\mathrm{obs}} \in \mathbb{R}^{n_t}$ containing experimental noise. This pressure signal is shown in Figure 4.16b for various noise levels.

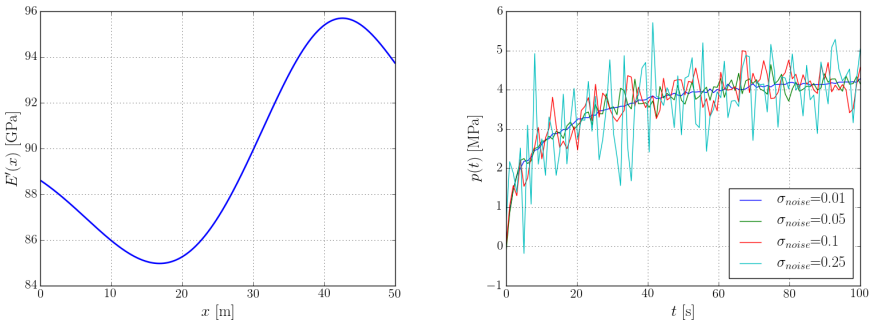

(a) **(b)**

Figure 4.16: (a) The "true" plane strain modulus considered in the data-scant scenario. (b) The synthetically generated pressure signal for various noise levels.

Uncertainty quantification using Bayesian inference

We again consider the same three steps in the uncertainty quantification procedure as outlined in Section 4.5.2:

(i) Construction of the likelihood function The construction of the likelihood function in the data-scant setting considered here is fundamentally different from that considered in the data-abundant scenario. Instead of forming the likelihood based on multiple pressure observations, it is postulated that the likelihood for a given model $\boldsymbol{m}_i$ with corresponding pressure signal $\boldsymbol{p}_i$ is given by (see, e.g., [60]):

$$\begin{aligned} L_i &= \prod_{i=1}^{n_t} \frac{1}{\sqrt{(2\pi)}\sigma_{\text{noise}}} \exp\left(-\frac{(p_{i,i} - p_{\text{obs},i})^2}{2\sigma_{\text{noise}}^2}\right) \\ &= \frac{1}{\sqrt{(2\pi)^{n_t}}\sigma_{\text{noise}}^{n_t}} \exp\left(-\frac{(\boldsymbol{p}_i - \boldsymbol{p}_{\text{obs}})^T(\boldsymbol{p}_i - \boldsymbol{p}_{\text{obs}})}{2\sigma_{\text{noise}}^2}\right) \end{aligned} \tag{4.51}$$

Since this likelihood function involves a product of n_t probabilities, it will typically be very small. In order to avoid underflow of the floating point representation of the likelihood function, the log-likelihood function is considered instead:

$$\ln(L_i) = -\frac{n_t}{2}\ln(2\pi) - n_t \ln(\sigma_{\text{noise}}) - \frac{(\boldsymbol{p}_i - \boldsymbol{p}_{\text{obs}})^T(\boldsymbol{p}_i - \boldsymbol{p}_{\text{obs}})}{2\sigma_{\text{noise}}^2}$$

Note that the acceptance condition (4.41) is also considered in its logarithmic form as to effectively make use of this log representation of the likelihood.

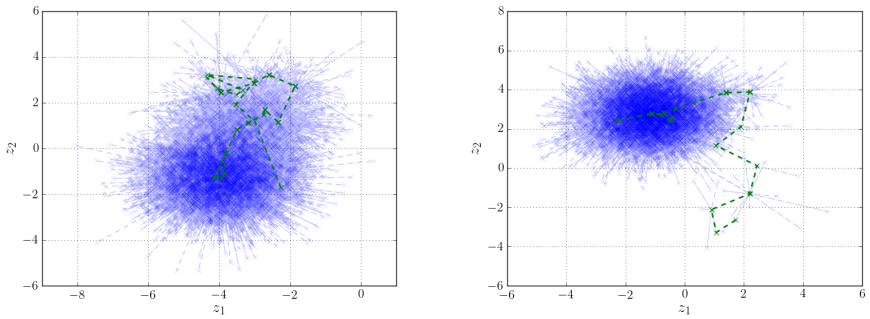

(a) $\sigma_{\text{noise}} = 1\%$ **(b)** $\sigma_{\text{noise}} = 5\%$

Figure 4.17: Random walk for the inversion procedure in the data-scant scenario for two different noise levels before burn-in removal and thinning. The figures display both the accepted (in green) and the rejected (in blue) proposals for a chain of length 10^4. Note that the previously accepted sample is retained in the chain upon rejection (see Algorithm 2), so that the accepted points in the above plots in general have a multiplicity greater than one.

(ii) Prior postulation and inference of the posterior distributions We consider the same prior information for the plane strain modulus field as for the data-abundant scenario, *i.e.*, a log-normal random field with mean $\mu_{E'} = 50\,[\text{GPa}]$, standard deviation $\sigma_{E'} = 25\,[\text{GPa}]$, and auto-correlation length $l_{E'} = 10\,[\text{m}]$. This prior field and the inferred posterior are discretized using $n_{kl} = 3$ Karhunen-Loève modes. A Gaussian proposal distribution with covariance $\boldsymbol{I} \in \mathbb{R}^{n_{kl} \times n_{kl}}$ is considered, which is relatively high in comparison to that considered for the data-abundant case. The reason for selecting this higher proposal variation is to limit the burn-in period for all considered noise levels. We note that this comes at the expense of having a high rejection rate once the region in which the majority of the mass of the likelihood function resides is reached.

Figure 4.17 shows the random walk for two different noise levels ($\sigma_{\text{noise}} = 1\%$ and $\sigma_{\text{noise}} = 5\%$) in the (z_1, z_2)-plane. The plot shows all 10^4 proposed samples of a single chain, *i.e.*, both accepted and rejected. The observed clustering of the samples is in accordance with the expected shifts in the random variables of the Karhunen-Loève discretization, very similar to that observed for the data-abundant case. The observed spread depends on the selected proposal distribution, and is hence similar for the two noise levels.

Figure 4.18 displays the diagnostics for 4 chains of length 10^4 for the case of 1 percent noise. From Figure 4.18a it is observed that the PSRF becomes stationary (deviation from unity of less than 5%) at approximately 500 realizations,

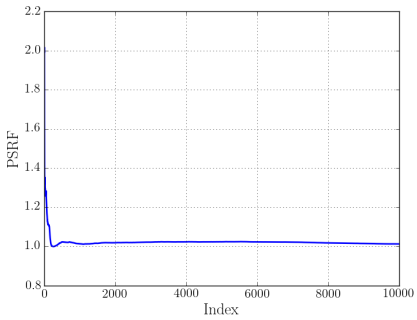

(a) PSRF

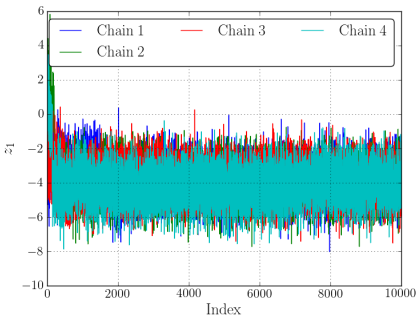

(b) Trace plot

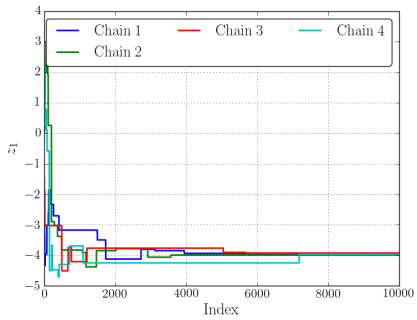

(c) Trace plot of the accepted samples

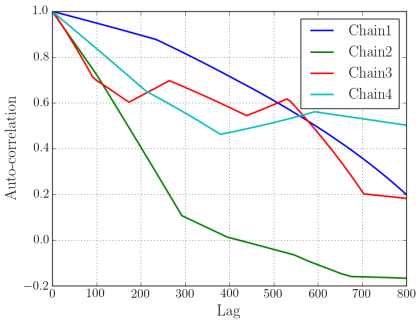

(d) Auto-correlation of the original chain

Figure 4.18: Random walk diagnostics for the data-scant simulation with 1 percent noise based on 4 chains with 10^4 realizations.

which is a proper indication for the required burn-in size. This burn-in period is also observable from the trace plots shown in Figure 4.18b and Figure 4.18c. Figure 4.18d displays the auto-correlation of the samples versus lag, indicating a significant lag of, for example, approximately 800 samples for chain 1 (note that the lag of chain 4 exceeds the lag range of the auto-correlation plot). This lag is explained by the fact that the variation of the employed proposal distribution is very large compared to that of the posterior. As a consequence, once the region of high-likelihood is reached, it is very unlikely to accept proposals. The effective sample size after burn-in removal and thinning of the 4 chains combined is equal to 61 for the case of 1 percent noise, and 107 for 5 percent noise.

The posterior distributions of the random variables $\boldsymbol{z}$ are displayed in Figure 4.19 for the 1% noise case and in Figure 4.20 for the 5% noise case. Both cases

show a posterior shift similar to that observed in the data-abundant scenario. The corresponding moments of the posterior distributions are shown in Figure 4.21. For the 1% noise case the spatially-averaged mean is equal to 151 [Gpa] (with a coefficient of variation 0.13), and for the 5% noise case the spatially-averaged mean is 88 [GPa] (with a coefficient of variation of 0.28). The synthetically generated plane strain modulus has a spatial average of 90 [GPa]. In a spatially-averaged sense, the posterior plane strain modulus thus significantly improves upon the prior information for the 5% noise case. For the 1% noise case the spatially-averaged posterior significantly overestimates the true plane strain modulus. As for the data-abundant case, substantial spatial fluctuations in the moments of the posterior plane strain modulus field emerge on account of the inability of the three employed KL modes to represent a spatially-uniform shift. In particular in the 1% noise case this results in substantial deviations from the synthetic data. The difference in noise level is reflected in these plots by the increased standard deviation of the posterior plane strain modulus field for the 5% noise case. Note, however, that due to the high rejection rate of the sampling procedure, the obtained posterior distributions are still under-sampled.

(iii) Uncertainty quantification of fracture length and aperture Figure 4.22 finally shows the mean and standard deviation of the fracture length and the fracture aperture at the well. It is observed that for both noise levels the inference process based on the synthetically-generated noisy pressure data is capable of attaining a reasonable approximation of the real fracture length and fracture aperture, despite the poorly-informed prior. The influence of the noise is also observed in the considered quantities of interest, as the standard deviation is higher for the moderate noise level than for the low noise level.

4.6 Conclusions

Based on a prototypical model for fluid-driven fracture propagation, the Perkins-Kern-Nordgren (PKN) model, we have developed an uncertainty quantification (UQ) framework for hydraulic fracturing based on the theory of Bayesian inference. The developed framework has the ability to systematically combine prior information on the uncertain model parameters (most notably the reservoir properties) with observational data (most importantly well pressures and injection rates).

Application of Bayesian UQ to the considered problem class requires the information, both in the prior and in the observations, to be represented in forms that are adequate in relation to the employed stochastic inverse solver. In this work, we consider a representation of the random fields for the reservoir properties via a

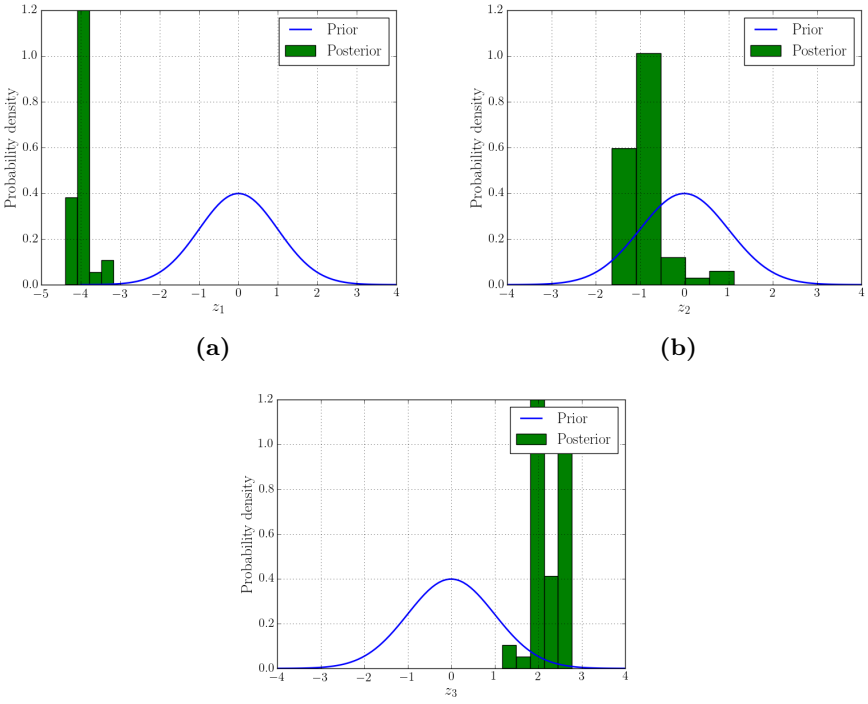

Figure 4.19: Binned representation of the marginal posterior distributions for the coefficients of the Karhunen-Loève expansion at 1% noise.

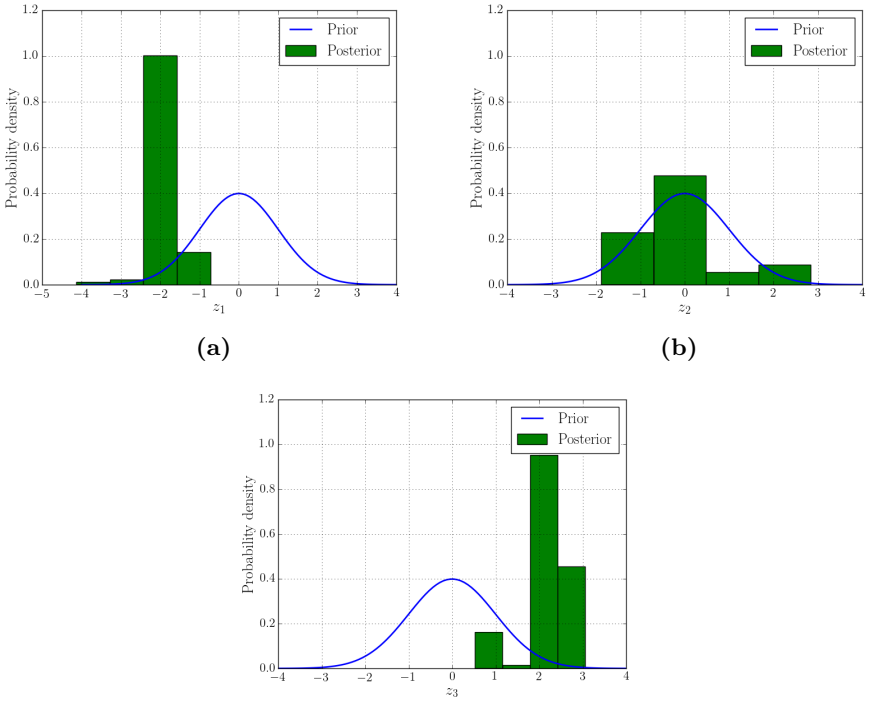

Figure 4.20: Binned representation of the marginal posterior distributions for the coefficients of the Karhunen-Loève expansion at 5% noise.

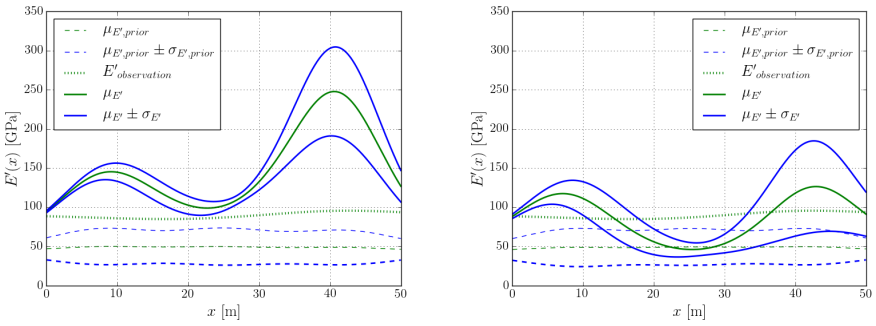

(a) 1% noise **(b)** 5% noise

Figure 4.21: Mean $\mu_{E'}$ and confidence interval $\mu_{E'} \pm \sigma_{E'}$ of the posterior and prior distributions of the plane-strain-modulus field for the data-scant scenario with two different noise levels.

Karhunen-Loève expansion. A reduced-basis representation based on the singular value decomposition was considered for the low-dimensional parametrization of the time-dependent pressure observations.

As a stochastic inverse solver to infer the model uncertainties we have considered the Metropolis-Hastings algorithm, which is a Markov chain Monte Carlo method that naturally fits the Bayesian inference setting. In essence, the Metropolis-Hastings algorithm can be directly applied to the considered problem, but several aspects have to be considered in order to render the solver effective and efficient, *viz.*:

(i) The forward model should be computationally efficient, as the sampler typically requires a large number of forward model evaluations. We have considered an assumed-mode Galerkin discretization in space to achieve this.

(ii) The initial part of the random walk, referred to as the burn-in period, must be discarded from the sample as this initial part does not follow the posterior distribution. We employ the Gelman and Rubin diagnostic tool to assess the burn-in period.

(iii) The steps in the random walk must be sufficiently large to ensure independence between the accepted realizations. We consider the sample auto-correlation to assess this independence and apply an acceptance lag to remove auto-correlation if needed.

The uncertainty quantification framework has been tested using two scenarios with synthetic data. In the first scenario the elastic properties of a reservoir

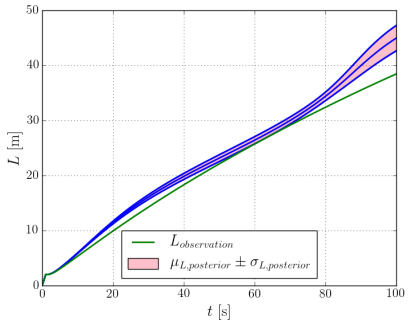

(a) 1% noise

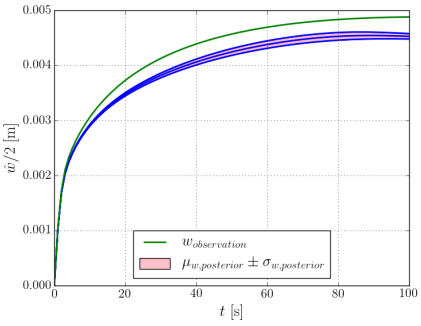

(b) 1% noise

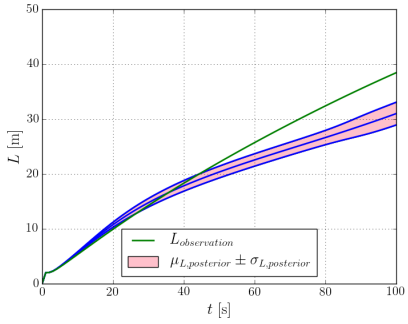

(c) 5% noise

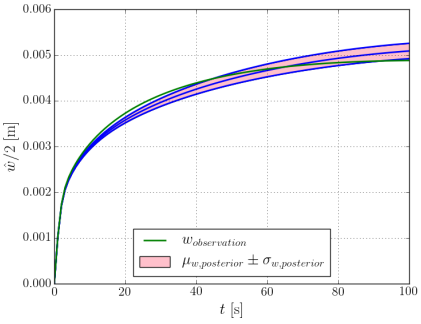

(d) 5% noise

Figure 4.22: Evolution of the mean and standard deviation of the fracture length and the fracture aperture at the inflow boundary obtained from the uncertainty quantification framework.

are inferred based on multiple well observations. This so-called *data-abundant* scenario corresponds to the typical hydraulic stimulation setting in which a large number of wells is present in a reservoir, and a large number of experimental observations is available. The second scenario pertains to the consideration of a single well. In this so-called *data-scant* scenario only a single pressure observation is available for the inference process of the elastic properties in the reservoir near the well. The proposed UQ framework is applicable to both scenarios, with the most substantial difference being the construction of the likelihood from the observations.

For both considered scenarios the Bayesian-inference process was deliberately provided with an ill-informed prior to assess the robustness of the method. The results convey that in a spatially-averaged sense the plane strain modulus can be inferred by combining prior information with pressure observations. However, the inability of the considered low-dimensional Karhunen-Loève expansion to represent a spatially-uniform shift of the elastic properties, results in substantial spatial fluctuations in the inferred elastic field. To improve the posterior elastic field, the number of KL modes should be increased or an alternative representation of the random field should be considered.

Application of the framework to real data sets is part of ongoing work. Although the presented framework can be applied in an identical manner to real pressure observations, an aspect to carefully regard is that the employed forward model should appropriately capture the essential influences of the model parameters on the observational outcomes. The suitability of the PKN model to uncertainty quantification based on real data is questionable in this regard. On the other hand, the present investigation underscores the importance of model efficiency, as in the Markov chain Monte-Carlo method many forward problems must be solved for each effective realization, typically 100:1 in the present study.

In relation to the general suitability of the PKN model, it would be preferable if one would have a class of models of varying complexity available. Model selection can then be treated as an integral part of the UQ framework [60], which has the potential to only use more sophisticated (computationally intensive) models when needed, and resort to simpler (computationally cheap) models otherwise. Such a hierarchical consideration of models can improve the UQ framework both in terms of accuracy and in terms of computational effort.

Chapter 5

Conclusions & recommendations

Pressure-driven fracture processes are surrounded by uncertainties, particularly in the context of subsurface engineering, where available information on reservoir properties is typically scant. There is a strong need to quantitatively analyze such processes, as such analyses are instrumental to risk assessment and operational optimizations. The uncertainty quantification framework developed in this dissertation – which specifically targets the systematic combination of prior information, observed data, and mathematical-physical models – provides a computational analysis tool for the quantitative assessment of pressure-driven fracture processes.

In Section 5.1 we draw conclusions from the work discussed in this dissertation, after which we discuss the recommendations and topics for further study in Section 5.2.

5.1 Conclusions

In a typical pressure-driven fracture process in subsurface engineering, uncertainties pertain primarily to reservoir properties, as observations on such parameters (especially away from a well) are not generally available. Some quantities of interest can be measured, such as injection pressures and volumes, but others, such as fracture geometries, are hard (and/or expensive) to monitor. Information on quantities of interest that are not directly measurable must therefore be inferred from the available data. Physical models are essential in this regard, as they bridge the gap between the uncertain quantities of interest and the observational data.

An uncertainty quantification framework capable of providing information on quantities of interest that are not directly measurable must contain the following components: *(i)* a mathematical-physical model capable of reliably mapping the system parameters onto output variables for both the uncertain quantities of interest and the measurement data; *(ii)* an inverse solver capable of inferring the uncertain system parameters from the observed system data; and *(iii)* a systematic way of reducing the complexity of the used models, as to enable the rapid evaluation of the mathematical physical model. Our conclusions regarding each of these components are discussed below.

The mathematical-physical model and forward uncertainty analysis In selecting a suitable mathematical-physical model for uncertainty quantification it is essential that the model is capable of adequately incorporating the prominent sources of uncertainty. Moreover, the model should be capable of deriving the quantities of interest – encompassing both the observables and the uncertain quantities of interest – from the model input. Based on these requirements we have considered the Perkins-Kern-Nordgren (PKN) model [29, 30] for planar fractures.

Although the PKN model is based on various limiting assumptions, most notably regarding the geometry of the fracture, high-fidelity solutions require the consideration of computational methods. The reason for this is that the model is time-dependent, has a moving boundary in the form of the evolving fracture, is non-linear, and has singular solution behavior in the vicinity of the fracture tip. We have herein proposed a finite element method to solve the PKN model.

In relation to uncertainty quantification it is essential that the errors with respect to the solution procedure do not pollute the stochastic response of the system. At the same time, the model should remain computationally tractable, as it is typically required to evaluate the model many times when uncertainty analysis is considered. Our results and the analysis thereof lead to the conclusion that it is necessary to enforce volume conservation through a Lagrange multiplier constraint, and that it is required to enrich the solution space with a tip function that mimics the singular behavior of the solution to strike the balance between accuracy and computational effort. Comparison of the proposed computational model with benchmark results presented in the literature indicates that some of the contemporary available models lack the accuracy required for consideration in a UQ context.

The proposed finite element discretization of the PKN model has been assessed in the context of a two-stage forward uncertainty analysis. In the first stage, the model is used to perform a sensitivity analysis of the model parameters, including random fields for the reservoir properties. In the second stage, a Monte Carlo analysis is performed to study the impact of the random input

parameters on the quantities of interest. An important insight derived from this study, is that the uncertainty analysis does not only yield information on the stochastic properties of the output, but it also elucidates the relation between the model-parameter realizations and particular system behavior.

Both types of stochastic analysis, *i.e.*, sensitivity analysis and Monte Carlo sampling, are considered to be non-intrusive, in the sense that they can be applied to existing solvers. Although alternative stochastic techniques, such as, *e.g.*, spectral stochastic finite elements, have the potential to enhance the efficiency of the forward uncertainty analysis, the non-intrusive character of such methods degrades their attractiveness.

The Bayesian inference method The forward stochastic analysis is an essential ingredient of the uncertainty quantification framework, but from a practical perspective the prior information on the model parameters, most notably the reservoir parameters, is frequently of insufficient quality to provide useful information on the quantities of interest. It is therefore essential that observational data can be integrated in the analysis, as to obtain quantitatively meaningful results. The Bayesian inference method provides a natural framework to incorporate such information.

In order to use the Bayesian update rule to combine prior information on the model parameters with measurement data into posterior model parameter probabilities, it is essential that the employed model can map the input data to the observables. In this regard, the considered PKN model is suitable for the incorporation of well observables such as pressures and injection rates. The model as considered here is not suitable for the incorporation of seismic data, as seismicity is not incorporated in the model. With respect to the incorporation of a large number of pressure measurements, it has been found to be important to represent the data observables in a low-dimensional stochastic space, as the dimensionality of that space impacts the accuracy with which the probabilistic information can be represented. An important conclusion we draw in this data-abundant setting is that the singular value decomposition is a powerful method for the representation of correlated signals, with the additional advantage that it naturally filters noise from the observations.

We have employed the Metropolis-Hastings algorithm to solve the stochastic inverse problem. This algorithm is a Markov-chain Monte Carlo (MCMC) method that naturally fits the Bayesian update rule. As for the forward uncertainty analysis, an advantage of the Metropolis-Hastings algorithm is that it is non-intrusive with respect to the computational model. A disadvantage of the method is that the involved sampling routine requires the evaluation of many forward problems. In order to be able to evaluate the posterior model information with reasonable computational effort, in the context of the Bayesian inference method

we have therefore considered a Ritz-Galerkin technique to attain the solution to the PKN model.

The Bayesian inference framework is tested using manufactured data, which allows us to assess the quality of the obtained posterior distribution. We have found that reliable posterior updates can be obtained, provided that the numerical parameters in the Metropolis-Hastings algorithm are selected adequately. In this regard it is particularly important to properly select the burn-in period for the random walk, as initial steps in the MCMC procedure do not follow the posterior distribution. Also thinning of the obtained sample can be important as to remove auto-correlation within the random walk and to reduce memory usage. We can conclude that the Bayesian framework we developed in combination with all these elements would help to improve the knowledge about the process parameters.

Reduced order modeling In relation to the uncertainty quantification for pressure-driven fractures, various assumptions made in relation to the PKN model limit its usability. Consideration of a full (three-dimensional) finite element model is impractical, however, on account of the computational effort involved when using such models in combination with Monte Carlo techniques. Reduced order modeling (ROM) techniques can be employed to generate model representations that appropriately balance computational effort and accuracy.

As a step toward the incorporation of ROMs in the developed uncertainty quantification framework, we have studied the possibilities of applying ROMs to fracture problems in specimens that are loaded on their external boundaries. We have found the online-offline paradigm provided by the proper generalized decomposition (PGD) method to be an ideal companion to the sampling-based techniques considered in this work, as realizations can be evaluated very quickly once the decomposition has been established in a (computationally intensive) pre-processing step.

An essential aspect of the application of the PGD technique to propagating fractures is the mapping between a reference domain in which the fracture is stationary and the physical domain in which the fracture propagates. This mapping has been demonstrated to enable high quality PGD approximations for the case of a horizontally propagating fracture. An advantageous property of the PGD approximation in the context of linear elastic fracture mechanics is that the fracture length is parametrized through the geometry mapping, which facilitates the (semi-)analytical evaluation of the energy release rate. In general, we conclude that the PGD setting we presented requires negligible computational effort when applied in a Monte Carlo setting when compared to the corresponding finite element simulations.

Extension of the PGD framework to more general classes of fracture problems is feasible to some extent, but will require the design of case-specific fracture geometry mappings. Although application of the PGD technique to geometrically complex fracture problems is not evident, this does not necessarily impede its application in the context of UQ, where the ROM can serve the purpose of a simplified surrogate model. Integration of the PGD technique in the UQ framework considered in this work requires the consideration of pressure-loaded fractures. Extension of the studied PGD framework is particularly challenging on account of the non-constant, and even singular, distribution of the pressure load in typical fluid-driven fracture problems.

Overall we conclude that uncertainty quantification for the typical setting of a pressure-driven fracture process, specifically in the context of subsurface engineering, requires the combination of prior information on the model parameters with observational data. The Bayesian inference inverse problem, which can be solved using Markov-chain Monte Carlo methods, provides a natural framework to combine these sources of information. The selection of the mathematical-physical model (and the associated solution strategy) used to relate the model parameters to the observable data is subject to requirements in terms of modeling accuracy and computational effort. In this regard the UQ framework should be combined with model order reduction techniques, as this offers the opportunity to select a (reduced) model with a tailored balance between accuracy and computational effort.

5.2 Recommendations & future research

The choice for the PKN model in this work is driven by the requirement to balance model versatility with computational feasibility in a many-query setting. Although the PKN model is of practical use, in the sense that it represents a relevant class of stimulation processes, the assumptions underlying this model do restrict its application to a limited range of pressure-driven fracture problems. Moreover, the PKN model in its natural form does not incorporate poromechanical reservoir behavior and seismicity, which prevents the usage of datasets based on tiltmeters and seismic data. In this regard (computational) models should be explored that are of a more generic character than the PKN model. One should bear in mind that, in the UQ context, these models should remain practical from a computational effort point of view. Moreover, their robustness, in the sense of the ability to find reliable solutions for a large range of model parameters, is of essence in the context of the considered sampling methods. Phase-field methods, which have been successfully demonstrated in the context of pressure-driven fracture processes over the past years [55–58], form a prominent class of models to be considered.

As already addressed above, reduced-order modeling would provide the user with the possibility to find a suitable balance between model accuracy and computational effort. Moreover, application of the online-offline paradigm is essential if the UQ framework is to be applied in real time. Our work on PGD for mechanically-driven fractures pioneers ROMs for fracture problems, and stipulates the need for extensive further research in this direction. In the UQ context, a minimally-intrusive reduced order modeling approach would be beneficial, as the ability to use existing solvers in combination with data would promote adoption of the proposed Bayesian framework. Currently, in terms of intrusiveness, the ROM is not up to par with the considered sampling-based solution strategy.

Both the development and consideration of more sophisticated models and the development of improved ROM functionality underline the most prominent restriction of the framework as it is currently considered, namely that there is only one mathematical-physical model, rather than a hierarchy of models. In the context of uncertainty quantification, methods have already been developed to accommodate model hierarchies [60, 201]. Such UQ strategies enhance the efficiency of the framework by selecting models based on their adequacy. Detailed models, which are generally computationally expensive, could only be used when the data indicates a need therefore, and simpler models (like PKN) would be considered otherwise.

Model hierarchies can also be used to improve the efficiency of the inverse solver. For example, a simple model can be used to translate an uninformative prior into a data-calibrated posterior. This posterior, which is considerably more informative than the original prior, would then be used as prior information for an inversion with a more advanced model. The better quality of the prior for the advanced model can be used to enhance the efficiency of the sampling method. Multi-level Monte Carlo techniques [202, 203] form another class of solution strategies that can enhance the efficiency of the framework.

Bibliography

[1] Zissis Moschovidis, Ronald Steiger, Richard Peterson, Norm Warpinski, Chris Wright, Ed Chesney, Joe Hagan, Ahmed Abou-Sayed, Richard Keck, and Matt Frankl. The mounds drill-cuttings injection field experiment: Final results and conclusions. In *IADC/SPE Drilling Conference*. Society of Petroleum Engineers, 2000.

[2] Francis H Harlow and William E Pracht. A theoretical study of geothermal energy extraction. *Journal of Geophysical Research*, 77(35):7038–7048, 1972.

[3] C Boschi, A Dini, L Dallai, G Ruggieri, and G Gianelli. Enhanced co2-mineral sequestration by cyclic hydraulic fracturing and si-rich fluid infiltration into serpentinites at malentrata (tuscany, italy). *Chemical Geology*, 265(1-2):209–226, 2009.

[4] Wiri Heo, Wonsuk Lee, and Dae Sung Lee. Hydraulic fracturing design for coalbed methane in barito basin, indonesia. *Geosystem Engineering*, 18(3):151–162, 2015.

[5] Quangui Li, Baiquan Lin, and Cheng Zhai. A new technique for preventing and controlling coal and gas outburst hazard with pulse hydraulic fracturing: a case study in yuwu coal mine, china. *Natural Hazards*, 75(3):2931–2946, 2015.

[6] Antonin Settari and Michael P Cleary. Three-dimensional simulation of hydraulic fracturing. *Journal of Petroleum Technology*, 36(07):1–177, 1984.

[7] L Vandamme and JH Curran. A three-dimensional hydraulic fracturing simulator. *International Journal for Numerical Methods in Engineering*, 28(4):909–927, 1989.

[8] BJ Carter, J Desroches, AR Ingraffea, and PA Wawrzynek. Simulating fully 3d hydraulic fracturing. *Modeling in geomechanics*, 200:525–557, 2000.

[9] J Adachi, E Siebrits, A Peirce, and J Desroches. Computer simulation of hydraulic fractures. *International Journal of Rock Mechanics and Mining Sciences*, 44(5):739–757, 2007.

[10] Lujun Ji, Antonin Settari, and Richard B Sullivan. A novel hydraulic fracturing model fully coupled with geomechanics and reservoir simulation. *Spe Journal*, 14(03):423–430, 2009.

[11] S Secchi and BA Schrefler. A method for 3-d hydraulic fracturing simulation. *International journal of fracture*, 178(1-2):245–258, 2012.

[12] Shawn Maxwell. Microseismic location uncertainty. *CSEG Recorder*, 34(4):41–46, 2009.

[13] Souleymane Zio and Fernando A Rochinha. A stochastic collocation approach for uncertainty quantification in hydraulic fracture numerical simulation. *International Journal for Uncertainty Quantification*, 2(2), 2012.

[14] Brice Lecampion, R Jeffrey, E Detournay, et al. Real-time bayesian inversion of hydraulic fracturing treatment efficiency from tiltmeter measurements. In *SPE Annual Technical Conference and Exhibition*. Society of Petroleum Engineers, 2004.

[15] B Lecampion and J Gunning. Model selection in fracture mapping from elastostatic data. *International journal of solids and structures*, 44(5):1391–1408, 2007.

[16] Pedro J Ballester and Jonathan N Carter. Tackling an inverse problem from the petroleum industry with a genetic algorithm for sampling. In *Genetic and Evolutionary Computation Conference*, pages 1299–1300. Springer, 2004.

[17] Rui Huang, Xiaodong Wu, Wang Ruihe, Changhao Xu, Lipeng Wang, Pengwei Xie, and Li Hui. A study of reservoir dynamic analysis method based on different injection profile in petroleum engineering. In *AASRI International Conference on Industrial Electronics and Applications (IEA 2015)*. Atlantis Press, 2015.

[18] Fernando Alves Rochinha and Anthony Peirce. Monitoring hydraulic fractures: state estimation using an extended kalman filter. *Inverse Problems*, 26(2):025009, 2010.

[19] Bob C Crittendon. The mechanics of design and interpretation of hydraulic fracture treatments. *Journal of petroleum technology*, 11(10):21–29, 1959.

[20] Eugene Harrison, WF Kieschnick Jr, and WJ McGuire. The mechanics of fracture induction and extension. 1954.

[21] George C Howard and CR Fast. Optimum fluid characteristics for fracture extension. In *Drilling and production practice*. American Petroleum Institute, 1957.

[22] M King Hubbert and David G Willis. Mechanics of hydraulic fracturing. 1972.

[23] Brice Lecampion, Andrew Bunger, and Xi Zhang. Numerical methods for hydraulic fracture propagation: a review of recent trends. *Journal of natural gas science and engineering*, 49:66–83, 2018.

[24] Emmanuel Detournay. Mechanics of hydraulic fractures. *Annual Review of Fluid Mechanics*, 48:311–339, 2016.

[25] J Adachi, E Siebrits, A Peirce, and J Desroches. Computer simulation of hydraulic fractures. *International Journal of Rock Mechanics and Mining Sciences*, 44(5):739–757, 2007.

[26] René de Borst. *Computational Methods for Fracture in Porous Media: Isogeometric and Extended Finite Element Methods*. Elsevier, 2017.

[27] Peter Valkó and Michael J Economides. *Hydraulic fracture mechanics*, volume 28. Wiley Chichester, 1995.

[28] Ian Naismith Sneddon. The distribution of stress in the neighbourhood of a crack in an elastic solid. *Proceedings of the Royal Society of London. Series A. Mathematical and Physical Sciences*, 187(1009):229–260, 1946.

[29] TK Perkins and LR Kern. Widths of hydraulic fractures. *Journal of Petroleum Technology*, 13(09):937–949, 1961.

[30] RP Nordgren. Propagation of a vertical hydraulic fracture. *Society of Petroleum Engineers Journal*, 12(04):306–314, 1972.

[31] Peter Valkó and MJ Economides. Propagation of hydraulically induced fractures – a continuum damage mechanics approach. In *International journal of rock mechanics and mining sciences & geomechanics abstracts*, volume 31, pages 221–229. Elsevier, 1994.

[32] A Khristianovic Zheltov. 3. formation of vertical fractures by means of highly viscous liquid. In *4th world petroleum congress*. World Petroleum Congress, 1955.

[33] J Geertsma and F De Klerk. A rapid method of predicting width and extent of hydraulically induced fractures. *Journal of petroleum technology*, 21(12):1–571, 1969.

[34] Antonin Settari and Michael P Cleary. Development and testing of a pseudo-three-dimensional model of hydraulic fracture geometry. *SPE Production Engineering*, 1(06):449–466, 1986.

[35] SH Advani, TS Lee, and JK Lee. Three-dimensional modeling of hydraulic fractures in layered media: part I - finite element formulations. *Journal of Energy Resources Technology*, 112(1):1–9, 1990.

[36] Bernhard A Schrefler, Stefano Secchi, and Luciano Simoni. On adaptive refinement techniques in multi-field problems including cohesive fracture. *Computer methods in applied mechanics and engineering*, 195(4-6):444–461, 2006.

[37] S Secchi, L Simoni, and BA Schrefler. Numerical procedure for discrete fracture propagation in porous materials. *Int J Numer Anal Methods Geomech*, 31:331–345, 2007.

[38] Julien Réthoré, Rene De Borst, and Marie-Angèle Abellan. A two-scale model for fluid flow in an unsaturated porous medium with cohesive cracks. *Computational Mechanics*, 42(2):227–238, 2008.

[39] MM Hossain, MK Rahman, and SS Rahman. Hydraulic fracture initiation and propagation: roles of wellbore trajectory, perforation and stress regimes. *Journal of Petroleum Science and Engineering*, 27(3-4):129–149, 2000.

[40] MM Rahman, MK Rahman, and SS Rahman. An integrated model for multiobjective design optimization of hydraulic fracturing. *Journal of Petroleum Science and Engineering*, 31(1):41–62, 2001.

[41] Norman R Warpinski, ZA Moschovidis, CD Parker, and IS Abou-Sayed. Comparison study of hydraulic fracturing models - test case: Gri staged field experiment no. 3 (includes associated paper 28158). *SPE Production & Facilities*, 9(01):7–16, 1994.

[42] AP Peirce and E Siebrits. A dual mesh multigrid preconditioner for the efficient solution of hydraulically driven fracture problems. *International journal for numerical methods in engineering*, 63(13):1797–1823, 2005.

[43] Donna Calhoun and Randall J LeVeque. A cartesian grid finite-volume method for the advection-diffusion equation in irregular geometries. *Journal of Computational Physics*, 157(1):143–180, 2000.

[44] JA Ryder and JAL Napier. Error analysis and design of a large-scale tabular mining stress analyser. In *Proceedings of the 5th International Conference on Numerical Methods in Geomechanics, Nagoya*, pages 1549–1555, 1985.

[45] Sunder H Advani and JK Lee. Finite element model simulations associated with hydraulic fracturing. *Society of Petroleum Engineers Journal*, 22(02):209–218, 1982.

[46] Axel KL Ng and John C Small. A case study of hydraulic fracturing using finite element methods. *Canadian geotechnical journal*, 36(5):861–875, 1999.

[47] Magnus Wangen. Finite element modeling of hydraulic fracturing on a reservoir scale in 2d. *Journal of Petroleum Science and Engineering*, 77(3-4):274–285, 2011.

[48] Brice Lecampion and Emmanuel Detournay. An implicit algorithm for the propagation of a hydraulic fracture with a fluid lag. *Computer Methods in Applied Mechanics and Engineering*, 196(49-52):4863–4880, 2007.

[49] Brice Lecampion. An extended finite element method for hydraulic fracture problems. *Communications in Numerical Methods in Engineering*, 25(2):121–133, 2009.

[50] Elizaveta Gordeliy and Anthony Peirce. Implicit level set schemes for modeling hydraulic fractures using the xfem. *Computer Methods in Applied Mechanics and Engineering*, 266:125–143, 2013.

[51] Anthony R Lamb, Gerard J Gorman, and Derek Elsworth. A fracture mapping and extended finite element scheme for coupled deformation and fluid flow in fractured porous media. *International journal for numerical and analytical methods in geomechanics*, 37(17):2916–2936, 2013.

[52] EW Remij, JJC Remmers, JM Huyghe, and DMJ Smeulders. The enhanced local pressure model for the accurate analysis of fluid pressure driven fracture in porous materials. *Computer Methods in Applied Mechanics and Engineering*, 286:293–312, 2015.

[53] EW Remij, JJC Remmers, JM Huyghe, and DMJ Smeulders. On the numerical simulation of crack interaction in hydraulic fracturing. *Computational Geosciences*, 22(1):423–437, 2018.

[54] Benjamin Ganis, Mark E Mear, A Sakhaee-Pour, Mary F Wheeler, and Thomas Wick. Modeling fluid injection in fractures with a reservoir simulator coupled to a boundary element method. *Computational Geosciences*, 18(5):613–624, 2014.

[55] Mary F Wheeler, T Wick, and W Wollner. An augmented-lagrangian method for the phase-field approach for pressurized fractures. *Computer Methods in Applied Mechanics and Engineering*, 271:69–85, 2014.

[56] Christian Miehe, Steffen Mauthe, and Stephan Teichtmeister. Minimization principles for the coupled problem of darcy–biot-type fluid transport in porous media linked to phase field modeling of fracture. *Journal of the Mechanics and Physics of Solids*, 82:186–217, 2015.

[57] Zachary A Wilson and Chad M Landis. Phase-field modeling of hydraulic fracture. *Journal of the Mechanics and Physics of Solids*, 96:264–290, 2016.

[58] Christian Miehe and Steffen Mauthe. Phase field modeling of fracture in multi-physics problems. part III. crack driving forces in hydro-poro-elasticity and hydraulic fracturing of fluid-saturated porous media. *Computer Methods in Applied Mechanics and Engineering*, 304:619–655, 2016.

[59] Howard Wainer. *Picturing the uncertain world: How to understand, communicate, and control uncertainty through graphical display.* Princeton University Press, 2009.

[60] John Tinsley Oden, Ivo Babuška, and Danial Faghihi. Predictive computational science: Computer predictions in the presence of uncertainty. *Encyclopedia of Computational Mechanics Second Edition*, pages 1–26, 2017.

[61] Hermann G Matthies. Computational aspects of probability in non-linear mechanics. *Engineering Structures under Extreme Conditions. Multi-physics and multi-scale computer models in non-linear analysis and optimal design of engineering structures under extreme conditions*, 194, 2004.

[62] Ronald A Fisher. On the mathematical foundations of theoretical statistics. *Philosophical Transactions of the Royal Society of London. Series A, Containing Papers of a Mathematical or Physical Character*, 222(594-604):309–368, 1922.

[63] Donald Gillies. *Philosophical theories of probability.* Routledge, 2012.

[64] Charles J Geyer. 5601 notes: the sandwich estimator. *School of Statistics, University of Minnesota*, 2003.

[65] Jerzy Neyman. Frequentist probability and frequentist statistics. *Synthese*, 36(1):97–131, 1977.

[66] Susanne Rässler. *Statistical matching: A frequentist theory, practical applications, and alternative Bayesian approaches*, volume 168. Springer Science & Business Media, 2012.

[67] Albert Tarantola. *Inverse problem theory and methods for model parameter estimation*, volume 89. siam, 2005.

[68] Robert E Melchers and André T Beck. *Structural reliability analysis and prediction*. John Wiley & Sons, 2018.

[69] John Tinsley Oden, Ivo Babuška, and Danial Faghihi. Predictive computational science: Computer predictions in the presence of uncertainty. *Encyclopedia of Computational Mechanics Second Edition*, pages 1–26, 2017.

[70] J Tinsley Oden, Robert Moser, and Omar Ghattas. Computer predictions with quantified uncertainty, part ii. *SIAM News*, 43(10):1–4, 2010.

[71] Andrea Saltelli, Stefano Tarantola, Francesca Campolongo, and Marco Ratto. Sensitivity analysis in practice: a guide to assessing scientific models. *Chichester, England*, 2004.

[72] Hermann G Matthies. Uncertainty quantification with stochastic finite elements. *Encyclopedia of computational mechanics*, 2004.

[73] Ali H Nayfeh. *Perturbation methods*. John Wiley & Sons, 2008.

[74] Xiaoping Du. Unified uncertainty analysis by the first order reliability method. *Journal of mechanical design*, 130(9):091401, 2008.

[75] Norman R Draper and Harry Smith. *Applied regression analysis*, volume 326. John Wiley & Sons, 1998.

[76] Karl K Sabelfeld. *Monte Carlo methods in boundary value problems*. Springer, 1991.

[77] S Engelund and R Rackwitz. A benchmark study on importance sampling techniques in structural reliability. *Structural safety*, 12(4):255–276, 1993.

[78] Pol D Spanos and Roger Ghanem. Stochastic finite element expansion for random media. *Journal of engineering mechanics*, 115(5):1035–1053, 1989.

[79] R Ghanem and PD Spanos. Galerkin-based response surface approach for reliability analysis. In *Structural Safety and Reliability*, pages 1081–1088. ASCE, 1989.

[80] Roger G Ghanem and Pol D Spanos. *Stochastic finite elements: a spectral approach*. Courier Corporation, 2003.

[81] Michel Loeve. Probability theory: foundations, random sequences. 1955.

[82] Andrew Gelman, Hal S Stern, John B Carlin, David B Dunson, Aki Vehtari, and Donald B Rubin. *Bayesian data analysis*. Chapman and Hall/CRC, 2013.

[83] George P Rédei. Markov chain monte carlo algorithm. *Encyclopedia of Genetics, Genomics, Proteomics and Informatics*, pages 1156–1156, 2008.

[84] Nicholas Metropolis, Arianna W Rosenbluth, Marshall N Rosenbluth, Augusta H Teller, and Edward Teller. Equation of state calculations by fast computing machines. *The journal of chemical physics*, 21(6):1087–1092, 1953.

[85] Daphne Koller and Nir Friedman. *Probabilistic graphical models: principles and techniques*. MIT press, 2009.

[86] Christophe Andrieu, Nando De Freitas, Arnaud Doucet, and Michael I Jordan. An introduction to mcmc for machine learning. *Machine learning*, 50(1-2):5–43, 2003.

[87] John Von Neumann. 13. various techniques used in connection with random digits. *Appl. Math Ser*, 12(36-38):5, 1951.

[88] Isabel Beichl and Francis Sullivan. The metropolis algorithm. *Computing in Science & Engineering*, 2(1):65, 2000.

[89] Heikki Haario, Eero Saksman, and Johanna Tamminen. An adaptive metropolis algorithm. *Bernoulli*, 7(2):223–242, 2001.

[90] James E Gubernatis. Marshall rosenbluth and the metropolis algorithm. *Physics of plasmas*, 12(5):057303, 2005.

[91] Borek Puza. *Bayesian Methods for Statistical Analysis*. ANU Press, 2015.

[92] Andrew Gelman, Jessica Hwang, and Aki Vehtari. Understanding predictive information criteria for bayesian models. *Statistics and computing*, 24(6):997–1016, 2014.

[93] S Geman and D Geman. Stochastic relaxation, gibbs distributions, and the bayes restoration of images. *IEEE transactions on pattern analysis and machine intelligence*, pages 721–741, 1984.

[94] Alan E Gelfand and Adrian FM Smith. Sampling-based approaches to calculating marginal densities. *Journal of the American statistical association*, 85(410):398–409, 1990.

[95] Hasini Garikapati, Clemens V Verhoosel, E Harald van Brummelen, Sergio Zlotnik, and Pedro Díez. Sampling-based stochastic analysis of the pkn model for hydraulic fracturing. *Computational Geosciences*, 23(1):81–105, 2019.

[96] T. K. Perkins and L. R Kern. Widths of hydraulic fractures. *Journal of Petroleum Technology*, 1961.

[97] RP Nordgren. Propagation of vertical hydraulic fractures. *Society of Petroleum Engineers Journal*, 1972.

[98] Ian N. Sneddon. A note on the problem of the penny-shaped crack. *Mathematical Proceedings of the Cambridge Philosophical Society*, 61(2):609–611, 1965.

[99] Ian N. Sneddon. The distribution of stress in the neighbourhood of a crack in an elastic solid. *Proceedings of the Royal Society of London A: Mathematical, Physical and Engineering Sciences*, 187(1009):229–260, 1946.

[100] A Khristianovic Zheltov et al. 3. formation of vertical fractures by means of highly viscous liquid. In *4th World Petroleum Congress*. World Petroleum Congress, 1955.

[101] Paul Meakin, G Li, LM Sander, E Louis, and F Guinea. A simple two-dimensional model for crack propagation. *Journal of Physics A: Mathematical and General*, 22(9):1393, 1989.

[102] J Geertsma, F De Klerk, et al. A rapid method of predicting width and extent of hydraulically induced fractures. *Journal of Petroleum Technology*, 21(12):1–571, 1969.

[103] Antonin Settari, Michael P Cleary, et al. Development and testing of a pseudo-three-dimensional model of hydraulic fracture geometry. *SPE Production Engineering*, 1(06):449–466, 1986.

[104] ER Simonson, AS Abou-Sayed, RJ Clifton, et al. Containment of massive hydraulic fractures. *Society of Petroleum Engineers Journal*, 18(01):27–32, 1978.

[105] J Adachi, E Siebrits, A Peirce, and J Desroches. Computer simulation of hydraulic fractures. *International Journal of Rock Mechanics and Mining Sciences*, 44(5):739–757, 2007.

[106] Y. Kovalyshen and E. Detournay. A reexamination of the classical PKN model of hydraulic fracture. *Transport in Porous Media*, 81:317–339, 2010.

[107] AP Peirce and EDUARD Siebrits. An eulerian finite volume method for hydraulic fracture problems. *Finite volumes for complex applications IV, ISTE, London*, pages 655–664, 2005.

[108] S.H. Advani and J. Lee. Finite element model simulations associated with hydraulic fracturing. *Society of Petroleum Engineers Journal*, 1982.

[109] Axel KL Ng and John C Small. A case study of hydraulic fracturing using finite element methods. *Canadian Geotechnical Journal*, 36(5):861–875, 1999.

[110] Magnus Wangen. Finite element modeling of hydraulic fracturing on a reservoir scale in 2d. *Journal of Petroleum Science and Engineering*, 77(3):274 – 285, 2011.

[111] Benjamin Ganis, Mark E. Mear, A. Sakhaee-Pour, Mary F. Wheeler, and Thomas Wick. Modeling fluid injection in fractures with a reservoir simulator coupled to a boundary element method. *Computational Geosciences*, 18(5):613–624, Oct 2014.

[112] A Munjiza, DRJ Owen, and N Bicanic. A combined finite-discrete element method in transient dynamics of fracturing solids. *Engineering computations*, 12(2):145–174, 1995.

[113] Brice Lecampion. An extended finite element method for hydraulic fracture problems. *Communications in Numerical Methods in Engineering*, 25(2):121–133, 2009.

[114] Elizaveta Gordeliy and Anthony Peirce. Coupling schemes for modeling hydraulic fracture propagation using the xfem. *Computer Methods in Applied Mechanics and Engineering*, 253:305 – 322, 2013.

[115] M. F. Wheeler, T. Wick, and W. Wollner. An augmented-Lagrangian method for the phase-field approach for pressurized fractures. *Computer Methods in Applied Mechanics and Engineering*, 271:69–85, 2014.

[116] A. Mikelić, M.F. Wheeler, and T. Wick. Phase-field modeling of a fluid-driven fracture in a poroelastic medium. *Computational Geosciences*, 19(6):1171–1195, Dec 2015.

[117] Z. A. Wilson and C. M. Landis. Phase-field modeling of hydraulic fracture. *Journal of the Mechanics and Physics of Solids*, 96:264–290, nov 2016.

[118] C. Miehe and S. Mauthe. Phase field modeling of fracture in multi-physics problems. Part III. Crack driving forces in hydro-poro-elasticity and hydraulic fracturing of fluid-saturated porous media. *Computer Methods in Applied Mechanics and Engineering*, 304:619–655, jun 2016.

[119] Emmanuel Detournay. Mechanics of hydraulic fractures. *Annual Review of Fluid Mechanics*, 2016.

[120] Hongbo Zhao, Zhen Li, Changxing Zhu, and Zhongliang Ru. Reliability analysis models for hydraulic fracturing. *Journal of Petroleum Science and Engineering*, 162:150 – 157, 2018.

[121] D.J. Youn and D.V. Griffiths. Stochastic analysis of hydraulic fracture propagation using the extended finite element method and random field theory. In *Integrating Innovations of Rock Mechanics: Proceedings of the 8th South American Congress on Rock Mechanics, 15–18 November 2015, Buenos Aires, Argentina*, page 189. IOS Press, 2015.

[122] Merle E Hanson, Ronald J Shaffer, Gordon D Anderson, et al. Effects of various parameters on hydraulic fracturing geometry. *Society of Petroleum Engineers Journal*, 21(04):435–443, 1981.

[123] GM Zhang, H Liu, J Zhang, HA Wu, and XX Wang. Three-dimensional finite element simulation and parametric study for horizontal well hydraulic fracture. *Journal of Petroleum Science and Engineering*, 72(3):310–317, 2010.

[124] LF Kemp. Study of Nordgren's equation of hydraulic fracturing. *SPE Production Engineering*, 1990.

[125] Peter Valko and Michael J Economides. *Hydraulic fracture mechanics*, volume 28. Wiley Chichester, 1995.

[126] R.W. Zimmerman and Yeo In-Wook. *Fluid Flow in Rock Fractures: From the Navier-Stokes Equations to the Cubic Law*, pages 213–224. American Geophysical Union (AGU), 2013.

[127] George Keith Batchelor. *An introduction to fluid dynamics*. Cambridge university press, 2000.

[128] George C. Howard and C. R. Fast. *API-57-261*, chapter Optimum Fluid Characteristics for Fracture Extension. American Petroleum Institute, New York, New York, 1957.

[129] José I. Adachi and Anthony P. Peirce. Asymptotic analysis of an elasticity equation for a finger-like hydraulic fracture. *Journal of Elasticity*, 90(1):43–69, Jan 2008.

[130] M. Lowengrub. A note on Griffith cracks. *Proceedings of the Edinburgh Mathematical Society*, 15(2):131–134, 1966.

[131] A. H. England and A. E. Green. Some two-dimensional punch and crack problems in classical elasticity. *Mathematical Proceedings of the Cambridge Philosophical Society*, 59(2):489–500, 1963.

[132] JI Adachi and E Detournay. Self-similar solution of a plane-strain fracture driven by a power-law fluid. *International Journal for Numerical and Analytical Methods in Geomechanics*, 26(6):579–604, 2002.

[133] D Garagash and E Detournay. The tip region of a fluid-driven fracture in an elastic medium. *Transactions-American Society of Mechanical Engineers Journal of Applied Mechanics*, 67(1):183–192, 2000.

[134] Jens M Melenk and Ivo Babuška. The partition of unity finite element method: basic theory and applications. *Computer methods in applied mechanics and engineering*, 139(1-4):289–314, 1996.

[135] S Gutiérrez, M. A nd Krenk. *Stochastic Finite Element Methods*, chapter 20, pages 1–25. Wiley, New York, 2017.

[136] Jerzy Neyman. Outline of a theory of statistical estimation based on the classical theory of probability. *Philosophical Transactions of the Royal Society of London. Series A, Mathematical and Physical Sciences*, 236(767):333–380, 1937.

[137] John Francis Kenney. *Mathematics of statistics*. D. Van Nostrand Company Inc; Toronto; Princeton; New Jersey; London; New York,; Affiliated East-West Press Pvt-Ltd; New Delhi, 2013.

[138] Elaine Barker, William Barker, William Burr, William Polk, and Miles Smid. Recommendation for key management part 1: General (revision 3). *NIST special publication*, 800(57):1–147, 2012.

[139] Armen Der Kiureghian and Pei-Ling Liu. Structural reliability under incomplete probability information. *Journal of Engineering Mechanics*, 112(1):85–104, 1986.

[140] Roger G Ghanem and Pol D Spanos. *Stochastic finite elements: a spectral approach*. Courier Corporation, 2003.

[141] N.R. Warpinski, I.S. Abou-Sayed, Z Moschovidis, and C Parker. Hydraulic fracture model comparison study: Complete results. Technical report, Sandia National Labs., Albuquerque, NM (United States); Gas Research Inst., Chicago, IL (United States), 1993.

[142] Hasini Garikapati, Sergio Zlotnik, Pedro Díez, Clemens V Verhoosel, and E Harald van Brummelen. A proper generalized decomposition (pgd) approach to crack propagation in brittle materials: with application to random field material properties. *Computational Mechanics*, pages 1–23, 2019.

[143] D. Amsallem and C. Farhat. Interpolation method for adapting reduced-order models and application to aeroelasticity. *AIAA Journal*, 46(7):1803–1813, Jul 2008.

[144] Rubén Ibañez, Emmanuelle Abisset-Chavanne, Jose Vicente Aguado, David Gonzalez, Elias Cueto, and Francisco Chinesta. A manifold learning approach to data-driven computational elasticity and inelasticity. *Archives of Computational Methods in Engineering*, 25(1):47–57, Jan 2018.

[145] E. Capiez-Lernout, C. Soize, and M. P. Mignolet. Computational stochastic statics of an uncertain curved structure with geometrical nonlinearity in three-dimensional elasticity. *Computational Mechanics*, 49(1):87–97, Jan 2012.

[146] J Oliver, M Caicedo, Alfredo Edmundo Huespe, JA Hernández, and Emmanuel Roubin. Reduced order modeling strategies for computational multiscale fracture. *Computer Methods in Applied Mechanics and Engineering*, 313:560–595, 2017.

[147] Francisco Chinesta, Pierre Ladeveze, and Elías Cueto. A short review on model order reduction based on proper generalized decomposition. *Archives of Computational Methods in Engineering*, 18(4):395, 2011.

[148] Sergio Zlotnik, Pedro Díez, David Modesto, and Antonio Huerta. Proper generalized decomposition of a geometrically parametrized heat problem with geophysical applications. *International Journal for Numerical Methods in Engineering*, 103(10):737–758, 2015.

[149] Marianna Signorini, Sergio Zlotnik, and Pedro Díez. Proper generalized decomposition solution of the parameterized helmholtz problem: application to inverse geophysical problems. *International Journal for Numerical Methods in Engineering*, 109(8):1085–1102, 2017.

[150] Francisco Chinesta, Amine Ammar, and Elías Cueto. Recent advances and new challenges in the use of the proper generalized decomposition for

solving multidimensional models. *Archives of Computational methods in Engineering*, 17(4):327–350, 2010.

[151] Pierre Ladevèze, J-C Passieux, and David Néron. The latin multiscale computational method and the proper generalized decomposition. *Computer Methods in Applied Mechanics and Engineering*, 199(21-22):1287–1296, 2010.

[152] Anthony R Ingraffea. Computational fracture mechanics. *Encyclopedia of computational mechanics*, 2004.

[153] Alberto Sibileau, Alberto García-González, Ferdinando Auricchio, Simone Morganti, and Pedro Díez. Explicit parametric solutions of lattice structures with proper generalized decomposition (PGD). *Computational Mechanics*, 62(4):871–891, 2018.

[154] David Percy Rooke and David John Cartwright. *Compendium of stress intensity factors*. London: H.M.S.O, 1976.

[155] M Loève. Elementary probability theory. In *Probability Theory I*, pages 1–52. Springer, 1977.

[156] Francisco Chinesta, Roland Keunings, and Adrien Leygue. *The proper generalized decomposition for advanced numerical simulations: a primer*. Springer Science & Business Media, 2013.

[157] Amine Ammar, Bechir Mokdad, Francisco Chinesta, and Roland Keunings. A new family of solvers for some classes of multidimensional partial differential equations encountered in kinetic theory modeling of complex fluids. *Journal of Non-Newtonian Fluid Mechanics*, 139(3):153 – 176, 2006.

[158] Amine Ammar, Bechir Mokdad, Francisco Chinesta, and Roland Keunings. A new family of solvers for some classes of multidimensional partial differential equations encountered in kinetic theory modelling of complex fluids: Part ii: Transient simulation using space-time separated representations. *Journal of Non-Newtonian Fluid Mechanics*, 144(2):98 – 121, 2007.

[159] Francisco Chinesta, Amine Ammar, and Elías Cueto. Recent advances and new challenges in the use of the proper generalized decomposition for solving multidimensional models. *Archives of Computational Methods in Engineering*, 17(4):327–350, Dec 2010.

[160] Pedro Díez, Zlotnik Sergio, Alberto García-González, and Antonio Huerta. Algebraic PGD for tensor separation and compression: An algorithmic approach. *in preparation*, 2019.

[161] David Modesto, Sergio Zlotnik, and Antonio Huerta. Proper generalized decomposition for parameterized helmholtz problems in heterogeneous and unbounded domains: Application to harbor agitation. *Computer Methods in Applied Mechanics and Engineering*, 295:127–149, 2015.

[162] Pedro Díez, Zlotnik Sergio, and Huerta Antonio. Generalized parametric solutions in stokes flow. *Computer Methods in Applied Mechanics and Engineering*, 326:223 – 240, 2017.

[163] Sergio Zlotnik, Pedro Díez, David Gonzalez, Elías Cueto, and Antonio Huerta. Effect of the separated approximation of input data in the accuracy of the resulting PGD solution. *Advanced Modeling and Simulation in Engineering Sciences*, 2(1):28, 2015.

[164] Pedro Díez, Sergio Zlotnik, Alberto García-González, and Antonio Huerta. Algebraic PGD for tensor separation and compression: An algorithmic approach. *Comptes Rendus Mècanique*, 346(7):501 – 514, 2018.

[165] L. De Lathauwer, B. De Moor, and J. Vandewalle. A multilinear singular value decomposition. *SIAM Journal on Matrix Analysis and Applications*, 21(4):1253–1278, 2000.

[166] J. Douglas Carroll and Jih-Jie Chang. Analysis of individual differences in multidimensional scaling via an n-way generalization of "eckart-young" decomposition. *Psychometrika*, 35(3):283–319, Sep 1970.

[167] R. A. Harshman. Foundations of the PARAFAC procedure: Models and conditions for an "explanatory" multimodal factor analysis. *UCLA Working Papers in Phonetics*, 16(3):1–84, 1970.

[168] Ledyard R. Tucker. Some mathematical notes on three-mode factor analysis. *Psychometrika*, 31(3):279–311, Sep 1966.

[169] T. Kolda and B. Bader. Tensor decompositions and applications. *SIAM Review*, 51(3):455–500, 2009.

[170] Amine Ammar, Francisco Chinesta, and Antonio Falco. On the convergence of a greedy rank-one update algorithm for a class of linear systems. *Archives of Computational Methods in Engineering*, 17(4):473–486, 2010.

[171] Francisco Chinesta, Roland Keunings, and Adrien Leygue. *The proper generalized decomposition for advanced numerical simulations: a primer*. Springer Science & Business Media, 2013.

[172] AA Griffith and John J Gilman. The phenomena of rupture and flow in solids. *Transactions of the ASM*, 61:855–906, 1968.

[173] Ted L Anderson. *Fracture mechanics: fundamentals and applications*. CRC press, 2017.

[174] Hasini Garikapati, Jassin van De Poll, Sergio Zlotnik, Pedro Díez, E Harald van Brummelen, and Clemens V Verhoosel. Uncertainty quantification for pressure-driven fracture processes: Sampling-based bayesian inference using the pkn model. *Computational Geosciences(in preparation)*.

[175] Albert Tarantola. *Inverse problem theory and methods for model parameter estimation*, volume 89. siam, 2005.

[176] R. G. Ghanem and P. D. Spanos. Spectral techniques for stochastic finite elements. *Archives of Computational Methods in Engineering*, 4(1):63–100, Mar 1997.

[177] Thomas Bayes. LII. an essay towards solving a problem in the doctrine of chances. By the late Rev. Mr. Bayes, FRS communicated by Mr. Price, in a letter to John Canton, AMFR S. *Philosophical transactions of the Royal Society of London*, (53):370–418, 1763.

[178] Armen Der Kiureghian and Pei-Ling Liu. Structural reliability under incomplete probability information. *Journal of Engineering Mechanics*, 112(1):85–104, 1986.

[179] SP Huang, ST Quek, and KK Phoon. Convergence study of the truncated karhunen–loeve expansion for simulation of stochastic processes. *International journal for numerical methods in engineering*, 52(9):1029–1043, 2001.

[180] Harry L Van Trees Jr, Arthur B Baggeroer, LD Collins, RR Kurth, and TJ Cruise. Detection and estimation theory. Technical report, Research Laboratory of Electronics (RLE) at the Massachusetts Institute of Technology, 1968.

[181] Eivind Fonn, Harald van Brummelen, Trond Kvamsdal, and Adil Rasheed. Fast divergence-conforming reduced basis methods for steady navier–stokes flow. *Computer Methods in Applied Mechanics and Engineering*, 346:486–512, 2019.

[182] Wei Liu and Weisi Lin. Additive white gaussian noise level estimation in svd domain for images. *IEEE Transactions on Image processing*, 22(3):872–883, 2012.

[183] Alan C Bovik. *Handbook of image and video processing*. Academic press, 2010.

[184] Rafael C Gonzalez, Richard E Woods, et al. Digital image processing [m]. *Publishing house of electronics industry*, 141(7), 2002.

[185] David P Doane. Aesthetic frequency classifications. *The American Statistician*, 30(4):181–183, 1976.

[186] David W Scott. On optimal and data-based histograms. *Biometrika*, 66(3):605–610, 1979.

[187] Herbert A Sturges. The choice of a class interval. *Journal of the american statistical association*, 21(153):65–66, 1926.

[188] David Freedman and Persi Diaconis. On the histogram as a density estimator: L 2 theory. *Probability theory and related fields*, 57(4):453–476, 1981.

[189] David W Scott and Stephan R Sain. Multidimensional density estimation. *Handbook of statistics*, 24:229–261, 2005.

[190] Peter H Peskun. Optimum monte-carlo sampling using markov chains. *Biometrika*, 60(3):607–612, 1973.

[191] PH Peskun. Guidelines for choosing the transition matrix in monte carlo methods using markov chains. *Journal of Computational Physics*, 40(2):327–344, 1981.

[192] Nicholas Metropolis and Stanislaw Ulam. The monte carlo method. *Journal of the American statistical association*, 44(247):335–341, 1949.

[193] W Keith Hastings. Monte carlo sampling methods using markov chains and their applications. 1970.

[194] Andrew Gelman, Donald B Rubin, et al. Inference from iterative simulation using multiple sequences. *Statistical science*, 7(4):457–472, 1992.

[195] Stephen P Brooks and Andrew Gelman. General methods for monitoring convergence of iterative simulations. *Journal of computational and graphical statistics*, 7(4):434–455, 1998.

[196] Robert E Kass, Bradley P Carlin, Andrew Gelman, and Radford M Neal. Markov chain monte carlo in practice: a roundtable discussion. *The American Statistician*, 52(2):93–100, 1998.

[197] Brian D Ripley. *Stochastic simulation*, volume 5. Wiley Online Library, 1987.

[198] John Francis Kenney and Ernest Sydney Keeping. Mathematics of statistics-part one. 1954.

[199] NR Warpinski, PT Branagan, RE Peterson, SL Wolhart, et al. An interpretation of m-site hydraulic fracture diagnostic results. In *SPE rocky mountain regional/low-permeability reservoirs symposium*. Society of Petroleum Engineers, 1998.

[200] Bridget R Scanlon, Robert C Reedy, Frank Male, and Mark Walsh. Water issues related to transitioning from conventional to unconventional oil production in the permian basin. *Environmental science & technology*, 51(18):10903–10912, 2017.

[201] Noel Cressie, Catherine A Calder, James S Clark, Jay M Ver Hoef, and Christopher K Wikle. Accounting for uncertainty in ecological analysis: the strengths and limitations of hierarchical statistical modeling. *Ecological Applications*, 19(3):553–570, 2009.

[202] Stefan Heinrich. Multilevel monte carlo methods. In *International Conference on Large-Scale Scientific Computing*, pages 58–67. Springer, 2001.

[203] Michael B Giles. Multilevel monte carlo path simulation. *Operations Research*, 56(3):607–617, 2008.

Curriculum vitae

Hasini Garikapati was born in Guntur, India in 1986. She finished her schooling in Vijaywada and was awarded a gold medal for academic excellence. After finishing her secondary education in 2003, she studied Mechanical Engineering at National Institute of Technology, Warangal (NITW). During her bachelors at NITW, she was awarded a merit scholarship for excellence academic record for being 1% and received full financial aid. Hasini chose to get industrial research exposure and joined as a Scientist/Engineer at Indian Space Research Organisation (ISRO) in 2009. In her three year period at ISRO, she worked at Solid Propellant Space Booster Plant and involved in design, development and testing of different sub-systems involved in the solid stage of existing Indian launch vehicles such as PSLV and GSLV. In 2012, she received an Erasmus Mundus scholarship to pursue double master's in computational mechanics at Technical University of Catalonia, Spain and University of Stuttgart, Germany. After her graduation, she received an Erasmus Mundus Join Doctorate Fellowship (EMJD-SEED) offered by European Commission, and started her PhD project at the Eindhoven University of Technology, The Netherlands and Technical University of Catalonia, Spain. The results of her PhD research are presented in this dissertation.

Acknowledgements

I am a combined effort of everyone who has directly or indirectly influenced and supported me. This is too little space to mention all of them. However, I would like to mention a few people who made this PhD possible.

Firstly I would like to thank Harald van Brummelen who has given me this wonderful opportunity to be a doctoral student in his group. I still remember the first time Harald has interviewed me back in January 2015. I felt very positive and enthusiastic after my interview and till today I feel the same after every interaction with him. I cannot thank enough for all the constructive feedback, positivity and support he has provided me all through my PhD. I equally thank my daily supervisor Clemens Verhoosel who has always been there and provided me all the support I need during the ups and downs of this PhD journey. I always admired his motivation and passion for work. His encouragement gave me the courage and confidence to broaden my knowledge and skills. Both Harald and Clemens gave me a lot of guidance and freedom at each step of my PhD and played an important role in shaping up the person I am today. Next, I would like to thank Pedro Díez and Sergio Zlotnik who were my supervisors in Barcelona. I have first known them as a master's student at UPC, Barcelona. I took their courses during my masters and it is because of such excellent teachers at UPC, I was motivated to do a PhD in computational mechanics. I always admired Pedro's knowledge and a bird's eye perspective in the field of computational mechanics. I thank you, Sergio, for all the patience and answering even the most trivial questions I asked. I admire all my four supervisors and learnt a lot from their unique and awe-inspiring personalities. Additionally, I would want to extend my thanks to ever-smiling Linda Essink and Lelia Zielonka who have helped me navigate all the administrative processes with so much ease. I cherish how welcoming they both have been when I first joined the group at Eindhoven and Barcelona.

I thank the Erasmus Mundus program for giving me a great opportunity to pursue my masters and PhD. My first foreign outing was in Barcelona for my masters and, I feel grateful to the city of Barcelona which made me fall in love

with Europe, gave me life-long friends, a life partner, and the best football club. I look forward to every single day to be at the university. One of the main reasons for that is my colleagues at Eindhoven and Barcelona. I would like to thank each one of you for providing such a great work atmosphere. I relish all the coffee breaks and lunch discussions we had over the course of these years. With some of the colleagues, the relationship extended beyond the university. In particular, I would like to mention a few of them. My first friend at TUE who was my work buddy, Mahnaz. Thanks for being such a lovely friend who has listened patiently to everything I have to say and always came up with great advice. Frits, I can't thank you enough for being my work-partner and often going to inexplicable lengths to make me feel good (and sometimes not so good) about myself. Sai, thanks for being my 3am friend and bringing so much warmth. I also want to thank Timo and Gertjan, two people I admire a lot for their knowledge and opinions. I also like to thank my former office mates and colleagues, Tuong, Chaozhang, Nitish, Micheal, Xun Xun Elisa, Triston and Daan with whom I had more personal discussions than professional that provided much-needed relief at the office. I was in Barcelona for ten months away from my house and my partner, yet I felt my stay so enjoyable and thanks to a few people who made this possible. I would want to thank David, Olga, Alex, Karim, Alberto, Arash for being such good friends. I enjoyed a lot from all the discussions we had about 'saving the world' which often extending my stay at the university till late hours in the evening.

I feel grateful to have wonderful friends in my life. They have supported me and instilled a lot of confidence when I was in self-doubt during my PhD. I never felt these friends of mine are on the other side of the world. They made sure they are there with me through all those video calls, phone calls, greeting cards, and letters. They took my tears as gracefully as my smiles. In particular, I want to mention a few of my best friends, Harika, Ridhima, Vijju, Satya, Claudia, Pranav, Revathi, Manasa. I also would like to extend my gratitude to all the friends I made in Eindhoven who have become my extended family. Sai Sandeep and Gokul thanks for always being there for me.

Nothing would have been possible without the support of my family. During my PhD, I got married and my family became bigger and so as my support system. Thanks, Vidya, Visu and appa for always encouraging me. I miss my father, who would have been so proud of my education. My fondest memories with him always been conversations about physics, politics and philosophy which are still my favorite topics. Thanks for instilling interest in such powerful topics when I was still a child. I am indebted to my parents for the best gift they presented in my life in the form of my brother. Tammudu is my alter-ego, makes my life complete in every way and I can't thank him enough for being the better half of me. I am always short of words when it comes to thanking my husband,

Vinoth. He has been my love, laughter and sunshine even in never-ending grey days we have in the Netherlands. Vinothi, thanks for being the best human being I ever met and making my life so beautiful.

From the bottom of my heart, I want to thank four wonderful women of my life who have influenced me the most, my two grandmothers, my mother-in-law and my mother. Unfortunately, I lost one of my grandmother and my mother-in-law during my PhD and nobody can fill the void they left in my life. I have learnt patience, kindness, and tolerance from them and I thank them for being my role-models and laying such strong moral foundations in my life. Finally, I dedicate my thesis to my mother. Her words - 'Education is the only way of (woman) empowerment' inspired me to take learning with so much commitment. Her patience, perseverance and unconditional love motivated me all along. Amma, this is for you.

Being an avid book reader, I always admired writers. And I conclude by quoting one of my favorite author, Fyodor Dostoevsky 'But how could you live and have no story to tell?' and this PhD has been the most insightful story of my life. I once gain thank everybody who are part of my story.

Hasini Garikapati,
Veldhoven, February 2020.

Summary

Improved understanding of pressure-driven fracture processes is important in a wide range of fields, such as environmental engineering, biomechanical engineering, and geomechanics. This thesis focuses on the simulation of hydraulic fracturing as a technique to enhance reservoir connectivity. Simulation of fluid-driven fracturing is challenging as it involves the coupling of various models, *viz.*: *i)* a solid model for the deformation of the rock due to induced pressure by the fluid; *ii)* a flow model for the fluid which includes a model for fluid leak off into the rock formation; *iii)* a fracture propagation model. Moreover, the parameters involved in hydraulic fracturing processes are surrounded by uncertainty, as available data on, e.g., rock formations are scant and available models are still rudimentary. Because of the risks involved in the hydraulic fracturing process, there is an increasing need to quantify the uncertainty in pressure-driven fracturing models and to improve their predictive capabilities.

The primary objective of this doctoral thesis is to develop a computational framework that combines simulation techniques for pressure-driven fracturing processes with state-of-the-art uncertainty quantification techniques. The critical elements in the developed computational uncertainty quantification framework are: *i)* a forward model that predicts the evolution of a pressure-driven fracture in the presence of parameter uncertainty, e.g., random formation properties; *ii)* a model order reduction step to reduce the complexity of the computational problem, and *iii)* an inverse model capable of using measurements, e.g. well pressures, to infer uncertain system parameters. The effective combination of these computational techniques improves the knowledge of the uncertain parameters involved in the fracturing process.

For the forward model, we consider the Perkins-Kern-Nordgren (PKN) model for hydraulic fracturing, as this is a well-established model in the petroleum industry. The PKN model is strongly non-linear on account of its free-boundary character, its time-dependence, and the presence of a solution singularity at the moving tip. We have proposed a simulation technique for the PKN model based on the Finite Element Method (FEM). To endow the computational model with predictive capabilities in the context of the developed uncertainty quantification

framework, it is essential to enrich the computational basis in order to adequately represent the singular tip behavior, and to enforce the global mass balance in the simulation through a Lagrange multiplier technique. This computational PKN model - which is validated based on results reported in the literature - is used in a sensitivity analysis to quantify the influence of various parameters on the fracturing process. Furthermore, a detailed probabilistic analysis of the hydraulic fracturing process is performed using the Monte Carlo sampling method. The results acquired from this forward problem setting provide insight into the uncertain system parameters and their influence on the fracture process.

To infer uncertain system parameters based on observables, an inverse problem must be solved. From an algorithmic perspective, the considered inverse solution procedure solves the forward problem many times (typically thousands). In this regard, it is essential that the forward model provides a practical balance between model accuracy and affordability in terms of computational effort. For finite element simulation this typically implies that a model order reduction step must be conducted. In this thesis we propose a model order reduction framework for fracture problems which combines the Proper Generalized Decomposition (PGD) reduction technique with the Griffith's model for crack propagation in brittle materials. The developed framework provides explicit parametric solutions, which can efficiently be employed in non-intrusive sampling-based techniques (e.g., Monte Carlo type sampling techniques).

The considered inverse model is based on Bayesian inference techniques, which in essence provide a framework to update information regarding uncertain model parameters using measurement data. The uncertain parameter inference is conducted through the Markov chain Monte Carlo sampling technique, in which the forward model is used to assess the likelihood of a parameter realization in relation to the observables. We have explored various data representations for both the uncertain system parameters and for the observables, where in particular the representation of the observables based on a Singular Value Decomposition is a novel contribution that makes the proposed framework practical in the context of data-abundant pressure-driven fracture propagation models.

The computational uncertainty quantification framework is demonstrated for hydraulic fracturing applications, where it is shown that the systematic combination of the model properties with the observed data provides a better estimation of the fracturing process than would be obtained by either the model or the data separately. The suitability of the proposed framework for uncertainty quantification for pressure-driven fractures is verified based on two scenarios with synthetically generated data, namely a data-abundant and a data-scant setting. For both cases, the Bayesian inference framework is capable of improving upon the prior information by using the measurement data.